SURFACE CHEMISTRY CONTROL OF 2D NANOMATERIAL MORPHOLOGIES, OPTOELECRONIC RESPONSES, AND PHYSICOCHEMICAL PROPERTIES

by

Jacob T. Lee

A Dissertation

Submitted to the Faculty of Purdue University
In Partial Fulfillment of the Requirements for the degree of

Doctor of Philosophy

Department of Chemistry and Chemical Biology at IUPUI
Indianapolis, Indiana
May 2022

THE PURDUE UNIVERSITY GRADUATE SCHOOL
STATEMENT OF COMMITTEE APPROVAL

Dr. Rajesh Sardar
Chemistry and Chemical Biology, Chair

Dr. Frédérique Deiss
Chemistry and Chemical Biology

Dr. Eric Long
Chemistry and Chemical Biology

Dr. Ian Webb
Chemistry and Chemical Biology

Approved by:
Dr. Eric Long

To my parents, for laying the foundation to the journey. To my wife, for the support and encouragement along the way. To my girls, for making it all worth it.

ACKNOWLEDGMENTS

First and foremost, I would like to thank my research advisor Dr. Rajesh Sardar for accepting me into his group. After my time here, I now realize that choice is not trivial considering the amount of time, effort, and care he invested in my growth as a scientist and as a person. At every turn he has provided support, guidance, and encouragement towards achieving and surpassing the goals I set for myself in our first meeting. His passion for doing good science is infectious and is something I will take with me for the rest of my career. Upon entering the lab, I felt I was treated as an early career colleague/mentee where my ideas and opinions were listened to and considered. Most of the time, those ideas were incorrect at best; nevertheless, he spent time explaining and discussing my ideas. These discussions are some of my most valued experiences, as the importance he placed on scientific discourse allowed for some of my greatest leaps in knowledge and skill as a scientist. His relentless drive and work ethic was an example I wanted and still want to emulate. It is a high bar, but it has led to some truly great accomplishments and experiences such as publishing high impact work, attending national and international conferences, and conducting research at national labs. I also appreciate the importance he places on family and the support he has given me as my family grew by two members during my tenure in the group. I cannot express enough thanks and gratitude for the impact you have had on me in my journey as a scientist and individual.

I would like to thank my dissertation committee, Dr. Frédérique Deiss, Dr. Eric Long, and Dr. Ian Webb. I chose all of you based upon positive experiences and interactions both in and out of the classroom early in my graduate career. I thank each of you for your time and ongoing support and dedication as my graduate experience nears the finish line.

I would like to express special thanks to Dr. Deiss for her support and encouragement throughout my time at IUPUI. I appreciate the time you spent reviewing my scientific work such as presentations and for the more mundane conversations regarding the program and science in general. Your approachability and the care you show for students made me feel part of the community at IUPUI.

Additionally, I must thank Dr. Parth Basu for all the conversations we had at poster sessions, in the hallways, and at conferences. Your willingness to be open and honest with my numerous questions is greatly appreciated. I learned a great deal of science from you, but the example you set also highlights how to be a scientist within the greater community.

None of this would have been possible without the help of Dr. Anne Shanahan, Wai Ping, Caroline Miller, Jim Crase, Beverly Foley, Lynn Gerrard, and Kitty O'Doherty. Without your support the research and would be even more difficult to complete and graduate students would never meet a deadline. Anne, you are a miracle worker without whom the UV-vis-NIR would have been buried long ago.

I want to thank all my peers and especially my fellow lab members. Having others to share experiences with, bounce ideas off, and get advice from made the lab an enjoyable place to work! Many challenges would never have been surmounted if it wasn't for all of you.

Finally, yet most importantly, I would like to thank my family for always being there to encourage and provide the necessary push to see this journey to completion. Betsy, you supported my goal of returning to school to obtain a PhD and have steadfastly encouraged me along the way. I thank you, for I may have never taken the first step without you. To my girls, Moira and Josie, coming home to you every day puts a smile on my face no matter how research was progressing. To my loving parents, for always being there to listen and helping with the girls when we needed you, I cannot express enough gratitude for enabling my achievements.

Thank you all.

TABLE OF CONTENTS

LIST OF TABLES 9

LIST OF FIGURES 10

LIST OF ABBREVIATIONS 16

ABSTRACT 18

CHAPTER 1. THE IMPORTANCE OF 2D NANOMATERIAL SURFACES 20

- 1.1 Motivation 20
- 1.2 Electronic Structure of 2D Nanomaterials 25
- 1.3 2D Nanomaterials of Focus 29
  - 1.3.1 Halide Perovskites – $Cs_3Bi_2X_9$, where X is -Cl, -Br, -I 29
  - 1.3.2 Transition metal oxides (TMOs) – Oxygen deficient tungsten oxide (WO_{3-x}) 32
  - 1.3.3 Transition metal carbides and nitrides – $Ti_3C_2T_x$ (MXenes) 34
- 1.4 Surface Related Properties of 2D Nanomaterials 36
  - 1.4.1 Programmable Morphology 37
  - 1.4.2 Optoelectronic Properties 39
  - 1.4.3 Physicochemistry Properties 42
- 1.5 Purpose and Specific Aims of Dissertation 45
- 1.6 Future Outlook 45

CHAPTER 2. COLLOIDAL SYNTHESIS OF SINGLE LAYER QUASI-RUDDLESDEN-POPPER PHASE BISMUTH-BASED TWO-DIMENSIONAL PEROVSKITE NANOSHEETS WITH CONROLLABLE OPTOELECTORNIC PROPERTIES 47

- 2.1 Synopsis 47
- 2.2 Introduction 47
- 2.3 Results and Discussion 49
- 2.4 Conclusions 62
- 2.5 Experimental Section 62
  - 2.5.1 Materials. 62
  - 2.5.2 Synthesis of Cs-caroboxylate-PEG6. 62
  - 2.5.3 Synthesis of (PEG6-NH3+)n$Cs_{3-n}Bi_2X_9$, X = Cl, Br, and I) Perovskite Nanosheets. 63
  - 2.5.4 Characterizations 63

CHAPTER 3. SURFACE LIGAND CONTROLLED ENHANCEMENT OF CARRIER DENSITY IN PLASMONIC TUNGSTEN OXIDE NANOCRYSTALS: SPECTROSCOPIC OBSERVATION OF TRAP STATE PASSIVATION *VIA* MULTIDENTATE METAL-PHOSPHONATE BONDING 65
3.1 Synopsis 65
3.2 Introduction 66
3.3 Results and Discussion 69
3.3.1 Ligand Treatment and the LSPR Property of WO_{3-x} NPLs. 69
3.3.2 Microscopy, Diffraction, and Spectrometry Characterizations to Delineate the Mechanism(s). 71
3.3.3 X-ray Photoelectron and Electron Paramagnetic Resonance Spectroscopic Characterizations of WO_{3-x} NPL Electronic Properties. 76
3.3.4 Vibrational Spectroscopic Evidence of Multidentate W-Phosphonate Bonding in TDPA-Passivated WO_{3-x} NPLs. 78
3.3.5 Determination of N_e Values of WO_{3-x} NPLs via Redox Titration. 83
3.3.6 Refractive Index Sensitivity of LSPR-Active WO_{3-x} NPLs. 85
3.4 Conclusion 86
3.5 Experimental Section 87
3.5.1 Materials. 87
3.5.2 Synthesis and Purification of LSPR-active WO3-x NPLs. 87
3.5.3 Microscopy and Spectroscopy Characterizations. 88
3.5.4 Density Function Theory (DFT) Calculations. 89
3.5.5 NOBF4 Titration Description: 90
3.5.6 Calculation of Free Carrier Density: 90
3.6 Appendix A 91
CHAPTER 4. COVALENT SURFACE MODIFICATION OF $TI_3C_2T_X$ MXENE WITH CHEMICALLY ACTIVE POLYMERIC LIGANDS PROducING HIGHLY CONDUCTIVE AND ORDERED MICROSTRUCTURE FILMS 99
4.1 Synopsis 99
4.2 Introduction 100
4.3 Results and Discussion 103

4.3.1 Synthesis and Characterization of PEG6-Ester-Modified Ti_3C_2 MXene (Ti_3C_2-PEG6 Flakes)........ 103
4.3.2 Physicochemical and Electrical Conductivity Properties of Ti_3C_2-PEG6........ 108
4.3.3 Structural Characteristic of Ti_3C_2-PEG6 Thin-Films........ 112
4.3.4 Introducing Chemical Functionality (“Valance”) onto Ti_3C_2 MXene Flakes........ 115
4.4 Conclusion........ 117
4.5 Experimental Section........ 118
4.5.1 Materials........ 118
4.5.2 $Ti_3C_2T_x$ MXene Synthesis........ 118
4.5.3 Ti_3C_2-PEG6 Synthesis........ 119
4.5.4 Characterization........ 119
CHAPTER 5. CONCLUDING REMARKS........ 122
REFERENCES........ 124
PUBLICATIONS........ 154

LIST OF TABLES

Table 2.1: Summarized optical and electronic values obtained from UPS and UV-vis spectroscopy analyses. [a] Value obtained from the secondary energy cutoff. [b] Calculated work function (Φ). [c] Value obtained from the valence band (VB) region of the UPS spectra, [d] Calculated valence band edge (VB), [e] Optical band gap (BG) determined from Tauc analyses, and [f] Calculated conduction band (CB). All values are with respect to vacuum. 61

Table 3.1: Morphological parameters of NPLs. Width, height, shape factor, LSPR (eV), gamma, Ne of WO_{3-x} NPLs. 75

Table 3.2: DFT-calculated Raman vibration modes of tetradecylphosphonic acid. 91

Table 3.3: DFT-calculated Raman vibration modes of MA bound to tungsten atom via bidentate chelating bonding. 92

Table 3.4: Theoretical Raman vibration modes of bidentate bound TDPA through deprotonated hydroxy oxygen. All vibrations scaled by 0.951 according to ν(C-P). 93

Table 3.5: DFT-calculated Raman stretches of bidentate and chelating bound TDPA through deprotonated hydroxy oxygen. Scaled by 1.012 according to ν(C-P). 94

Table 3.6: DFT-calculated Raman stretches of tridentate bound TDPA. Scaled by 1.046 according to ν(C-P). 95

Table 3.7: DFT-calculated Raman stretches of tridentate chelating bound TDP. Scaled by 1.030 according to ν(C-P). 96

Table 3.8: Comparison of LSPR refractive index unit (RIU) sensitivity of various metal oxide and noble metal nanostructures. 97

LIST OF FIGURES

Figure 1.1: This schematic highlights the major discoveries being discussed in this dissertation regarding the surface chemistry of 2D nanomaterials. 24

Figure 1.2: Simple schematic highlighting the band gap differences between metals (no band gap), semiconductors (small band gap), and insulators (large band gap).The location, size, and manipulation of these band gaps give rise to the electronic and optical properties observed in the different nanomaterials discussed. 26

Figure 1.3: (A) Schematic representation of the quantum confinement effect in semiconductor NCs where the optical band gap (E_g) increases with decreasing size. Also, observed is the appearance of discrete energy levels at the HOMO and LUMO bad edges. (B) The impact of quantum confinement observed in colloidal CdSe NCs as the size decreases from 6 nm to 2 nm. When excited with UV light the color of the photoluminescence changes from red to blue or lower to higher energy, respectively. Adapted from reference 72. (C) The density of states of a metal. (D) The density of states of a semiconductor. Both highlight the discrete band levels at the edges in NCs. However, the band overlap of the metal (C) results in no overall impact of these states even at low temperatures. Adapted from reference 73. 27

Figure 1.4: Idealized density of states for one band in a semiconductor material with varying morphologies. Adapted from reference 73. 29

Figure 1.5: (A) ABX_3 cubic perovskite crystal structure where A is a charge neutralizing cation, B is a small cation ion such as Pb, and X is a halide. Adapted from reference 81. (B) Solution of all inorganic lead halide perovskites highlighting the band gap tunability by altering the halide as observed in the photoluminescence. Adapted from reference 78. (C) A schematic comparison of the defect tolerance between classic semiconductor NCs and all inorganic lead halide perovskites. Adapted from reference 85. (D) Schematic representation of four-layer n=2 2D Ruddlesden-Popper phase perovskite. The long chain ligands/spacers are highlighted. Adapted from reference 90.. 30

Figure 1.6: (A) A graphic representation of the many plasmonic TMOs and their typical LSPR related UV-vis-NIR absorption regions. Adapted from reference 50. (B) Electronic band structure schematic of n-doped semiconductor NCs. In the case of O_v in WO_{3-x} the free carriers (yellow) begin to fill the conduction band. Adapted from reference 114. (C) Graphical representation of increasing N_e in WO_{3-x} caused by increased O_v as the synthesis temperature is raised. Adapted from reference 115. (D) The crystal structure of $WO_{2.72}$ as viewed form the (010) direction. The arrows are highlighting the shear planes caused by edge sharing octahedra. 33

Figure 1.7: (A) Schematic representation of the elemental etching process using HF. (i) Ti3AlC2 MAX phase. (ii) Al atoms replaced with -OH after etching, only -OH is shown for ease of representation. (iii) Individual nanoflakes being separated through sonication. Adapted from reference 54. (B) MXenes reported thus far in literature with the possible structures of different n layers. Mono-M elements, mixed double-M elements, and ordered double-M elements. A list of the formulae that have successfully been characterized and those that are theoretically possible but have not been characterized experimentally. Adapted from reference 55. 35

Figure 1.8: Common surface ligand functional groups used in colloidal synthesis of nanomaterials. (A) X-type ligands are anionic and preferentially bind to cationic surfaces. (B) L-type ligands are neutral with a lone pair of electrons that can be donated to the NCs surface atoms. (C) Z-type ligands are metal complexes that are charge neutral and accept electrons. (D) Preferential binding to different types of facets. Schematically represented using CdSe NCs zinc blende crystal facets. Adapted from reference 159. 38

Figure 1.9: Schematic representation of how typically high N_e plasmonic oxides (blue) form low N_e insulation barriers (grey) which negatively impact their LSPR response and impedes electron transport between NCs. Adapted from reference 185... 42

Figure 1.10: Dispersions of $Ti_3C_2T_x$ highlighting the hydrophilic character based upon the dispersibility in various solvents over a range of polarities. Adapted from reference 153. 44

Figure 2.1: (A) UV-vis spectra of $(PEG6\text{-}NH_3^+)_nCs_{3-n}Bi_2Cl_9$ (blue), $(PEG6\text{-}NH_3^+)_nCs_{3-n}Bi_2Br_9$ (red) and $(PEG6\text{-}NH_3^+)_nCs_{3-n}Bi_2I_9$ (green). The inset displays a typical photoluminescent spectrum of $(PEG6\text{-}NH_3^+)_nCs_{3-n}Bi_2Br_9$ perovskite. (B) A representative SAXS spectrum of $(PEG6\text{-} NH_3^+)_nCs_{3-n}Bi_2Br_9$ nanosheets. Low (C) and high (D) magnification TEM images of $(PEG6\text{-}NH_3^+)_nCs_{3-n}Bi_2Br_9$ nanosheets with the scale bar of 500 and 200 nm, respectively. Yellow dashed lines in (D) outline the presence of single-layer nanosheets. (E) Histograms of lateral and folded edge sizes of D, minimum 50 measurements. (F) XRD of $(PEG6\text{-}NH_3^+)_nCs_{3-n}Bi_2Br_9$ compared to reference for hexagonal $Cs_3Br_2Br_9$. 50

Figure 2.2: TEM image of $(PEG6\text{-}NH_3^+)xCs_{3-x}Bi_2Br_9$. An example of how Image J was used to estimate the thickness of the nanosheet based upon overlap/folds (yellow circles) and provide lateral dimensions of large single layer sheets (yellow lines). The scale bar is 200 nm. Over 50 measurements were taken across multiple images of multiple samples to determine lateral dimensions. 51

Figure 2.3: FTIR Spectrum of purified $(PEG6\text{-}NH_3^+)_nCs_{3-n}Bi_2Br_9$ nanosheets........................... 52

Figure 2.4: XPS spectra for $(PEG6\text{-}NH_3^+)_nCs_{3-x}Bi_2Br_9$ with characteristic fittings of their binding energies and characteristic orbital splitting for (A) bismuth, (B) bromide, (C) cesium and (D) nitrogen. Two types of nitrogen are present: a neutral amine near 400 eV and a protonated amine near 401.6 eV. 53

Figure 2.5: Schematic representation showing conversion of initial precursors to nanocrystals, and then to the formation of individual nanosheets with further stacking of nanosheets under solvent evaporation conditions. 54

Figure 2.6: Synthesis of bromide product with 4 times the typical amount of Cs-PEGylate precursor showing a clear lack of nanosheet formation. Scale bar is 50 nm 54

Figure 2.7: : (A) TEM microscopy image of perovskites nanocrystals synthesized using oleylamine and oleic acid as surface passivating ligands. Scale bar is 100 nm. (B) UV-vis absorption spectrum of the purified nanocrystals.. 55

Figure 2.8: Data for $(PEG6\text{-}NH_3^+))_xCs_{3-x}Bi_2Cl_9$ A) TEM image with representation of Image J analysis for lateral dimensions. Scale bar is 500 nm. (B) PXRD diffractogram comparing the standard for $Cs_3Bi_2Cl_9$. XPS spectra with fittings for (C) bismuth, (D) chloride, (E) cesium, and (F) nitrogen. 56

Figure 2.9: Data for (PEG6-NH_3^+))$_x$Cs$_{3-x}$Bi$_2$I$_9$ A) Low magnification TEM image with a 1.0 µm scale bar. B) Higher magnification TEM image. scale bar is 200 nm. C) PXRD data comparing to the standard for $Cs_3Bi_2I_9$. XPS spectra for (PEG6-NH_3^+))$_x$Cs$_{3-x}$Bi$_2$I$_9$ with characteristic fittings of their binding energies and tell-tale orbital splitting of (D) bismuth, (E) bromide, (F) cesium and (G) nitrogen There are two types of nitrogen present: a neutral amine near 400 eV and a protonated amine near 401 eV. 57

Figure 2.10: UPS high energy cut-off spectra for (PEG6-NH_3^+))$_x$Cs$_{3-x}$Bi$_2$X$_9$ where X chloride (A), bromide (B), iodide (C). See table 2.1 for values. 58

Figure 2.11: (A) Valance band region and (B) secondary energy cut off UPS spectra of (PEG6-NH_3^+)$_n$Cs$_{3-n}$Bi$_2$Cl$_9$ (blue), (PEG6-NH_3^+)nCs$_{3-n}$Bi$_2$Br$_9$ (red) and (PEG6-NH_3^+)$_n$Cs$_{3-n}$Bi$_2$I$_9$ (green). (C) Direct band gap Tauc plot analysis of (PEG6-NH_3^+)$_n$Cs$_{3-n}$Bi$_2$Br$_9$. (D) Band diagram with respect to vacuum where CB is conduction band minimum, VB is valence band edge and E_f is the Fermi energy level. 59

Figure 2.12: SEM images (PEG6-NH_3^+)$_n$Cs$_{3-n}$Bi$_2$Br$_9$ microstructures upon controlled evaporation to obtain hexagonal (A and B) structures. Scale bars in (A) and (B) are 1 µm and 100 nm, respectively. (C) A representative SEM image of petaled structures, and the inset show an individual petal-type structure. Scale bars 1 µm and 100 nm, respectively. (D) PXRD of evaporated hexagonal product. 60

Figure 2.13: Direct band gap tauc plots for (PEG6-NH_3^+))$_x$Cs$_{3-x}$Bi$_2$X$_9$ perovksite nanosheets where X is chloride (A) and iodide (B). 60

Figure 2.14: A representative TEM image of exfoliated (PEG6-NH_3^+))$_x$Cs$_{3-x}$Bi$_2$X$_9$ perovskite nanosheets in dichloromethane. The scale bar is 200 nm. 61

Figure 3.1: A schematic representation of the TDPA ligand treatment in unpurified mixed myristic acid (MA)- and oleylamine (OLA)-passivated WO_{3-x} NPLs. (Left) Tungsten atoms at the edges and corners are passivated with bidentate carboxylate head group of MA. For simplicity, OLA is not shown. (Right) Most of the tungsten atoms at the edges and corners are passivated by phosphonate binding head group of TDPA through tridentate bonding along with the presence of MA. 69

Figure 3.2: (A) UV-Vis-NIR absorption spectrum and (B) TEM of WO_{3-x} nanocrystals (NCs) synthesized using a mixture of tetradecylphosphonic acid (TDPA), myristic acid (MA) and olelyamine (OLA) as surface passivating ligands Scale bar is 20 nm. 70

Figure 3.3: (A) UV-Vis-NIR absorption spectra of as synthesized (black) and TDPA-treated WO_{3-x} NPLs (blue). A blue shift of ~100 nm is observed upon TDPA treatment. Spectra of both samples were collected after purification followed by dispersion in CCl_4. (B) ^{31}P NMR spectra of pure TDPA (red) and TDPA-treated WO_{3-x} NPLs (blue). Spectra were recorded in $CDCl_3$. 71

Figure 3.4: HRTEM images as synthesized (A and B) and (C) and TDPA-treated WO_{3-x} NPLs. In (B), the d-spacing corresponds to the (010) plane of monoclinic WO_{3-x}. The inset shows FFT diffraction of the (010) plane. (D) Histogram of width and length of as synthesized (D) and (E) TDPA-treated NPLs. For the size analysis, a minimum of 300 NPLs were counted. 72

Figure 3.5: (A) XRD diffraction patterns of as synthesized (top, black) and TDPA-treated (bottom, blue) WO_{3-x} NPLs as compared to the monoclinic WO2.72 standard (red, PDF# 71-2450). (B)

Raman spectra of as synthesized (black) and TDPA-treated WO_{3-x} NPLs (blue). Raman spectra were collected using a 532.5 nm laser source. 73

Figure 3.6: High resolution XPS spectra with fittings for W^{+6} and W^{+5} 4f orbital splitting of (A) as synthesized and (B) TDPA-treated WO_{3-x} NPLs. (C) EPR spectra of as synthesized (black) and TDPA-treated NPLs (blue). EPR spectra were acquired at room temperature under identical conditions. EPR spectra were collected under identical experimental conditions. 77

Figure 3.7: Chemical structures with possible bonding motifs between the phosphonate binding head group and tungsten atoms. Monodentate (i and ii), bidentate (iii and iv), bidentate chelating (v and vi), tridentate (vii) and tridentate chelating (viii). 78

Figure 3.8: (A) FTIR spectra of pure TDPA (red), and as synthesized (black) and TDPA-treated WO_{3-x} NPLs (blue) The yellow shaded area represents peaks related to phosphorous oxygen bonding. The symbol (♦) highlights the presence of the amino headgroup from OLA and the symbol (♠) represents carbonyl stretching from MA. (B) Raman spectra of as synthesized (black) and TDPA-treated WO_{3-x} NPLs (blue). (C) Experimental Raman spectrum (blue), and DFT-calculated Raman spectra of TDPA bound to W atoms as bidentate (dark green), bidentate chelating (light green), tridentate (dark red), and tridentate chelating (light red). Black dashed lines are P=O stretching, and yellow shaded areas refer to (O=P-C) deformations. 79

Figure 3.9: DFT calculated Raman spectra of (A) TDPA and (B) MA. 80

Figure 3.10: (A) Schematic illustration of the proposed tridentate bonding between the surface W atoms of a WO_{3-x} NPL and alkylphosphonate group. For simplicity, only a few surface oxygen vacancies are depicted, however most of the oxygen atoms from the corners and edges are removed during the synthesis. (B) Conduction band filling through passivation of shallow trap states via TDPA treatment and transfer of trap electrons. The energy gap between the valance and conduction bands is not to scale. 82

Figure 3.11: UV-Vis-NIR spectra of as synthesized and MA-treated to highlight no blue shift with carboxylic acid treatment. 83

Figure 3.12: UV-Vis-NIR absorption spectra of colloidal (A) as synthesized and (B) TDPA-treated WO_{3-x} NPL solutions recorded after addition of titrated amounts of NOBF4 solution. Graphs of integrated absorption area as a function of NOBF4 molecules for (C) as synthesized and (D) TDPA-treated WO_{3-x} NPLs with fittings of the linear portions (red dashed lines). 84

Figure 3.13: (A) UV-Vis-NIR absorption spectra of (A) as synthesized and (B) TDPA-treated WO_{3-x} NPLs in various solvents with varying refractive index. (C) Relationship between LSPR peak position (λ_{LSPR}) of as synthesized (black squares) and TDPA-treated (blue diamonds) NPLs and the refractive index of the bulk solution. The corresponding sensitivities are 324 and 428 nm/RIU, respectively, determined from the slope of the graph. 86

Figure 3.14: Raw UV-Vis-NIR spectra of (A) as synthesized WO_{3-x} NPLs and (B) TDPA treated WO_{3-x} NPLs in chloroform (black), carbon tetrachloride (red), and tetrachloroethylene (green). 98

Figure 4.1: Schematic diagram of covalent surface modification of pristine $Ti_3C_2T_x$ (T_x: –F, –OH, and/or =O) MXene via esterification reaction where the hydroxy terminations are modified with ester bonded ω-PEG6-COOH forming Ti_3C_2-PEG6. 102

Figure 4.2: (A) UV-vis absorption spectra of Ti_3C_2 MXene flakes before (778 nm) and post covalent surface modification with PEG6-COOH (781 nm). (B) TEM image of pristine Ti_3C_2 MXene flakes. (C) TEM image of post surface modification of Ti_3C_2 MXene with PEG6-COOH. Inset in (C) shows magnified TEM image with a 100 nm scale bar. (D) Raman spectra of Ti_3C_2 MXene flakes and Ti_3C_2-PEG6 flakes highlighting the resonance peak (yellow box), A1g peaks (red dashed lines) and surface E_g related vibrational modes (green arrowed line). (E) FTIR spectra of Ti_3C_2 MXene flakes and Ti_3C_2-PEG6 flakes. Characteristic Ti_3C_2 vibrations are assigned by green dashed lines and box, and the IR vibrational stretches of PEG6-COOH are shown in red. (F) TGA analysis of pristine Ti_3C_2 MXene, pure PEG6-COOH, and Ti_3C_2-PEG6. A 14% mass loss is observed between pristine Ti_3C_2 MXene and Ti_3C_2-PEG6. 104

Figure 4.3: As obtained Raman Spectra of Ti_3C_2-PEG6 (blue) and Ti_3C_2 (black). This highlights the absence of D and G disordered carbon vibrational bands (100-1800 cm^{-1}). The asterisk at ~520 cm^{-1} arises from the silicon substrate. 105

Figure 4.4: FTIR spectrum of lab synthesized PEG6-COOH with the -CH related vibration peaks (2931 cm^{-1}) and carbonyl (1735 cm^{-1}) labeled for reference. 106

Figure 4.5: (A) Solvation study of Ti_3C_2-PEG6 flakes in various organic solvents (left to right) acetonitrile (CH_3CN), methanol (CH_3OH), chloroform ($CHCl_3$), dichloromethane (CH_2Cl_2), and toluene (Ph-CH_3). (B) UV-vis absorption spectra of dispersed Ti_3C_2-PEG6 flakes in those five organic solvents. The inset shows offset peaks to show good peak shape and minimal absorption peak shifts. (C) Dispersibility profile of pristine Ti_3C_2 MXene flakes (left) Ti_3C_2-PEG6 flakes (right) in $CHCl_3$. High concentration of MXene flakes were dispersed via bath sonication and then Images were taken 5 min after the sonication. (D) Contact angles of 2.0 µL water droplet on drop cast films of Ti_3C_2-PEG6 (top) and pristine Ti_3C_2 MXene (bottom). (E) Zeta potential value of aqueous dispersions of pristine Ti_3C_2 MXene and Ti_3C_2-PEG6 flakes. (F) Conductivity values of vacuum filtered films of pristine Ti_3C_2 MXene, Ti_3C_2-PEG6 and Li^+-intercalated Ti_3C_2-PEG6. Error bars include uncertainty from the instrumental reading and SEM cross-section measurement. 108

Figure 4.6: Image of Ti_3C_2-PEG6 dispersed in H_2O at a concentration of ~1 mg/mL. The lingering flakes above the solution occur due to residual immiscible chloroform post reaction solvent exchange back to water. 109

Figure 4.7: SEM cross sections of (A) pristine Ti_3C_2 (B) Ti_3C_2-PEG6 and (C) Li^+@ Ti_3C_2-PEG6 used to calculate height for conductivity calculation. The scale bars are 10 µm. 111

Figure 4.8: (A) Hot stage XRD data showing changes of pre- and post-annealed films of Ti_3C_2-PEG6 vs. pristine Ti_3C_2 MXene. Arrows show the shift in peak position of the basal plane (002) and (004) peaks of each Ti_3C_2 film upon annealing. The diamond marked peaks arise from the Al_2O_3 substrate and are not characteristic of the Ti_3C_2 MXene films. (B) Expanded XRD data with y-axis offset of Ti_3C_2 MXene shift in peak position of the basal plane (002) and (004) peaks of Ti_3C_2 during annealing. (C) Expanded XRD data with y-axis offset of Ti_3C_2-PEG6 shift in peak position of the basal plane (002) and (004) peaks of Ti_3C_2 during annealing. (D) The graph showing changes in the c-lattice parameter during annealing of Ti_3C_2-PEG6 vs. pristine Ti_3C_2 MXene. 112

Figure 4.9: Vacuum filtered prepared films of (A) pristine Ti_3C_2 and (B) Ti_3C_2-PEG6 on alumina membrane substrate. Later used for hot stage XRD analysis. XRD analysis taken on location where good film was formed. 113

Figure 4.10: Graph of inter-flake distance between vacuum filtered films of pristine Ti_3C_2 MXene (red) and modified Ti_3C_2-PEG6 MXenes (blue) calculated using the c-lattice parameter obtained from the hot-stage XRD experiment and a theoretical Ti_3C_2 unit cell dimension. 114

Figure 4.11: (A) Schematic representation of the crystal structure of Ti_3C_2-PEG6 single flake and (B) stacked Ti_3C_2-PEG6 flakes through cooperative ligand-ligand hydrophobic and vdWs interactions. (C) A representative cross sectional SEM image of drop casted Ti_3C_2-PEG6 flakes on the silicon wafer substrate. Scale bar is 100 nm. (D) XRD spectrum of Ti_3C_2-PEG6 after drop casting flakes flowed by solvent evaporation under ambient conditions. The XRD spectrum of drop cast pristine Ti_3C_2 MXene flakes dispersed in water. 115

Figure 4.12: (A) UV-vis spectra of four terminal groups –CH_3 (Ti_3C_2-PEG6), -CH=CH_2, -N_3, -NH_2 and unfunctionalized pristine Ti_3C_2 MXene. (B) FTIR spectrum of Ti_3C_2-PEG6-NH_2 with important NH_2-related vibrational stretched shown with arrows. (C) FTIR spectrum of Ti_3C_2-PEG6-CH=CH_2 with the carbonyl group (-C=O) identified in the red dotted box. (D) Expanded region of ^{1}H NMR spectrum of Ti_3C_2-PEG6-CH=CH_2 showing alkene (-CH=CH_2) region chemical shifts. (E) FTIR spectrum of Ti_3C_2-PEG6-N_3 with azide (-N_3) related stretch identified in the red dotted box. 116

LIST OF ABBREVIATIONS

0D	zero dimensional
1D	one dimensional
2D	two-dimensional
ACN	acetonitrile
CCl_4	carbon tetrachloride
$CDCl_3$	deuterated chloroform
$CHCl_3$	chloroform
$Cl_2C=CCl_2$	tetrachloroethylene
DCC	N,N’-dicylcocarbodiimide
DCM	dichloromethane
DMAP	4-(dimethylamino)pyridine
DMF	dimethylformamide
DMSO	dimethyl sulfoxide
FTIR	Fourier transform infrared spectroscopy
HOMO	highest occupied molecular orbital
LSPR	localized surface plasmon resonance
LUMO	lowest unoccupied molecular orbital
MA	myristic acid
MeOH	methanol
NCs	nanocrystals
N_e	free carrier concentration
NMR	nuclear magnetic resonance spectroscopy
$NOBF_4$	nitrosonium tetrafluoro borate
NPLs	nanoplatelets
ODE	1-octadecene
OLA	oleylamine
PC	propylene carbonate
PEG6	poly(ethylene glycol)6
$Ph\text{-}CH_3$	toluene

QD	quantum dot
SAXS	small angle X-ray scattering
SEM	scanning electron microscopy
SERS	surface enhanced Raman spectroscopy
TDPA	tetradecyl phosphonic acid
TEM	transmission electron microscopy
TMOs	transition metal oxides
UV-vis-NIR	ultraviolet-visible-near infrared spectroscopy
vdWs	van der Waals
XPS	X-ray photoelectron spectroscopy
XRD	X-ray diffraction

ABSTRACT

The field of two-dimensional (2D) nanomaterials first began in earnest with the discovery of graphene in 2004 due to their unique shape-dependent optical, electronic, and mechanical properties. These properties arise due to their one-dimensional confinement and are further influenced by the elemental composition of the inorganic crystal lattice. There has been an intense focus on developing new compositions of 2D nanomaterials to take advantage of their intrinsic beneficial properties in a variety of applications including catalysis, energy storage and harvesting, sensing, and polymer nanocomposites. However, compared to the field of bulk materials, the influence of surface chemistry on 2D nanomaterials is still underdeveloped.

2D nanomaterials are considered an “all-surface” atomic structure with heights of a single to few layers of atoms. The synthetic methods used to produce 2D materials include bottom-up colloidal methods and top-down exfoliation related techniques. Both cases result in poorly controlled surface chemistry with many undercoordinated surface atoms and/or undesirable molecules bound to the surface. Considering the importance surfaces play in most applications (*i.e.*, catalysis and polymer processing) it is imperative to better understand how to manipulate the surface of 2D nanomaterials to unlock their full technological potential. Through a focus of the ligand-surface atom bonding in addition to the overall ligand structure we highlight the ability to direct morphological outcomes in lead free halide perovskites, maximize optoelectronic responses in substoichiometric tungsten oxide, and alter physicochemical properties titanium carbide MXenes.

The careful control of precursor materials including poly(ethylene glycol) (PEG) surface ligands during the synthesis of bismuth halide perovskites resulted in the formation of 2D quasi-Ruddlesden-Popper phase nanomaterials. Through small angle X-ray scattering (SAXS) and in conjunction with X-ray photoelectron spectroscopy (XPS) we were able to conclude that an in-situ formation of an amino functional group on our PEG-amine ligand was inserted into the perovskite crystal lattice enabling 2D morphology formation. Additionally, through UV-vis absorption and ultraviolet photoelectron spectroscopies we were able to develop a complete electronic band structure of materials containing varying halides (*i.e.*, Cl, Br, and I). Furthermore, through the increased solubility profile of the PEG ligands we observed solvent controlled assemblies of varying mesostructures.

We developed an ex-situ ligand treatment to manipulate the localized surface plasmon resonance (LSPR) response of anion vacancy doped tungsten oxide (WO_{3-x}) nanoplatelets (NPLs). Upon ligand treatment to alter the surface passivating ligand from carboxylic acid containing myristic acid (MA) to tetradecylphosphonic acid (TDPA) we observed a >100 nm blue shift in the LSPR response. Using Fourier transform infrared (FTIR) and Raman spectroscopies in conjunction with DFT calculated Raman spectra we were able to conclude this shift was due to the formation of tridentate phosphonate bonds on the NPLs surface. Phosphonate bonding allows for an increase in surface passivation per ligand decreasing surface trapped electrons. These previously trapped electrons were then able to participate as free electrons in the LSPR response. Electron paramagnetic spectroscopy (EPR) further supported this decrease in surface traps through a decrease and shift of the EPR signal related to metal oxide surface trapped electrons.

Lastly, using our knowledge of PEG ligands we were able to modify esterification chemistry to covalently attach PEG ligands to a MXene surface. The successful formation of an ester bond between a carboxylic acid containing PEG ligand and hydroxyl terminating group on the MXene surface was supported by FTIR spectroscopy and thermogravimetric analysis. The attachment of PEG resulted in a drastic change in the hydrophilicity of the MXene surface. Where MXenes were previously only processed in extremely polar solvents the PEG attachment allowed for high dispersibility in a wide range of polar and non-polar organic solvents, effectively increasing their processability. Further, this chemistry was modified to include an additional functional group on the PEG ligand to increase the valency of the post-modification MXene nanoflakes.

Overall, work presented in this dissertation represents the development and application of surface chemistry to relatively new 2D nanomaterials. We believe our work significantly increases the knowledge of 2D halide perovskite formation, manipulation of LSPR active metal oxide materials, and the future processing of MXene materials.

CHAPTER 1. THE IMPORTANCE OF 2D NANOMATERIAL SURFACES

1.1 Motivation

Physicist Richard Feynman is often touted as the "father of nanotechnology" resulting from a talk given at an American Physical Society conference in 1959 entitled "There's Plenty of Room at the Bottom," [1] in which he described a future possibility of obtaining diverse unique property outcomes through manipulation at the atomic scale. Although his speech had little direct impact on the actual realization of the field of nanotechnology, it nonetheless coincides with a scientific movement towards realization of development on the nanometer scale throughout all of science and notably, in the field of inorganic nanomaterials development. The foundation of nanomaterials is based in early experimental and theoretical work describing the phenomenon of how reduction in a material size to tens of nanometers or less results in unique physical, optical, and electronic properties that vary vastly from properties found in its bulk counterpart.[2-3] This early work examined quantum dots (QDs), 0-dimensional (0D) semiconductor materials which exhibit quantum confinement in all directions. However, with the discovery of two-dimensional (2D) graphene in 2004 by Novoselov and Geim an eruption of research into 2D nanomaterials occurred as nanomaterials confined in only one direction produced unexpected shape-dependent properties.[4] Generally, 2D nanomaterials, defined as being only a few atoms in height with lateral dimensions much larger often reaching hundreds of nanometers, offer strong intralayer atomic bonding with only weak van der Waals interlayer interactions, ultrahigh specific surface area, robust mechanical properties, excellent optical transparency, and high charge carrier mobility.[5-6] These general properties are conducive to an extremely large number of applications ranging from energy harvesting and storage, photo-and electro-catalysis, sensing, optics, and electronics to name a few.[6-9] Material specific properties and the ability to manipulate desired outcomes for particular applications of 2D nanomaterials are dependent on the elemental composition of the inorganic core in conjunction with the chemical signature at the surface or interfacial layer.

The scope of possible 2D nanomaterials and their applications is enormous considering the synthesis methods available to today's scientists allow for the use of most of the periodic table as building blocks. The methods are broken down into two categories either top-down or bottom-up. Top-down methods produce 2D nanosheets from bulk layered materials and consist largely of exfoliation methods or selective element etching.[10-13] Bottom-up approaches rely on chemical vapor deposition and colloidal syntheses.[10, 14-15] Compositionally, 2D nanomaterials are often separated into groups based upon similar crystal structures, synthesis methods used in fabrication, and broadly defined properties. These groups generally are divided into metal-free, noble metal, transition metal chalcogenides and dichalcogenides, transition metal oxides, transition metal carbides and nitrides often referred to as MXenes, and transition metal halide perovskite materials.[8, 16] An in-depth description of the materials investigated in this work can be found in **Section 1.4**; however, a brief description of the various 2D nanomaterial groups follows.

The group of metal-free 2D nanomaterials is dominated by graphene, the original 2D nanomaterial, consisting of a single layer of sp^2-hybridized carbon atoms in a honeycomb shape that displays unexpected mechanical robustness and unusually high electronic conductivity.[17-18] Graphene has been implemented in an array of applications including as a conductive substrate/composite in catalysis and sensors, mechanical strengthener in coatings, and as a conductor in flexible electronics.[19-23] Hexagonal boron nitride (hBN) is similar in structure to graphene and consists of repeating atoms of boron and nitrogen. The major difference between these two is that hBN is an insulator.[24] This insulating property and similar structure to graphene allow them to be used in tandem in many nano-electronic devices.[25] It is valued for its high thermal and chemical stability allowing for its use in composite materials.[26-27] Another well-studied metal-free nanomaterial is black phosphorous (BP) which is a semiconducting material with a variable bandgap and high electron mobility with promising optoelectronic and photocatalytic applications.[28-30] Unlike graphene and hBN, BP has a puckered structure in which phosphorus atoms are sp^3-hybridized and neighboring atoms are out of plane with each other.

Single element noble metal 2D nanomaterials (*e.g.,* Au, Ag, Pd, etc.,) have been extensively studied from fundamental research to practical applications. Their bottom-up, wet-chemistry syntheses allow for a wide variety of anisotropic 2D structures including sheets, hexagons, and prisms.[31] They also are inherently metallic in nature meaning they have no band gap between their highest occupied molecular orbital (HOMO) and lowest unoccupied molecular orbital (LUMO) which is ideal for electronic conductivity. Interestingly, confinement of their size into 2D nanomaterials gives rise to a property known as localized surface plasmon resonance (LSPR).[32] LSPR originates due to the oscillation of free carriers, electrons or holes, that have been confined by a nanomaterial size and are excited by electromagnetic oscillation.[33] The metallic nature of these nanomaterials and their LSPR property make them ideal for nanoelectronics, catalysts, and use as sensors due to the local dielectric sensitivity of their LSPR response.[34-36]

The quantity of 2D transition metal chalcogenides (TMCs) and dichalcogenides nanomaterials attained to date is astounding. In general, these are semiconducting materials with the formula of MX or MX_2 where M is a transition metal (*e.g.*, W, Mo, Cd, Zn, *etc.*,.) or post transition metal (*e.g.* Pb) and X is a chalcogen (*i.e.*, S, Se, or Te).[37] This plethora of materials represents a wide range of optoelectronic and chemical possibilities allowing for their use in applications such as energy conversion and storage, optoelectronic devices (*e.g.*, LEDs and lasing), and catalysis.[38-39] They are found in a number of layered and non-layered crystal structures and thus have been synthesized by both top-down and bottom-up strategies.[40] Notable representatives of these 2D materials are CdSe and MoS_2. CdSe represents a non-layered nanomaterial in which top-down fabrication methods are possible, but are often difficult or ineffective, and thus colloidal bottom-up synthesis strategies are employed.[41-42] On the contrary, MoS_2 is a traditional layered semiconductor where Mo is bound covalently between layers of S atom. These S-Mo-S layers are weakly bound to other S-Mo-S layers through van der Waals (vdWs) forces allowing for facile top-down fabrication while also allowing for bottom-up strategies.[43-44]

Transition metal oxides (TMOs) can be fabricated as layered (*e.g.*, MoO_3) or non-layered (*e.g.*, TiO_2 and WO_3) materials similar to transition metal chalcogenides, and thus use, both top-down and bottom-up synthesis methods. They are largely identified by their wide band gaps and transparent nature in the visible region of the electromagnetic spectrum.[45-46] Applications of these materials range from carrier conducting layers in optoelectronic devices to photocatalysis.[47-48] Interestingly, under certain synthesis conditions, defects can be introduced into the crystal lattices in the form of oxygen vacancies producing n-type semiconductor materials as in oxygen deficient WO_{3-x}.[49] These vacancies give rise to excess free electrons creating plasmonic materials exhibiting LSPR responses similar to noble metal 2D nanomaterials.[50] This plasmonic property of TMOs can then be applied to various technologies including photocatalysis and sensing.[51-52] Additionally, as observed in WO_{3-x}, there exists an intrinsic electrochromic property where the previously transparent material can be colored by modulation of the free carriers electrochemically.[53]

Transition metal carbides and nitrides, often referred to as MXenes, are a new class of 2D layered material that have been widely researched since their first reported fabrication of $Ti_3C_2T_x$ in 2011.[54] They are synthesized via top-down elemental etching of a parent MAX phase to produce a material with the general formula $M_{n+1}X_nT_x$ (n= 1-4), where M is a transition metal layer between layers of X which is carbon or nitrogen. Here T_x represents surface termination produced by the etching process, usually –F, --OH, and –O.[55] These materials exhibit robust mechanical properties and high electron conductivities making them ideal for energy storage and conversion as well as sensing applications.[56-58]

The final major 2D nanomaterial group are halide perovskites, semiconductor materials where the traditional crystal structure is ABX_3. Here, A is a monovalent organic or inorganic cation (*e.g.*, $CH_3NH_3^+$ or Cs^+), B is a divalent metal cation (*e.g.*, Pb^{2+}), and X is a halide anion Cl, Br, or I.[59] These are non-layered structures which differ significantly from previously discussed nanomaterial groups as their bonding is largely ionic in character as opposed to covalent.[60] This allows for a wide range of bottom-up synthesis and processing strategies to be applied to produce these materials, as ionic bond formation can occur at much lower temperatures.[60] As discussed in depth below, there exist other empirical formulae in this class of materials, but all of the materials share similar ionic character introduced through octahedral halide anion binding and cation charge neutralization between neighboring octahedra.[61] These materials are widely applied in optoelectronic technologies, especially photovoltaics, due to their intrinsic high molar absorptivity and photon emissive properties.[62]

The varying compositions of these materials along with numerous crystal phases and the possibility of defect engineering results in a wide range of properties of 2D nanomaterials. The materials listed represent zero band gap metals, small and large band gap semiconductors, and wide band gap insulators all with varying chemical, optical, electronic, and physical properties. Additionally, the synthesis method used, top-down or bottom-up, to fabricate 2D nanomaterials creates intrinsic surface characteristics at the interfacial layer that affect the specific property outcomes. The interfacial layer encompasses the surface atoms of the inorganic nanomaterial and the constituents that are bound or terminate these surface atoms, sometimes called the capping layer.[63-64] For instance, top-down elemental etching to create MXenes is often conducted in hydrofluoric acid aqueous solutions causing the surface to be populated with -OH, -F, and -O terminating groups.[55] Altering these groups have been theoretically shown to directly impact the electronic properties of the nanomaterial.[65] Additionally, colloidal and many other wet chemical bottom-up syntheses take place in the presence of organic surface passivating organic ligands with an anchoring head group and hydrocarbon tail.[64] These surface ligands can directly control morphology and assembly, solvent stability, optoelectronic properties and electronic transport.[66-70] The vast majority of what is known regarding the impact of the interfacial layer on manipulating desired property outcomes stems from 0D quantum dot research. However, unlike QDs, the large anisotropy of 2D nanomaterials resulting in heights of only a few atoms inherently places added significance to their surface chemistry. These "all-surface" morphologies provide an extremely large percentage of under coordinated surface atoms, or dangling bond architectures, which can be exploited through surface chemistry. Considering the relatively recent discovery of many of the 2D nanomaterial compositions, and the overall field of 2D nanomaterials in general, much of the surface chemistry related research is still unexplored.

The scientific scope of this dissertation is to study how surface chemistry can programmably be used to control morphology, physicochemical, and optoelectronic properties of chemically and compositionally diverse 2D nanomaterials including lead free halide perovskite nanosheets, metallic titanium carbide MXenes, and semiconducting tungsten oxide nanoplatelets. The scientific breakthroughs of this dissertation are shown in Figure 1.1.

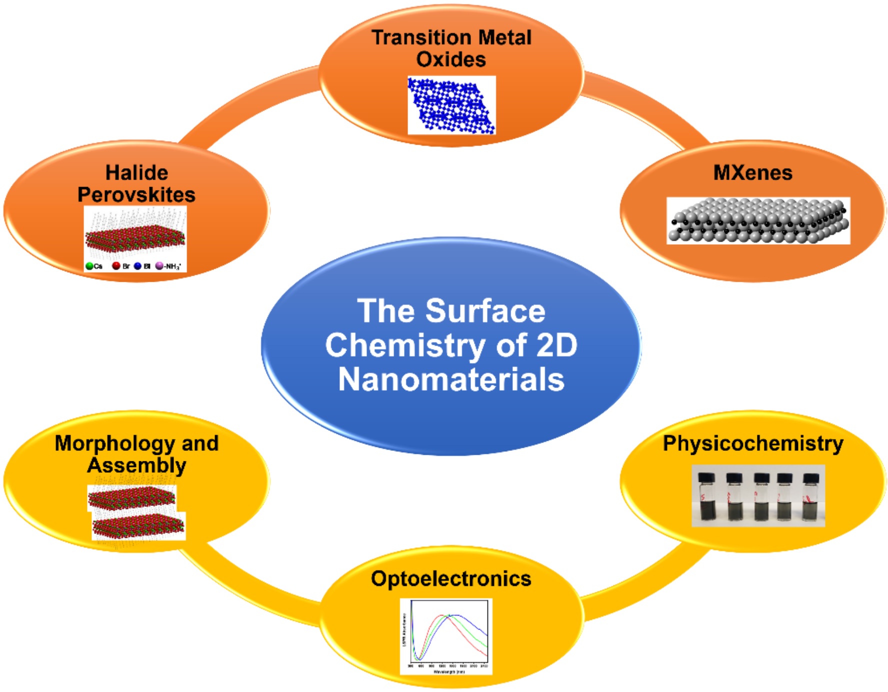

Figure 1.1: This schematic highlights the major discoveries being discussed in this dissertation regarding the surface chemistry of 2D nanomaterials.

- **Surface Ligand Chemistry Driven Synthesis of Quasi-Ruddlesden-Popper 2D Bismuth Halide Perovskites.** We developed a colloidal synthesis using surface ligand engineering to form single-layer quasi-Ruddlesden-Popper phase lead free bismuth halide perovskites. Through careful control of poly(ethylene glycol) (PEG) containing surface ligands, we studied the impact in the overall morphology of resulting 2D perovskite nanosheets, their electronic band structures, and vdWs force-driven mesoscale assembly to hierarchical superstructures.
- **Enhanced Optoelectronic Properties of Plasmonic WO_{3-x} Nanoplatelets Through Surface Chemistry Treatment.** We maximized the free carrier concentrations LSPR active, ultrathin oxygen deficient tungsten oxide nanoplatelets through surface trap state passivation via an ex-situ surface chemistry approach. This work includes a robust spectroscopic characterization of the local surface bonding and empirical quantitation of the free carrier concentration through redox titration.
- **Covalent Surface Modification of $Ti_3C_2T_x$ MXenes and the Physicochemical Impact.** An esterification process was conducted to covalently bond “short” PEG ligands to the typically hydrophilic MXene surface. The solvent polarity dispersibility of the MXene nanoflakes was greatly broadened with the PEG attachment along with increased vdWs interaction between flakes for improved microstructured film formation.

In summary, this dissertation investigates the unique role of the surface chemistry on a diverse group of 2D nanomaterials, and how their surfaces can be modified for advantageous morphological, optoelectronic, and physicochemical properties. Surface chemistry at the interfacial layer has been used to impact the shape during synthesis, ex-situ surface trap passivation to increase free carriers, and post exfoliation to alter solvation and assembly properties. To understand the overall importance of understanding how our surface chemistry impacts the 2D nanomaterials field, we outlined what a 2D material is and how its outer surface can be used in specific applications along with descriptions of each of the materials studied in this dissertation.

1.2 Electronic Structure of 2D Nanomaterials

Nanomaterials are defined as any structure with at least one dimension reduced to 100 nm or less leading to unique physical, optical, and/or electronic properties that differ from their bulk states. This change in properties correlates with an increase in surface-to-volume ratio and confinement of charge carriers (electrons and holes) known as quantum confinement. These concepts were first being developed for transition metal containing semiconductors, materials with a noticeable band gap between the valence and conduction bands also known as the highest occupied molecular orbital (HOMO) and lowest unoccupied molecular orbital (LUMO), respectively. However, as demonstrated by the brief descriptions of 2D nanomaterial groups above, nanomaterials are not limited to only semiconductors but also include metals with no discernable band gap and insulators with extremely large bandgaps (Figure 1.2). Though the concept of quantum confinement dates back to the 1980s when Alexei Ekimov and Alexander Efros were working to understand the nanometer size effect of cadmium chalcogenides and copper halides[3] while Louis Brus and his team at Bell Laboratories were developing quantum confinement theory using QD semiconductor CdS nanoparticles.[2] With the carriers of a QD confined in all three directions they experimentally found that the band gap, $E_{g(QD)}$, increased with a decrease in the

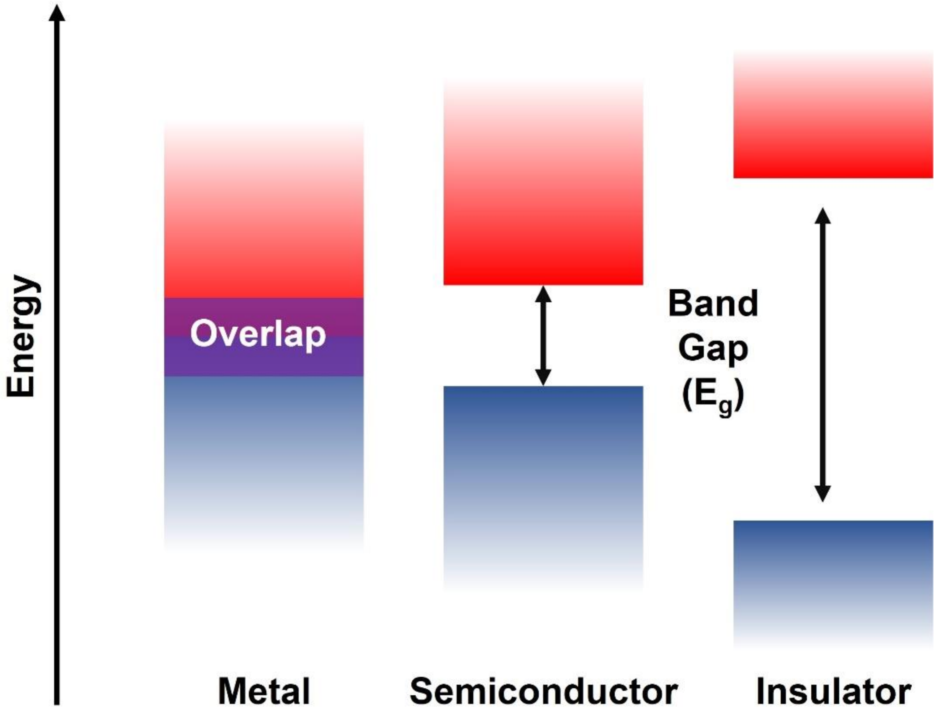

Figure 1.2: Simple schematic highlighting the band gap differences between metals (no band gap), semiconductors (small band gap), and insulators (large band gap).The location, size, and manipulation of these band gaps give rise to the electronic and optical properties observed in the different nanomaterials discussed.

QD radius. Considering the spatial confinement of the electronic wavefunction they mathematically modeled this inverse relationship as:

$$E_{g(QD)} = E_{bulk} + \frac{h^2}{8R^2}\left(\frac{1}{m_e^*} + \frac{1}{m_h^*}\right) - \frac{1.786e^2}{4\pi\varepsilon_0\varepsilon_r R^2}$$

Equation 1.1

where, E_{bulk} is the band gap of the bulk semiconductor, R is the radius of the QD, h is Planck's constant, m_e^* is the effective mass of the excited electron, m_h^* is the effective mass of the excited

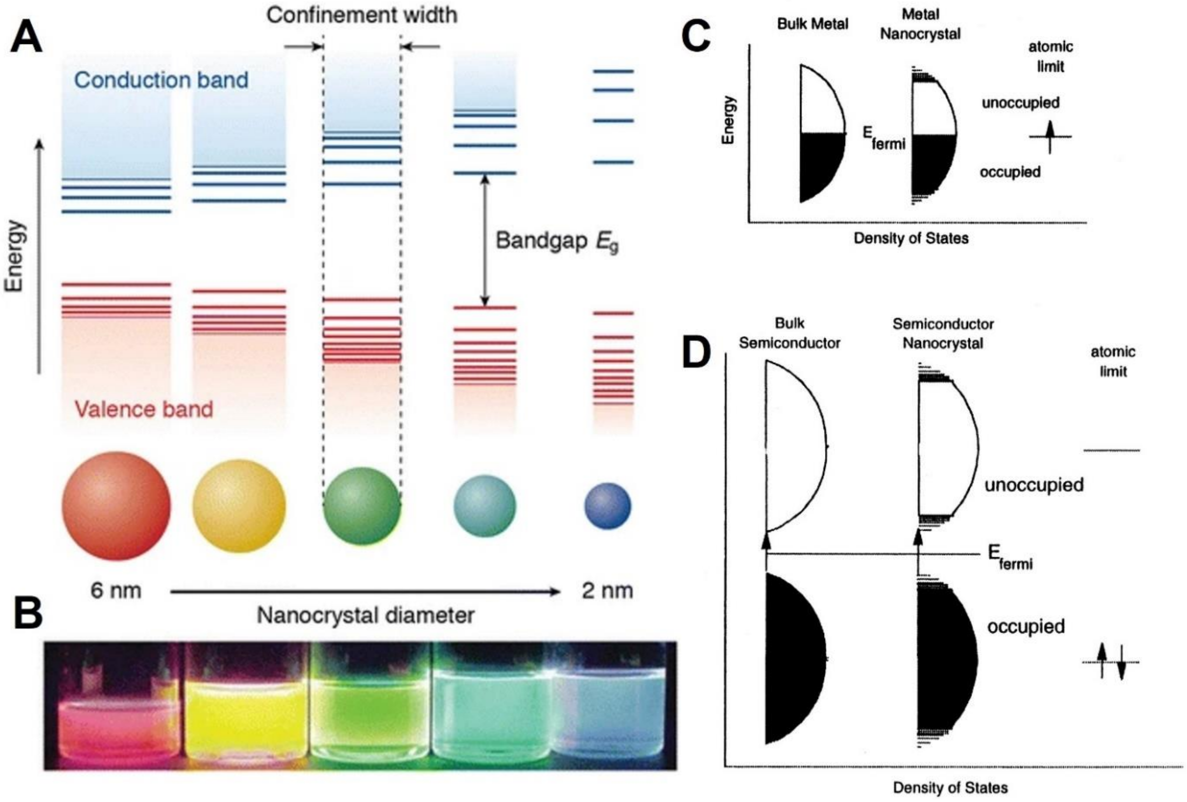

Figure 1.3: (A) Schematic representation of the quantum confinement effect in semiconductor NCs where the optical band gap (E_g) increases with decreasing size. Also, observed is the appearance of discrete energy levels at the HOMO and LUMO bad edges. (B) The impact of quantum confinement observed in colloidal CdSe NCs as the size decreases from 6 nm to 2 nm. When excited with UV light the color of the photoluminescence changes from red to blue or lower to higher energy, respectively. Adapted from reference 72. (C) The density of states of a metal. (D) The density of states of a semiconductor. Both highlight the discrete band levels at the edges in NCs. However, the band overlap of the metal (C) results in no overall impact of these states even at low temperatures. Adapted from reference 73.

hole, ε_0 is the permittivity of free space, ε_r is the relative permativity, and e is the electron charge.[2, 71] This relationship is exhibited in Figure 1.3 for semiconductor QDs.[72] Additionally, the increasing of the E_g can be described through the density of states (DOS) of a nanomaterial, where DOS solves the electron wavefunction and provides the allowable states an electron can have at any given energy. In Figure 1.3, the DOS results in the HOMO and LUMO being displayed as bands with discrete energy levels near their respective edges. These bands and discrete levels at the edges are formed due to individual nearby atomic orbitals collectively interacting within the material.[73] This is described quantum mechanically by the Pauli exclusion principle that no two electrons can simultaneously have the same energy, or quantum state. Therefore, a collection of atomic orbitals of a semiconductor form energy bands.[74] As a nanomaterial decreases in size the number of atoms decreases, and thus the number of atomic orbitals decreases which shrinks the collective band. Additionally, the discrete energy levels at the edges are greatly impacted resulting in a widening of the E_g.[73] This phenomenon is directly responsible for QD uses in display technologies as this size controllable band gap allows for manipulation of optical properties such as light absorption and corresponding photoluminescent wavelengths. As in the case of QDs, confinement in any direction will alter the band gap of a semiconductor material, even if it is in only one dimension as in the case of 2D nanomaterials. This is most notably exhibited in the same semiconductor transition metal chalcogenides that were first used to explain quantum confinement. When CdSe exists in its 2D nanoplatelet form the band gap decreases as the height of the platelets increases.[42] Metallic nanomaterials exhibit similar band and edge related trends; however, with the complete overlapping of HOMO and LUMO bands resulting in no measurable band gap (Figure 1.2) the overall electrical and optical properties maintain the resemblance of a continuum.[73] Confinement in metallic nanomaterials does result in other optoelectronic properties (*i.e.,* LSPR) which is discussed in Section 1.3.2.

As materials become anisotropic, one-dimensional (1D) wires and rods or 2D nano-platelets (NPLs) and -sheets, the dimensional electronic confinement also alters the possible DOS of the wavefunction in an energy band. As shown in Figure 1.4, the allowable solution for the varying geometries is very different.[66, 73] Beginning at QDs the quantized energy levels become a continuum band as materials become unconfined in the bulk. The nanomaterial geometry dependent DOS impacts the electronic properties, specifically movement and transfer of electrons that impacts the design of materials for different applications, most notably in the field-effect transistors for digital integrated circuit fabrication. Recognizing the geometrical impact on the DOS is an import reason for choosing specific dimensional materials; however, the focus of this dissertation does not involve solving nor discussing the DOS of the materials researched.

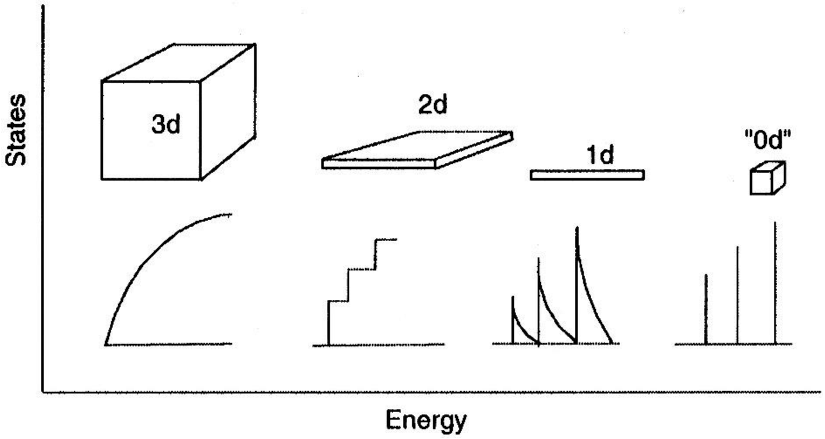

Figure 1.4: Idealized density of states for one band in a semiconductor material with varying morphologies. Adapted from reference 73.

1.3 2D Nanomaterials of Focus

Considering the near endless number of 2D materials possible as briefly described above this work chooses to focus on three specific materials from three different groups described above. Halide perovskites are represented by lead free cesium bismuth halides ($Cs_3Bi_2X_9$ where X is Cl, Br, or I), transition metal oxides are represented by oxygen vacant tungsten oxide (WO_{3-x}), and transition metal carbides and nitrides are represented by titanium carbide MXene ($Ti_3C_2T_x$ where T_x are surface termination -OH, -O, and -F). Physically they represent the gamut from ionic to completely covalent bonding crystals and are developed for specific applications using physical, optical, and conductive properties. Their synthesis methods also represent both bottom-up ($Cs_3Bi_2X_9$ and WO_{3-x}) and top-down ($Ti_3C_2T_x$) approaches. These materials were chosen as their compositions encompass a vast amount of scientific research yet study of their 2D counterparts and surface related phenomena to control morphology and properties is still in its infancy.

1.3.1 Halide Perovskites – $Cs_3Bi_2X_9$, where X is -Cl, -Br, -I

Perovskites, named after a Russian mineralogist, were originally discovered as the mineral calcium titanate ($CaTiO_3$), and interest has grown since the colloidal discovery of lead halide perovskites. Today, halide perovskites are a class of materials defined by the crystal structure ABX_3 where B represents a +2 charged cation, most often Pb, forming octahedral bonds to X, an anionic halide Cl, Br or I, and A is a cation that balances the charge of the crystal lattice (Figure 1.5A).[75-76] In hybrid organic-inorganic perovskites A is an ammonium compound (*e.g.*, methylammonium),[62, 77] and in completely inorganic perovskites A is a large cation like cesium.[78-79] These semiconducting materials have been extensively studied for photovoltaic applications due to their highly tunable band gaps (Figure 1.5B), low-cost solution processing, extremely large absorption coefficients, and high charge carrier mobility.[59, 80-81] Additionally, due to their

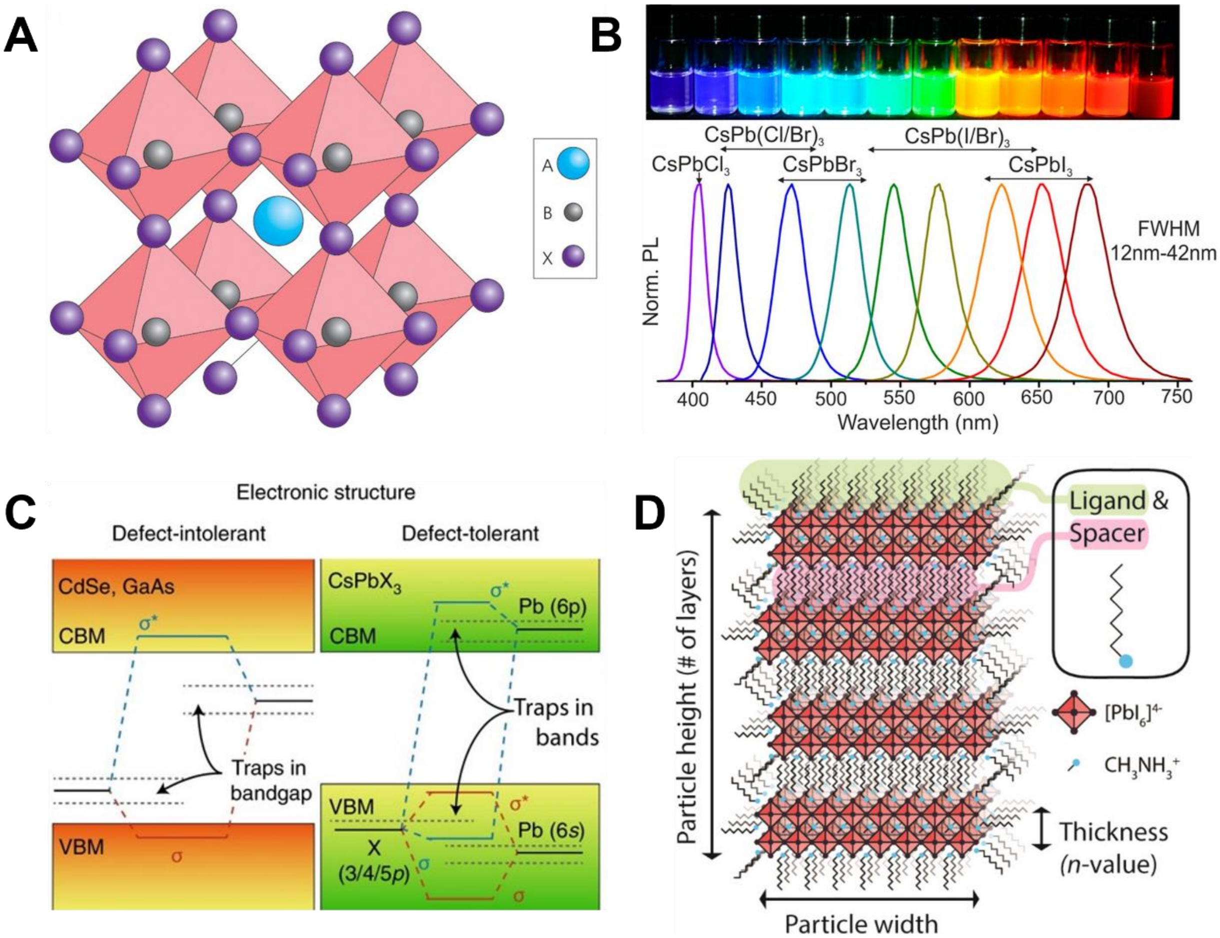

Figure 1.5: (A) ABX_3 cubic perovskite crystal structure where A is a charge neutralizing cation, B is a small cation ion such as Pb, and X is a halide. Adapted from reference 81. (B) Solution of all inorganic lead halide perovskites highlighting the band gap tunability by altering the halide as observed in the photoluminescence. Adapted from reference 78. (C) A schematic comparison of the defect tolerance between classic semiconductor NCs and all inorganic lead halide perovskites. Adapted from reference 85. (D) Schematic representation of four-layer n=2 2D Ruddlesden-Popper phase perovskite. The long chain ligands/spacers are highlighted. Adapted from reference 90.

electronic band structure defect tolerance (Figure 1.5C) and large photoluminescent quantum yields they are current candidates for next-generation display technologies.[82-85]

Lead halide perovskites are largely ionic, especially the charge balancing A-site cation, offering a wide range of tunability in their overall composition and structure. This tunability of the A-site cation and the facile solution processing enabled by their ionic nature has resulted in formation of a wide range of 2D lead halide perovskite nanomaterials by a number of methods most of which require an A-site cation of RNH_3 where R is a long alkyl chain or aromatic moiety.[86] One of the first synthesis of 2D lead halide perovskites used $C_4H_9NH_3$ in the A-site and achieved 2D formation of the material by fast recrystallization method using fast evaporation of a dilute solution under heating.[87] Other approaches include the use of long chain amino containing ligands including hexadecylamine[88] or a mixture of small methyl ammonium and large octylammonium cations to colloidally synthesize large nanosheets.[89] Using these longer chain amino containing ligands has proven the capability of achieving 2D formation in inorganic cesium lead halide nanomaterials also (Figure 1.5D).[82, 90-93] These syntheses have led to the labeling of a new family of halide perovskites called Ruddlesden-Popper phase perovskites. This family is characterized by the formula $(A')_2(A)_{n-1}M_nX_{3n+1}$ where A's represent a large cation or mixture of large and small cations, M is a transition metal, and X is a halide -Cl, -Br, or -I. Here n represents the number of layers of the metal halide octahedra that are separated by the large cations in the A-site between layers (Figure 1.8).[94-96] Section 1.4.1 discusses how the surface chemistry of these large cations induce the formation of 2D nanomaterials.

Although the use of Pb has shown the greatest optoelectronic potential in these materials its presence causes a severe limitation of their potential applications due to environmental toxicity limits worldwide. To overcome this drawback, there has been extensive research into lead-free forms of perovskites including using different valency transition metals.[97-100] The use of different B-site cations has shown to slightly alter the crystal structure of the classic cubic ABX_3 into slightly altered crystal structures with different empirical formulae. One such example is the non-toxic alternative $Cs_3B_3X_9$ (Figure 1.8).[101-102] Even with the crystal structure alteration these materials are still defined by their metal-halide octahedra and A site charge neutralizing cations.[103] They still exhibit similar properties including tunable band gaps based on size and halide of choice, large absorption coefficients, and facile solution processing. As shown in chapter 2, this new structure of halide perovskites using bismuth makes it possible to use surface chemistry through the incorporation of large ammonium cations that can only insert at the surface the interfacial layer to manipulate morphology of the nanomaterial into 2D structures. These surface chemistries can then be used to impact the assembly of the nanomaterials and their subsequent properties for specific applications.

1.3.2 Transition metal oxides (TMOs) – Oxygen deficient tungsten oxide (WO_{3-x})

TMO nanomaterials represent a large field of materials that encompasses a vast array of technologies stemming from a variety of catalytic, redox, optoelectronic, and conductive properties.[104] The wide range of properties arises from the unique nature of their outer d-electrons.[105] Common examples of TMOs are ZnO, TiO_2, In_2O_3, MoO_3, and WO_3.[106-109] Additionally, IrO_2 and RuO_2 are benchmark materials for the important oxygen evolution reaction.[110] These materials all have varying morphologies often dependent on their crystal structure. For example, MoO_3 has a layered structure and is commonly found in 2D shapes (*e.g.* nanosheets and nanoplates) but rarely observed in 1D forms.[111-112] Although there are many important materials in this field, this dissertation focuses on LSPR active transition metal oxides , specifically nonstoichiometric tungsten oxide (WO_{3-x}).

Plasmonic behavior in tungsten oxide is induced through the insertion of anion vacancies resulting in an oxygen deficient n-doped semiconductor nanomaterial where free carriers begin to fill the valence band.[113-114] WO_{3-x} is known to comprise a variety of thermodynamically stable crystal phases, called Magnéli phases, and a number of synthetically controllable nano-morphologies, from 0D to 3D.[53, 113, 115] The diverse oxygen vacancy (O_v) chemistry of the Magnéli phases result in stoichiometries from $WO_{2.9}$ to $WO_{2.72}$.[116] These phases were studied in-depth in the 1980's by Salje and co-workers. It was found an oxygen vacancy (O_v) resulted in two phenomena. 1) As oxygens are removed from the stable W^{+6} octahedra, a reduction event can occur creating W^{+5} centers. This has continued to be highlighted in the literature that with increase O_v there is also an increase in W^{+5}. 2) O_v inclusion results in the formation of polarons, an electron that is bound to a crystal lattice phonon.[117-120] Interestingly, it was found an Anderson transition, a shift from semiconductor to metallic nature in the electron dynamics, occurred when O_v formation reached concentrations >0.1.[121] This transition occurs as polaron wavefunctions begin to overlap and delocalization occurs allowing electrons to act as a free electron gas described by Drude theory. The bulk oscillation of the free electron gas can be confined by nanostructuring, resulting in LSPR responses upon interaction with incident photons in the visible and near infrared (NIR) regions of the electromagnetic spectrum.[50] This phenomenon has been extensively studied both empirically and theoretically in many metal oxide nanomaterials including doped semiconductor ZnO nanoparticles (Figure 1.6A).[122] However, this work focuses on the thermodynamically stable n-doped $WO_{2.72}$ crystal lattice, due to the large tunability of the LSPR response (Figure 1.6B,C) resulting in a wide range of applications including catalytic, electrochromic, sensing, and energy harvesting.[123-126]

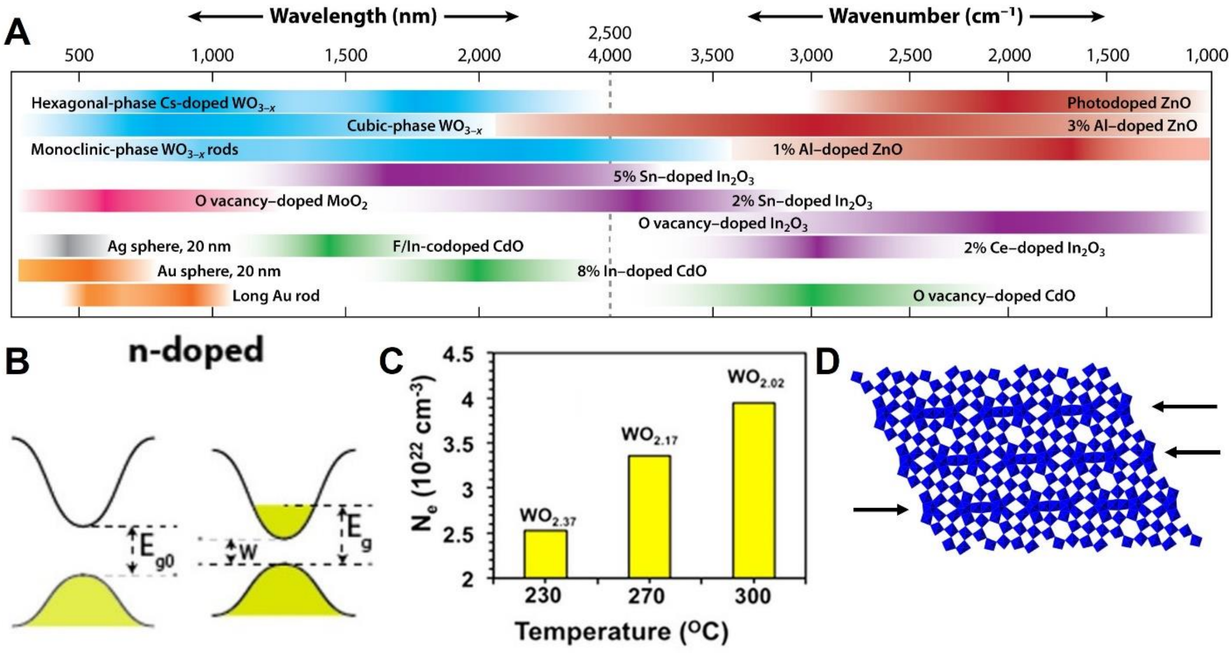

Figure 1.6: (A) A graphic representation of the many plasmonic TMOs and their typical LSPR related UV-vis-NIR absorption regions. Adapted from reference 50. (B) Electronic band structure schematic of n-doped semiconductor NCs. In the case of O_v in WO_{3-x} the free carriers (yellow) begin to fill the conduction band. Adapted from reference 114. (C) Graphical representation of increasing N_e in WO_{3-x} caused by increased O_v as the synthesis temperature is raised. Adapted from reference 115. (D) The crystal structure of $WO_{2.72}$ as viewed form the (010) direction. The arrows are highlighting the shear planes caused by edge sharing octahedra.

The $WO_{2.72}$ crystal lattice consists of corner sharing WO_6 octahedra in the (010) direction, but in all other direction the O_v results in a lattice distortion resulting in edge sharing octahedra that are segregated along specific planes (103) creating crystallographic shear planes and repeating hexagonal pores (Figure 1.6D).[127] The vast majority of $WO_{2.72}$ synthesis methods results in 1D growth due to the large kinetic preference for growth in the (010) direction.[53, 128] Remarkably, under the correct synthesis conditions, the shear planes can be used to limit growth in the height direction, thus forming 2D nanomaterials with a large amount of oxygen vacancies.[115] These 2D $WO_{2.72}$ structures have a large surface-to-volume ratio causing a subsequent increased significance on their surface characteristics. A large amount of oxygen atoms exist on the surface which can be removed under high temperature and low oxygen partial pressures which result in local defects or surface traps greatly impacting their plasmonic response. This is often referred to as a depletion layer as the total number of free carriers is depleted as they are trapped at these surface vacancies.[128-129] Chapter 3 discusses how surface chemistry and ligand engineering can be used to passivate these traps thus positively impacting the LSPR response.

1.3.3 Transition metal carbides and nitrides – $Ti_3C_2T_x$ (MXenes)

2D transition metal carbide and nitrides, known collectively as MXenes, are relatively new group of materials dating back to their discovery in 2011. [54] Unlike previous materials mentioned, MXenes are fabricated via top-down elemental etching of a bulk layered MAX phase, where M is an early transition metal, A is an element of groups 13-16, and X is carbon or nitrogen.[55, 130] Commonly, hydrofluoric acid is used to etch away the A group element resulting in intrinsically layered nanosheets of only a few atoms in height and up to microns in lateral dimensions. The resulting empirical formula is $M_{n+1}X_nT_x$ (n=1-4) where M is interleaved by layers of X. Here, T_x represents the surface terminations (-O, -F, or -OH) stemming directly from the etching process in aqueous solvent (Figure 1.10).[131] As suggested by n, altering the parent MAX phase can give rise to materials of varying number of layers post etching. Common examples of these multiple layers are Ti_2CT_x, $Ti_3C_2T_x$, and $Nb_4C_3T_x$.[54, 132-133] The 2D structure of MXenes resulting in extremely robust mechanical properties is often compared to graphene.[134-135] Similar to transition metal oxides, MXenes offer a wide gamut of properties (*e.g.*, electrical and optical) by altering the transition metal(s) used in fabrication. The most extensively studied MXene is $Ti_3C_2T_x$, providing a large amount of empirical data on how the etching parameters can be used to create the largest and most stable 2D nanoflakes.[136] Additional examples of common transition metals used in MXene synthesis include niobium, vanadium, and molybdenum which have been studied for their activity as hydrogen evolution catalysts and battery anodes.[137-139] Figure 1.10 highlights the many other experimentally synthesized MXenes and those that are theoretically possible based upon lattice binding energies. Interestingly, it has been theorized that semiconductor MXenes could be synthesized through surface termination or transition metal control, but as yet all MXenes are metallic in nature.[140-141] The intrinsic metallic nature gives rise to a plasmonic property which has been studied for use in sensing applications as seen in $Ti_3C_2T_x$.[142] Overall, the tunability of properties makes MXenes highly attractive for technologies such as catalysis, electromagnetic interference shielding, sensing, energy storage, and mechanical strength improvement of polymer composites.[57-58, 143-146]

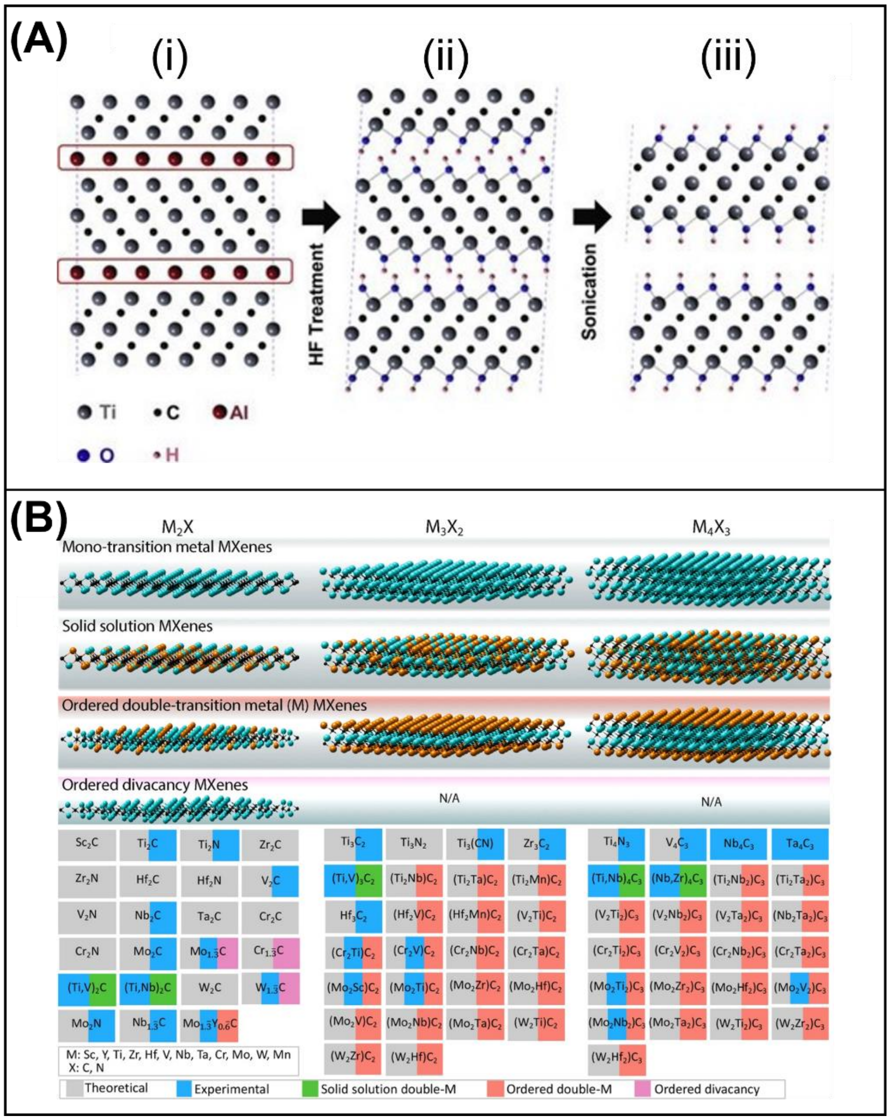

Figure 1.7: (A) Schematic representation of the elemental etching process using HF. (i) Ti3AlC2 MAX phase. (ii) Al atoms replaced with -OH after etching, only -OH is shown for ease of representation. (iii) Individual nanoflakes being separated through sonication. Adapted from reference 54. (B) MXenes reported thus far in literature with the possible structures of different n layers. Mono-M elements, mixed double-M elements, and ordered double-M elements. A list of the formulae that have successfully been characterized and those that are theoretically possible but have not been characterized experimentally. Adapted from reference 55.

As mentioned above, the etching process to fabricate 2D MXene imparts surface terminations from the acid and aqueous environment in the form of -O, -OH, and -F. These surface terminations create a hydrophilic surface and require storage in aqueous solvents. Considering the preference for most transition metals to form metal-oxide bonds these materials suffer greatly from oxidation under long storage and processing conditions.[147-148] Also, the hydrophilic nature of MXenes greatly limits their use in many applications due to necessary non-polar processing conditions. This is most evident in the attempt to use MXenes as fillers in polymer composites where aggregation occurs due to the native surface terminations.[149] There have been numerous studies regarding how to alter the surface chemistry of MXene to improve stability and allow for processing in non-aqueous less polar solvents with mixed results.[150-153] Chapter 4 highlights our work in covalently modifying the MXene surface with short-chain PEG ligands to greatly enhance the solubility of MXenes in organic solvents with a wide range of polarities. An added benefit is the ligand-ligand interactions between neighboring MXene nanoflakes to programmably assemble the nanoflakes. These enhancements enable facile incorporation of MXene nanomaterials into future technologies using a wider range of processing chemistries than previously achievable.

1.4 Surface Related Properties of 2D Nanomaterials

When discussing materials of tens of nanometers or less it is important to mention that other molecules such as ions and solvent molecules come within an order of magnitude in size. This means that forces including electrostatic, vdWs, and hydrophobic interactions that nanomaterials have with their surroundings become greatly increased relative to bulk material interactions.[63] For example, the normally small vdWs forces that can often be ignored in a bulk material dominates on a local scale for nanomaterials. As these forces become outsized with the shrinking scale of materials, they become difficult to measure instrumentally and the scale factor causes the collective interactions to become nonadditive forcing a heavy reliance on empirical data and observation.[63] This rise in importance of no-longer non-trivial forces along with an inherent surface-to-volume ratio increase with decrease in size creates an extraordinary relevance on a material surface chemistry. This chemistry occurs at the interface of the undercoordinated inorganic surface atoms and the molecules that passivate them along with the interaction between these passivating molecules of other nearby nanomaterials. As mentioned above, colloidal syntheses of 2D nanomaterials require passivating ligands, commonly, long chain saturated or unsaturated fatty acids and amines, to confine growth. Whereas the exfoliation of bulk layered materials to create 2D morphologies inherently produces terminations stemming from the exfoliation solvent. The manipulation of these terminations and passivating ligands provides an opportunity to control a material morphology, optoelectronic properties, and the physicochemistry or processability.

1.4.1 Programmable Morphology

Surface passivating ligands are ubiquitous to colloidal syntheses of nanomaterials. Noble metal nanomaterials are often synthesized via a seed mediated strategy at ambient or relatively low temperatures in the presence of organic ligands (*e.g.,* cetrimonium bromide).[31, 154-155] Semiconductor nanomaterials syntheses often adhere to the classical LaMer model of burst nucleation followed by growth.[156] This is true of the initial synthesis of metal chalcogenide QDs, in which metal precursors are injected in a high boiling non-coordinating solvent (*i.e.,* 1-octadecene) that also contains a mixture of organic ligands (*e.g.,* oleylamine, oleic acid, trioctylphosphine oxide, *etc*.,).[157] In both cases, these organic ligands are used as surfactants to passivate the surface and confine growth of the nanomaterial to achieve the desired shapes and optoelectronic properties.[158] In general, the binding of a ligand to the nanomaterial is a dynamic process with weak binding energies (20-40 kJ/mol).[159-160] Ligands are comprised of two important qualities: 1) the functional head group that directly interacts with the inorganic surface atoms. [161] 2) The tail which most directly interacts with the surrounding environment (*e.g.,* solvent and neighboring nanostructures) and through steric hinderance is largely responsible for the overall packing density on the inorganic surface.[159] Common ligands used in colloidal syntheses along with their electronic nature (*i.e.,* donating, withdrawing, or neutral) are described in Figure 1.11). The ligand variation in structure, number, and arrangement on the inorganic surface results in slight differences in binding affinities and, in conjunction with changes in crystal facet energies, can be used to programmably obtain desired 2D morphologies.[162-163]

In general, growth of preferred 2D morphologies occurs through specific crystal facet passivation. All crystalline nanomaterials can be described with a distinct crystal structure as defined by their highly ordered repeating 3D arrangement of atoms and bonds. The terminating face, or facet, of the nanomaterial exposed results in a specific facet surface energy depending on chemical, physical and structural parameters (*i.e.,* atom packing, electrostatic charge, atom coordination number, *etc.*,).[162] Atoms at facets are undercoordinated and either positive or negatively charged and these factors can increase surface energy.[159] Normally, a nanomaterial will find a thermodynamic minimum in total surface energy, most likely a sphere, where the area of the highest energy facets are minimized compared to the lower energy facets.[164] However, based upon ligand binding affinities, crystal surface-ligand engineering of specific facet reduces their

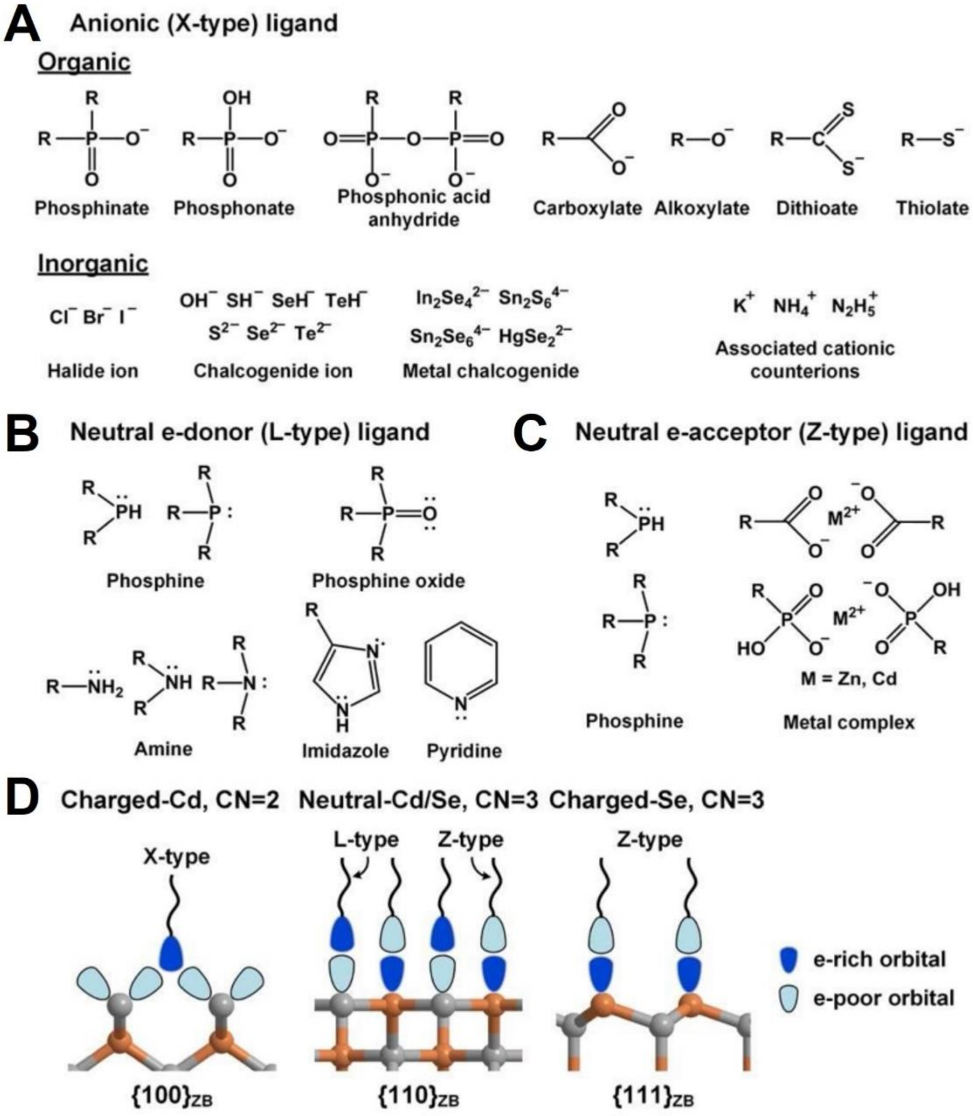

Figure 1.8: Common surface ligand functional groups used in colloidal synthesis of nanomaterials. (A) X-type ligands are anionic and preferentially bind to cationic surfaces. (B) L-type ligands are neutral with a lone pair of electrons that can be donated to the NCs surface atoms. (C) Z-type ligands are metal complexes that are charge neutral and accept electrons. (D) Preferential binding to different types of facets. Schematically represented using CdSe NCs zinc blende crystal facets. Adapted from reference 159.

surface energies providing kinetic control.[165] Overall, more tightly bound ligands will slow the growth of that specific facet, thus allowing for programmable directional growth. This is observed in the depth of research into the formation of metal chalcogenide nanoplatelets and more recently, cobalt oxide nanosheets.[42, 90, 166-168] For example, in CdSe nanoplatelets specific binding between cadmium and carboxylate ligands is used to observe the 2D confinement.[169]

Even in our own research, primary amine, oleylamine, is used to confine WO_{3-x} into 2D ultrathin nanoplatelets.[115] The dative binding of amine to the inorganic surface allowed ligand-ligand vdWs interactions between monomers to form in a mesophase templated assembly ultimately ending in 2D growth. This mesophase templated assembly is a common mechanism in the formation of 2D non-layered semiconductor materials through ligand engineering.[170] Overall, choice of the head group allows for specific facet binding and a lowering of the surface energy to control kinetics of monomer attachment. Ligand tail group engineering limits steric hinderance to allow high packing density of ligands and vdWs interactions between ligands of neighboring monomers thus promoting growth.

In our other work, quasi-Ruddlesden-Popper phase bismuth halide perovskites, the ligand can insert itself directly into the nanocrystal as an ionic charge neutralizing head group. This is common for hybrid organic-inorganic perovskites where the ligand contains a positively charged ammonium head group and a large bulky tail.[171-172] The tail then interacts through ligand-ligand vdWs forces in much the same way as mesophase templated growth forming 2D nanomaterials. MXenes on the other hand are formed through elemental etching and exfoliation from a layered bulk structure. Thus, there are no organic ligands necessary in the fabrication to form 2D nanomaterials; however, as seen in Section 1.4.3, organic ligands become extremely important for physicochemical property manipulation.

1.4.2 Optoelectronic Properties

The optoelectronic properties (*e.g.*, absorption, emission, LSPR etc.,) of 2D nanomaterials are defined by their electronic band structure which is greatly influenced by their surfaces. As observed in Figure 1.2 the composition of a nanomaterial results in metal (no band gap), semiconductor (small band gap), or insulator (large band gap) characteristics. This inherent difference in the band structure results in materials with differing optoelectronic properties that are applied in separate distinct technologies. Halide perovskites are tunable band gap semiconductors best suited for photovoltaic and display technologies due to their large absorption coefficient and high exciton binding energy.[173] Whereas oxygen deficient transition metal oxides are 2D semiconductor nanomaterials that exhibit LSPR responses upon interaction with incident light, akin to metal nanomaterials, that are used in photocatalysis and sensing applications.[174-176] MXenes are classified as metallic and exhibit LSPR responses also; however, surface chemistry control of their optoelectronic properties is largely theoretical at this point and not covered in this work.[177] Not shown in the simplified band structures in Figure 1.2 are the shallow inter-band trap states that occur when point defects occur on the surface of 2D nanomaterials. These point defect are the result of undercoordinated or missing surface atoms that remain unpassivated by ligands. Due to the differing nature of the optoelectronic response between halide perovskites and oxygen deficient transition metal oxides there is a nuanced influence of surface defects.

Halide perovskites are often compared to classical QDs as their band gaps are tunable over the visible range through quantum confinement effects and choice of halide.[78] The choice of halide is important because the HOMO and LUMO bands are comprised of orbital contributions from the metal cation and halide anions in each octahedra (Figure 1.5C).[178] Chapter 2 discusses the band gap alteration caused by changing halide ions in 2D lead free halide perovskites. The A-site charge neutralizing cation does not play a direct role in the optoelectronic properties of the materials; however, through surface passivation and enhanced stability it does indirectly contribute to the overall efficiency of absorption and emission processes.[179] Interestingly, when compared to QDs, halide perovskites have a much larger tolerance for surface defects as shallow trap states are located within their LUMO bands, not inter-band gap as is the case for QDs (Figure 1.5C).[180] Overall, there is an critical need of surface ligands for passivation and stability because the ionic nature of the halide perovskite results in a low crystal lattice energy making it very susceptible to its chemical environment.[79] Any small change in the lattice of the halide perovskite causes distortion to the octahedra resulting in decreased efficiency of it optoelectronic properties such as quantum yield.[179]

Oxygen deficient metal oxides are LSPR active due to free carriers, electrons in this case, left behind when an oxygen atom is removed. Thus, the more oxygen that is removed the higher the free carrier concentration (N_e) in the material. Consequently, the LSPR response (λ_{LSPR}) is directly impacted by the N_e caused by oxygen vacancy. The Drude model for bulk materials relates N_e to the bulk plasma oscillation frequency (ω_p) as:[115]

$$\omega_p^2 = \frac{N_e e^2}{\varepsilon_0 m_e}$$

Equation 1.2

where e is the electron charge, ε_0 is the permittivity of free space, and $m_e$is the effective mass of the electron. Using the high frequency dielectric of the material (ε_∞), and the real part of the dielectric function (ε_r), and accounting for the damping effect using a bulk collision frequency (γ) the overall relationship to the frequency of the LSPR response (ω_{LSPR}) follows Equation 1.3:

$$\omega_{LSPR} = \sqrt{\frac{\omega_p^2}{\varepsilon_\infty - \varepsilon_r} - \gamma^2}$$

Equation 1.3

Here, ε_r can be represented using a shape factor (κ) and the dielectric constant of the surrounding medium taken as the bulk refractive index (ε_m):

$$\varepsilon_r = -\kappa\varepsilon_m$$

Equation 1.4

By relating to ε_m, it is clear the LSPR response of a material is sensitive to the refractive index of its environment. Interestingly, with the incorporation of the shape factor it becomes clear that anisotropic materials greatly impact the overall sensitivity of the material. This sensitivity is the reasoning for using LSPR active materials in sensing applications.[181]

Considering the Drude model was developed for spherical noble metal nanoparticles with intrinsic free carriers there arise inherent drawbacks for 2D semiconducting nanomaterials. Free carriers in a semiconductor are greatly influenced by shape, often resulting in multiple peaks in their LSPR response.[182] One reason for this is that effective masses of the carrier being different along each axis of the material.[183] Thus, it is important to incorporate a shape factor that can model this behavior as accurately as possible. An example of this is in $WO_{2.83}$ 1D nanorods where the dielectric environment of the diameter is modeled separately to that of the length. [113]

Also, the Drude model does not take in to account the changes at the surface of the nanomaterial. With the removal of surface oxygen atoms of transition metal oxides surface traps can appear creating a “depletion layer” (Figure 1.9).[184] This layer effectively removes free carriers from participation in the LSPR response decreasing sensitivity of the material and many other necessary optoelectronic properties for effective use in applications.[185] Overall, assumptions of the Drude model for noble metal nanoparticles based upon electronic band structure (no band gap) ultimately fail when considering the surface dependent nature of a semiconductor’s electronic band structure. Chapter 3 discusses the introduction of a shape factor to account for changes caused by 2D nanoplate morphology of WO_{3-x}. Also, this chapter discuses in-depth how appropriate passivation of the surface limits depletion layer effects, thus maximizing the LSPR response.

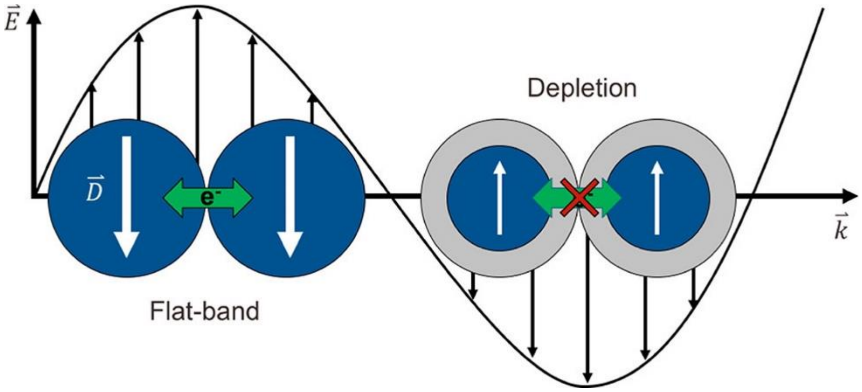

Figure 1.9: Schematic representation of how typically high N_e plasmonic oxides (blue) form low N_e insulation barriers (grey) which negatively impact their LSPR response and impedes electron transport between NCs. Adapted from reference 185.

1.4.3 Physicochemistry Properties

The preceding sections have described how a material surface chemistry can be used to direct morphological changes during synthesis and alter the optoelectronic properties through surface passivation. In addition, to these important outcomes, surface chemistry techniques can be applied to manipulate the physicochemical properties of a material. One of the most important physicochemical properties of materials is their inherently hydrophilic or hydrophobic character resulting from the ligands or surface terminations caused by synthetic conditions. This property is extremely important when considering a nanomaterial stability in particular environments or solubility/dispersibility for use in down-field device manufacturing. For example, inkjet printing is a common method to reliably manufacture circuitry or patterns of nanoparticles in sensors, photovoltaics, and electrical devices.[186] Often, due to the necessary conditions for the inkjet printing process, nanoparticles need to be hydrophilic to achieve large concentrations in polar solvents thus maximize printing and processing efficiencies.[187] Conversely, polymer processing to form nanocomposites often occurs in hydrophobic environments requiring nanoparticles to be highly dispersible in non-polar solvents for effective use in high loadings to achieve desirable outcomes.[188] Interestingly, when thinking about bio-related applications such as drug delivery, the nanoparticle may need to have a mixture of hydrophobic and hydrophilic character to effectively travel through the body then enter through a cell wall.[189] Thus, surface chemistry manipulation of a material surface layer becomes imperative to successful nanomaterial application performance. Alteration of this layer is most often achieved through post synthetic (ex-situ) surface ligand exchange or attachment procedures.

2D perovskites, which are synthesized via bottom-up methods in the presence of bulky organic cations (*e.g.*, alkylammonium and phenylethylammonium) are inherently hydrophobic and must be processed in non-polar solvents (*i.e.*, $CHCl_3$).[86] Due to the ionic nature of the halide perovskite crystal one of the major disadvantages is their poor stability in polar or aqueous environments.[190] Especially concerning is their long term instability in high humidity environment considering one major application is photovoltaic devices that are open to air.[191] However, these challenges continue to be circumvented through the use of ex-situ ligand exchange and treatments. Common approaches include introducing tighter binding surface ligands, such as bidentate binding 2,2'-iminodeibenzoic acid,[192]or incorporation of large protective hydrophobic layers, such as poly(4-vinylpyridine).[193] One novel approach which demonstrated enhanced stability in photovoltaic cells was to introduce a bifunctional ligand containing a hydrophilic functional terminal group which adsorbs water while distancing the perovskite surface through an alkyl chain.[194] This method of including hydrophilic outward facing functional groups is also employed to create aqueous processable halide perovskite materials; however, due to the extreme environment of being submerged in solvent a large block co-polymer was required.[195]

2D nanomaterials that are achieved through top-down methods such as specific elemental etching and exfoliation of layered bulk materials introduces terminating groups on the surface of the nanomaterial. This is the established procedure to fabricate MXene nanoflakes which are terminated with a mixture -O, -OH, and -F resulting from the hydrofluoric acid used during etching.

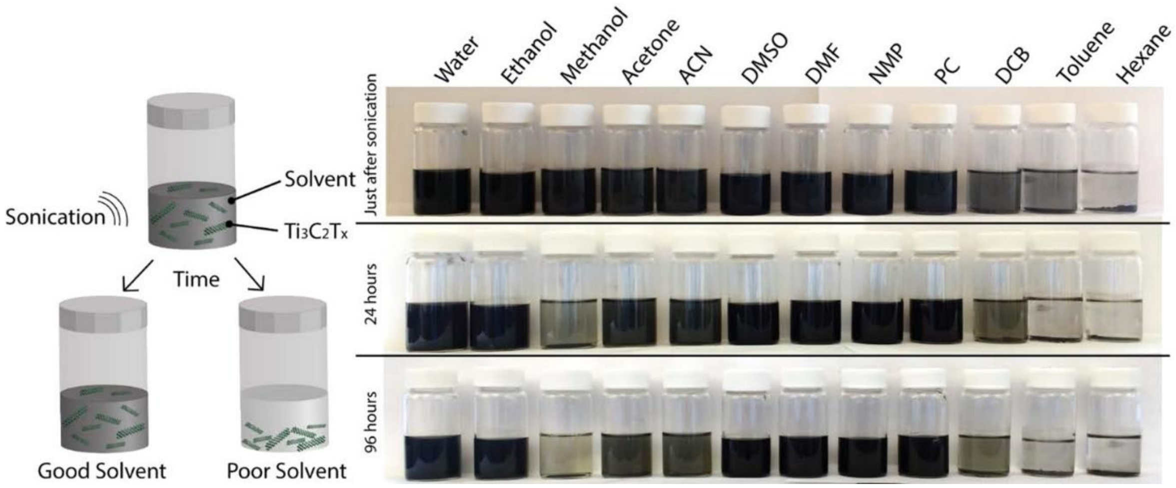

Figure 1.10: Dispersions of $Ti_3C_2T_x$ highlighting the hydrophilic character based upon the dispersibility in various solvents over a range of polarities. Adapted from reference 153.

This surface mixture of surface terminating groups leads to a hydrophilic surface as observed by high solubility concentrations of MXenes in water and polar organic solvents (Figure 1.10).[153] This inherent hydrophilicity lends itself well to many processing techniques such as spray coating and inkjet printing.[196-197] However, the surface termination of MXenes create a number of issues. First, MXenes will oxidize when stored in aqueous environment through the formation of transition metal oxides on their surface.[147] Many applications including the incorporation into polymer nanocomposites are detrimentally impacted by the hydrophilic character. When hydrophilic MXenes are placed in a hydrophobic environment the nanoflakes will agglomerate due to hydrogen bonds and electronic attraction.[198] This agglomeration decreases homogeneity of the material and results in negative outcomes in the polymer nanocomposite.[199] A number of studies have been conducted to modify the surface chemistry of MXene using hydrophobic organic ligands to both improve their long term stability and also to increase their solubility in non-polar organic solvents.[151, 200] The majority of these works utilize electrostatic interactions between the MXene surface and ligand to adsorb organic ligands thus altering their hydrophilic character. This concept will be further discussed in Chapter 4, where we highlight our work of modifying the MXene surface through covalent attachment of PEG6 ligands resulting in MXene nanoflakes that are dispersible in organic solvents with a wide range of polarities.

1.5 Purpose and Specific Aims of Dissertation

As mentioned above, this dissertation discusses how specific aspects of surface chemistry can be utilized to affect assembly, optoelectronic, and physicochemical properties of lead-free perovskites, oxygen deficient tungsten oxide, and titanium carbide MXenes, respectively. Chapter 2 focuses on synthesizing lead-free bismuth halide perovskites and how careful control of synthetic parameters can force the formation of 2D nanosheets in a quasi-Ruddlesden Popper phase. Through cation deficient reaction conditions, the surface ligand is enticed to enter the typically inorganic perovskite lattice. Through ligand-ligand interactions nanosheets are formed. Also, discussed is the electronic band structure impact of halide modulation and solvent evaporation impacts on assembly of the nanosheets. Chapter 3 delves into the optoelectronic property manipulation of WO_{3-x} ultrathin nanoplatelets through altering surface passivating ligands. Through the ex-situ treatment of bidentate bound carboxylate ligand passivated NPLs with tridentate binding tetradecylphosphonate ligands allowed an increase in surface passivation is achieved. This enhanced passivation equates to a filling of surface traps created by oxygen vacancy allowing the surface trapped electrons to occupy the conduction band and participate in the LSPR property. Chapter 4 explores the altering of physicochemical properties (solubility and assembly) of traditionally synthesized, hydrophilic $Ti_3C_2T_x$ by chemically converting hydroxyl surface terminations to ester bonded PEG6 ligands. This conversion greatly changes the solubility and processability profile of MXenes without greatly impacting their interlayer electronic conduction, which is unique for this material. All of these chapters use a combination of absorption and vibrational spectroscopic techniques along with X-ray diffraction and electron microscopies to analyze scientific outcomes. Lastly, chapter 5 provides short concluding remarks on where surface chemistry is heading and how it may be used in technologies that are currently under development.

1.6 Future Outlook

Surface chemistry has and will continue to play a vital role in developing novel technologies.[201] As unique and evermore complex materials are discovered for increasingly intricate technologies, previously gained fundamentals of surface chemistry must be adapted and developed to overcome modern challenges. The work presented in this dissertation has the ability to overcome inherent challenges in a number 2D nanomaterial groups. Our work represents an origin point for taking advantage of a range of materials in a variety of future applications. Notably, the expansion of the family of 2D halide perovskites into lead free alternatives while expanding the ligand options. We highlight the ability to fabricate 2D Bi-based halide perovskite nanosheets passivated with PEG ligands that provide solvent controlled assemblies. Non-2D forms of Bi halide perovskite have shown increased stabilization in ambient environments due to the ability of Bi to form thin oxidation layers while maintaining the core integrity of the perovskite.[101] These non-2D Bi nanomaterials have shown encouraging catalytic activity in the reduction of CO_2.[202] Lastly, applying PEG ligands opens up avenues into biocompatible perovskite materials.[203] Although there may be better alternatives to Bi-based 2D halide perovskites in specific applications, without expanded investigations into the fundamental optoelectronic response and catalytic activity of the material it remains unknown.

Our work studying the surface passivation of plasmonic WO_{3-x} denotes fundamental expansion on how the Drude model, developed for noble metals, continues to fall short in describing the optoelectronic response of plasmonic semiconductors. There has been much research into LSPR active doped semiconductors; however, knowledge of oxygen vacancy driven LSPR in the extremely important class of transition metal oxides is still lacking. WO_{3-x} has been shown to be a prized material for catalytic and surface enhanced Raman spectroscopy (SERS) applications, but there is little fundamental understanding of how oxygen vacancies at the surface may impact the disparate mechanisms of these applications.[174, 204] Thus, continued advancements in the understanding of the impact of surface chemistry in these materials may one day provide economical alternatives to noble-metal LSPR based technologies.

The covalent modification of MXene surfaces that we highlight imparts processability to a material that currently has not been commercialized. MXene compositions are ever expanding and as a more stable alternative to the original 2D material, graphene, the applications are near endless.[55] Our work features the creation of a MXene surface with functional group containing ligands that will allow for the use of MXenes in a range of technologies requiring covalent attachments. Markedly, the use of MXenes as nanofillers in polymer nanocomposites.[205] Overall, this dissertation represents fundamental first steps and an expansion of possibilities to utilizing some of the most important materials existing today.

CHAPTER 2. COLLOIDAL SYNTHESIS OF SINGLE LAYER QUASI-RUDDLESDEN-POPPER PHASE BISMUTH-BASED TWO-DIMENSIONAL PEROVSKITE NANOSHEETS WITH CONROLLABLE OPTOELECTORNIC PROPERTIES

This article has been adapted with permission from, Jacob T. Lee, Soenke Seifert, and Rajesh Sardar. *Chemistry of Materials* **2021** *33* (15), 5917-5925 DOI: 10.1021/acs.chemmater.1c00857

2.1 Synopsis

In this chapter we report the colloidal synthesis of Bi-based 2D perovskite nanosheets, $(PEG6\text{-}NH_3^+)_nCs_{3-n}Bi_2X_9$, where X=Cl, Br, and I, through careful design of reaction conditions and selection of polyethylene glycol (PEG6) surface passivating ligands. The 2D nanosheets are ~5 nm in thickness with micron-sized lateral dimensions and display composition dependent band gap and work function modulation. Small angle X-ray scattering analysis substantiates that the individual inorganic crystal layer, $Cs_{3-n}Bi_2X_9$, is separated by the spacer, PEG6 ligand. Additionally, we determined that $PEG6\text{-}NH_2$ is an essential passivating ligand and spacer for the formation of Bi-based 2D nanosheets. Most importantly, controlled crystallization of the colloidal dispersion of nanosheets results in the formation of superlattice microstructures of the quasi-Ruddlesden-Popper phase. These microstructures can be exfoliated to ultrathin nanosheets by overcoming the vdWs interaction between the organic passivating layers. The controlled synthesis of lead-free 2D perovskite nanosheets presented here can expand their utility to photocatalytic and optoelectronic applications with reduced toxicity.

2.2 Introduction

The discovery of atomically thin graphene by mechanical exfoliation of graphite[4] has led to significant research activities involving synthesis, characterization, and solid-state device application of two-dimensional (2D) materials that are a single or few-layers thick. 2D materials offer unique physical, optical, and electronic properties unlike those of their bulk counterparts due to increased carrier mobility, high surface-to-volume ratios, and excitonic confinement in multiple dimensions.[206] Most widely studied 2D materials such as graphene, transition metal dichalcogenides, and MXenes are derived from physical and chemical exfoliation of their bulk counterparts or through vapor deposition methods.[40, 55, 207-209] In recent years, 2D perovskite nanomaterials have shown tremendous promise for various applications[210-211] because of their inherently high molar absorptivity and large defect tolerances.[180, 212-213] However, colloidal synthesis of ultrathin perovskites has proven to be extremely difficult. A few reports on the synthesis of lead-based inorganic-organic 2D perovskite nanosheets are known that commonly use the solution phase re-crystallization approach.[87, 172, 214] Shamsi et al. presented thin $CsPbX_3$ nanosheets synthesized via a colloidal method.[89]

To obtain 2D relevant properties for photovoltaic and optoelectronic applications from fundamentally 3D perovskite structures most research is focused on creating hybrid organic-inorganic Ruddlesden-Popper phase structures, $(A)_2(CH_3NH_3)_{n-1}M_nX_{3n+1}$, where A represents a bulky ammonium based cation, M is the metal of choice usually Pb, X is the halide, and “n” represents the number of perovskite units in the inorganic layer.[215-217] These large ammonium cations in the A site cannot fit within the perovskite but passivate the edge creating bulk layered materials with electronic structures similar to quantum wells. The unique electronic properties arise from the difference in dielectric values between the inorganic and organic layers.[218-220] When preparing thin films using 2D materials for optoelectronic and photovoltaic applications, the materials show a tendency to assemble into heterogenous multilayered (multiple n-values) structures. Importantly, these heterogeneous films have been shown to act as energy funnels in which layers containing a lower n-value greatly improve charge separation and movement in comparison to larger n-valued layers.[221-224] These charge separation and funneling properties are still dependent on both direction of layer growth and movement between layers which in most cases are bulky insulating organic ligands.[225]

The intrinsic toxicity and lack of long-term stability of Pb-based materials have prompted the use of relatively non-toxic metals for the synthesis of either fully inorganic or inorganic-organic hybrid perovskites nanomaterials.[101-102, 226] Metallic Pb has been replaced by Bi, Sn and Sb to synthesize relatively non-toxic perovskite spherical nanocrystals.[227-229] However, to the best of our knowledge, no literature report is currently available on the colloidal synthesis of lead-free, ultrathin 2D nanosheets. In this article, using Bi^{3+} as the b-site cation forming the center of the perovskite octahedron and functional polyethylene glycols (PEGs) as passivating ligands, we report a new Pb-free, perovskite $[(PEG6\text{-}NH_3^+)_nCs_{3-n}Bi_2X_9$, X = Cl, Br, and I] nanosheet synthetic route. Here we use "n" as an integer to represent the number of $PEG6\text{-}NH_3^+$ ligands inserting into the crystal lattice, not the number of perovskite units as it is used in the given Ruddlesden-Popper formula above. These nanosheets form through the control of the inorganic lattice crystal structure, careful manipulation of the metal precursor concentration, and interplanar van der Waals interactions. We show that altering the halide ion in the inorganic crystal results in a shift of the optical band gap from 3.16 to 2.70 to 2.34 eV for chloride, bromide, and iodide, respectively. We also observe ~300 meV change in the work function of the Bi-based perovskite nanosheets by changing the halide ion in the perovskite crystal structure. Furthermore, we are able to produce Quasi-Ruddlesden-Popper phase superlattice structures (hexagonal stacked and petal-type structures) by controlling the evaporation process of colloidal $(PEG6\text{-}NH_3^+)_nCs_{3-n}Bi_2Br_9$ nanosheets. Owing to their expected, unique chemical and physical properties, we believe that our newly synthesized 2D nanosheets could be useful for a number of applications.

2.3 Results and Discussion

In an optimized reaction condition, $(PEG6\text{-}NH_3^+)_nCs_{3-n}Bi_2Br_9$ nanosheets were synthesized by mixing surface passivating PEG6 ligands ($PEG6\text{-}NH_2$ and PEG6-COOH) and cesium-PEGylate in 1-octadecene at 100 °C followed by addition of a dimethyl sulfoxide solution of $BiBr_3$. UV-vis spectroscopic analysis of the purified product shows an absorption peak of the bromine containing material at 425 nm (Figure 2.1A). Photoluminescence study of the bromine product (Figure 2.1A inset) reveals a low intensity emission near 458 nm which we assign to a direct band-gap emission.[226] Theoretical calculations have shown that 2D confined materials display high exciton binding energies that result in low photoluminescence quantum efficiency.[230] As illustrated in Figure 2.1B, small angle X-ray scattering (SAXS) analysis of the materials shows a strong peak near 0.369 $Å^{-1}$ with a lamellar repeating pattern (n=1, n=2, n=3). Transmission electron microscopy (TEM) characterization shows the formation of individual, ultrathin nanosheets (Figure 2.1C,D) with variable densities or layers, and typical edge folding and overlapped layers (Figure 2.2).

An average lateral dimension of nanosheets is ~360 ± 94 nm (Figure 2.1E, top panel) while the folding edges provide an estimated thickness of 5.1 ± 1.1 nm (Figure 2.1E, bottom panel). We believe this thickness is an over estimation of the actual thickness because 2D nanosheets have a tendency to stack during the drying process on the TEM grid. Powder X-ray diffraction (XRD) analysis confirms the hexagonal crystal lattice ($P\bar{3}m1$), which is common for Cs3Bi2Br9 perovskites (Figure 2.1F). One would expect broad XRD peak due to ultrathin dimension of the nanosheets. However, we observe sharp peaks in the XRD analysis that could be due to the formation of microstructures during the sample preparation steps. We observed that the nanosheets possess an inherent ability to form stacked microstructures when a high concentration colloidal solution is drop-casted onto a solid surface. Further, FTIR spectroscopy characterization of purified perovskite nanosheets (Figure 2.3) reveals a strong peak at 1106 cm^{-1} which is assigned as the C-O-C stretching mode of PEGs ligands. Peaks in the range of 3200-3435 and at 1453 cm^{-1} represent the N-H stretching and bending modes of the amine of PEG6-NH$_2$ ligands, respectively.[231] The inclusion of the peak at 1633 cm^{-1} denotes the presence of -C=O appearing

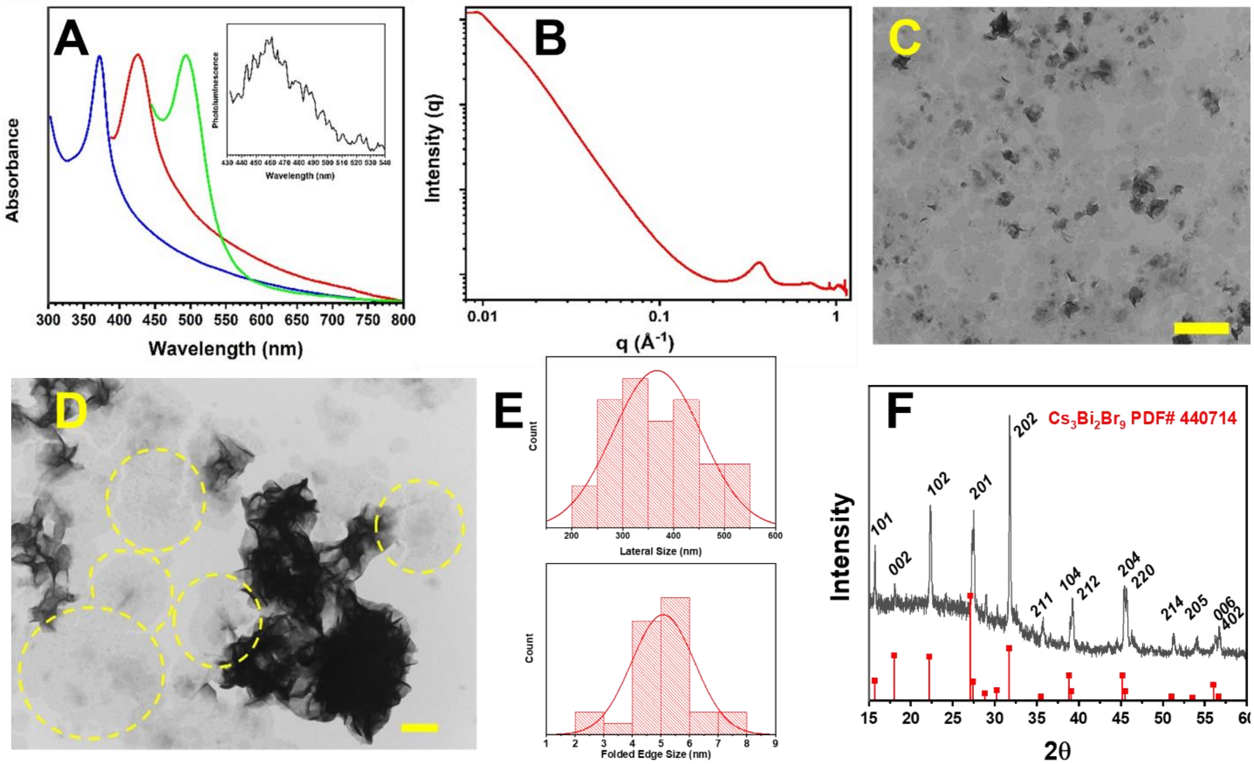

Figure 2.1: (A) UV-vis spectra of (PEG6-NH$_3^+$)$_n$Cs$_{3-n}$Bi$_2$Cl$_9$ (blue), (PEG6-NH$_3^+$)$_n$Cs$_{3-n}$Bi$_2$Br$_9$ (red) and (PEG6-NH$_3^+$)$_n$Cs$_{3-n}$Bi$_2$I$_9$ (green). The inset displays a typical photoluminescent spectrum of (PEG6-NH$_3^+$)$_n$Cs$_{3-n}$Bi$_2$Br$_9$ perovskite. (B) A representative SAXS spectrum of (PEG6- NH$_3^+$)$_n$Cs$_{3-n}$Bi$_2$Br$_9$ nanosheets. Low (C) and high (D) magnification TEM images of (PEG6-NH$_3^+$)$_n$Cs$_{3-n}$Bi$_2$Br$_9$ nanosheets with the scale bar of 500 and 200 nm, respectively. Yellow dashed lines in (D) outline the presence of single-layer nanosheets. (E) Histograms of lateral and folded edge sizes of D, minimum 50 measurements. (F) XRD of (PEG6-NH$_3^+$)$_n$Cs$_{3-n}$Bi$_2$Br$_9$ compared to reference for hexagonal Cs$_3$Br$_2$Br$_9$.

from the PEG6-COOH in the PEG6-COO$^-$ form. We selected PEG ligands because glycol units in the PEG chain offer many advantages over aliphatic chains including increased conductivity via the electron density of the oxygen atoms, increased solubility in a wide range of solvents and flexibility to form brush or mushroom type structures.[232] Additionally, Wang et al. used PEG ligands when synthesizing antimony based perovskite quantum dots to show PEG's superior hydrophilicity increases the perovskite stability against water in ambient atmosphere and overall biocompatibility opening up future possible applications in bioimaging.[97]

It is shown that organic cations play a vital role in the formation of 2D nanosheets of lead-based perovskite in which some Cs atoms are replaced by alkylammonium cations.[96] Energy dispersive X-ray spectroscopy (EDS) analysis determines the surface composition of our nanosheets with Bi to Br ratio is 1 : 4.54 (data not shown). The data support a $Cs_3Bi_2Br_9$ type crystal structure in which bismuth ions create an octahedra with bromine ions and overall charge of the crystal is balanced through insertion of Cs^+ atoms or in our case a mixture of Cs^+ and PEG6-NH_3^+. Alkylammonium ions are often formed during colloidal syntheses and passivate the surface of nanocrystals; however, ammonium insertion in the crystal is feasible and necessary due to our

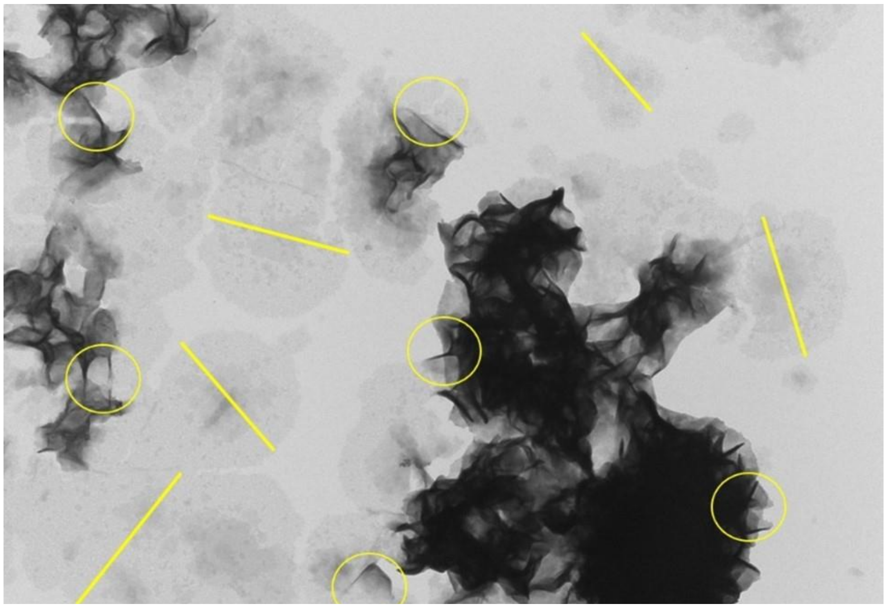

Figure 2.2: TEM image of (PEG6-NH_3^+)$_x$$Cs_{3-x}Bi_2Br_9$. An example of how Image J was used to estimate the thickness of the nanosheet based upon overlap/folds (yellow circles) and provide lateral dimensions of large single layer sheets (yellow lines). The scale bar is 200 nm. Over 50 measurements were taken across multiple images of multiple samples to determine lateral dimensions.

cesium deficient reaction conditions (see Section 2.5.3). X-ray photoelectron spectroscopy (XPS) analyses also support a cesium deficient inorganic lattice composition by analyzing binding energy peaks of Bi 4f, Cs 3d, Br 3d, and N 1s (Figure 2.4). Bi 4f peaks in XPS appear at 158.8 and 164.1 eV for $4f_{7/2}$ and $4f_{5/2}$, respectively. The doublet of Cs 3d manifest at 723.9 and 737.8 eV for $3d_{5/2}$ and $3d_{3/2}$, respectively. The Br 3d at 67.8 and 68.9 eV for $3d_{5/2}$ and $3d_{3/2}$ respectively. The appearance of the broad N 1s can be fitted with two peaks at 399.7 and 401.2 eV. Generally, no splitting is involved in N 1s orbitals. Therefore, appearance of two peaks represents two types of nitrogen environments. We believe the peak near 400 eV represents the $-NH_2$ of the surface passivating ligand (PEG6-NH_2), and the peak near 401 eV represents $-NH_3^+$, the protonated amine that inserts into the inorganic crystal to provide overall charge neutrality to the perovskite structure.[233] Therefore, we define the chemical composition of Bi-based 2D perovskite as (PEG6-NH_3^+)$_n$$Cs_{3-n}Bi_2Br_9$.

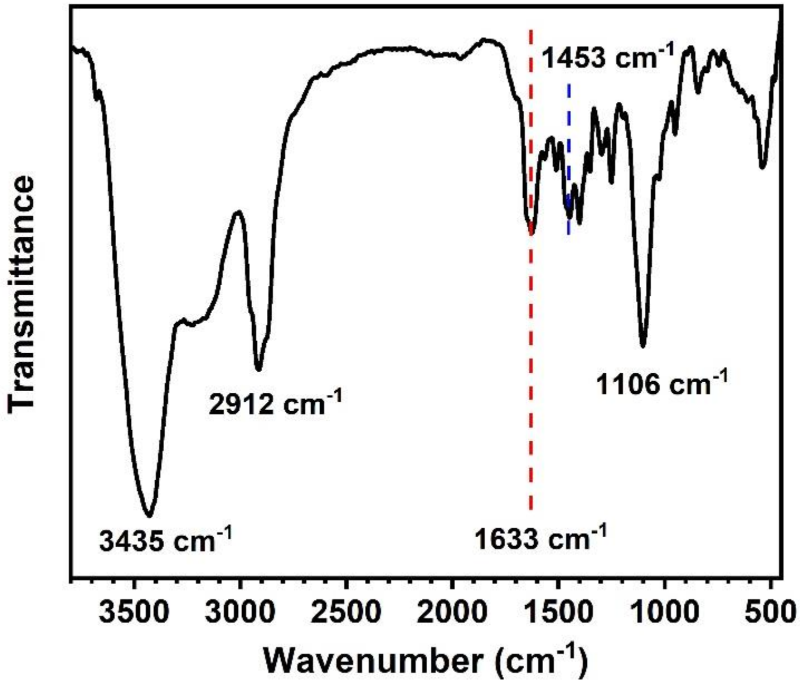

Figure 2.3: FTIR Spectrum of purified (PEG6-NH_3^+)$_n$$Cs_{3-n}Bi_2Br_9$ nanosheets.

We hypothesize that the formation of our (PEG6-NH_3^+)$_n$$Cs_{3-n}Bi_2Br_9$ 2D nanosheets occurs through a combination of van der Waals interactions and mesoscale growth (Figure 2.5). The cesium deficiency facilitates the insertion of PEG6-NH_3^+ into the crystal to maintain the overall charge neutrality once the nuclei convert to larger nanocrystals. The hydrophilic-hydrophilic

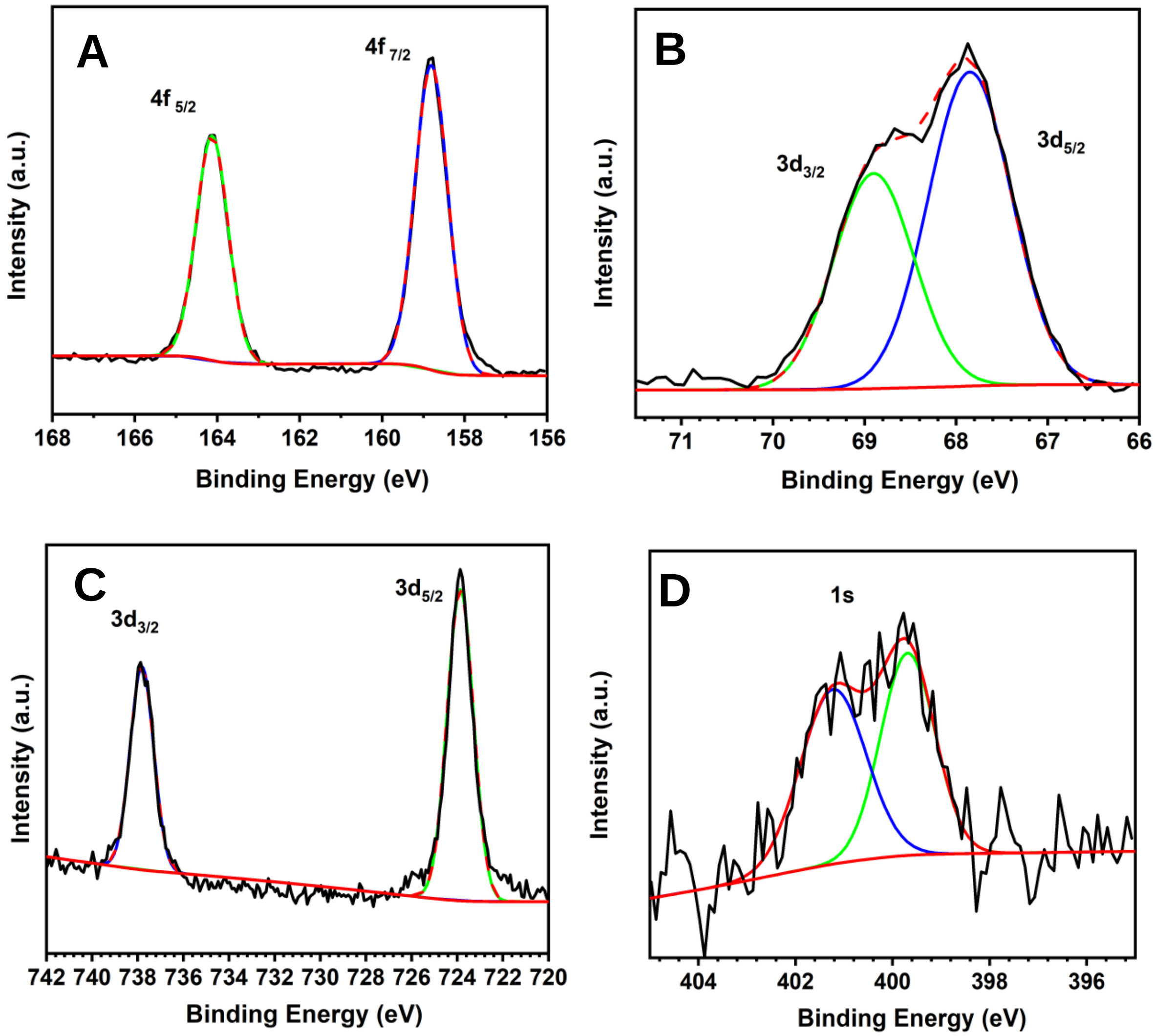

Figure 2.4: XPS spectra for (PEG6-NH$_3^+$)$_n$Cs$_{3-x}$Bi$_2$Br$_9$ with characteristic fittings of their binding energies and characteristic orbital splitting for (A) bismuth, (B) bromide, (C) cesium and (D) nitrogen. Two types of nitrogen are present: a neutral amine near 400 eV and a protonated amine near 401.6 eV.

interaction of PEG tails and the flexibility of PEG chains allow mesoscale assembly that lead to attachment of nanocrystals parallel to our substrate surface for the formation of nanosheets. Creutz, et al. has observed a natural cleavage along the (002) plane in nanoplatelet structures and we believe a similar cleavage supports our hypothesis.[234] As shown in Figure 2.5, the (002) plane provides access to vacant surface sites for the insertion of PEG6-NH$_3^+$ due to a combination of hydrogen and ionic bonding interactions. 2D nanosheets stack over time in solution aided by ligand-ligand van der Waals interactions. SAXS of this stacking reveals a lamellar repeating

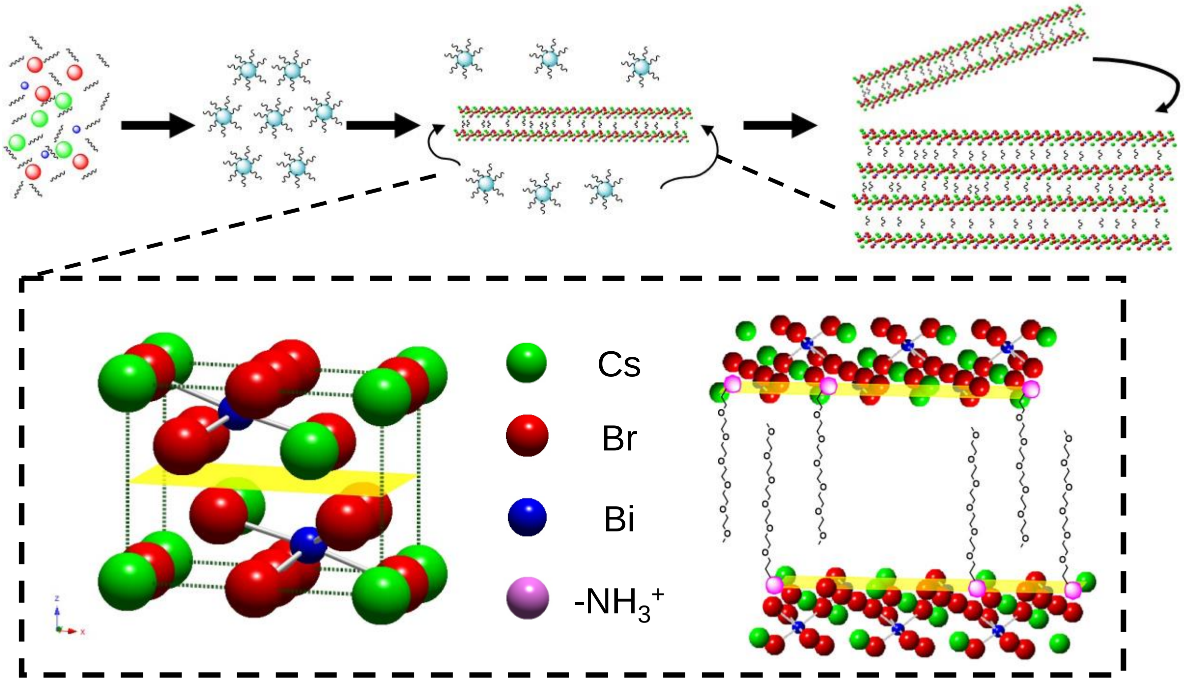

Figure 2.5: Schematic representation showing conversion of initial precursors to nanocrystals, and then to the formation of individual nanosheets with further stacking of nanosheets under solvent evaporation conditions.

pattern (n=1, n=2, n=3) with an inter-layer gap of ~1.7 nm (Figure 2.1B).[88, 235] 3D modeling (ChemDraw 3D) of a PEG6-COOH molecule provides an estimated molecule length of 2.1 nm. The inter-layer distance determined from SAXS of $(PEG6\text{-}NH_3^+)_nCs_{3-n}Bi_2Br_9$ is ~1.7 nm. Therefore, some interdigitation between the PEG6 chains of neighboring perovskite layers has

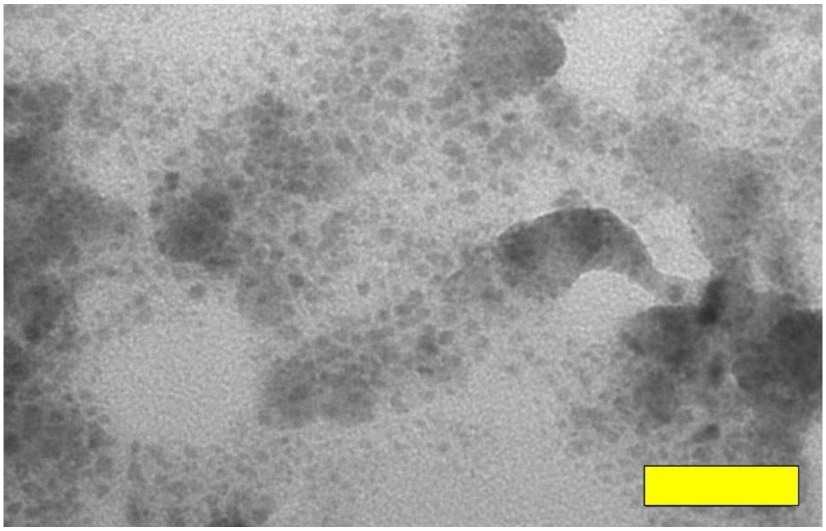

Figure 2.6: Synthesis of bromide product with 4 times the typical amount of Cs-PEGylate precursor showing a clear lack of nanosheet formation. Scale bar is 50 nm

taken place. To test the proposed formation mechanism involving PEG6-NH_3^+ insertion into the crystal lattice, we increased the amount of Cs-PEGylate precursor four times the original concentration and that results in formation of mostly spherical nanocrystals rather than nanosheets (Figure 2.6). We also used a rigid amine such as oleylamine, which is very commonly used in perovskite nanocrystal synthesis,[78] but no nanosheet formation was observed (Figure 2.7A). Also, the absorption peak (Figure 2.7B) is located at 386 nm, which is closely related to other non-stoichiometric bismuth-based perovskites nanocrystals as reported by Creutz et al.[234] Taken together, our experimental results strongly suggest that the choice of PEG-ylated ligands and an appropriate stoichiometry of metal precursor in the synthetic condition are crucial for the formation of ultrathin perovskite nanosheets.

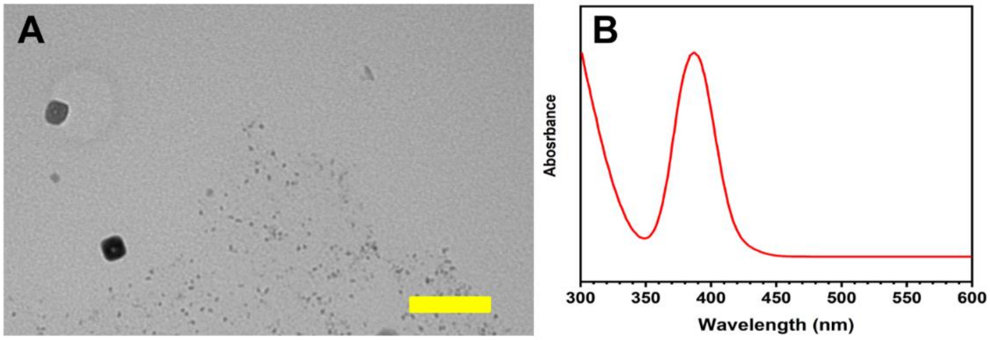

Figure 2.7: : (A) TEM microscopy image of perovskites nanocrystals synthesized using oleylamine and oleic acid as surface passivating ligands. Scale bar is 100 nm. (B) UV-vis absorption spectrum of the purified nanocrystals

Our experimental data presented above suggest that PEGs are the unique ligands for the formation of Bi-based, ultrathin perovskite nanosheets. We extended the synthetic method of 2D Bi-based nanosheets to other halide ions (Cl and I) because it is shown that halide ions play significant role in the catalytic rates in Bi-based perovskite materials.[202] As shown in Figure 2.1A, $(PEG6\text{-}NH_3^+)_nCs_{3-n}Bi_2Cl_9$ and $(PEG6\text{-}NH_3^+)_nCs_{3-n}Bi_2I_9$ nanosheets display absorption peaks at 372 and 493 nm, respectively, with corresponding energy values 3.16 and 2.34 eV, respectively, as determined from Tauc plot analyses in accordance with methods for cesium bismuth halide found in the literature.[226] A strong composition dependent band gap effect is observed between 2D nanosheets depending on the halide ions. XRD data show good crystallinity of $(PEG6\text{-}NH_3^+)_nCs_{3-n}Bi_2Cl_9$ and $(PEG6\text{-}NH_3^+)_nCs_{3-n}Bi_2I_9$ nanosheets with the hexagonal crystal lattice ($P\bar{3}m1$) as similar to $Cs_3Bi_2Cl_9$ and $Cs_3Bi_2I_9$, respectively (Figure 2.8-2.9). The XRD spectrum of (PEG6-

$NH_3^+)_nCs_{3-n}Bi_2Cl_9$ shows some distortion especially at higher angles which could arise from lattice strain upon attachment of binding head groups (-NH_2 and/or -OOC) from the surface passivating ligands.[236-237] TEM analyses demonstrate up to 230 nm lateral dimension nanosheets (Figure 2.8). Although we are able to synthesize iodide containing perovskite nanosheets (Figure 2.9), our XRD analysis shows distortion or mixing of possible crystal phases (Figure 2.9). Iodine containing perovskites often require a high temperature for colloidal synthesis[78]; however, our standardized synthetic conditions were unable to form single crystal lattice products with the reaction temperatures >150 °C because PEG6 ligands undergo decomposition at elevated temperature.

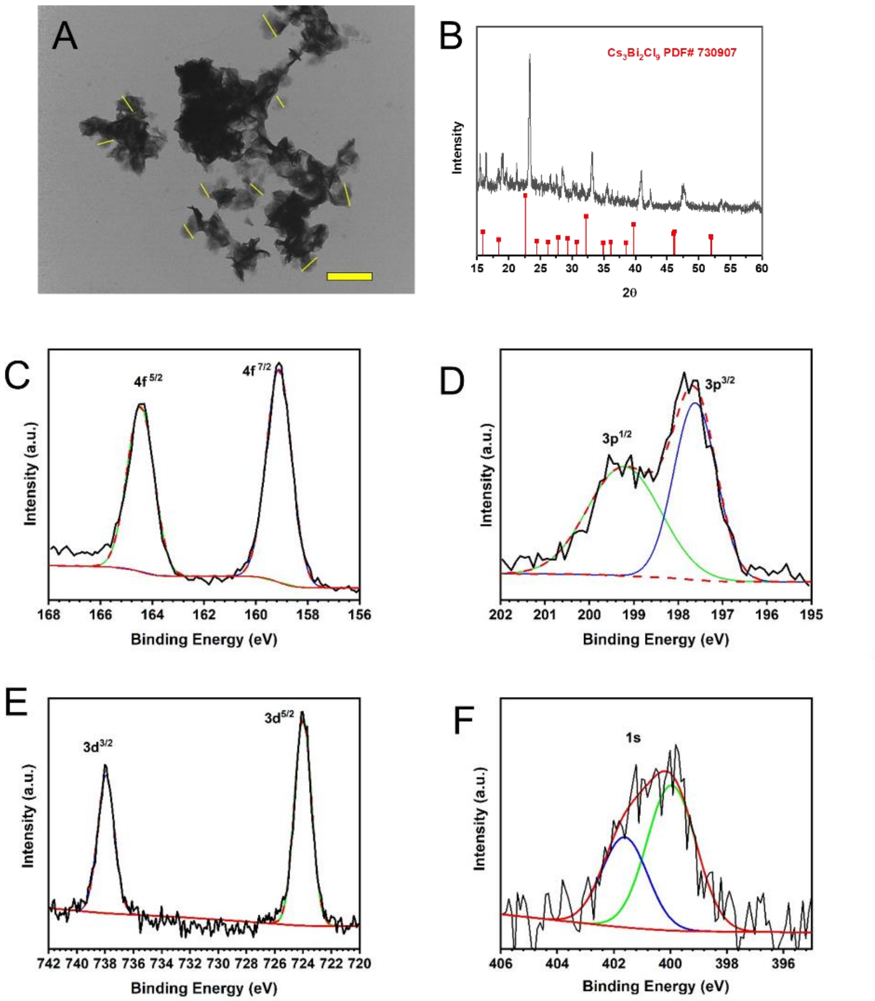

Figure 2.8: Data for (PEG6-NH_3^+))$_x$$Cs_{3-x}Bi_2Cl_9$ A) TEM image with representation of Image J analysis for lateral dimensions. Scale bar is 500 nm. (B) PXRD diffractogram comparing the standard for $Cs_3Bi_2Cl_9$. XPS spectra with fittings for (C) bismuth, (D) chloride, (E) cesium, and (F) nitrogen.

Determination of precise band structure (valance and conduction band positions, and fermi level) of our newly synthesized Bi-based 2D perovskite nanosheets should be extremely important for catalytic applications and solid-state device development. We used ultraviolet photoelectron spectroscopy (UPS) to analyze (PEG6-NH_3^+)$_n$$Cs_{3-n}Bi_2Br_9$ nanosheets and the work function is determined to be 3.52 eV (Figure 2.10B and Figure 2.11), and the position of valence band region is 2.82 eV (Figure 2.10A). A direct band gap Tauc plot provides an optical band gap of 2.70 eV

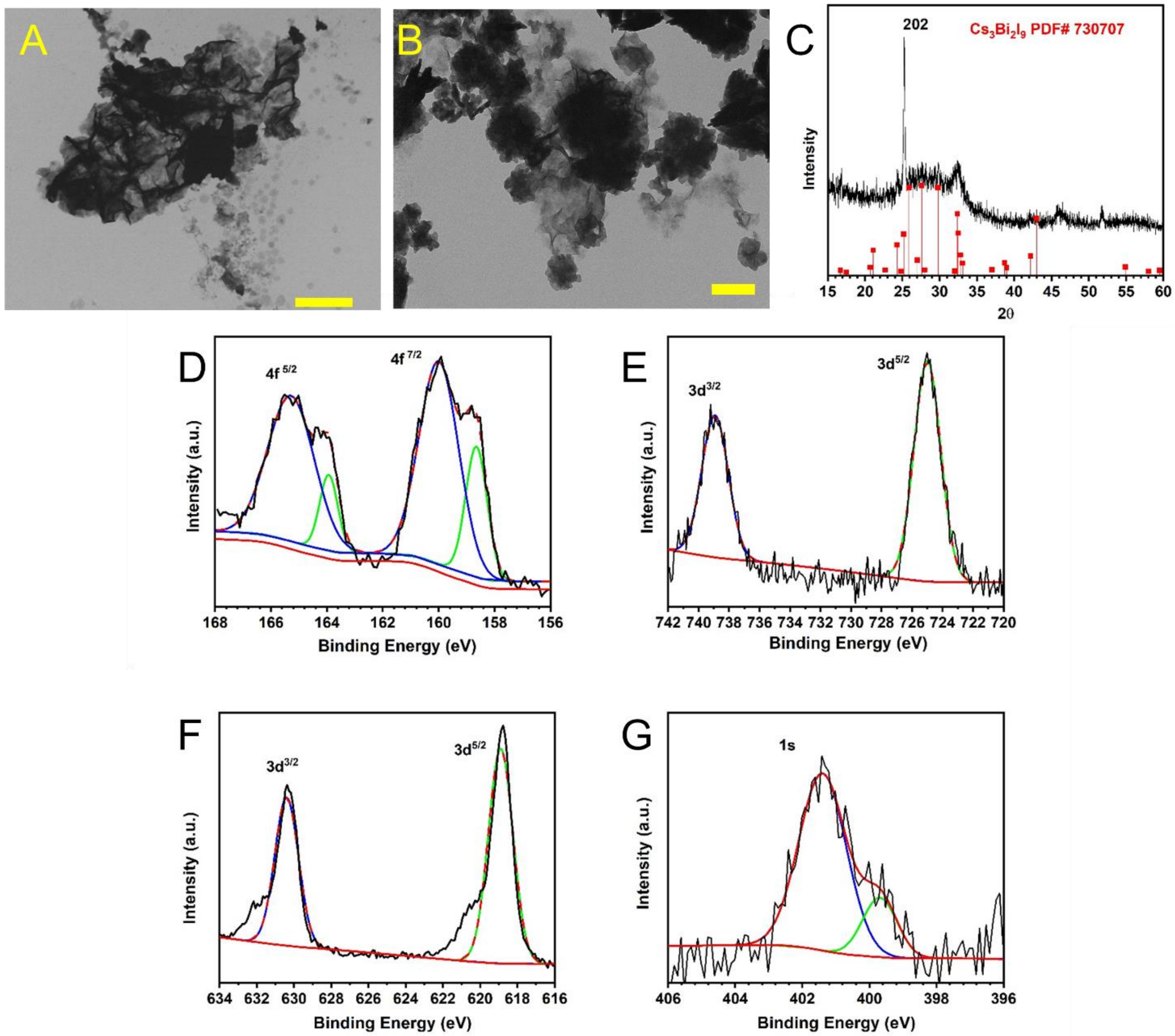

Figure 2.9: Data for (PEG6-NH_3^+))$_x$$Cs_{3-x}Bi_2I_9$ A) Low magnification TEM image with a 1.0 µm scale bar. B) Higher magnification TEM image. scale bar is 200 nm. C) PXRD data comparing to the standard for $Cs_3Bi_2I_9$. XPS spectra for (PEG6-NH_3^+))$_x$$Cs_{3-x}Bi_2I_9$ with characteristic fittings of their binding energies and tell-tale orbital splitting of (D) bismuth, (E) bromide, (F) cesium and (G) nitrogen There are two types of nitrogen present: a neutral amine near 400 eV and a protonated amine near 401 eV.

(Figure 2.10C and Figure 2.12). Therefore, the conduction band position with respect to vacuum is 3.10 eV. Based on the UPS and UV-visible spectroscopy analyses, we have developed a band diagram for 2D (PEG6-NH_3^+)$_n$$Cs_{3-n}Bi_2X_9$ perovskites nanosheets (Figure 2.10D). Similar to lead-based perovskites, we observe a band gap decrease moving from chloride to bromide to iodide.[178, 223, 238] This is due to the absorption taking place between the bismuth and halide ions within the octahedra. This directional shift is also applicable to the work function values from 3.67 eV for chloride to 3.43 eV for iodide. Table 2.1 provides a full list of all values and calculations involved in formation of the band diagram.

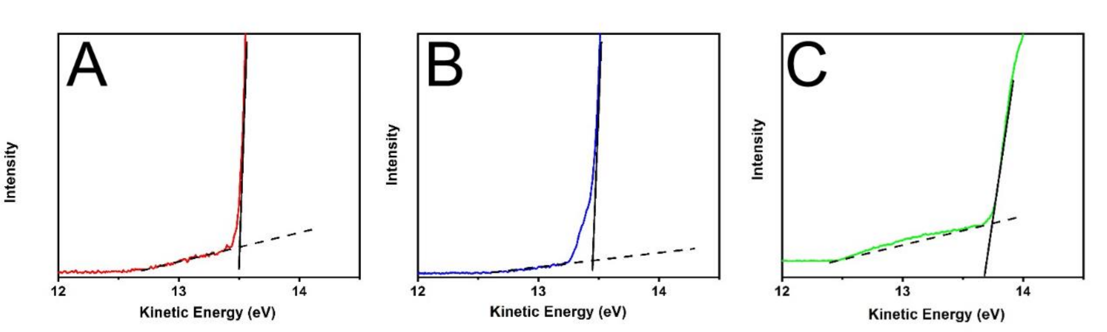

Figure 2.10: UPS high energy cut-off spectra for (PEG6-NH_3^+))$_x$$Cs_{3-x}Bi_2X_9$ where X chloride (A), bromide (B), iodide (C). See table 2.1 for values.

Previous work showed that controlled solvent evaporation of alkylammonium containing Ruddlesden-Popper phase perovskite materials created stacked superstructures of varying sizes.[87, 96] To further expand the potential utility of Bi-based 2D perovskite nanosheets for future applications, we investigated the assembly process of nanosheets by controlling the evaporation temperature of their colloidal dispersions in chloroform. At a slow evaporation rate, appearance of flat hexagonal 2D layered superlattices with an average dimension of 490 ± 23 nm are observed in the SEM analysis (Figure 2.13A and B). In contrast, petal type structures are formed at a faster evaporation rate (Figure 2.13C). Although it is our understanding that the solvent evaporation rate is just one of the variables that controls the self-assembly process and the resulting structure of the superlattice, we do not fully understand the mechanism underlying such processes. The XRD analysis of hexagonal 2D layered superlattices (Figure 2.13D) suggests the formation of quasi-

Ruddlesden-Popper phase perovskites with an n-value of 1.0 as characterized by the 0k0 peak (2θ = 5.7). The growth has very little contamination along the (111) crystal plane which is similar to n=1 growth in lead iodide Ruddlesden-Popper phase perovskites.[239] Our data suggests Ruddlesden-Popper type insertion of the ammonium group into the crystal lattice; however, without further in-depth in-situ characterization and study, specifically synthesizing other n-value sheets, we choose to act cautiously and define this material as a quasi-Ruddlesden-Popper phase perovskite.[240] To the best of our knowledge, this is the first demonstration of the synthesis of a Bi-based quasi-Ruddlesden-Popper perovskite phase. We believe that PEG6-NH_2 ligands act as a spacer to separate bismuth bromide octahedra layers, while both PEG6-NH_2 and PEG6-COOH

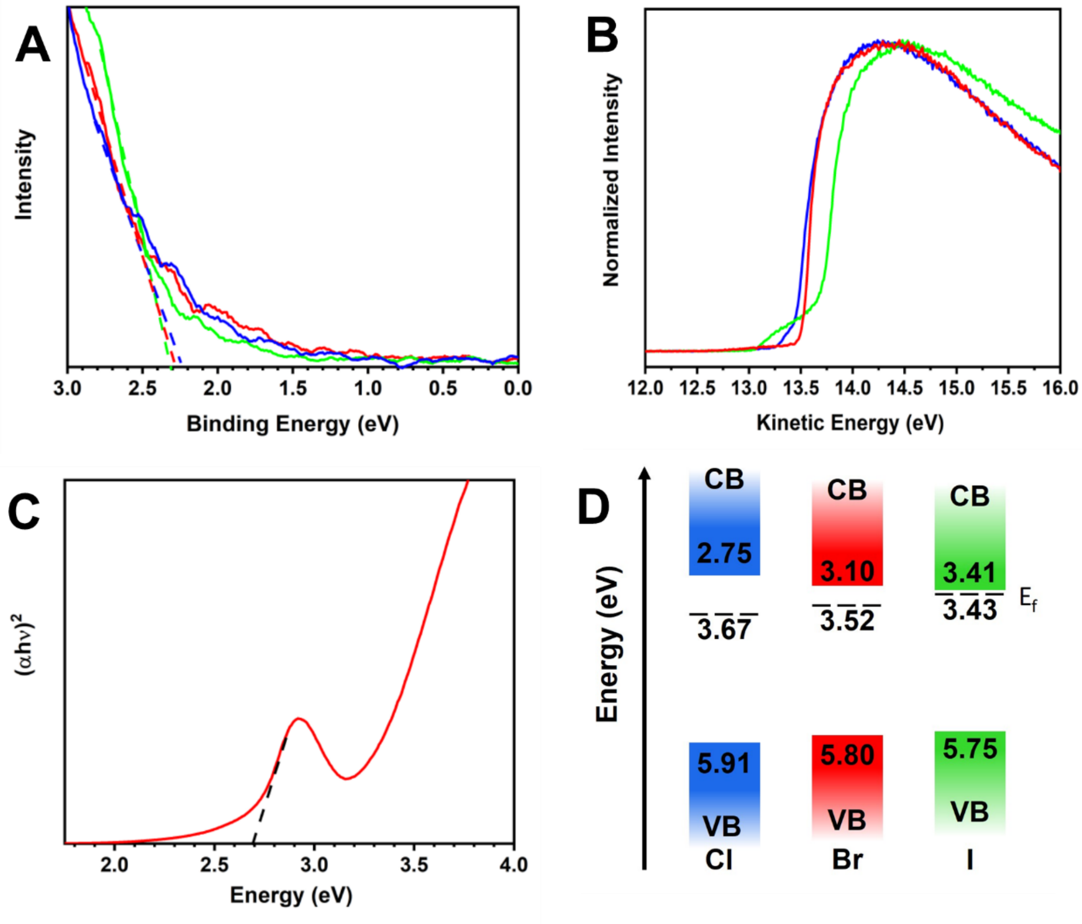

Figure 2.11: (A) Valance band region and (B) secondary energy cut off UPS spectra of $(PEG6\text{-}NH_3^+)_nCs_{3\text{-}n}Bi_2Cl_9$ (blue), $(PEG6\text{-}NH_3^+)nCs_{3\text{-}n}Bi_2Br_9$ (red) and $(PEG6\text{-}NH_3^+)_nCs_{3\text{-}n}Bi_2I_9$ (green). (C) Direct band gap Tauc plot analysis of $(PEG6\text{-}NH_3^+)_nCs_{3\text{-}n}Bi_2Br_9$. (D) Band diagram with respect to vacuum where CB is conduction band minimum, VB is valence band edge and E_f is the Fermi energy level.

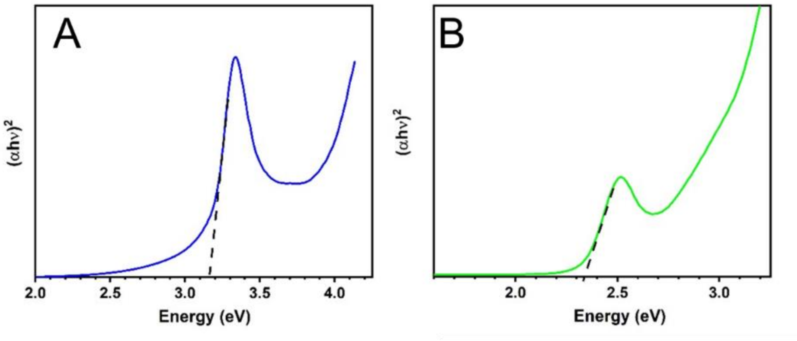

Figure 2.13: Direct band gap tauc plots for (PEG6-NH_3^+))$_x$$Cs_{3-x}Bi_2X_9$ perovksite nanosheets where X is chloride (A) and iodide (B).

ligands passivate the surface of nanosheets to dictate their height and width. In our system the inter-layer interaction between the glycol chain via van der Waals forces through a mesoscale assembly process is the key for the formation of quasi-Ruddlesden-Popper perovskite phase.[88] The van der Waals force is weak in nature, therefore we would expect that 2D layered superlattices can

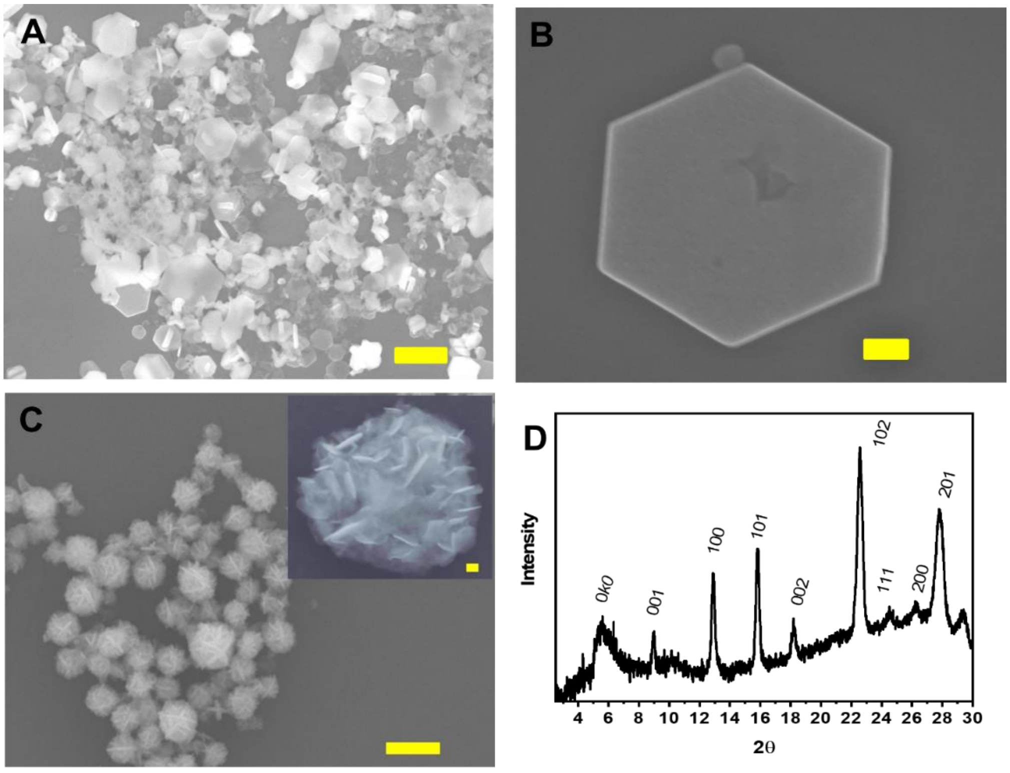

Figure 2.12: SEM images (PEG6-NH_3^+)$_n$$Cs_{3-n}Bi_2Br_9$ microstructures upon controlled evaporation to obtain hexagonal (A and B) structures. Scale bars in (A) and (B) are 1 µm and 100 nm, respectively. (C) A representative SEM image of petaled structures, and the inset show an individual petal-type structure. Scale bars 1 µm and 100 nm, respectively. (D) PXRD of evaporated hexagonal product.

be exfoliated through mechanical forces such as sonication as shown for MXenes.[241] To validate this, hexagonal 2D superlattices composed of $(PEG6\text{-}NH_3^+)_nCs_{3-n}Bi_2Br_9$ were dispersed in polar solvents such as dichloromethane and sonicated for 10 min at room temperature, which results in the formation of individual $(PEG6\text{-}NH_3^+)_nCs_{3-n}Bi_2Br_9$ nanosheets (Figure 2.14).

Table 2.1: Summarized optical and electronic values obtained from UPS and UV-vis spectroscopy analyses. [a] Value obtained from the secondary energy cutoff. [b] Calculated work function (Φ). [c] Value obtained from the valence band (VB) region of the UPS spectra, [d] Calculated valence band edge (VB), [e] Optical band gap (BG) determined from Tauc analyses, and [f] Calculated conduction band (CB). All values are with respect to vacuum.

Halide ion	cut-off (eV)[a]	calc. Φ (eV)[b]	VB region (eV)[c]	calc. VB (eV)[d]	optical BG (eV)[e]	calc. CB (eV)[f]
chlorine	13.67	3.67	2.24	5.91	3.16	2.75
bromine	13.51	3.52	2.28	5.80	2.70	3.10
iodine	13.43	3.43	2.32	5.75	2.34	3.41

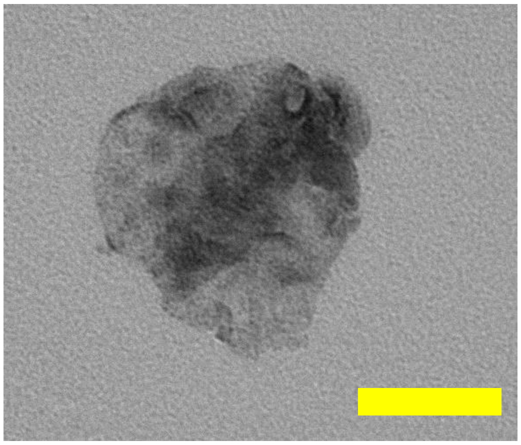

Figure 2.14: A representative TEM image of exfoliated $(PEG6\text{-}NH_3^+))_xCs_{3-x}Bi_2X_9$ perovskite nanosheets in dichloromethane. The scale bar is 200 nm.

2.4 Conclusions

In summary, through manipulation of inorganic precursor concentrations and constructive PEG ligand interactions, we have successfully synthesized Bi-based, 2D perovskite nanosheets with a composition of $(PEG6\text{-}NH_3^+)_nCs_{3-n}Bi_2X_9$ (X=Cl, Br). These syntheses resulted in a halide dependent optical band gap from 2.34 to 3.16 eV for chloride and iodide, respectively. Elemental analysis unequivocally proved a cesium deficient crystal lattice, and those Cs vacancy sites were filled by ammonium head groups of $PEG6\text{-}NH_3^+$ ligands to drive the formation of 2D nanosheets. We have shown that the appropriate selection of the surface passivating ligands is the key for the formation of the first Pb-free perovskite nanosheets. These nanosheets form a single layer (n=1) which, in addition to electronic benefits of PEG6 ligands, will provide ideal materials for charge separation and energy funneling heterogenous multilayered materials. We have also demonstrated that controlled self-assembly of individual nanosheets via mesoscale-directed growth resulted in the formation of quasi-Ruddlesden-Popper phase perovskite superlattices that can be reversibly exfoliated to individual nanosheets via mechanical forces. Taken together, we believe that the Bi-based perovskite nanosheets will expand the 2D nanomaterial-based photocatalytic and optoelectronic applications with reduced toxicity.

2.5 Experimental Section

2.5.1 Materials.

Bismuth bromide ($BiBr_3$, >99%), bismuth iodide (BiI_3, >99%), cesium carbonate (99.9%), 1-octadecene (90% technical grade), toluene (99.9%), hexane (99%), chloroform (>99%), and were purchased from Sigma Aldrich and used without further purification. Bismuth chloride ($BiCl_3$, >97%) was purchased from TCI. Tetrahydrofuran (99.9%), sodium hydroxide, sodium sulphate anhydrous, and methanol (99.9%) were purchased from Fisher and used without further purification. mPEG6-COOH (≥95%) and $mPEG6\text{-}NH_2$ (≥95%) were purchased from Biochempeg.

2.5.2 Synthesis of Cs-caroboxylate-PEG6. .

PEG6-COOH (0.75 mL) and cesium carbonate (0.2 g) were added to a 25-mL two-neck round bottom flask along with 7.5 mL ODE. The reaction mixture was heated at 150° C under nitrogen for 3 h under vigorous and stirring until a clear solution formed, indicating complete conversion of cesium carbonate to Cs-caroboxylate-PEG6. The reaction was cooled to room temperature, collected through centrifugation, and dried on filter paper.

2.5.3 Synthesis of (PEG6-NH3+)nCs$_{3-n}$Bi$_2$X$_9$, X = Cl, Br, and I) Perovskite Nanosheets.

In a 25 mL round bottom flask, 3.0 mL ODE along with PEG6-amine (60 µL) and PEG$_6$-acid (20 µL) were added together. Separately, 5.0 mg of Cs-carboxylate-PEG6 was placed in a small vial and dispersed in ODE (200 µL) by sonication then added to the round bottom flask, and then the reaction mixture was heated at 100° C for 45 min while stirring under N$_2$. Next, 0.06 mmol BiX$_3$ was dissolved in 200 µL DMSO and injected into the flask and allowed to react for 15 sec. At this point, ice-cold, 5.0 mL hexane and toluene mixture (7:3 volume ratio) mixture was quickly injected to quench the reaction. The product was isolated through centrifugation at 7000 rpm for 5 min. The product then further purified from chloroform dispersion by adding hexane and toluene mixture for two additional times before spectroscopic and microscopic analyses.

2.5.4 Characterizations

UV-vis absorption spectra were collected using a Varian-Cary 50 Scan UV-visible spectrophotometer with 1 cm quartz cuvettes over a range of 300-800 nm. All spectra were recorded in chloroform, and chloroform was used as a background for all measurements. The photoluminescence emission (PL) spectra were collected using a Cary Eclipse fluorescence spectrophotometer from Varian Instruments with 1.0 cm quartz cuvettes. Fourier transform infrared (FTIR) spectra were collected using a Thermo Scientific Nicolet iS10 spectrometer and analyzed using Omnic 8.2 software package. Samples were pelletized with vacuum dried KBr, and 100 scans were collected. The background was recorded in air with 64 scans. Elemental analysis was conducted on a field emission scanning electron microscopy system (Hitachi S-4700), which was equipped with an energy dispersive X-ray (EDS) analyzer, to determine the Cs : Bi ratio. Wide-angle Powder X-ray diffraction (PXRD) analysis were recorded on a Bruker D8 Discover X-ray diffractometer (Cu Kα, $\lambda = 1.54$ Å). Nanocrystals were drop-cast from the chloroform dispersion onto cleaned glass coverslips All samples were run with 0.015° increments at 1.5 s per step. Samples for transmission electron microscopy (TEM) characterization were prepared by placing 10 μL of the sample dissolved in chloroform onto a carbon-coated copper grid (Electron Microscopy Science). The sample was allowed to set for 30 seconds, and any excess solution was by wicked away with filter paper in order to avoid particle aggregation. Images were acquired using a Tecnai G2 12 Bio Twin. equipped with AMT CCD Camera operating at 120 kV. Small angle X-Ray scattering (SAXS) analysis measurements were taken of colloidal dispersion in quartz capillaries with an incident X-ray energy of 18 keV, a sample to detector distance of 2.255 m, and exposure time of 0.5 s. Data were analyzed using Igor Pro software. X-ray photoelectron spectroscopy (XPS) and ultraviolet electron spectroscopy (UPS) analysis were conducted at the Chapel Hill Analytical and Nanofabrication Laboratory (CHANL). Samples were prepared by drop casting purified samples onto piranha cleaned silicon wafers. A Kratos Axis Ultra DLD X-ray Photoelectron Spectrometer was used for both XPS and UPS. XPS was conducted with Al Kα x-ray irradiation, and pass energies of 80 eV and 20 eV for survey and high-resolution scans, respectively. For samples that were electrically conductive, the sample was grounded, and the charge neutralizer was turned off. Other samples showed some slight differential charging, and in these cases the charge neutralizer was used but the sample was isolated from ground. All spectra were corrected to the C 1s peak at 284.6 eV. UPS was conducted with the He I line (21.2eV) from a He discharge lamp and charge neutralizer turned off.

CHAPTER 3. SURFACE LIGAND CONTROLLED ENHANCEMENT OF CARRIER DENSITY IN PLASMONIC TUNGSTEN OXIDE NANOCRYSTALS: SPECTROSCOPIC OBSERVATION OF TRAP STATE PASSIVATION *VIA* MULTIDENTATE METAL-PHOSPHONATE BONDING

This article has been adapted with permission from, Jacob T. Lee, Sumon Hati, Mackenzie M. Fahey, Jeffrey M. Zaleski and Rajesh Sardar. *Chemistry of Materials* **2022** *34* (7), 3053-3066

DOI: 10.1021/acs.chemmater.1c04042

3.1 Synopsis

This chapter focuses on the surface chemistry-controlled manipulation of the optoelectronic properties of semiconducting 2D transition metal oxide nanomaterials. Specifically, the LSPR response of oxygen deficient tungsten oxide (WO_{3-x}) (NPLs) as viable alternative to expensive noble metal NCs. The LSPR of NCs allow manipulation of the optical responses by controlling their morphology, free carrier density, and local dielectric environment. Although extensive work has been done to control the LSPR properties of semiconductor NCs via doping, the role of surface ligand chemistry in the enhancement of LSPR properties remains poorly understood. Insufficient passivation of surface atoms creates dangling bonds and surface trap states that together could compromise the free carrier density and consequently optoelectronic properties. Here, we report the impact of metal-ligand bonding interactions on the free electron density (N_e) and the LSPR response of monoclinic WO_{3-x} NPLs. The LSPR properties of WO_{3-x} NPLs arise from the presence of free electrons in the conduction band as a result of oxygen vacancies in the monoclinic crystal. In-situ surface passivation of unpurified colloidal WO_{3-x} NPLs with X-type alkylphosphonate ($R-PO_3^{2-}$) produces an LSPR peak in the near infrared region of the electromagnetic spectrum. X-ray photoelectron, electron paramagnetic, and Raman spectroscopic data support the presence of a tridentate PO_3-W_3 bonding motif that allows increased passivation of shallow surface trap states leading to an experimentally determined N_e value of 8.4×10^{22} cm^{-3}. Furthermore, experimentally determined bonding characteristics are correlated with density functional theory calculations. The effect of the high N_e values of NPLs on their refractive index sensitivity is also evaluated. Together, the knowledge gained regarding surface ligand chemistry-controlled manipulation of the plasmonic properties in semiconducting metal oxide NPLs and the high N_e values of WO_{3-x} NPLs achieved, may result in sizable advancement in various LSPR-driven applications such as sensing and energy storage and conversion schemes.

3.2 Introduction

Localized surface plasmon resonance (LSPR) properties of nanomaterials arise from the collective oscillation of free charge carriers (electrons or holes) upon interaction with an external electromagnetic field.[242] LSPR properties are often associated with noble metal nanostructures (Au, Ag, etc.) as their metallic characteristic provides an extremely large free electron density (N_e) value (10^{23} cm^{-3}) leading to LSPR responses spanning the visible to near infrared regions of the electromagnetic spectrum.[243-245] Additionally, these large N_e values produce local electromagnetic fields as a consequence of the enhanced polarization of the free carriers that depends on the morphology of the nanomaterial.[246] In general, maximizing N_e is beneficial and necessary for the most effective and efficient use of nanomaterials in a wide variety of applications including biosensing,[247-249] surface enhanced Raman spectroscopy (SERS),[9, 250-251] and catalysis.[252-255] However, due to the prohibitive cost of noble metal nanostructures, low-cost and highly stable earth-abundant materials have been sought as viable alternatives. LSPR responses in semiconductor nanocrystals (NCs) can be created through atom vacancies, redox and photochemical charging, and introducing dopants into inorganic crystals. Appropriate composition for the creation of LSPR active materials can be established in metal chalcogenides (e.g., $Cu_{2-x}E$, E =S, Se, and Te),[182, 256-257] anion vacancy metal oxides,[113, 258] metal oxides with extrinsic dopants (e.g., Sn-doped In_2O_3, Al-/In-/F-doped ZnO, and In-doped CdO)],[259-262] and group IV elements (B/P-doped Si).[263-264]

Amongst all the above-mentioned semiconductor NCs capable of displaying LSPR properties, metal oxide NCs are highly desirable because their conduction band electrons are stable under ambient conditions.[50] Most LSPR active metal oxide NCs synthesized at high temperature contain extrinsic dopants which can vastly alter their performance whether dopants reside near the surface or are deep within the core.[129] Moreover, each host crystal can only allow a certain percentage of extrinsic dopants which makes the process highly challenging to achieve $N_e > 10^{21}$ cm^{-3}.[265] Anion vacancy metal oxides, such as sub-stoichiometric WO_{3-x},[266-267] offer a high degree of structure and composition tunability that make it an ideal material for a wide array of applications including electrochromic windows, photothermal therapy, sensing, photovoltaics, and photocatalysis, etc.[49] A high temperature reduced oxygen partial pressure synthesis creates oxygen atom vacancies in the LSPR active WO_{3-x} NCs. The thermodynamically stable oxygen vacancy at room temperature donates two electrons into the conduction band while generating a dianion point defect.[246] Importantly, for charge compensation created by the oxygen vacancy, surface W^{6+} can undergo reduction to form W^{5+} and/or W^{4+}. As the amount of oxygen vacancies increases, the chances of the formation of reduced W sites such as W^{+5} are higher.[118, 125] This reduction of tungsten atoms provides the potential for the creation of defect sites (trap states) in which electrons, normally able to participate in the conduction band, can be trapped or pinned, thus lowering the N_e value and impacting the optoelectronic properties.[117, 121, 184] Theoretically, a higher N_e value for WO_{3-x} NCs should be achievable if all W are present in +6 oxidation states or most of the surface trap states are passivated.

Surface ligand chemistry is ubiquitous to colloidal NCs to provide stability, control optoelectronic properties, and enhance NC performance for various applications. Appropriately selected surface ligands can tune the band-gap and the Fermi level of semiconductor NCs.[67, 268] The ligand chemistry of non-LSPR-active metal chalcogenide NCs is well established.[64, 269-271] In contrast, such chemistry is much less developed for semiconductor NCs displaying plasmonic properties. Particularly in doped semiconductor NCs, inappropriate surface passivation can lead to surface defect and trap state formation that together produce surface depletion layers, which can substantially alter the N_e value and influence their dielectric functions.[184] One would expect that surface ligand chemistry will have profound effects on oxygen deficient, LSPR active, semiconductor metal oxide NCs, however the knowledge of the role of surface ligands on controlling the N_e of these NCs is lacking. Reported syntheses of LSPR active WO_{3-x} NCs were conducted in the presence of aliphatic ligands containing carboxylate binding head groups, [113, 258] which are designated as X-type of ligands[271] and potentially form bidentate bridging with surface ionized W lattice atoms. Even with possible bidentate binding between carboxylate group and metal centers, the steric repulsion between the aliphatic hydrocarbon chains may not allow the formation of a tightly packed ligand layer, leaving some percentage of unpassivated surface W sites. This poor passivation leaves dangling bonds behind that are detrimental to optoelectronic properties of semiconductor NCs in general. One approach capable of passivating a maximum number of surface W sites, while obviating the steric repulsion problem, is using X-type ligands containing at least a tridentate binding head group. In this article, we strive to investigate the W-ligand bonding characteristics and to ultimately enhance the resulting plasmonic properties.

Herein, we report a surface passivation approach, which significantly increases the N_e value of two-dimensional, LSPR-active WO_{3-x} nanoplatelets (NPLs). Recently, we reported that colloidally synthesized WO_{3-x} NPLs possessed N_e value of 3.2 X 10^{22} cm^{-3}.[115] We postulated that the large surface area and the presence of sharp corners and edges of atomically-thin NPLs allowed the removal of maximum surface oxygen atoms during synthesis to create a large number of anion vacancies, and thus produced an unprecedentedly high N_e value.[115] We now show that the stabilization of dangling bonds (due to oxygen vacancy) of WO_{3-x} NPLs, after synthesis but before purification with alkylphosphonic acid ligands, results in an ~100 nm blue shift of the LSPR peak of WO_{3-x} NPLs. Experimental optical spectroscopy data support the passivation of trap states leading to the transfer of most of the oxygen vacancy-generated electrons to the conduction band resulting in an experimentally determined N_e of 8.7 X 10^{22} cm^{-3}, determined using a redox titration method. Experimental Raman spectroscopy results, which have been supported by the density functional theory (DFT) calculation, show the formation of dominant W-phosphonate tridentate (PO_3-W_3) bonding, which mitigate most of the shallow surface trap states that is further supported by the electron paramagnetic resonance (EPR) spectroscopy characterization. Newly ligand-passivated WO_{3-x} NPLs display high refractive index sensitivity as comparable to anisotropically shaped noble metal nanostructures that would be beneficial for LSPR-based sensing applications. Taken together, we demonstrated a new surface passivation approach to stabilize trap states of NPLs that fundamentally offers a promising route to enhance the charge carrier density and LSPR properties for anion vacancy, LSPR active metal oxide NCs.

3.3 Results and Discussion

3.3.1 Ligand Treatment and the LSPR Property of WO_{3-x} NPLs.

Atomically-thin WO_{3-x} NPLs were synthesized according to our previously reported colloidal synthetic method with a slight modification.[115] Briefly, under N_2 atmosphere, in a mixture of myristic acid (MA) and 1-octadecene (ODE) at 290 °C, tungsten (V) ethoxide was injected, followed by an immediate injection of a N_2 purged mixture of oleylamine (OLA) in ODE. Immediately, the color of the solution turned blue indicating the formation of LSPR-active tungsten oxide NCs.[113] The reaction mixture was allowed to stir for 1.0 h and then quickly cooled to 100 °C. At this desired temperature, the reaction mixture was transferred under inert atmosphere to a separate N_2 purged flask containing tetradecylphosphonic acid (TDPA), see Figure 3.1. The reaction mixture was then slowly heated to 140 °C under N_2 for another 1 h and then cooled to room temperature for purification (see experimental section for complete details).The purpose of performing TDPA treatment in unpurified WO_{3-x} NPLs is to achieve a better surface passivation that would prevent additional trap state formation and possible surface degradation through undesired solvent adsorption during the sample processing as has been highlighted in cadmium selenide NC post-synthesis processing.[272] Understanding that one hundred percent complete passivation of the surface trap states is unlikely in our system, our specific reaction conditions (*i.e.* amount of TDPA and treatment time) were selected based upon the largest LSPR shift observed.

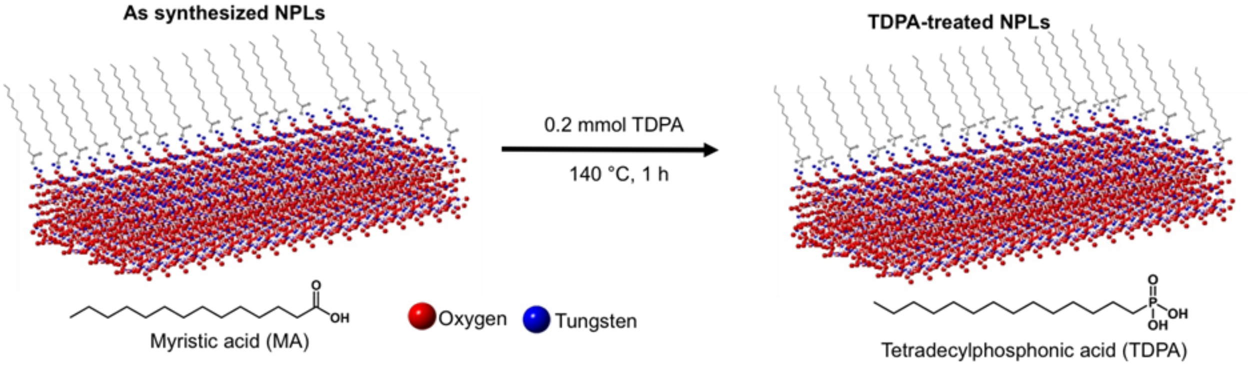

Figure 3.1: A schematic representation of the TDPA ligand treatment in unpurified mixed myristic acid (MA)- and oleylamine (OLA)-passivated WO_{3-x} NPLs. (Left) Tungsten atoms at the edges and corners are passivated with bidentate carboxylate head group of MA. For simplicity, OLA is not shown. (Right) Most of the tungsten atoms at the edges and corners are passivated by phosphonate binding head group of TDPA through tridentate bonding along with the presence of MA.

We selected X-type,[271] TDPA as a surface passivating ligand because transition metal oxide macrostructure thin-films are commonly passivated with phosphonic acid ligands due to their ability to form strong metal-phosphonate bonds that provide exceptional stability against oxidation.[273] Also, alkylphosphonic acids have been shown to be useful passivating ligands in the synthesis of metal chalcogenide NCs due to their strong multidentate binding capability with surface metal atoms.[274-276] The multidentate binding ability of alkylphosphonic acid intrigued us to use it as a passivating ligand to stabilize the coordination sphere of surface W atoms and prevent unwanted trap state formation in our as synthesized WO_{3-x} NPLs. Before we pursue in-depth characterizations, it is important to mention that our attempt to synthesize WO_{3-x} NPLs in the presence of a mixture of TDPA and MA failed to produce ultra-thin, two-dimensional NPLs (see Figure 3.2). UV-vis-NIR spectroscopy analysis was conducted to determine the impact on the LSPR response of the without ("as synthesized") and with TDPA-treated WO_{3-x} NPLs by determining the LSPR peak positions (λ_{LSPR}). As illustrated in Figure 3.3A, the λ_{LSPR} of as synthesized NPLs appears at 1198 nm, whereas more than 100 nm (~105 meV) blue-shifts in λ_{LSPR} are observed for TDPA-treated NPLs (λ_{LSPR} = 1085 nm). We conducted ^{31}P NMR (Figure 3.3B) spectroscopy analysis to confirm the TDPA attachment onto NPLs (Figure 3.3A). It is a common technique for analyzing phosphorus containing surface passivating ligands for inorganic NCs.[277] The TDPA treated NPLs (blue spectrum) exhibits a broad resonance at 34.6 ppm. In contrast, a sharp peak appears for free TDPA (red spectrum). This NMR peak broadening is attributed to

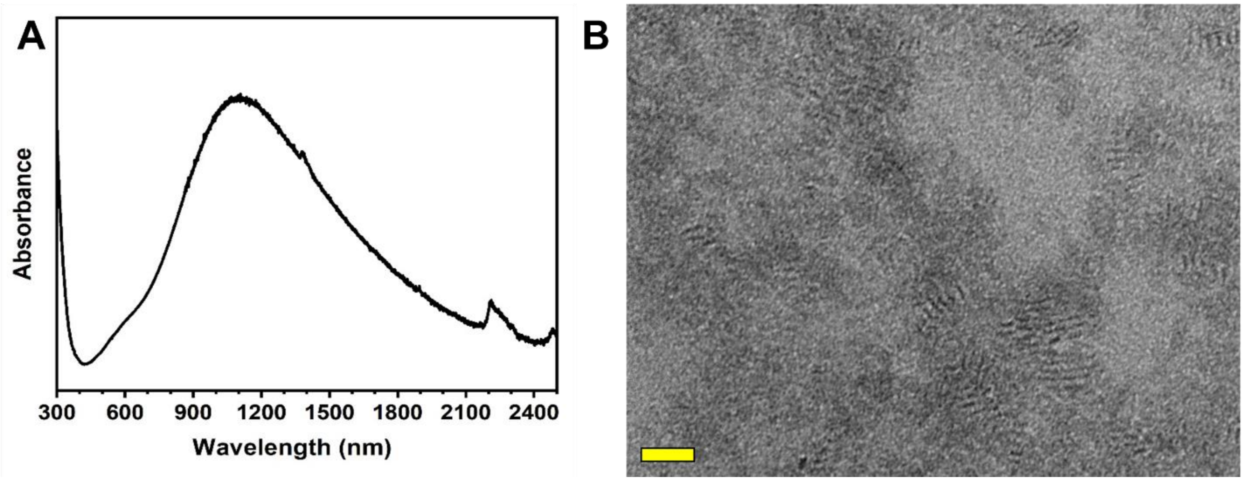

Figure 3.2: (A) UV-Vis-NIR absorption spectrum and (B) TEM of WO_{3-x} nanocrystals (NCs) synthesized using a mixture of tetradecylphosphonic acid (TDPA), myristic acid (MA) and olelyamine (OLA) as surface passivating ligands Scale bar is 20 nm.

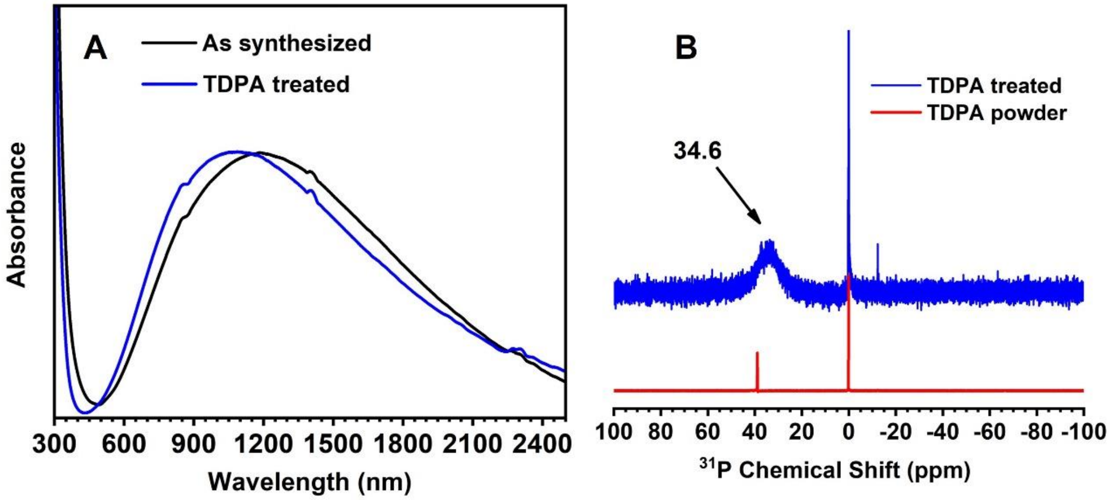

Figure 3.3: (A) UV-Vis-NIR absorption spectra of as synthesized (black) and TDPA-treated WO_{3-x} NPLs (blue). A blue shift of ~100 nm is observed upon TDPA treatment. Spectra of both samples were collected after purification followed by dispersion in CCl_4. (B) ^{31}P NMR spectra of pure TDPA (red) and TDPA-treated WO_{3-x} NPLs (blue). Spectra were recorded in $CDCl_3$.

binding of TDPA onto the NPL surface via the formation of metal-phosphonate bonding that is in agreement with the literature.[236, 278] This NMR result is significant in terms of achieving the desired surface passivation of WO_{3-x} NPLs. We believe the NPL surface is passivated with mixed TDPA and MA ligands (*vide infra*). Below, we address, in detail, various mechanisms that could cause our observed λ_{LSPR} shift in TDPA-treated NPLs.

3.3.2 Microscopy, Diffraction, and Spectrometry Characterizations to Delineate the Mechanism(s).

There are three main mechanisms, which can potentially alter the structural and electronic properties of WO_{3-x} NPLs and influence this LSPR peak shift: (1) Changes in the NPL dimensions during TDPA treatment in unpurified samples, (2) alteration in the crystal structure, and (3) variation in N_e values.

Mechanism (1): To ascertain that no morphological changes occurred during the TDPA treatment, we performed transmission electron microscopy (TEM) analysis to determine the dimensions of WO_{3-x} NPLs. As shown in Figure 3.4A and B, distinct formation of NPLs is observed in as synthesized NPL samples. A d-lattice spacing of 0.38 nm is calculated from a high resolution-TEM (HRTEM) image (Figure 3.4B). This value corresponds to the (010) plane and indicates the growth direction of monoclinic WO_{3-x}. Figure 3.4C represents a TEM micrograph of TDPA treated NPLs where the NPL shape is clearly maintained. Based upon dimensional analysis using ImageJ software, the length and width of as synthesized NPLs are determined to be 13.8 ± 2.2 nm and 4.8 ± 0.8 nm, respectively (Figure 3.4D). Dimension analysis of the TDPA-treated product shows NPLs with 13.4 ± 3.5 nm length and 5.4 ± 1.1 nm width (Figure 3.4E). The height measured form NPLs that appear to be on their sides in the TEM images are ~1.1 nm and ~1.2 nm for as synthesized and TDPA-treated NPLs, respectively. This height is consistent with our previously published results on WO_{3-x} NPLs that were determined by small angle X-ray scattering.[115] Together, the structural analysis suggests that NPL dimension is not the prevalent factor for the ~100 nm λ_{LSPR} blue-shift of TDPA-treated samples.

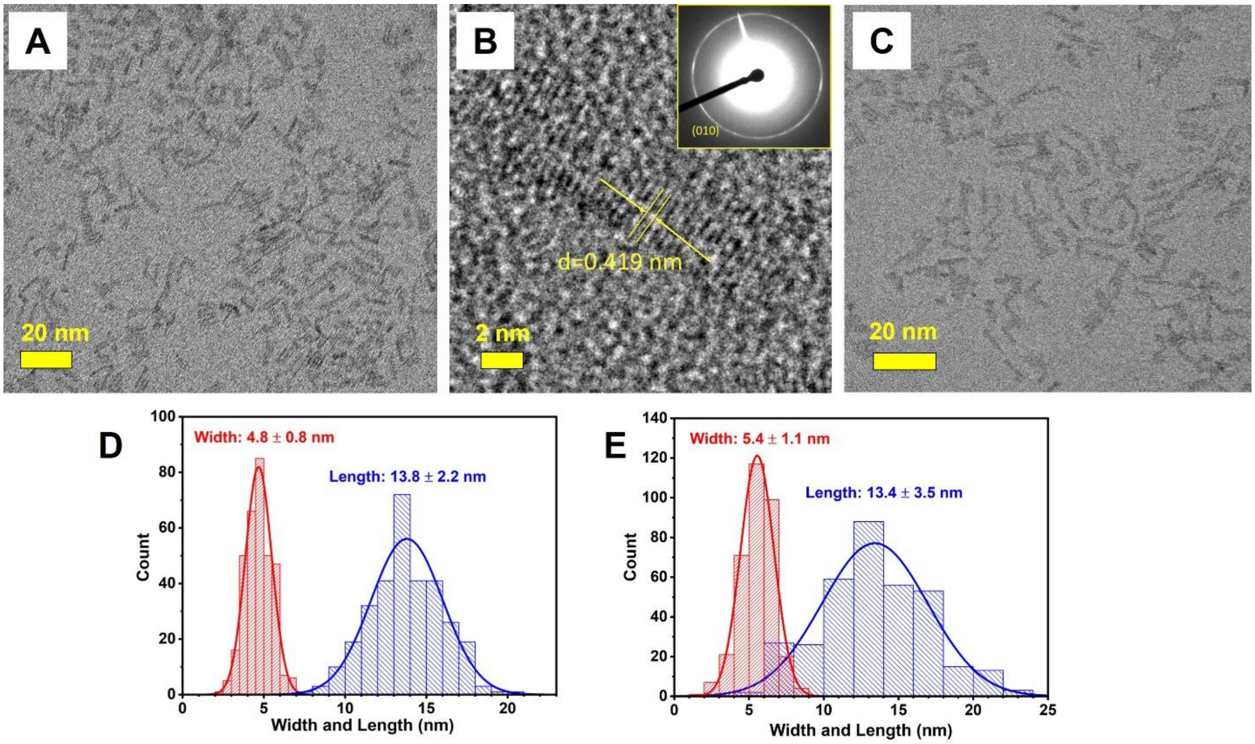

Figure 3.4: HRTEM images as synthesized (A and B) and (C) and TDPA-treated WO_{3-x} NPLs. In (B), the d-spacing corresponds to the (010) plane of monoclinic WO_{3-x}. The inset shows FFT diffraction of the (010) plane. (D) Histogram of width and length of as synthesized (D) and (E) TDPA-treated NPLs. For the size analysis, a minimum of 300 NPLs were counted.

Mechanism (2): To examine the crystal structure deformation, as synthesized and TDAP-treated WO_{3-x} NPLs were analyzed by powder X-ray diffraction (XRD) and Raman spectroscopy. Figure 3.5A illustrates the XRD diffraction patterns of as synthesized (top, black) and TDPA-treated NPLs (bottom, blue). No apparent changes in the crystal phase between either sample are observed, and importantly each diffraction pattern matches with the monoclinic WO$_{2.72}$ crystal (PDF #71-2450). This crystal phase is known to commonly grow along the (010) direction[124, 279] which is consistent with the appearance of high intensity peaks in both samples at 2θ ~23.5° (010) and ~48.1° (020). Also, this growth direction is supported by the HRTEM analysis (Figure 3.4B). The broadening of the XRD peaks can be attributed to a decrease in crystallinity of the NPLs due to their ultrathin dimension that is commonly observed in ultrasmall inorganic NCs.[280] Next, Raman spectroscopy was used to confirm the monoclinic phase of the WO$_{2.72}$ crystal and to investigate any plausible distortions that may be caused by TDPA passivation. The Raman spectrum of as synthesized NPLs includes distinct monoclinic tungsten oxide vibrational modes (Figure 3.5B, black line). These peaks are assigned as the crystal lattice vibration of $(W_2O_2)_n$ chains at 71 cm^{-1}, W—O stretch at 123 cm^{-1}, bending vibration of (O—W—O) at 252 cm^{-1}, and (O—W—O) stretches of the WO$_6$ octahedra at 692 cm^{-1} and 797 cm^{-1}.[281-285] The Raman stretch at 318 cm^{-1} can also be attributed to a monoclinic bending mode.[281] The Raman vibrations appear to be broader and shifted to lower wavenumbers as compared to the tungsten oxide films and larger structures.[283, 286] This is due to the distortion in the overall crystal lattice resulting from oxygen vacancies that reduces the crystallinity compared to larger bulk-like structures.[287] All the above-mentioned Raman vibrational modes are also observed in the TDPA-treated WO$_{3-x}$ NPLs and the

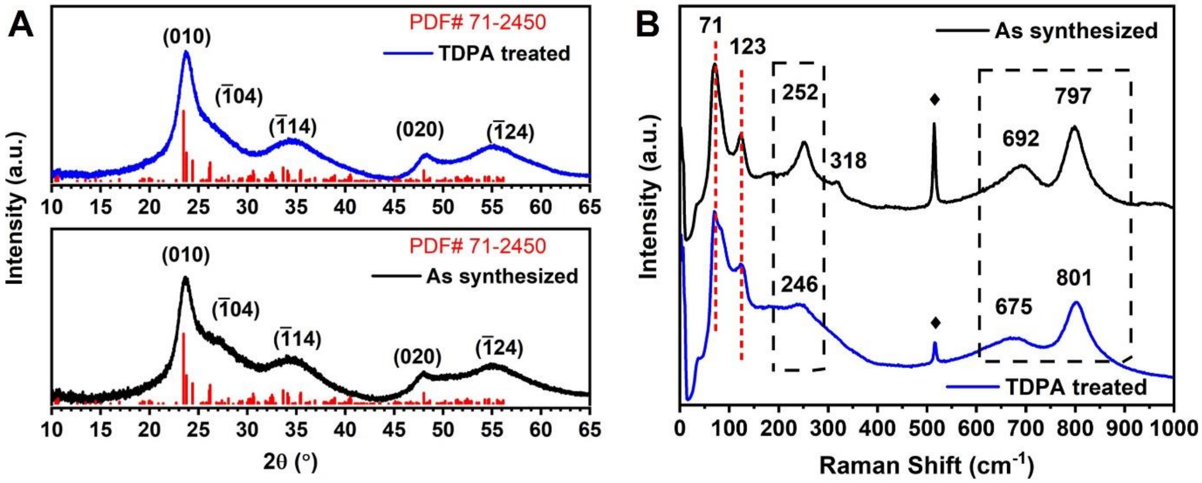

Figure 3.5: (A) XRD diffraction patterns of as synthesized (top, black) and TDPA-treated (bottom, blue) WO$_{3-x}$ NPLs as compared to the monoclinic WO2.72 standard (red, PDF# 71-2450). (B) Raman spectra of as synthesized (black) and TDPA-treated WO$_{3-x}$ NPLs (blue). Raman spectra were collected using a 532.5 nm laser source.

position of only a few Raman stretches are minorly different in comparison to as synthesized NPLs. Slight changes in the (O—W—O) bending mode at 246 cm^{-1} and a shift of the WO_6 octahedra (O—W—O) stretching modes to 675 cm^{-1} and 801 cm^{-1} are observed in TDPA-treated NPLs (highlighted in black dashed boxes) when compared to as-synthesized WO_{3-x} NPLs. We believe that the multi-dentate binding of TDPA to the surface of the NPL causes the slight variation in the position of these Raman stretches. Moreover, local assembly of the sample may also influence the Raman response by the presence of TDPA due to differences in the organic ligand attachment onto the solid inorganic surface.[288] Finally, increases in oxygen vacancy and the presence of a high density of free carriers could shift the Raman vibrational modes to lower wavenumbers,[281-282] particularly the appearance of Raman stretches at 252 cm^{-1} and 692 cm^{-1} that resemble in highly oxygen deficient $W_{18}O_{49}$ nanomaterials.[176] Nevertheless, the above-mentioned diffraction and spectroscopic characterizations invalidate the possibility of alteration in the crystal structure of WO_{3-x} NPLs upon TDPA treatment, and rather support the concept of the variation in N_e values.

Mechanism (3): We employed the empirical Drude approximation for bulk materials (Eq. 3.1) to calculate the free electron density (N_e) of WO_{3-x} NPLs.[122, 260, 289]

$$\omega_{LSPR} = \sqrt{\frac{\omega_p^2}{\varepsilon_\infty - \varepsilon_r} - \gamma^2}$$

Equation 3.1

Here ω_{LSPR} represents the LSPR frequency, ω_p the bulk plasma oscillation frequency of electrons, and ε_∞ the high-frequency dielectric constant (4.8 for tungsten oxide).[290] The real part of the complex dielectric function of plasmonic nanostructures (ε_r) can be represented by Eq. 3.2:

$$\varepsilon_r = -\kappa\varepsilon_m$$

Equation 3.2

Based upon our previous work with ultrathin WO_{3-x} NPLs, we define κ as the shape factor of the NPL, which was treated as an oblate spheroid structure, understanding that this assumption may introduce some error as the assumption is weighted towards the height and width dimensions.[115] Here, ε_m represents the bulk refractive index of the surrounding medium (CCl_4 = 2.24). The damping of the incident field induced oscillation of the electrons is represented by the bulk collision frequency (γ) as determined by Lorentz fitting of the NIR spectra. Thus, ω_p is dependent upon N_e as:

$$\omega_p^2 = \frac{N_e e^2}{\varepsilon_0 m_e}$$

Equation 3.3

Where m_e is the effective mass of an electron in tungsten oxide ($1.2m_0$),[113] where m_0 is the rest mass of an electron. Using our NPL specific spectroscopic values (Table 3.1) in the Drude model with appropriate shape factors, N_e values for as-synthesized and TDPA-treated WO_{3-x} NPLs are determined to be 3.82 and 5.56 x 10^{22} cm^{-3}, respectively. This is an ~45% increase of N_e due to the TDPA treatment. Although we used LSPR resonance energy to calculate the N_e value, it is not always obvious that a higher energy LSPR peak would provide a greater N_e value. This is because the collision frequency in Eq. 3.1 depends on the linewidth of the LSPR spectrum. Nevertheless, our calculated N_e is unprecedentedly high when compared to currently reported LSPR-active metal oxide NCs where free carriers are generated via aliovalent doping or through oxygen deficiency.[246] Our theoretically calculated N_e value is comparable to the free electron density found in noble metal nanostructures (10^{23} cm^{-3}).[243] Since oblate spheroid model takes the height and width into account, the assumption of NPL as oblate spheroid may introduce some errors in our N_e value calculations. Due to the ultrathin nature of our NPLs the shape factor simplification of our two-dimensional material is largely dependent on the height. For example, a ten percent alteration in

Table 3.1: Morphological parameters of NPLs. Width, height, shape factor, LSPR (eV), gamma, Ne of WO_{3-x} NPLs.

Sample	**Length (nm)**	**Width (nm)**	**Height (nm)**	**Shape Factor (κ)**	**λ_{LSPR} (eV)**	**Collision frequency (γ, eV)**	**N_e (cm^{-3})**
As synthesized	13.8 ± 2.2	4.8 ± 0.8	~1.1	6.2	1.04	1.3	3.82 x 10^{22}
TDPA treated	13.4 ± 3.5	5.4 ± 1.1	~1.2	6.3	1.14	1.4	5.56 x 10^{22}

the height dimension may result in roughly a six percent change in N_e; however, this still maintains a magnitude of 10^{22}.

A limitation of the Drude model is that it does not account for the depletion layer that is created by trap states in semiconductor NCs.[184] Therefore, a more quantitative N_e value can only be determined through redox titration scavenging free electrons residing in the crystal. We have performed this experiment and the result is presented in the later part of this article. Additionally, changes in the local dielectric environment of LSPR-active NCs also influence the λ_{LSPR}.[247, 291] In this context, TDPA ligand contains 13 -CH_2 units in the hydrocarbon chain whereas 12-CH_2 units are present in the MA. Therefore, one would expect that the refractive index of TDPA would be higher in comparison to MA, thus TDPA treatment should not lower the local refractive index value around WO_{3-x} NPLs that may cause λ_{LSPR} blue shift. Taken together, based on the above-presented results, we hypothesize that the TDPA treatment results in the passivation of most surface W sites through the formation of multidentate bonding, and thus reduces the number of trap states.

3.3.3 X-ray Photoelectron and Electron Paramagnetic Resonance Spectroscopic Characterizations of WO_{3-x} NPL Electronic Properties.

The mechanism underlying the increase of N_e values upon TDPA treatment of WO_{3-x} NPLs was investigated by XPS and EPR. FTIR and Raman spectroscopy were used to further understand the metal-ligand bonding. There are two possibilities for the increase of N_e values in TDPA-treated samples: (1) an increase of oxygen vacancies being created during the TDPA treatment, and/or (2) changes in surface passivation allowing passivation of trap states leading to a larger participation of oxygen vacancy-derived electrons as free carriers. First, we conducted XPS analysis to determine whether a greater number of oxygen vacancies were being created during TDPA treatment that would significantly increase the N_e value. It is well known that a single oxygen vacancy theoretically produces two free electrons. In fact, the presence of oxygen vacancies near W^{+6} atoms often cause the formation of W^{+5} which in turn creates defects that can cause electrons to be trapped or pinned. [176] Thus, all free electrons created through oxygen vacancies may not participate as free carriers in the LSPR response. This phenomenon has also been observed in oxygen deficient titanium dioxide films.[292-293] Figure 3.6A,B shows XPS spectra of as synthesized and TDPA-treated NPLs. Peaks representing $4f_{7/2}$ and $4f_{5/2}$ of W^{+6} are located at ~35.7 eV and

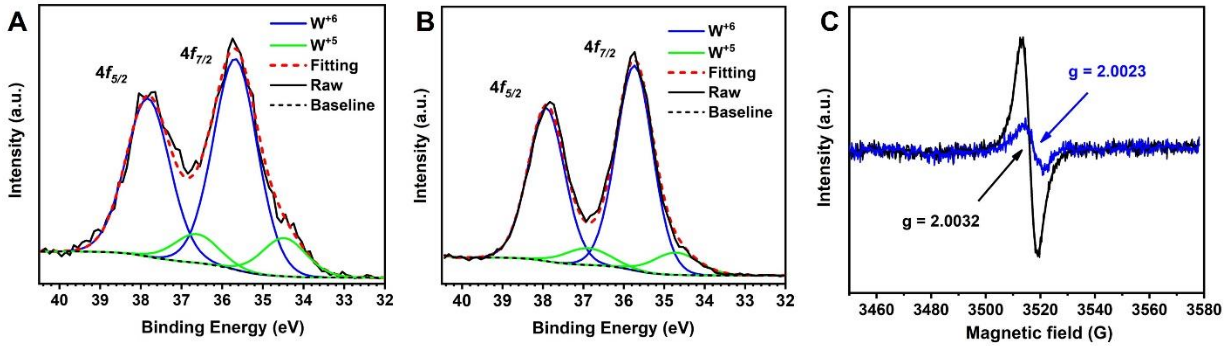

Figure 3.6: High resolution XPS spectra with fittings for W^{+6} and W^{+5} 4f orbital splitting of (A) as synthesized and (B) TDPA-treated WO_{3-x} NPLs. (C) EPR spectra of as synthesized (black) and TDPA-treated NPLs (blue). EPR spectra were acquired at room temperature under identical conditions. EPR spectra were collected under identical experimental conditions.

~37.9 eV, respectively, with a characteristic peak splitting of W. Peaks associated with W^{+5} are observed at ~34.6 eV and ~36.8 eV for the $4f_{7/2}$ and $4f_{5/2}$ orbitals, respectively. The ratio between W^{+6} to W^{+5} is 5.72 ± 0.22 which is nearly identical for both as synthesized and TDPA-treated WO_{3-x} NPLs. Our data are in agreement with the literature when comparing XPS analysis of W atoms under oxidation environment.[125] It is important to mention that oxygen vacancies in WO_3 crystals can only be created under reduced pressure and/or at high temperature.[246] Therefore, it is unlikely that the TDPA treatment at 140 °C under N_2 atmosphere would remove any additional oxygen and create more vacancies in WO_{3-x} crystals than those already existing before the TDPA treatment.

We next used electron paramagnetic resonance (EPR) spectroscopy to investigate the electron trapping phenomena in as synthesized and TDPA-treated WO_{3-x} NPLs. This is a very useful spectroscopic technique to investigate the oxygen vacancies in metal oxide NCs, as electrons can be localized at these vacancies.[294-297] Figure 3.6C displays a strong EPR signal for as synthesized NPL (black line) with a center g-value of 2.0032 which is in good agreement with tensor values reported in literature for oxygen vacancy electrons in tungsten oxide NCs.[298-299] In contrast, TDPA-treated WO_{3-x} NPL sample shows a low intensity peak with a g-value of 2.0023 (blue line). The decrease in the EPR signal and shifting of the g-value together suggest the presence of a smaller number of unpaired electrons in TDPA-treated WO_{3-x} NPLs in comparison to as synthesized samples. We believe this is caused by the passivation of unwanted trap states by TDPA, and thus freeing the trapped electrons.[300] Additionally, the low intensity EPR signal in

TDPA-treated WO_{3-x} NPLs can be assigned to deep trapped rather than existing shallow surface trapped electrons.[301] Taken together, XPS and EPR analyses support the hypothesis of increased trap state passivation leading to the transfer of oxygen vacancy directed electrons into the conduction band, resulting in a λ_{LSPR} blue shift.

3.3.4 Vibrational Spectroscopic Evidence of Multidentate W-Phosphonate Bonding in TDPA-Passivated WO_{3-x} NPLs.

Specific bonding modes cannot be decisively determined from solution-state ^{31}P NMR due to limited shifts of each bonding type and the overall peak broadening.[302-303] In contrast, vibrational spectroscopic techniques such as FTIR and Raman are very useful to examine the chemical environment of ligand-passivated, inorganic NCs. We utilized these techniques to determine the binding motif of the three oxygen atoms such as monodentate (i and ii), bidentate (iii-vi) or tridentate (vii and viii) in the phosphonic acid head group with W (Figure 3.7). The FTIR spectrum of neat TDPA (Figure 3.8A) displays several distinct peaks in the phosphonate binding region in the yellow shaded area, including a large peak at 1215 cm^{-1} corresponding to the P=O stretch.[304] Also, the IR stretch of P—OH bond is visible by the appearance of broad peaks near 2272 cm^{-1} (black dashed box) along with the expected broad peak beyond 3000 cm^{-1} found in alkyl phosphonic acid infrared spectra.[305-306] As expected, the FTIR spectrum of as synthesized NPL

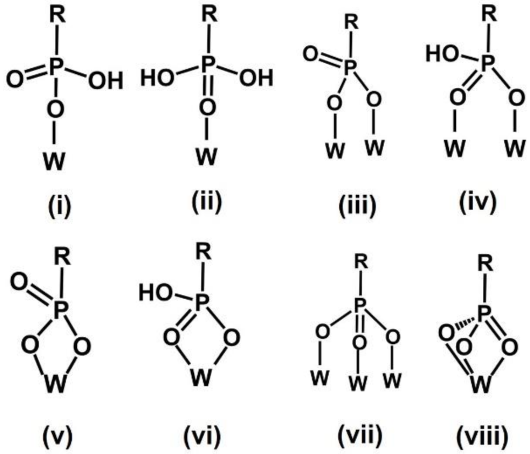

Figure 3.7: Chemical structures with possible bonding motifs between the phosphonate binding head group and tungsten atoms. Monodentate (i and ii), bidentate (iii and iv), bidentate chelating (v and vi), tridentate (vii) and tridentate chelating (viii).

samples does not show any of these characteristic P—O vibration related peaks (yellow shaded area) in the 950 cm^{-1} – 1250 cm^{-1} region. However, we do observe the presence of the OLA and MA ligands used during the synthesis as indicated by (♦) and (♠), respectively. This is also evident in the large C—H stretching observed at 2800-3000 cm^{-1} resulting from the aliphatic backbone of the ligands.

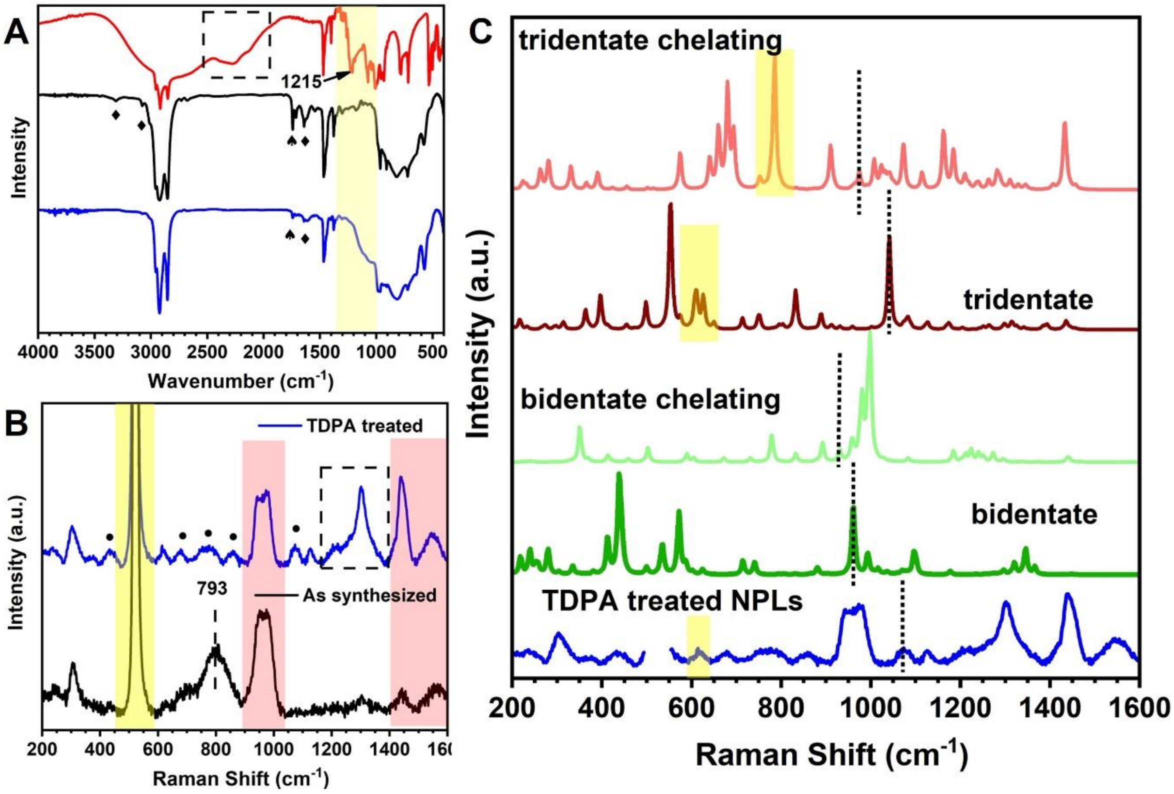

Figure 3.8: (A) FTIR spectra of pure TDPA (red), and as synthesized (black) and TDPA-treated WO_{3-x} NPLs (blue) The yellow shaded area represents peaks related to phosphorous oxygen bonding. The symbol (♦) highlights the presence of the amino headgroup from OLA and the symbol (♠) represents carbonyl stretching from MA. (B) Raman spectra of as synthesized (black) and TDPA-treated WO_{3-x} NPLs (blue). (C) Experimental Raman spectrum (blue), and DFT-calculated Raman spectra of TDPA bound to W atoms as bidentate (dark green), bidentate chelating (light green), tridentate (dark red), and tridentate chelating (light red). Black dashed lines are P=O stretching, and yellow shaded areas refer to (O=P-C) deformations.

The FTIR spectrum of TDPA-treated WO_{3-x} NPLs shows several interesting features. First, OLA (1632 cm^{-1}) and MA (1743 cm^{-1}) are still present in the TDPA-treated NPLs;[307] however, the intensity of these peaks have clearly reduced. This is expected because the TDPA treatment weakens metal-ligand bonding interactions of these ligands. Also, the main P—OH stretch vibration at ~ 2270 cm^{-1}, which is noted in the neat TDPA powder spectrum (red line) by a black dashed box, is not observed, suggesting the absence of -OH in phosphonate binding head group. Additionally, the appearance of a broad peak in the phosphonate binding region (yellow shaded area) is clearly visible with no corresponding P=O stretch near 1215 cm^{-1} as witnessed in neat TDPA powder. It is known that tridentate binding leads to broad IR stretches in this region due to all oxygen atoms participating in bonding. [304, 308]

We further conducted Raman spectroscopy analysis to investigate the bonding motifs because the broadness of the FTIR peaks makes it challenging to precisely determine the local vibrational response and bonding environment.[309] The Raman spectra of surface ligand binding to WO_{3-x} NPLs is presented in Figure 3.8B. Here, Raman spectra of as synthesized and TDPA-treated NPLs are shown by black and blue lines, respectively. To precisely assign the coordination environment of various ligands, DFT-calculated spectra were acquired for TDPA and MA (Figure 3.9). The corresponding vibrational modes are presented for both TDPA and MA in Tables 4.2 and 4.3 in Appendix A, respectively. The yellow shaded area in Figure 3.8B is attributed to the response from the silicon substrates used for sample deposition, and the red shaded areas are a combination of ligand tail, C—C, vibrations from the alkyl chains in all three ligands used in the NPL synthesis. The Raman peak located at 793 cm^{-1} in as synthesized NPLs (Figure 3.8B, black dashed line) is attributed to W—O asymmetric bonding (Table 3.3, Appendix A). The presence and intensity of this peak is due to experimental analysis conditions. It is also visible as a shoulder in the TDPA-treated spectrum. The TDPA-treated NPLs (blue line) clearly shows the presence of

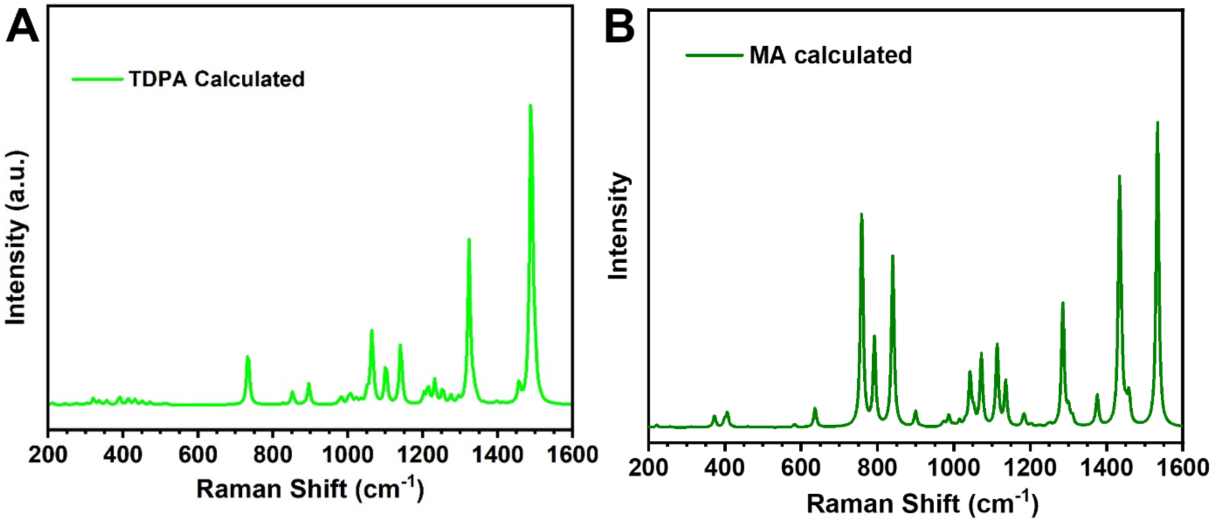

Figure 3.9: DFT calculated Raman spectra of (A) TDPA and (B) MA.

TDPA binding as indicated by the broad Raman band in the 1250-1400 cm^{-1} region (black dashed box) and multiple smaller peaks indicated by (●) in the spectrum. These peaks are present due to various P=O, C—P, P—O, and other coupled vibrations.[310-313] Considering the many vibrations participating in the response in this broad region from both alkyl chains and the phosphonate head group we chose not use this area when describing the specific type of bonding.

To further investigate and confirm the exact local binding nature of the TDPA ligand with WO_{3-x} NPL, we performed DFT calculations involving different bonding possibilities, as shown in Figure 3.7. Monodentate W-O bonding with a free -OH group (Figure 3.7 (i) and ii)) can be ignored because our FTIR and Raman analyses of TDPA-treated WO_{3-x} NPL samples showed no evidence of the presence of hydroxyl groups. Figure 3.8C provides the calculated spectra for four different binding modes and the relevant Raman peaks are listed in Tables 3.4-3.7 in Appendix A. A key difference between the bidentate and tridentate bonding is the involvement of the P=O, therefore we focus on P=O related vibrational modes. As explained above, we choose to only focus on well resolved P=O related vibrations below 1200 cm^{-1}due to peak overlap and coupling with alkyl related vibrations from the ligand backbone. We assign the P=O stretching vibrations in each DFT-calculated spectrum and the experimental spectrum of TDPA-treated NPLs as black dashed lines. All the relevant Raman stretches are assignments in Tables 3.4-3.7, Appendix A. It is apparent from the above-mentioned results and Figure 3.8C that the tridentate non-chelating bonding is most likely, as the calculated P=O stretching is assigned at 1089 cm^{-1} that closely matches with the experimental Raman stretch at 1074 cm^{-1} in our experimental spectrum. This slight shift in the peak position could be due to change in the chemical environment between the gas-phase DFT calculations and experimental Raman spectroscopy characterizations on thin WO_{3-x} NPL films. For further confirmation we considered the coupled (O=P-C) bonding which according to our DFT results, the linking of a double bonded oxygen to a tungsten atom causes an in-plane scissoring deformation (O=P-C). This deformation is highlighted in the tridentate bonding spectra by the yellow shaded area. The DFT-simulated peaks can be found at 809 cm^{-1} for the tridentate chelating bond and 640 cm^{-1} for the tridentate bond without chelation. The extreme tridentate bonding of three oxygen atoms chelating to the same tungsten site does not match, as well as being unlikely due to energy required and valency necessary of the tungsten atom. However, the tridentate non-chelating bond is in good agreement with our TDPA treated NPLs as we have a peak located at 619 cm^{-1}. Taken together, our Raman analysis confirms the majority of binding occurs through a tridentate bound TDPA ligand. TDPA allows for tridentate bonding which equates to three passivation sites per molecule, thus increasing passivation of defect sites without increasing the steric hinderance issues on the surface.

Our in-depth spectroscopic analyses support the appropriate passivation of surface defects by TDPA due to the formation of tridentate binding. The structure of WO_{3-x} NPLs is linked by edge and corner sharing WO_3 octahedra where a large percentage of W atoms reside on the sharp edges and corners, see Figure 3.10A. The monoclinic crystal of $WO_{2.72}$ is shown on the left with most of the surface oxygen, in the non-growth direction, removed to highlight the surface tungsten atoms with defects caused by the oxygen vacancy. The minimum distance between tungsten atoms is ~3.1 Å. When comparing the binding ability of TDPA and MA to passivate the surface, two factors are at play: (1) the oxygen-to-oxygen distance of MA is ~2.2 Å, whereas this distance increases to ~2.6 Å for TDPA. This increase in bond distance allows the oxygen atoms in the phosphonate group to passivate the nearest neighboring atoms without causing strain, and (2) three W atoms can be passivated through tridentate bonding of TDPA versus only two for MA. Sterically it is difficult to increase the number of MA ligands on the surface of these NPLs. To support this hypothesis, unpurified, as synthesized NPLs were treated with additional MA where no LSPR peak shifts are observed (Figure 3.11). Taken together, as synthesized WO_{3-x} NPLs possess inherent trap states due to the oxygen vacancy in the crystals where the shallow surface traps can be

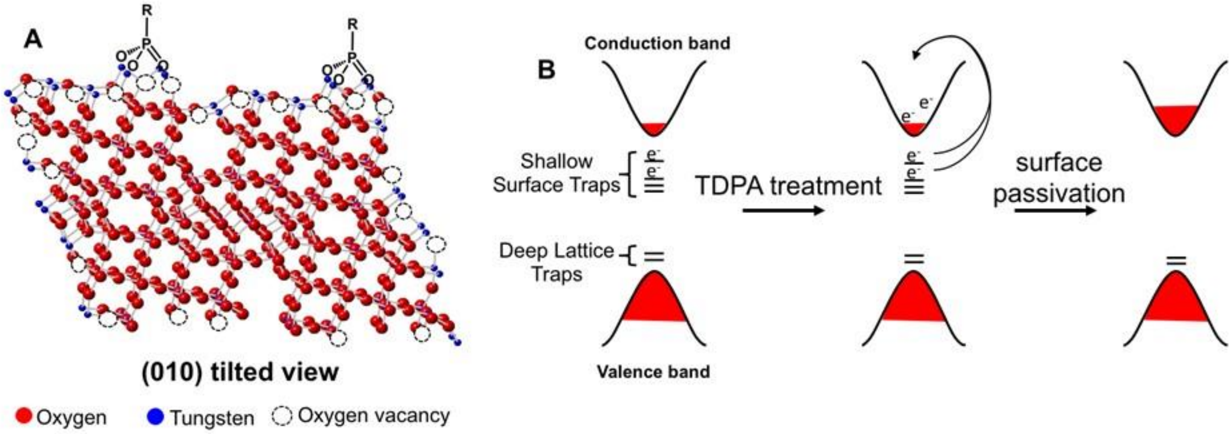

Figure 3.10: (A) Schematic illustration of the proposed tridentate bonding between the surface W atoms of a WO_{3-x} NPL and alkylphosphonate group. For simplicity, only a few surface oxygen vacancies are depicted, however most of the oxygen atoms from the corners and edges are removed during the synthesis. (B) Conduction band filling through passivation of shallow trap states via TDPA treatment and transfer of trap electrons. The energy gap between the valance and conduction bands is not to scale.

passivated through TDPA treatment, allowing electrons to transfer into the conduction band to participate as free carriers in the LSPR response. The deep trap states were still unpassivated, as observed in the EPR signal (Figure 3.6C).

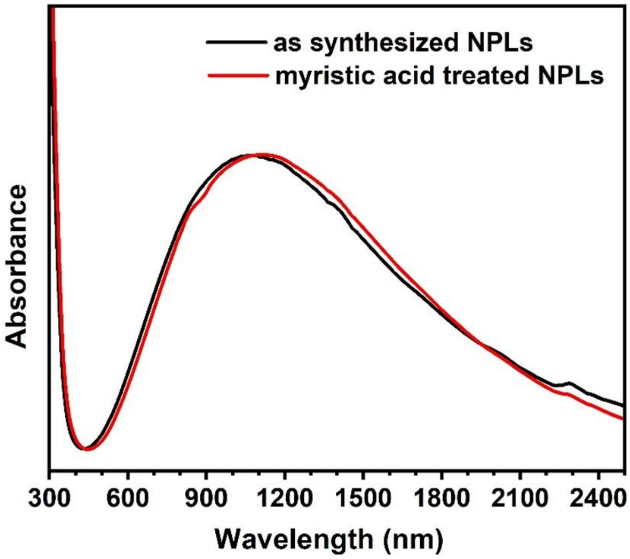

Figure 3.11: UV-Vis-NIR spectra of as synthesized and MA-treated to highlight no blue shift with carboxylic acid treatment.

3.3.5 Determination of N_e Values of WO_{3-x} NPLs via Redox Titration.

Spectroscopic data unequivocally support the tridentate binding of TDPA to the surface of NPLs leading to the passivation of trap states and an increase in participation of oxygen vacancy generated electrons as free carriers. Next, we sought to determine how quantitative is the previously determined N_e values which were calculated using the empirical Drude approximation. To experimentally determine the N_e value, we applied a single electron redox titration using nitrosonium tetrafluoroborate ($NOBF_4$) as reported by Strouse and coworkers and others on plasmonic metal oxide and nitride NCs.[314-315] It is important to note the possibility of $NOBF_4$ to interact with ligands causing precipitation. To circumvent this and other challenges, bulkier redox agents such as decamethylferrocenium have been used in the literature.[316] However, under our specific conditions we chose to utilize $NOBF_4$. A known concentration of $NOBF_4$ was added to WO_{3-x} NPL samples (as synthesized and TDPA-treated) and allowed to react for 15 min before the LSPR spectra were recorded (see experimental section for additional details). All spectra were integrated from 500-2500 nm to account for peak broadening and peak shifting to lower energies that is known to occur as free carrier density decreases. Plotting the absorbance area vs known NOBF$_4$ concentrations and fitting the linear portion of the graph to find the x-intercept, we could determine the total number of free electrons in the system. As illustrated in Figure 3.12A, with the increase of NOBF$_4$ concentrations, the LSPR spectra of as synthesized NPLs continuously decrease in intensity along with λ_{LSPR} red shifting. Similar results are shown for the titration of TDPA-treated NPLs (Figure 3.12B). We determined the N_e value of as synthesized NPLs to be 7.93 x 10^{22} cm^{-3} based on the absorbance area versus number of NOBF$_4$ molecules (Figure 3.12C). Under similar experimental conditions, TDPA-treated WO$_{3-x}$ NPL samples provide a N_e value of 8.74 x 10^{22} cm^{-3} (Figure 3.12D).

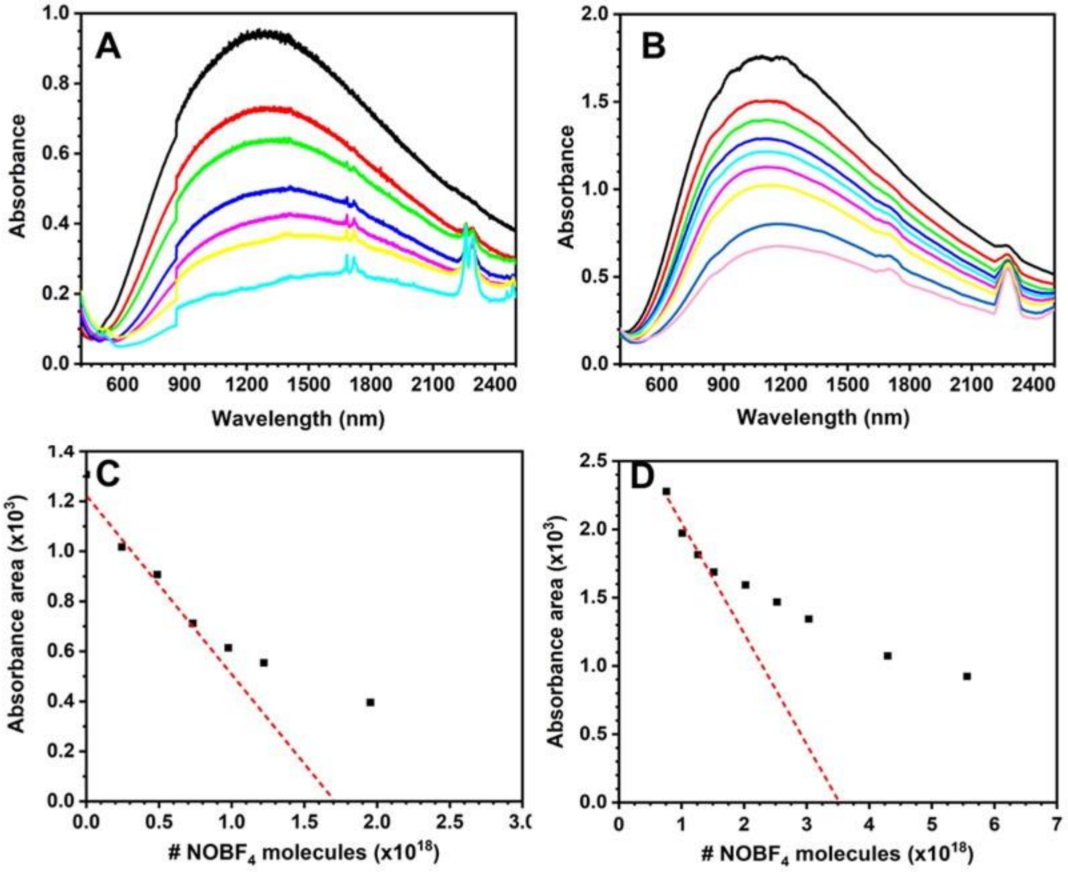

Figure 3.12: UV-Vis-NIR absorption spectra of colloidal (A) as synthesized and (B) TDPA-treated WO$_{3-x}$ NPL solutions recorded after addition of titrated amounts of NOBF4 solution. Graphs of integrated absorption area as a function of NOBF4 molecules for (C) as synthesized and (D) TDPA-treated WO$_{3-x}$ NPLs with fittings of the linear portions (red dashed lines).

The higher N_e value in TDPA-treated WO_{3-x} NPLs in comparison to as synthesized NPLs is in agreement with the trap state passivation. Furthermore, the N_e value of TDPA-treated WO_{3-x} NPLs has a nearly 57% higher in comparison to the Drude approximation of 5.56×10^{22} cm^{-3}. This is not surprising because in a recent report on cation-doped zinc oxide NCs, the authors showed nearly 80% difference in N_e values between redox titration and Drude model-based calculations.[314] Nevertheless, we predict that this large difference between experimental and empirical formula-based calculations in N_e values of WO_{3-x} NPLs is due to in proper approximation of several parameters: (1) The original Drude model was developed for spherical, NCs where shape factor (κ) is 2.0 (Eq. 3.2). In contrast, our NPLs are rectangular in shape, and their shape factor can only be determined from the aspect ratio. Due to their ultrathin height, we may have introduced some errors in the κ value calculation. (2) The Drude model is valid for NCs where no depletion layer is present, such as noble metal NCs.[184] Plasmonic metal oxide NCs are n-type semiconductor, therefore one would expect the presence of a depletion layer due to formation of trap states and surface defects that together change the dielectric function of the materials. It is also shown that a depletion layer reduces the LSPR sensitivity.[184] We believe that an poor surface passivation in WO_{3-x} NPLs created surface defects and trap states that together altered the local electronic structures and thus the dielectric function of WO_{3-x} materials, resulting in an ~50% difference in the N_e values between experimental and theoretical calculations. Taken together, to the best of our knowledge, our experimentally determined N_e value of 8.74×10^{22} cm^{-3} of TDPA-passivated WO_{3-x} NPLs is the highest free electron density ever reported for non-noble metal NCs.[115]

3.3.6 Refractive Index Sensitivity of LSPR-Active WO_{3-x} NPLs.

It is evident that the inclusion of tridentate bonding of TDPA in WO_{3-x} NPLs causes an increase in free carriers participating in the LSPR response. Therefore, it is important to examine the LSPR-based RIU sensitivity of NPLs so that they can be used in plasmonic-based sensing applications.[113] As synthesized and TDPA-treated WO_{3-x} NPLs were dispersed in non-polar solvents (carbon tetrachloride (CCl_4), chloroform ($CHCl_3$), and tetrachloroethylene ($Cl_2C{=}CCl_2$)) and their λ_{LSPR} values in the different solvents were recorded. The LSPR spectra show red shifting of λ_{LSPR} as a function of the solvent refractive indices (Figure 3.13A,B). It is important to note that the spectra in Figure 3.13A,B was processed to remove NIR peaks arising from the solvent. Raw UV-Vis-NIR spectra are provided in Figure 3.14, Appendix A. Bulk refractive index sensitivities

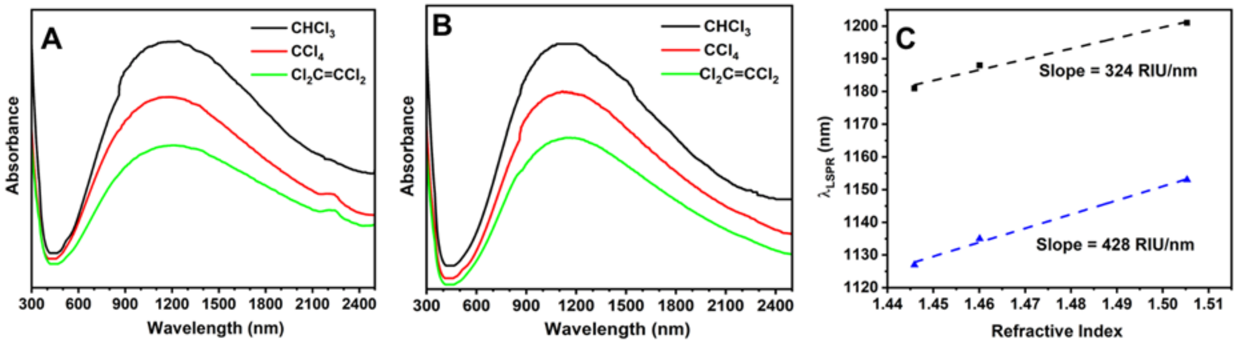

Figure 3.13: (A) UV-Vis-NIR absorption spectra of (A) as synthesized and (B) TDPA-treated WO_{3-x} NPLs in various solvents with varying refractive index. (C) Relationship between LSPR peak position (λ_{LSPR}) of as synthesized (black squares) and TDPA-treated (blue diamonds) NPLs and the refractive index of the bulk solution. The corresponding sensitivities are 324 and 428 nm/RIU, respectively, determined from the slope of the graph.

of as synthesized and TDPA-treated NPLs are determined to be 324 and 428 RIU/nm, respectively (Figure 3.13C). This large 428 RIU/nm sensitivity value is similar to plasmonic metal oxide NCs with the highest reported sensitivities and is comparable to uniquely-shaped noble metal nanostructures such as gold nanobipyramids and nanoprisms, see Table S8.[181, 317] This places the figure of merit (sensitivity divided by the full width at half max)[318] of our TDPA-treated NPL at ~0.48, which is relatively low compared to noble metal nanostructures. We believe this is due to the broadness of the LSPR peak originating from large scattering cross sectional area of the platelet geometry.

3.4 Conclusion

In summary, we have developed a colloidal chemistry-based surface modification approach to further enhance the plasmonic properties of anion deficient, atomically-thin $WO_{2.72}$ NPLs. TDPA-treated NPLs display a shape factor dependent and redox titration-based N_e value of 5.56 x 10^{22} and 8.74 x 10^{22} cm^{-3}, respectively. Between the morphology and large N_e value of our TDPA treated NPLs, we have achieved a refractive index sensitivity of 428 RIU/nm which is comparable to anisotropically shaped, noble metal nanostructures. Based on FTIR and Raman spectroscopy studies along with other structural characterizations, we have deduced the mechanism involving the formation of tridentate PO_3-W_3 bonding that prevented the formation of shallow surface trap states, which has resulted in transferring of most of the oxygen vacancy-related electrons into the conduction bands. This photophysical property has been further supported by EPR analysis where the optical signal from unpaired electrons is being decreased after TDPA treatment of unpurified $WO_{2.72}$ NPLs. We believe that an appropriate bond length in the phosphonate binding head group is able to coordinate with three neighboring W atoms without encountering any steric hindrances, which is responsible for the positive LSPR response. This response is unlikely in original $WO_{2.72}$ NPLs where X-type, alkylcarboxylate ligands were predominate in surface passivation. Taken together, our work on surface ligand-controlled maximization of the LSPR response in oxygen deficient nanostructures provides new knowledge and mechanisms, and opens new possibilities to produce low-cost, earth-abundant plasmonic nanomaterials with exceptionally high free electron densities that would be extremely useful to design highly efficient nanomaterials for sensing, optoelectronic device, and catalytic applications.

3.5 Experimental Section

3.5.1 Materials.

Tungsten (V) ethoxide was purchased from Alfa Aesar. Myristic acid (MA, ≥99%), 1-octadecene (ODE, 90%), oleylamine (OLA, 70%), tetradecylphosphonic acid (TDPA, 98%), carbon tetrachloride (CCl_4, 99.9%), tetrachloroethylene (TCE, ≥99%), and carbon disulfide (CS_2, 99.9%) were purchased from Sigma-Aldrich. Chloroform (99.9%), toluene (99.9%), and ethanol (99%) were purchased from Fisher Scientific. All chemicals were used without further purification unless otherwise noted in the synthesis procedure. Hydrocarbon organic solvents were purged with N_2 prior to use.

3.5.2 Synthesis and Purification of LSPR-active WO3-x NPLs.

WO_{3-x} NPLs were synthesized using standard Schlenk line techniques. Briefly, 2.25 mmol (0.513 g) of MA and 5.0 mL of 1-ODE were added to a 50 mL 3-neck round bottom flask and the mixture was purged with N_2 at 110 °C for 30 min. The homogeneous solution was then degassed at 130 °C under vacuum for 1.5 h, then placed under N_2, and slowly the temperature was raised to 290 °C. At this temperature, 0.25 mmol (0.70 mL) of tungsten (V) ethoxide was rapidly injected that resulted in an immediate change of solution from colorless to dark blue. Immediately, a N_2-purged solution of 0.5 mL ODE and 1.5 mmol (0.5 mL) OLA was injected via syringe and the reaction was allowed to continue for 1h. The reaction was quickly cooled to 100 °C by blowing compressed air across the outside of the flask. Under inert conditions, colloidal solution was then transferred into a 3-neck 50 mL round bottom containing 0.4 mmol (122.2 mg) of TDPA that was flushed with N_2 for 30 min. The temperature of the TDPA containing colloidal solution was raised to 140 °C and stirred for additional 1.0 h. The reaction was quenched by removing from the heat and stirred under N_2 until it reached room temperature. The reaction mixture was then diluted with 5 mL $CHCl_3$ and transferred into a 50 mL centrifuge tube. 25 mL ethanol was added to precipitate the NPLs, and the blue solid was collected via centrifugation at 10,000 rpm for 10 min. The supernatant was discarded, and the product dispersed in 5 mL chloroform. The purification steps were repeated two additional times. The final product was dispersed in the appropriate solvents for characterization.

3.5.3 Microscopy and Spectroscopy Characterizations.

XRD analysis: A Bruker D8 Discover X-ray diffractometer (Cu Kα, λ = 1.54 Å) was used to collect XRD diffraction patterns. Chloroform dispersion of purified WO_{3-x} NPLs was drop-cast onto cleaned glass coverslips. A 2D VÅNTEC-500 detector was used to obtain diffraction patterns from 5-60° 2θ with 5° 2θ steps and 30 s per step. Combined diffraction patterns were integrated to create 1D output.

TEM analysis: TEM analysis was conducted using a JEOL-JEM-F200 electron microscope with an accelerating voltage of 200 kV. TEM samples were prepared by dispersing in $CHCl_3$ and dropping 10 µL onto a carbon-coated 150 mesh copper grid (Electron Microscopy Science). The excess solution was drawn through with a filter paper.

UV-Vis-NIR absorbance measurements. The absorption spectra were collected using a Perkin Elmer Lambda 19 UV/Visible/NIR spectrometer in a 1 cm quartz cuvette over a range of 300-2500 nm. Samples were dispersed in carbon tetrachloride or other appropriate solvents for refractive index sensitivity study.

XPS analysis: XPS was conducted at the Chapel Hill Analytical and Nanofabrication Laboratory. Samples were prepared by drop-casting purified samples onto piranha-cleaned silicon wafers. A Kratos Axis Ultra DLD X-ray photoelectron spectrometer with Al Kα X-ray irradiation and energies of 80 and 20 eV were used for a survey and high-resolution scans, respectively. For samples that were electrically conductive, the sample was grounded, and the charge neutralizer was turned off. If samples showed some slight differential charging, then in these cases, the charge neutralizer was used, but the sample was isolated from ground. All spectra were corrected to the C 1s peak at 284.6 eV.

FTIR analysis: A Thermo Scientific Nicolet iS10 spectrometer with accompanying Omnic 8.2 software was used for all FTIR collection and processing. Samples were dispersed in $CHCl_3$ and placed onto a 4 mm KBr plate. Solvent was allowed to evaporate before the FTIR data acquisition with 100 scans subtracting a 64-scan background under ambient conditions.

Raman Spectroscopy: Samples were drop casted on cleaned silicon wafers and spectra were acquired using a XploRA Plus Raman Microscope from Horiba Scientific. Crystal lattice vibration related spectra were obtained using a 532 nm laser at 25% power, 1800 line/mm grating and 10x objective were used to collect spectra with an acquisition time of 3 second and 3 to 5 accumulations. Spectra delineating the vibrational modes of ligands were obtained using 532 nm laser at 1% power with a 100x objective and 60 second acquisition times over 3 accumulations.

EPR Spectroscopy: EPR analysis was conducted using a Bruker EMX-X instrument with an ER 4119 HS cavity using 100 kHz field modulation. WO_{3-x} NPLs were dissolved in $CHCl_{3,}$ and 0.5 mL of solution was transferred in an EPR tube for the analysis at room temperature. All the samples were placed at the same position inside the resonant cavity during the EPR analysis. The g value was determined from the magnetic field (B_0) using the following equation $g = h\nu/\beta B_0$. where h is the Planck's constant (6.626×10^{-34} J·s), ν is the frequency of the radiation (9.800475×10^{9} Hz) and β is the Bohr magneton (9.274×10^{-28} J·G^{-1}).

3.5.4 Density Function Theory (DFT) Calculations.

DFT calculations were performed to obtain frequenquency optimized geometry and determine Raman vibrational frequencies for different modes of tungsten bonded to the TDPA molecule via W-O bonds. Calculations were accomplished using Gaussian16[319] with the BP86 exchange-correlation functional in the GenECP variation. LanL2DZ effective core potential basis set[320] was used for tungsten atom while 6-311+G** basis set was used for rest of the atoms to perform the theoritical calculation. All TDPA bound to tungsten theoretical spectra were corrected according to the assigned stretching of C-P observed in the experimental spectrum. The visualization of optimized geometry and assigning vibrational frequencies for the active modes in Raman analysis were achieved using Gaussview 6.0.16 software.[321]

3.5.5 NOBF4 Titration Description:

$NOBF_4$ was dissolved in acetonitrile to create a saturated solution in an inert atmosphere inside a glovebox. The concentration of this solution was determined via ^{19}F NMR using 1,2,3,5-tetrafluorobenzene (Alfa Aesar, 99%) as an internal standard. The calculated concentration determined from 5 internal standard prepared solutions was determined to be 243.5 ± 8.2 mM. This solution was then diluted as necessary to conduct the titrations. Each aliquot addition was performed within the glovebox and the cuvette was sealed before removal for analysis.

3.5.6 Calculation of Free Carrier Density:

Free carrier density can be calculated directly via the total number of $NOBF_4$ molecules necessary to completely extinguish the LSPR response by extrapolating the linear portion of the absorption area vs. NOBF4 molecules graph. The total volume of WO_{3-x} in the sample was determined by knowing the initial concentration obtained using the molar absorption coefficient, 3200 cm^{-1} M^{-1},[322] of the solution, the molar mass of $WO_{2.72}$, and the density which we used 7.7 g/cm^3 obtained from CrystalMaker 9 software.

3.6 Appendix A

Table 3.2: DFT-calculated Raman vibration modes of tetradecylphosphonic acid.

Vibrational Descriptions	**Mode**	**DFT peak (cm^{-1})**
δ_{sc} (C-H) FAlk	102	1489
δ_{sc} (C-H) NAlk	96	1457
γ_{w} (C-H) FAlk	92	1398
γ_{w} (C-H)	80	1324
ν (P=O), γ_{w} (C-H)	77	1296
ν (P=O), γ_{w} (C-H)	75	1275
ν (P=O), γ_{w} (C-H)	73	1256
ν (P=O), γ_{w} (C-H)	71	1232
ν (P=O), γ_{w} (C-H)	69	1214
δ_{r} (C-H) FAlk; γ_{w} (C-H) NAlk	68	1203
δ_{r} (C-C)	67	1142
δ_{sc} (C-C) Nalk, δ_{r} (C-C) FAlk	66	1102
δ_{sc} (C-C), γ_{w} (O-H)	62	1065
ν_{sym} (C-C), γ_{w} (O-H)	54,53	1009,1002
ν_{asym} (C-C), γ_{w} (O-H)	53	1002
ν_{asym} ($C-CH_3$) FAlk	47	896
ν (C-P)	44	852
ν (P-O)	38	734
δ_{r} (P-O)	32	473
δ_{r} (P=O)	29	414
δ_{sc} (P=O)	28	390
β (Alk)	16	152
β (FAlk)	14	124

Table 3.3: DFT-calculated Raman vibration modes of MA bound to tungsten atom via bidentate chelating bonding.

Vibrational Descriptions	**Mode**	**DFT peak (cm^{-1})**
ν (C═O)	105	1533
δ_{sc} (C-H) alkyl	103,96	1459,1434
δ_{sc} (CH_2) NAlk	91	1375
γ_{w} (CH_2) alkyl	76	1285
δ_{r} (C-H) alkyl	67	1185
ν (C-O); δ (C-C) alkyl	65,64	1132,1113
δ (C-C) Falk	62	1071
ν (C-C) alkyl	61,58	1052,1043
δ_{sc} (O-C=O)	51	987
γ_{w} (CH_3)	46	900
ν_{sm} (W-O)	44	840
ν_{asm} (W-O)	41	792
ν (C-C(=O)O)	35	759
ν (W-C(=O)O)	34	636
δ (C-C) alkyl	28,26	407,373

Table 3.4: Theoretical Raman vibration modes of bidentate bound TDPA through deprotonated hydroxy oxygen. All vibrations scaled by 0.951 according to ν(C-P).

Vibrational Descriptions	**Mode**	**DFT peak (cm^{-1})**
δ_{sc} (C-H) NAlk	117	1299
γ_{w} (C-H) NAlk	115	1279
γ_{t} (C-H) NAlk	112	1256
γ_{w} (C-H) Falk	109	1233
γ_{t} (C-H) Falk	90	1119
δ_{sc} (C-C) alkyl	87	1042
δ_{r} (C-C) alkyl	84	1018
γ_{w} (C-C) alkyl	81	986
ν (C-C) alkyl	78	966
γ_{t} (C-C) alkyl	75	945
ν (P=O); δ (C-C) alkyl	73	914
ν_{sm} (W-O)	68	840
δ (C-H) alkyl	64,63,61	790, 767, 755
δsc (O-P-O); νasm (W-O)	58	709
ν (C-P)	57	680
δ (W-O)	56,55	607, 594
γw (P-O-W)	54	573
γw (O-P-O); δ (W-O)	52	544
δ (O-P-O)	51	509
δ (C-CH2-C) alkyl	49	481
δ (C-PO3); alkyl	45,44	417, 392

Table 3.5: DFT-calculated Raman stretches of bidentate and chelating bound TDPA through deprotonated hydroxy oxygen. Scaled by 1.012 according to ν(C-P).

Vibrational Descriptions	**Mode**	**DFT peak (cm^{-1})**
δ (C-H) alkyl	108	1460
γ (CH) alkyl	95, 92, 89,87,85	1311, 1288, 1266, 1255, 1239
γ (C-H) Falk	83	1231
δ (C-H) Falk	78	1198
ν (C-H) alkyl	76	1192
δ (C-C) alkyl	73	1096
ν (C-C) Nalk	70	1040
ν (C-C) alkyl	66,64,62	1010, 992, 986
ν (P=O); δ (C-C) alkyl	57	942
δ (C-CH) Falk	56	903
ν (W-O)	52	842
δ (C-C) alkyl	49	788
ν (W-O)	43	740
ν (C-P)	42	680
δsc (O-P-O)	41	611
γw (O-P-O); δr (C-H) Nalk	40	597
δ (W-O-P)	39	509
δ (O-P-O)	36	466
δ (C-PO3); alkyl	33	419

Table 3.6: DFT-calculated Raman stretches of tridentate bound TDPA. Scaled by 1.046 according to ν(C-P).

Vibrational Descriptions	**Mode**	**DFT peak (cm^{-1})**
δ_{sc} (C-H) FAlk	124	1504
δ_{sc} (C-H) NAlk	119,117	1457, 1449
γ_{w} (C-H) Falk	109,107	1374, 1359
γ_{w} (C-H) alkyl	102,100,97,95	1326, 1309, 1259, 1228
δ_{sc} (C-C) alkyl	93	1179
δ_{r} (C-C) alkyl	89	1133
ν (P=O); δ_{r} (CH_2) alkyl	83	1089
δ (C-H) alkyl	80,78	1047, 1003
ν (C-H) alkyl	77	979
ν_{sm} (W-O)	76,74	955, 930
ν_{asm} (W-O)	70,68	870, 832
δ (W-O)	63	787
δ (CH_2) alkyl	61	747
ν (C-P)	60	680
γw (P-O-W)	59	655
δsc (O=P-C)	58	640
δsc (O-P-O)	56	601
γw (O-P-O)	54	578
ν (P-O)	52	521
δ (C-CH2-C) alkyl	50	476
δsc (O-P=O); δ (C-CH2-C) alkyl	49	432

Table 3.7: DFT-calculated Raman stretches of tridentate chelating bound TDP. Scaled by 1.030 according to ν(C-P).

Vibrational Descriptions	**Mode**	**DFT peak (cm^{-1})**
γ_w (CH$_3$) FAlk	116	1501
δ_{sc} (C-H) alkyl	110	1476
δ_{sc} (CH$_2$) NAlk	104	1449
γ_w (C-H) FAlk	102	1392
γ_w (C-H) alkyl	97,96	1369, 1350
δ_r (C-H) alkyl	88,86,84,81,79	1320, 1301, 1278, 1246,
δ_r (C-H) Nalk	77	1197
δ (C-C) alkyl	76	1148
ν (C-C) alkyl	75	1105
ν (C-C) FAlk	70	1073
ν (C-C) NAlk	66,65	1054, 1037
ν (P=O); δ (C-C) alkyl	62	1003
νsm (W-O)	57	937
δsc (O=P-C)	52	809
γw (W-O=P); δr (C-H) Nalk	46	775
γw (W-O-P); δr (C-H) Nalk	45	715
νsm (W-O); δ (O-P-O)	44	700
ν (C-P)	43	680
δsc (W-O-P)	42	660
δ (C-PO3); alkyl	41	592

Table 3.8: Comparison of LSPR refractive index unit (RIU) sensitivity of various metal oxide and noble metal nanostructures.

Nanostructure (description)	**Approx. Sensitivity (nm/RIU)**
AgFON (Ag film over nanospheres) [323]	481
Au nanorod [249]	318
Au nanoprism [249]	225
Au spheres [249]	135
Au nanoprism (28 nm edge length) [181]	647
Au nanoholes [324]	100
S-P-AuNR (solution processed gold nanorod) [325]	196
Gold nanorings [326]	880
Au-hematite nanorice [245]	801
Au nanorattle [327]	285
Au gold nanostars [328]	643
Au nanobranches [317]	703
Ag nanoparticles [329]	191
Ag triangular nanoprisms [330]	205
ReO_3 nanocrystals [331]	112
$Cu_{2-x}S$ spherical nanoparticles	350
WO_{3-x} nanoplatelets [115]	330
$WO_{2.83}$ nanorods [113]	280
MoO_2 and MoO_{3-x} [332]	115-260
WO_{3-x} nanoplatelets (This work)	428

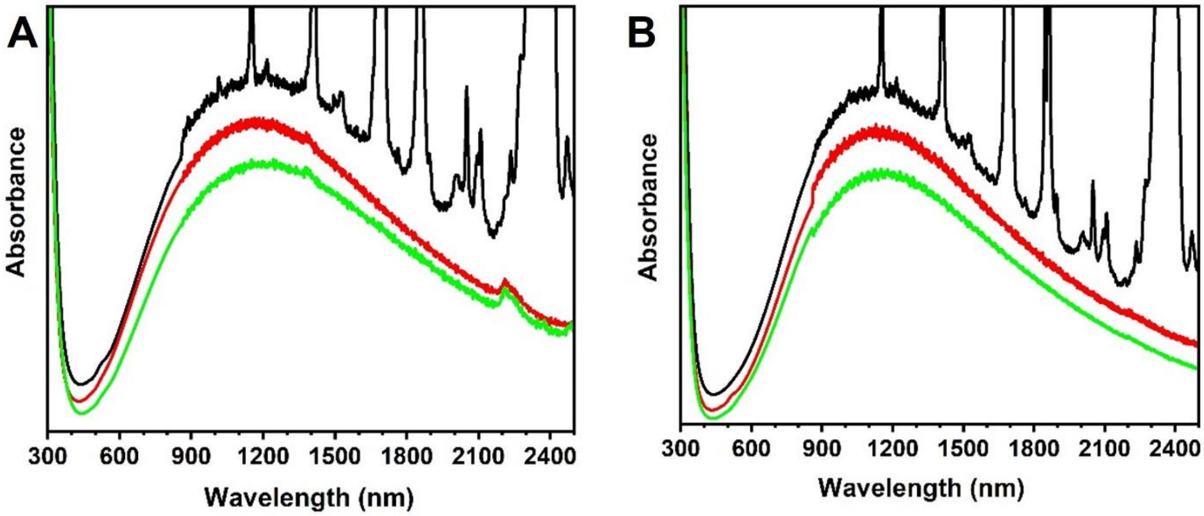

Figure 3.14: Raw UV-Vis-NIR spectra of (A) as synthesized WO_{3-x} NPLs and (B) TDPA treated WO_{3-x} NPLs in chloroform (black), carbon tetrachloride (red), and tetrachloroethylene (green).

CHAPTER 4. COVALENT SURFACE MODIFICATION OF $TI_3C_2T_X$ MXENE WITH CHEMICALLY ACTIVE POLYMERIC LIGANDS PRODUCING HIGHLY CONDUCTIVE AND ORDERED MICROSTRUCTURE FILMS

This article has been adapted with permission from, Jacob T. Lee, Brian C. Wyatt, Gregory A. Davis, Adrianna N. Masterson, Amber L. Pagan, Archit Shah, Babak Anasori, and Rajesh Sardar. *ACS Nano* **2021** *15* (12), 19600-19612 DOI: 10.1021/acsnano.1c06670

4.1 Synopsis

This chapter focuses on $Ti_3C_2T_x$ MXenes and advancing the methods of manipulation of their surface functional groups beyond synthesis-based surface terminations (T_x: –F, –OH, and =O).This knowledge can provide mechanisms to enhance solution processability as well as produce new solid-state device architectures and coatings. Here, we report a fundamentally new surface modification approach in which *"solvent-like"* polymers, polyethylene glycol carboxylic acid (PEG6-COOH), are covalently attached onto MXenes via esterification chemistry. Surface modification of $Ti_3C_2T_x$ with PEG6-COOH with large ligand loading (up to 14% by mass) greatly enhances dispersibility in a wide range of non-polar organic solvents (e.g., 2.88 mg/mL in chloroform) without oxidation of $Ti_3C_2T_x$ 2D flakes or changes in the structure ordering. Furthermore, cooperative interactions between polymer chains improve the nanoscale assembly of uniform microstructures of stacked MXene-PEG6 flakes into ordered thin films with excellent electrical conductivity (~16,200 $S.cm^{-1}$). Most importantly, our covalent surface modification approach with ω-functionalized PEG6 ligands (ω-PEG6-COOH, where ω: $-NH_2$, $-N_3$, $-CH=CH_2$) allows control over the degree of functionalization (incorporation of valency) of MXenes. We believe that installing valency onto MXenes through short, ion conducting PEG ligands without compromising MXenes' features such as solution processability, structural stability, and electrical conductivity further enhance MXenes surface chemistry tunability, performance, and widens their applications.

4.2 Introduction

The field of nanoscience has completely transformed since the discovery of the two-dimensional (2D) material graphene.[4] Since then, a wide range of 2D materials with varying elemental compositions (i.e., transition metal dichalcogenides, *h*-BN, transition metal oxides, etc.) have been extensively studied.[230, 333-336] MXenes, which are transition metal carbides, carbonitrides, and nitrides. These nanomaterials have been the forefront of 2D material-based research since their discovery in 2011.[54] MXenes' unique combination of properties such as their high in-plane electrical conductivity (up to 24,000 $S \cdot cm^{-1}$ for $Ti_3C_2T_x$),[145] high capacitance (up to ≈ 490 $F \cdot g^{-1}$ at 1 $A \cdot g^{-1}$),[145] and impressive elastic modulus (up to 386 GPa for $Nb_4C_3T_x$)[337] have driven their utilization in a vast number of applications including energy conversion and storage, electromagnetic interference shielding, and in composites for numerous functions such as membranes and sensors.[56, 58, 146, 241, 338-342]

MXenes are synthesized from their MAX phase precursors and have a general formula of $M_{n+1}X_nT_x$ ($n = 1 - 4$), where M is $n + 1$ layers of one or more early transition metals of the $3d – 5d$ block in groups 3 – 6 of the periodic table, interleaved by n layers of X, which represents carbon or nitrogen, and T_x represents the surface terminations (commonly –F, –OH, and –O).[55, 130] Over the last 10 years, $Ti_3C_2T_x$ (Ti_3C_2) MXene has been extensively studied due to its ease of synthesis and delamination, good physical and chemical stability,[136, 197] and demonstrated unique electronic and optical properties.[131] The standard synthesis conditions and etching process of the MAX phase, where A represents an A group element, commonly of groups 13 – 16 of the periodic table, results in hydrophilic surface terminations on the MXene flakes (–OH, =O, –F).[343] These hydrophilic chemical functionalities allow MXene flakes to be dispersed in water and other polar organic solvents such as dimethylformamide (DMF), dimethyl sulfoxide (DMSO), propylene carbonate (PC).[152-153] This dispersibility property of MXene flakes in various solvents enhances the processability of MXenes through spraying, inkjet printing, and stamping for solid-state device application.[344] However, highly hydrophilic $Ti_3C_2T_x$ flakes are prone to oxidation in water and thus lose the desired physicochemical properties that together limit downstream processing.[148] Therefore, it is extremely essential to be able to exert control over the surface groups of $Ti_3C_2T_x$ flakes so that surface modified MXene can be solubilized in water-immiscible nonpolar organic solvents to improve stability, long term storage, and the processability of the material.[153]

The surface functionalization of Ti_3C_2 flakes by various organic ligands has been conducted through multiple routes including catechol,[345] silane,[200, 346] isocyanate,[347-348] amino acid,[349-350] and phosphonic acid[151] chemistries. While these methods have been successful, there are still limitations on MXenes property control and stability: (1) Silane chemistry does not provide uniform surface modification due to severe homocondensation in water.[351] (2) Attachment of amino acids require an aqueous phase synthesis route which may result in oxidation of Ti_3C_2 flakes into TiO_2 due to the presence of dissolved oxygen or water itself.[147] (3) Surface modification with isocyanate and phosphonic acid group containing ligands bearing insulating, aliphatic hydrocarbon chains would impede the conductivity. (4) Lack of adequate knowledge to increase the range of solvent options for high concentrations of Ti_3C_2 dispersions because the existing approach only produces relatively low concentrations (0.5 mg/mL) in non-polar organic solvents.[152] High concentrations of MXenes in a wider range of non-polar organic solvents would allow for their implementation in a greater number of technologies. For example, polymerization reactions under anaerobic conditions and in non-polar organic solvents are commonly performed to prepare ink dispersions for coating applications. Furthermore, to the best of our knowledge, there are no reports available demonstrating the surface ligand modification to control the degree of chemical functionality or adding “valance” onto MXene flakes without compromising the 2D lattice structure and conductivity. Installing end-terminal, chemically reactive functional groups on the surface of nanostructures provides unique possibilities to control their structural and optoelectronic properties, higher order assemblies, and expand potential applications. Very recently, Mayorga-Burrezo et al. reported the synthesis of multifunctional 2D-MXenes by modifying their surface with amino acids.[350] However, this chemistry requires aqueous phase chemical transformation, which could reduce the overall stability of the multifunctional 2D-MXene materials.

These previous investigations on organic ligands to modify the surface groups of MXenes for increased functional behavior paired with the current limitations of the use of MXene in non-polar organic solvents led to our interest toward the functionalization of Ti_3C_2 MXene flakes with ω-PEG6-COOH ligands. This chemical modification strategy demonstrated a myriad of successes in ligand attachment in nanoparticle-based research.[352-353] We selected esterification chemistry because the covalent ester bond is chemically more stable than diazonium bonding and electrostatic interactions.[152, 354] Additionally, the attachment of PEG ligands expands the solubility range of MXene 2D flakes to both non-polar and polar organic solvents. In addition to the attachment method, PEG-modified Ti_3C_2 MXene flakes can offer a low barrier to electron conductance between MXene flakes in film applications, as compared to long hydrophobic alkyl chain containing ligands. This is, due to the charge transport capability of glycol units.[355-356] The aliphatic nature and flexibility of the PEG chains for constructive ligand-ligand hydrophobic and van der Waals (vdWs) interactions can also permit various self-assembly processes, which is expected to enhance optoelectronic properties in thin-films.[231-232, 357-360] Similarly, the addition of PEG functional surface groups paired with the already favorable 2D properties of MXenes could be useful for many biotechnology applications such as sensing, imaging, and drug delivery.[361] This is due to PEG ligands' inherent biocompatibility,[203, 362] as well as reducing non-specific biomolecule adsorption for the above-mentioned applications.[363-364]

In this manuscript, we demonstrate a Steglich esterification[365] route to covalently functionalize Ti_3C_2 MXene flakes with ω-PEG6-COOH ligands in a mild and non-aqueous reaction condition, as seen in Figure 3.1. Together, we show that the covalent attachment of PEG6 ligands onto Ti_3C_2 MXene flakes dramatically increases the dispersibility in a broad range of non-polar and polar solvents with concentrations as high as 2.88 mg/mL in chloroform. Furthermore, PEG ligand-functionalized Ti_3C_2 MXenes retain the conductive properties as similar to unmodified Ti_3C_2 MXene flakes. Most importantly, we show that our developed surface modification chemistry can be extended to a wide range of functional groups (ω-PEG6-COOH, where ω is -

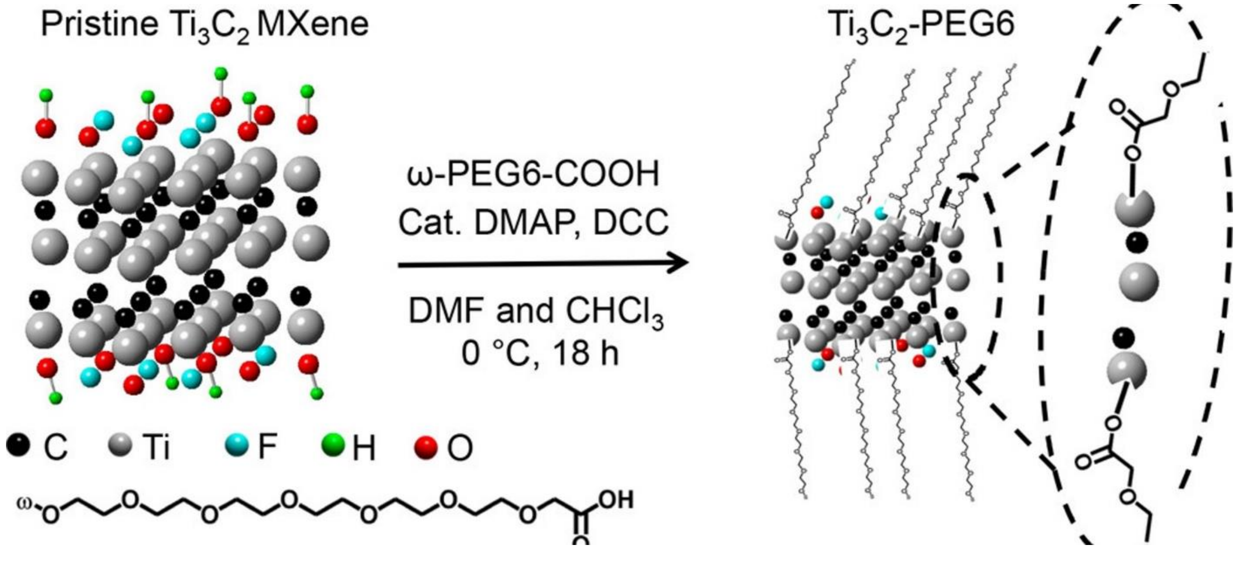

Figure 4.1: Schematic diagram of covalent surface modification of pristine $Ti_3C_2T_x$ (T_x: –F, –OH, and/or =O) MXene via esterification reaction where the hydroxy terminations are modified with ester bonded ω-PEG6-COOH forming Ti_3C_2-PEG6.

NH_2, -N_3, -CH=CH_2) on the opposite termini of the 2D structure which should allow for Ti_3C_2 flakes to take part in further covalent chemistries and have direct control over the assembly of Ti_3C_2 via bottom-up strategies towards the development of advanced MXene hybrid nanocomposites.[366-367]

4.3 Results and Discussion

4.3.1 Synthesis and Characterization of PEG6-Ester-Modified Ti_3C_2 MXene (Ti_3C_2-PEG6 Flakes).

In order to prepare the pristine Ti_3C_2 for the PEG6 modification, we first transferred an aqueous dispersion of Ti_3C_2 MXene into DMF *via* multiple steps of bath sonication and centrifugation. After fully dispersing Ti_3C_2 into the DMF, the resulting DMF dispersion of Ti_3C_2 MXene was then combined with PEG6-COOH (see Supporting Information for additional details) and 4-dimethylaminopyridine (DMAP). The combination of these components resulted in the appearance of small particulates, which we believe are formed due to inter-molecular hydrogen bonding between PEG6-COOH and –OH and –F groups onto Ti_3C_2 surface. The esterification reaction was then initiated by dropwise addition of the chloroform solution of dicyclohexylcarbodiimide (DCC) at 0 °C under N_2 environment. After continuous stirring of this solution overnight, the small particulates disappeared which resulted in an optically transparent solution. We believe once the surface of Ti_3C_2 is modified with PEG6 due to the formation of ester bond, most of the hydrogen bonding interaction between the flakes disappeared, whereas strong non-polar interaction between organic solvent and glycol chain-containing Ti_3C_2 flakes dictates the overall solvation properties. The product was centrifuged and washed with chloroform multiple times (See experimental section for further details). The purified product was dispersed into chloroform for spectroscopy and microscopy analyses.

After observing the synthesis process of the PEG6 modification of Ti_3C_2 MXene, we next focused on characterization methods of the resultant product. We observed two important optical properties of Ti_3C_2-PEG6 flakes. First, the UV-vis absorption spectrum shows good peak shape and lack of noise (Figure 4.2A, blue line), which is due to adequate dispersibility of Ti_3C_2-PEG6 flakes in chloroform. Second, Ti_3C_2-PEG6 flakes display an absorption peak at 781 nm in chloroform that is very close to the value for as prepared Ti_3C_2 flakes in DMF (778 nm). This 3.0

nm change in the absorption peak position can be attributed to the change in local refractive index appearing from the solvent change, as well as attachment of PEG6 ligands on the surface. As reported in the literature, a major absorption peak shift from the initial Ti_3C_2 in DMF (Figure 4.2A, black line) would be observed in the event of oxidation of Ti_3C_2 and the formation of TiO_2 during our synthesis.[136] Transmission electron microscopy (TEM) analyses also confirmed the lack of oxidation product in our synthesis conditions. Figure 4.2B and C show TEM images of as synthesized, pristine Ti_3C_2 MXene flakes and post modification Ti_3C_2-PEG6, respectively. We do not observe the clear formation of any small nanoparticles as a form of TiO_2 nanoparticles in the Ti_3C_2-PEG6 flake. Moreover, the Ti_3C_2-PEG6 flakes are in micrometer scale lengths. These results suggest that the chemical modification of Ti_3C_2 MXene flakes does not change the size nor induce

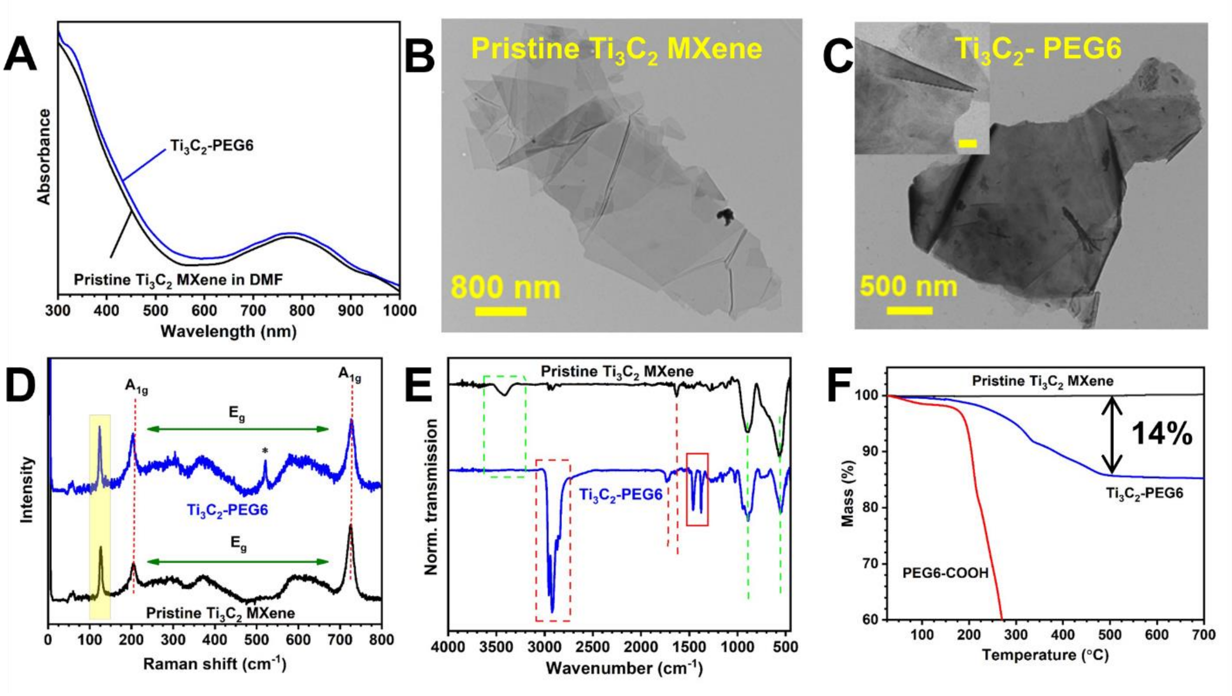

Figure 4.2: (A) UV-vis absorption spectra of Ti_3C_2 MXene flakes before (778 nm) and post covalent surface modification with PEG6-COOH (781 nm). (B) TEM image of pristine Ti_3C_2 MXene flakes. (C) TEM image of post surface modification of Ti_3C_2 MXene with PEG6-COOH. Inset in (C) shows magnified TEM image with a 100 nm scale bar. (D) Raman spectra of Ti_3C_2 MXene flakes and Ti_3C_2-PEG6 flakes highlighting the resonance peak (yellow box), A1g peaks (red dashed lines) and surface E_g related vibrational modes (green arrowed line). (E) FTIR spectra of Ti_3C_2 MXene flakes and Ti_3C_2-PEG6 flakes. Characteristic Ti_3C_2 vibrations are assigned by green dashed lines and box, and the IR vibrational stretches of PEG6-COOH are shown in red. (F) TGA analysis of pristine Ti_3C_2 MXene, pure PEG6-COOH, and Ti_3C_2-PEG6. A 14% mass loss is observed between pristine Ti_3C_2 MXene and Ti_3C_2-PEG6.

any oxidation of the MXene flakes. This is an important finding in terms of maintaining the structural integrity of the Ti_3C_2 MXene flakes.[147-148]

After establishing dispersion of PEG6 functionalized Ti_3C_2 MXene in chloroform with no oxidation observed in UV-Vis and TEM characterizations, we next focused on analysis of Ti_3C_2-PEG6 flakes with Raman spectroscopy. This technique is often used to characterize Ti_3C_2 and other related MXene compositions to identify possible oxidation of the material, and to determine changes to surface termination or structure.[288, 368] It is well known that Raman vibrational peaks can be impacted by synthesis and etching conditions along with specific changes in surface terminations (T_x), grain size, sample deposition techniques, and analysis parameters.[288] The Raman spectra shown in Figure 1D were collected at a 785 nm laser excitation. First, the appearance of the peak at 123 cm^{-1} (yellow box) results from the incident laser interaction with the plasmon resonance of the material.[369] Additionally, the A_{1g} out-of-plane peaks for (Ti,C,O) near 203 cm^{-1} and for (C) at 725 cm^{-1} (red dashed lines) are clearly visible. Second, a slight shift in Raman peak position of the A_{1g} (Ti,C,O) peak from 203 cm^{-1} to 202 cm^{-1} is detected when PEG6 is attached through an ester formation. Similar shifts have been reported when there is a change in the surface group termination.[368, 370] Third and the most important feature, is that no Raman stretches exist resulting from possible oxidation products during Ti_3C_2 MXene sample processing and analysis. If there was clear oxidation in the PEG6 functionalized Ti_3C_2 MXene samples, we would expect to observe very distinct Raman stretches due to the formation of rutile and/or anatase TiO_2

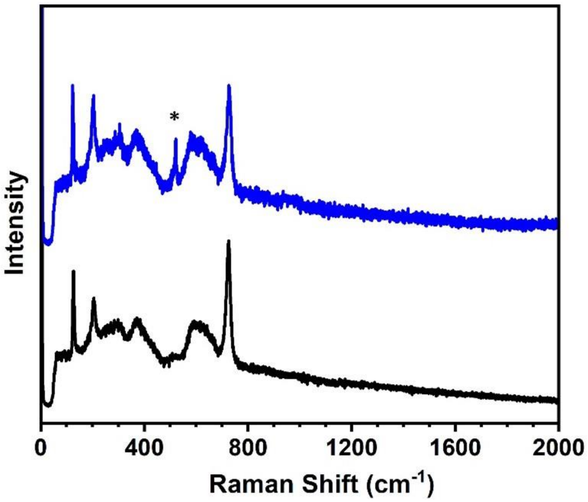

Figure 4.3: As obtained Raman Spectra of Ti_3C_2-PEG6 (blue) and Ti_3C_2 (black). This highlights the absence of D and G disordered carbon vibrational bands (100-1800 cm^{-1}). The asterisk at ~520 cm^{-1} arises from the silicon substrate.

materials[371]. Particularly, a high intensity peak near 153 cm^{-1} and additional D and G band carbon peaks between (1000-1800 cm^{-1}) would appear from the formation of disordered carbon structures (Figure 4.3). The surface E_g region (green arrowed line) represents in-plane vibrational modes resulting from surface terminations. As the surface termination peaks in Ti_3C_2 MXene are overlapping in nature, we were unable to identify actual surface termination changes in the Raman spectrum. Nevertheless, our Raman spectroscopy results support that no clear oxidation of Ti_3C_2 MXene flakes occurs during the synthesis process. We believe the prevention of this oxidation is due to extremely mild reaction conditions where the entire synthesis was conducted in organic solvents under N_2 environment below room temperature.

We next conducted FTIR and thermogravimetric analysis (TGA) to verify the covalent surface modification of Ti_3C_2 MXene flakes and the surface ligand loading. Figure 4.2E illustrates the FTIR spectra of pure Ti_3C_2 MXene flakes (black) and after surface modification with PEG6-COOH (blue). The green box indicates the presence of –OH within the flakes structure and the green lines represent typical surface groups bound to Ti atoms such as the vibration mode of Ti-O bond ~550 cm^{-1}.[372] The characteristic low energy vibrational modes (green dashed lines) remain unaltered even after the attachment of PEG6 (see blue spectrum). The O-H stretch at ~3400 cm^{-1} is not present, which we believe could be due to transformation of all the –OH to -COO bonds *via* the esterification chemistry. Importantly, the presence of PEG6 in Ti_3C_2-PEG6 is witnessed by the appearance of multiple -CH related vibrations from the $–CH_2-CH_2-O-$ units, as highlighted by the red dashed box (2850-2960 cm^{-1}) and the red solid box (1470 and 1371 cm^{-1}). These IR modes are

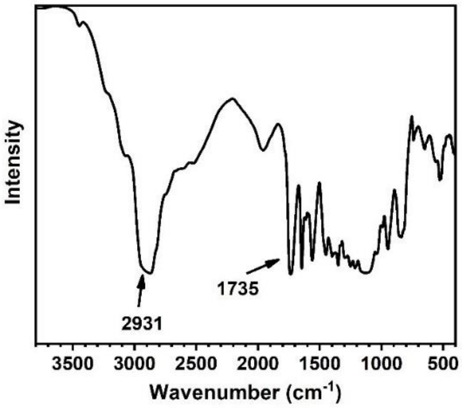

Figure 4.4: FTIR spectrum of lab synthesized PEG6-COOH with the -CH related vibration peaks (2931 cm^{-1}) and carbonyl (1735 cm^{-1}) labeled for reference.

not present in the unmodified Ti_3C_2 MXene flakes.[200] Additionally, the carbonyl stretch of pristine Ti_3C_2 is present in Ti_3C_2-PEG6 flakes along with an additional carbonyl stretch at 1704 cm^{-1}, which derives from the ester bonded carbonyl group. This carbonyl stretch has shifted in respect to the carbonyl stretch found in pure PEG6-COOH (1735 cm^{-1}, Figure 4.4). Therefore, our FTIR characterization strongly supports covalent surface modification of pristine Ti_3C_2 MXene with PEG6-COOH *via* formation of the ester bond.

In addition to FTIR characterization of the bonding nature of the PEG modification of Ti_3C_2 MXene, we also compared the mass of non-PEG6-functionalized Ti_3C_2, PEG6-functionalized Ti_3C_2, and PEG6-COOH alone by the TGA analysis, see Figure 1F. Unmodified Ti_3C_2 MXene shows no major mass loss, since there are no organic ligands to be removed (black curve). A slight mass aberration (<1%) is detected, which could be attributed to the loss of surface groups or phase change in the crystal structure at higher temperatures.[373-374] PEG6-COOH begins almost complete and sudden mass loss beginning near 200 °C (Figures 4.2F, red curve) which is near the boiling point of the polymer. Ti_3C_2-PEG6 flakes (blue) behave quite differently, with very little mass loss near the boiling point of PEG6-COOH. A gradual mass loss until ~330 °C and then a steady loss until nearly 480 °C are observed, and no additional loss takes place beyond this temperature. The higher temperature onset and much slower mass loss of PEG6-functionalized Ti_3C_2 than PEG6-COOH itself suggest the covalent attachment of our PEG6 ligands to the surface of Ti_3C_2. High temperature is required to break the covalent ester bond formed between oxygen and titanium. Also, the steady loss between 330-480 °C signifies the additional temperature and kinetic contributions in removing the interdigitated PEG6 ligands between stacked Ti_3C_2-PEG6 flakes. The data presented in Figure 1 suggests our PEG6-COOH ligands covalently attach to Ti_3C_2 MXene flakes through an esterification process using the surface hydroxyl groups forming Ti_3C_2-PEG6 flakes. Importantly, TGA analysis indicates a grafting density of ~14 wt % of PEG6 on Ti_3C_2 flakes. This is in good agreement with literature,[151] suggesting almost near maximum conversion of surface –OH with PEG-COO-. Our esterification reaction-based covalent surface modification provides an improved surface coverage compared to previously reported catalyst free, nucleophilic substitution-based attachment of amino acids.[350]

4.3.2 Physicochemical and Electrical Conductivity Properties of Ti_3C_2-PEG6.

After establishing the nature of the surface ligand bonding of pristine Ti_3C_2 MXene with PEG6, we next focused on investigating the effects PEG6 modification on inherent physicochemical and electrical conductivity properties. First, we analyzed the solution processability of our synthesized Ti_3C_2-PEG6 flakes as colloidal dispersions. We hypothesized that the covalent attachment of PEG6 ligands should significantly change the surface-controlled physicochemical properties of the Ti_3C_2-PEG6 flakes, including improved dispersibility in a wider range of non-polar organic solvents, zeta potentials, and contact angle values of water droplets on films. PEG ligands are known to be soluble in a very wide range of solvents, both polar and nonpolar organic solvents as well as in an aqueous medium. The solubility of PEGs in water arises

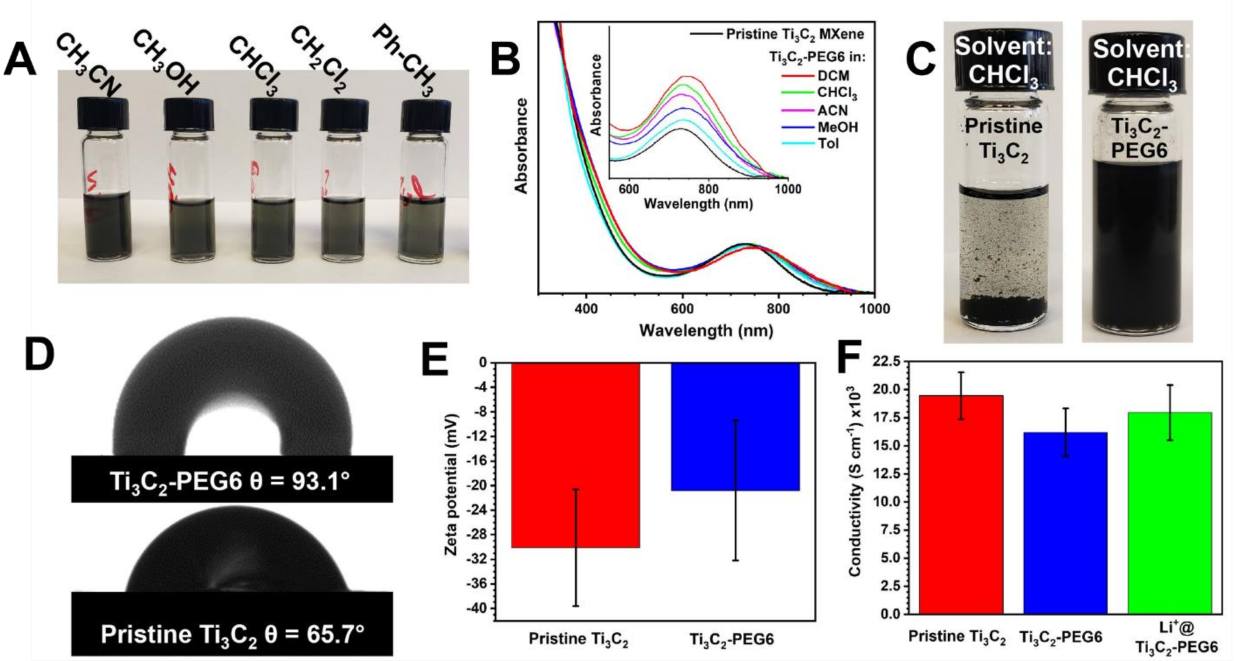

Figure 4.5: (A) Solvation study of Ti_3C_2-PEG6 flakes in various organic solvents (left to right) acetonitrile (CH_3CN), methanol (CH_3OH), chloroform ($CHCl_3$), dichloromethane (CH_2Cl_2), and toluene ($Ph-CH_3$). (B) UV-vis absorption spectra of dispersed Ti_3C_2-PEG6 flakes in those five organic solvents. The inset shows offset peaks to show good peak shape and minimal absorption peak shifts. (C) Dispersibility profile of pristine Ti_3C_2 MXene flakes (left) Ti_3C_2-PEG6 flakes (right) in $CHCl_3$. High concentration of MXene flakes were dispersed via bath sonication and then Images were taken 5 min after the sonication. (D) Contact angles of 2.0 µL water droplet on drop cast films of Ti_3C_2-PEG6 (top) and pristine Ti_3C_2 MXene (bottom). (E) Zeta potential value of aqueous dispersions of pristine Ti_3C_2 MXene and Ti_3C_2-PEG6 flakes. (F) Conductivity values of vacuum filtered films of pristine Ti_3C_2 MXene, Ti_3C_2-PEG6 and Li^+-intercalated Ti_3C_2-PEG6. Error bars include uncertainty from the instrumental reading and SEM cross-section measurement.

due to a large partial charge in the oxygen atom in the glycol unit that would result in an extremely high enthalpy of hydration.[375] In contrast, ethylene units in the backbone provide a non-polar aliphatic nature.[232] Figure 4.5A illustrates the dispersibility of our synthesized Ti_3C_2-PEG6 flakes in various solvents. Solvents representing a range of relative polarities and attributes including highly polar acetonitrile (ACN, 0.786) and methanol (MeOH, 0.791), moderately non-polar chloroform ($CHCl_3$, 0.259) and dichloromethane (DCM, 0.309) and highly non-polar toluene (Ph-CH_3, 0.099).[376]

For this diverse range of solvents, we used a qualitative approach in which Ti_3C_2-PEG6 flakes was dispersed *via* sonication with a minimum concentration of 0.4 mg/ml and allowed to rest for 5 min before capturing the photographs. The water dispersibility Ti_3C_2-PEG6 flakes is shown in Figure 4.6. It is noteworthy to mention that covalent surface modification of Ti_3C_2 flakes with silane compounds generally shows poor dispersion stability in alcohol medium;[153] whereas, our Ti_3C_2-PEG6 flakes display good dispersibility in MeOH. To further confirm the appropriate dispersibility in these solvents, UV-vis spectra were collected of Ti_3C_2-PEG6 in each solvent. All spectra show good peak shape and low signal to noise denoting quality dispersions (Figure 4.5B). We further selected $CHCl_3$ as a solvent to quantitatively determine the concentration of Ti_3C_2-PEG6 flakes. As shown in Figure 2C (left) unmodified Ti_3C_2 MXene flakes are barely dispersible in $CHCl_3$ where instantaneous formation of large particulates is observed even after prolonged bath sonication. In contrast Ti_3C_2-PEG6 flakes have exceptional dispersibility even at a high concentration (Figure 4.5C, right).

Figure 4.6: Image of Ti_3C_2-PEG6 dispersed in H_2O at a concentration of ~1 mg/mL. The lingering flakes above the solution occur due to residual immiscible chloroform post reaction solvent exchange back to water.

In order to determine the maximum concentration of PEG6-modified Ti_3C_2 in $CHCl_3$ achievable, an entire Ti_3C_2-PEG6 reaction product was dispersed in 0.5 mL $CHCl_3$ and allowed to rest for 45 min before the supernatant was removed and transferred in a pre-massed vial. The solvent was then completely removed using a Schlenk line vacuum and then placed in a vacuum oven. The final concentration of Ti_3C_2-PEG6 flakes is determined to be 2.88 mg/mL. This value is significantly higher than pristine Ti_3C_2 MXene in a non-polar organic solvent, specifically in which covalent surface modification was performed using hydrophobic ligands.[151] It is important to mention that the highly concentrated dispersion of Ti_3C_2-PEG6 flakes in non-polar organic solvents is mostly due to solvation effects with strong non-polar interactions between glycol chains on the MXene surface and organic solvent and not from electrostatic repulsion interactions.

Our FTIR spectroscopy and TGA analyses show that most of the surface –OH in Ti_3C_2 MXene is replaced by PEG6 through the formation of ester bonds, this resulted in more hydrophobic character of Ti_3C_2-PEG6 flakes, as evident in the dispersibility properties discussed above. To further verify the hydrophobic character of Ti_3C_2-PEG6 flakes, we performed water contact angle measurements. As shown in Figure 4.5D (bottom), the water contact angle on a pristine Ti_3C_2 MXene solid-state film is 65.7 ± 6.0° for Ti_3C_2, which is consistent with the literature and suggests the hydrophilic character.[152] On the other hand, a water contact angle of 93.1 ± 2.9° is measured for Ti_3C_2-PEG6, Figure 4.5D (top), which suggests slightly more hydrophobic character due to covalent PEG6 attachment. Additionally, this change in surface chemistry can be further confirmed *via* aqueous phase zeta potential measurements (Figure 4.5E). As synthesized, pristine Ti_3C_2 MXene flakes shows a zeta potential of -30.1 ± 9.5 mV (data not shown) as would be expected from the hydrophilic surface with =O, –OH, and –F terminations, which is in agreement with the literature.[377] Our Ti_3C_2-PEG6 flakes display a zeta potential value of -20.8 ± 11.4 mV indicating the presence of the PEG6 chains (data not shown). These results are the additional confirmation representing that the surface of pristine Ti_3C_2 MXene flakes are successfully modified with PEG6 *via* the covalent esterification reaction.

As previously mentioned in the MXene literature, one of the important electronic properties of Ti_3C_2 MXene flakes is high electrical conductivity in solid films because of their metallic characteristic.[136, 378] One possible concern of grafting ligands to the MXene surface is that these ligands may alter their ability of moving electrical charges across the inter-flake space either due to change in inter-flake distance and/or electrical conductivity properties of the ligands. As stated earlier, PEGs are important ligands, because of their ability to transport charges. In order to investigate the effects of electrically conductive PEG6 ligand modification on the electrical conductivity of films of Ti_3C_2 flakes, we further investigated the electrical conductivity of vacuum-filtered films of Ti_3C_2-PEG6 flakes. We determined that vacuum-filtered films of Ti_3C_2-PEG6 flakes show an electrical conductivity of 16,200 ± 2,100 S cm^{-1} (Figure 4.5F), which is slightly lower than pristine Ti_3C_2 MXene flakes of 19,400 ± 2,100 S cm^{-1}. Large standard deviations in our conductivity value could be resulted from the error of measuring film thickness using ImageJ software from cross sectional SEM analyses (Figure 4.8). The use of excess-aluminum route for the synthesis of Ti_3AlC_2 MAX phase is shown to give the most stable $Ti_3C_2T_x$ with one of the highest electrical conductivity values reported for the pristine vacuum-filtered $Ti_3C_2T_x$ film.[136] Overall, our measurements indicate a small (~16%) reduction in electrical conductivity after PEG6 modification. This decrease is minimal due to the electronic nature of the PEG ligand and a result of the low molecular weight of the polymer (average 350 g/mol) and incomplete surface coverage (~14% by mass). The low molecular weight polymer and incomplete surface coverage provides low resistivity and allows the PEG ligand to be disoriented (wet noodle-type structure) on the surface and minimize the increase in inter-flake distance. In contrast, covalent surface modification of pristine Ti_3C_2 MXene flakes with alkylphosphonic acid resulted in 85% decrease in conductivity, which could be due to the insulating nature of aliphatic alkyl chains.[151]

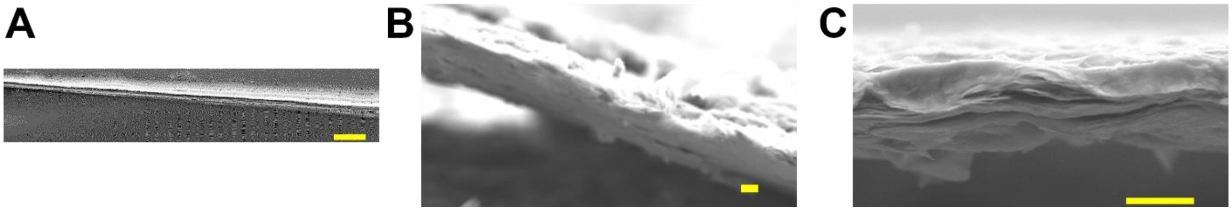

Figure 4.7: SEM cross sections of (A) pristine Ti_3C_2 (B) Ti_3C_2-PEG6 and (C) Li^+@ Ti_3C_2-PEG6 used to calculate height for conductivity calculation. The scale bars are 10 µm.

After establishing the small loss in conductivity after PEG6 grafting on Ti_3C_2 flakes, we next sought methods of reviving some of the lost electrical conductivity of these films. Oxygen-containing ethylene glycol unit in PEGs have the ability to interact with electrolyte cations, which is a beneficial factor in evaluating solid-state conductivity of nanomaterials.[379-382] Based on this previous literature, we hypothesized that the interaction between O atoms and electrolyte cations would further increase the conductivity of our Ti_3C_2-PEG6 flakes. To evaluate this hypothesis, Ti_3C_2-PEG6 flakes were dispersed in a 0.2 M $CHCl_3$ solution of lithium perchlorate ($LiClO_4$) and stirred for 18 h. The solid was collected *via* centrifugation and then redispersed in $CHCl_3$, and finally vacuum filtered on an alumina membrane to create a free-standing film (Li^+@ Ti_3C_2-PEG6). The film was used for resistance measurement using a four-probe method as similar to previous measurements described above. The resulting film conductivity is 18,000 ± 2,400 S cm^{-1}, a near 11% increase over Ti_3C_2-PEG6 films and only ~7% decrease from pristine Ti_3C_2 films, which makes PEG6 grafting a competitive candidate for covalent surface modification of Ti_3C_2 with ligands without severe effects on the electrical conductivity in thin-film applications.

4.3.3 Structural Characteristic of Ti_3C_2-PEG6 Thin-Films.

After establishing the solution stability and conductivity of the MXene films, we next sought to analyze the effects of PEG6 on the structure of Ti_3C_2 MXene films. The addition of surface

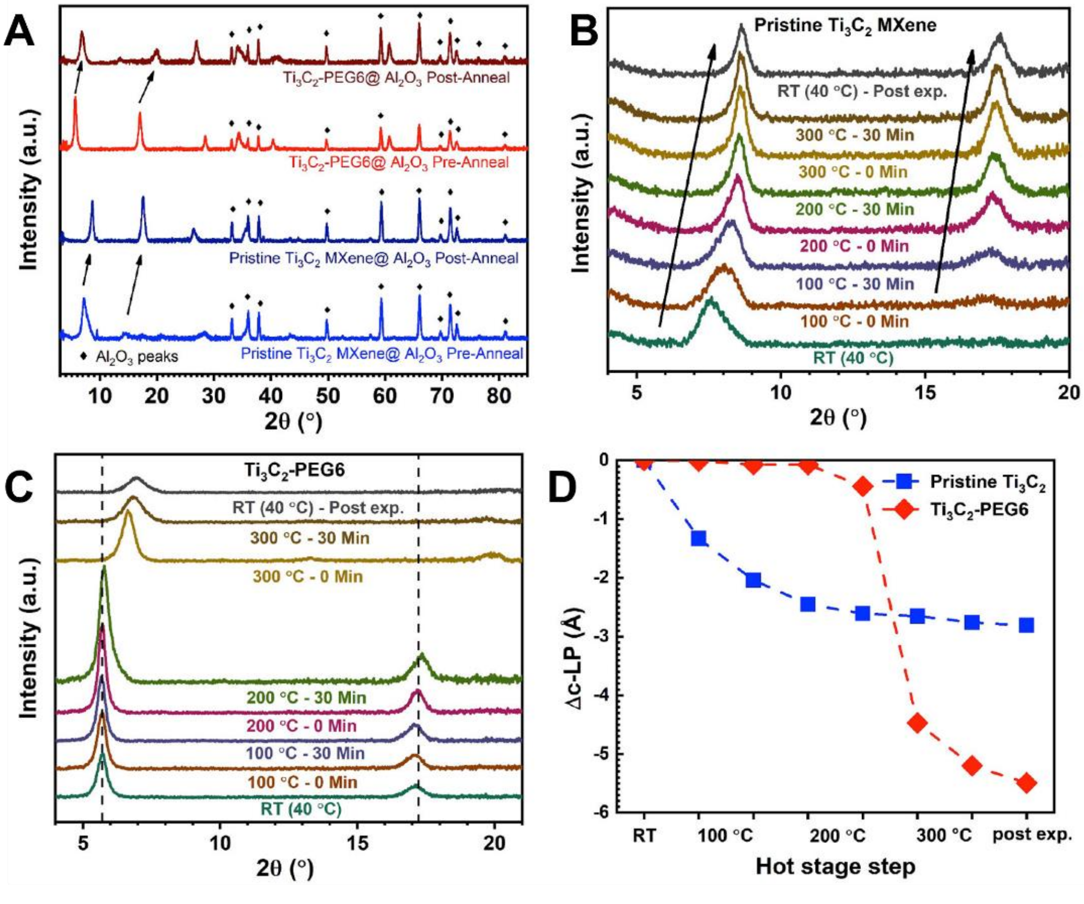

Figure 4.8: (A) Hot stage XRD data showing changes of pre- and post-annealed films of Ti_3C_2-PEG6 vs. pristine Ti_3C_2 MXene. Arrows show the shift in peak position of the basal plane (002) and (004) peaks of each Ti_3C_2 film upon annealing. The diamond marked peaks arise from the Al_2O_3 substrate and are not characteristic of the Ti_3C_2 MXene films. (B) Expanded XRD data with y-axis offset of Ti_3C_2 MXene shift in peak position of the basal plane (002) and (004) peaks of Ti_3C_2 during annealing. (C) Expanded XRD data with y-axis offset of Ti_3C_2-PEG6 shift in peak position of the basal plane (002) and (004) peaks of Ti_3C_2 during annealing. (D) The graph showing changes in the c-lattice parameter during annealing of Ti_3C_2-PEG6 vs. pristine Ti_3C_2 MXene.

elements or ligands to any nanostructure, especially 2D materials, often causes possible distortions to the material lattice along with changes to their layering when assembled that must be evaluated.[177, 237] The influence of PEG6 ligands on the lattice and inter-flake stacking of Ti_3C_2 MXene flakes was studied by in-situ hot-stage XRD analysis (Figure 4.9). This type of analysis has previously been used to gain a detail understanding of the crystal phase transformation in pristine Ti_3C_2 MXenes;[373] however, in our case it is a useful tool to investigate the impact of PEG6 ligands on inter-flake structural properties. Films of both pristine Ti_3C_2 MXene flakes and Ti_3C_2-PEG6 flakes were prepared on Al_2O_3 membrane substrates (Figure 4.10) and scans (2θ = 5-80°) were performed before and after all annealing steps were complete in addition to lower angle scans (2θ = 5-20°) at each temperature increase step. Figure 4.9A features the comparison of pre- and post-annealed films. Based on the diffraction pattern shown in Figure 4.9A, it is necessary to point out that the XRD spectra are in excellent agreement with the previously discussed data as there is an absence of oxidation of both pre-annealed pristine Ti_3C_2 and Ti_3C_2-PEG6.

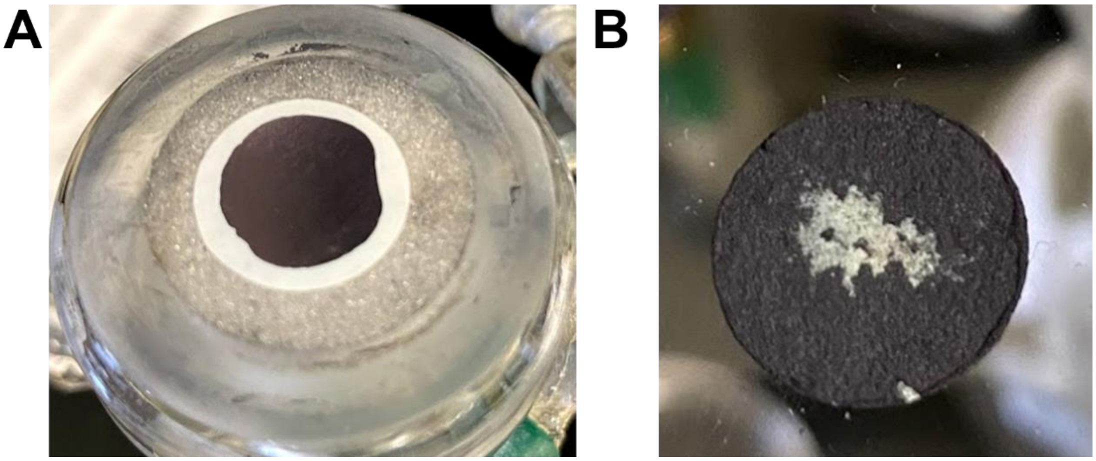

Figure 4.9: Vacuum filtered prepared films of (A) pristine Ti_3C_2 and (B) Ti_3C_2-PEG6 on alumina membrane substrate. Later used for hot stage XRD analysis. XRD analysis taken on location where good film was formed.

The absence of a peak near 25° 2θ, which would appear if TiO2 is formed, in the XRD analysis confirms there is no oxidation of Ti_3C_2-PEG6 flakes.[383] Distinctly present in both pre-annealed samples are the basal plane (002) peaks below 8.5° 2θ and typical Ti3C2 in-plane peaks at ~41° and ~61°.[373] The (002) plane of Ti_3C_2-PEG6 flakes is located at a lower 2θ (5.6°) than that of Ti3C2 MXene flakes (7.2° 2θ), which indicates a slightly longer center-to-center inter-flake distance for Ti_3C_2-PEG6 (~1.55 nm) than that of Ti_3C_2 (~1.16 nm) in the pre-annealed films. The changes in the center-to-center inter-flake distances during the in-situ hot-stage XRD analysis (Figure 4.11) were calculated from the c-lattice parameter and the unit cell for Ti3C2 MXenes. This longer inter-flake separation in Ti3C2-PEG6 compared to pristine Ti3C2 supports the inclusion of PEG6 ligands, which have hydrodynamic radii of ~0.6 nm, between the individual 2D Ti3C2 flakes.

To further test the self-assembly and highlight the facile processability of Ti_3C_2-PEG6 flakes we drop-casted thin-films of Ti_3C_2-PEG6 in $CHCl_3$ and pristine Ti_3C_2 in water onto a silicon wafer and the solvent was then allowed to evaporate under ambient conditions. Figure 4.12A and 4.12B schematically illustrate the modification of Ti_3C_2 MXene with PEG6 ligands in the process of the formation of Ti_3C_2-PEG6 stacked structures. A cross sectional SEM image of drop casted Ti_3C_2-PEG6 microstructure film is shown in Figure 4.12C. XRD analysis of this naturally evaporated film (Figure 4.12D) shows a sharp (002) diffraction peak along with other subtle (00*L)* peaks and an absence of any out of plane peaks. This diffraction pattern is very similar to the results we observed previously in pre-annealed vacuum filtered films (Figure 4.9A). The (002) diffraction

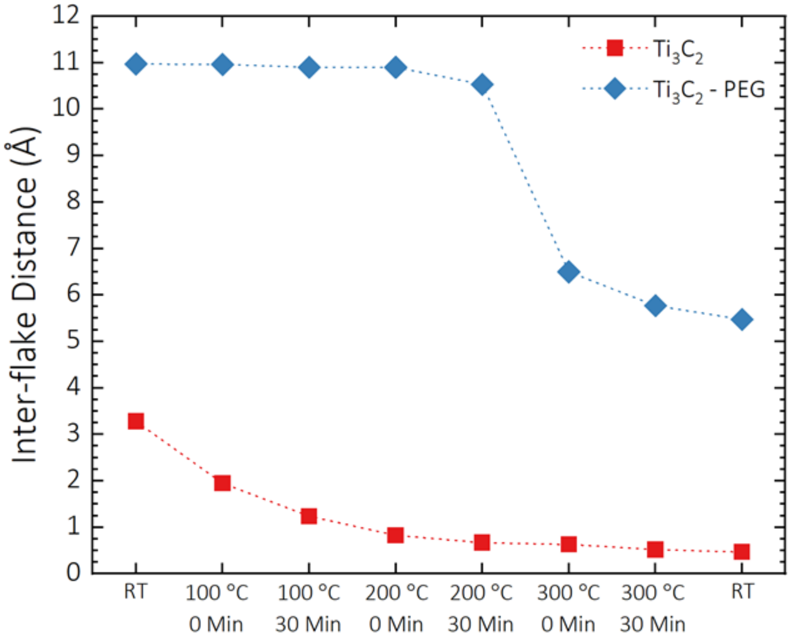

Figure 4.10: Graph of inter-flake distance between vacuum filtered films of pristine Ti_3C_2 MXene (red) and modified Ti_3C_2-PEG6 MXenes (blue) calculated using the c-lattice parameter obtained from the hot-stage XRD experiment and a theoretical Ti_3C_2 unit cell dimension.

peak is clearly observed. Importantly, the FWHM of (002) diffraction peak is narrower in Ti_3C_2-PEG6 than Ti_3C_2 MXene indicating improved ordering throughout the film in the former case.

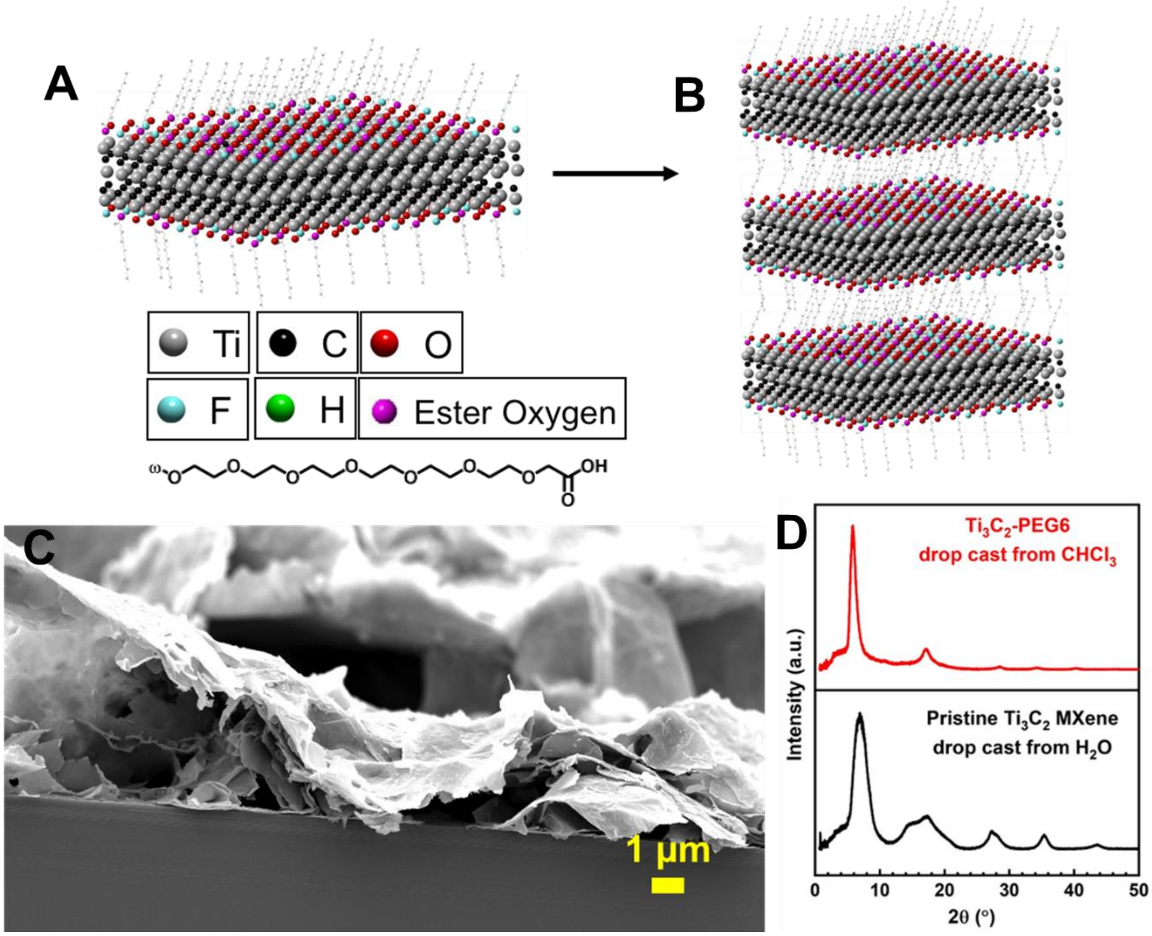

Figure 4.11: (A) Schematic representation of the crystal structure of Ti_3C_2-PEG6 single flake and (B) stacked Ti_3C_2-PEG6 flakes through cooperative ligand-ligand hydrophobic and vdWs interactions. (C) A representative cross sectional SEM image of drop casted Ti_3C_2-PEG6 flakes on the silicon wafer substrate. Scale bar is 100 nm. (D) XRD spectrum of Ti_3C_2-PEG6 after drop casting flakes flowed by solvent evaporation under ambient conditions. The XRD spectrum of drop cast pristine Ti_3C_2 MXene flakes dispersed in water.

4.3.4 Introducing Chemical Functionality (“Valance”) onto Ti_3C_2 MXene Flakes.

Beyond the synthesis of Ti_3C_2-PEG6 flakes, our surface modification approach method can be used to introduce end-terminal functional groups on pristine Ti_3C_2 MXenes. Taking the advantage of our Ti_3C_2-PEG6 synthesis, heterofunctional PEG6 ligands in which PEG6-COOH bearing additional chemically active functional group including amine ($-NH_2$), azide ($-N_3$), and alkene (-CH=CH2) on the opposite terminus of the ester bond (ω-PEG6-COOH, where ω = $-NH_2$, $-N_3$, $-CH=CH_2$) were used for the covalent surface modification (Figure 4.13). The $–N_3$ and $-CH=CH_2$ functional groups allow further chemical modification of MXene flakes *via* “click chemistry” and “cross metathesis”,[384] respectively. Whereas $–NH_2$ group can be successfully utilized to attach any molecules (small organic compounds, large polymers, and biomolecules) *via* amide bond formation. Therefore, these additional reactive sites will allow for covalent incorporation of our MXene materials in devices as composite materials and coatings.[385-386]

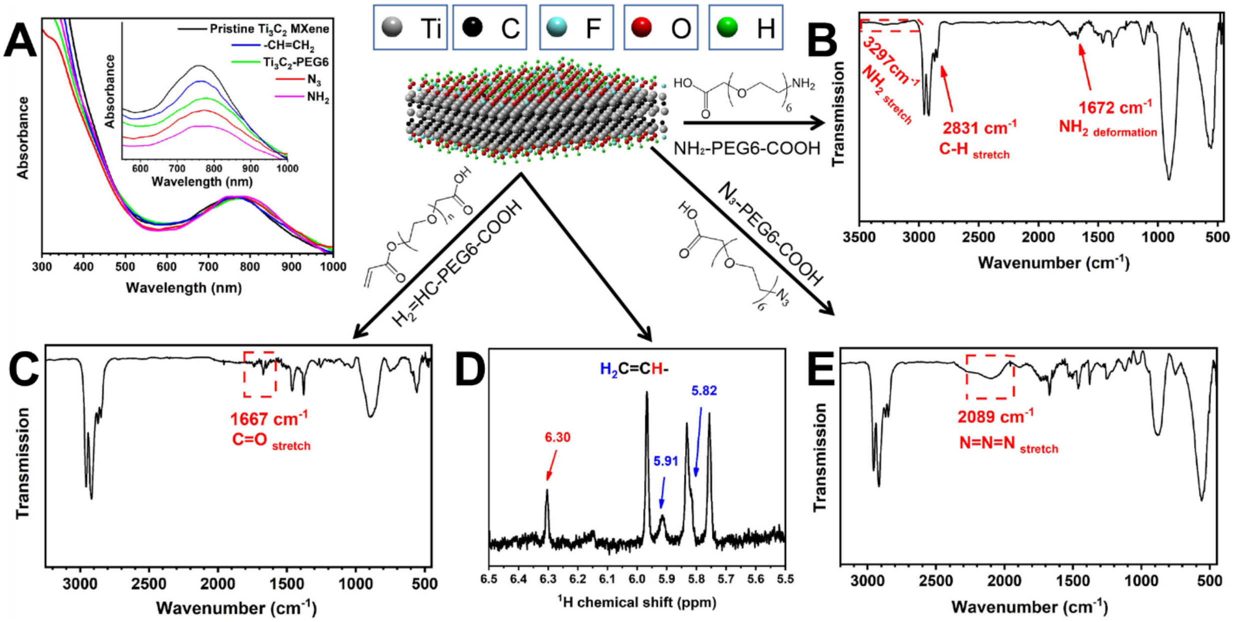

Figure 4.12: (A) UV-vis spectra of four terminal groups $–CH_3$ (Ti_3C_2-PEG6), $-CH=CH_2$, $-N_3$, $-NH_2$ and unfunctionalized pristine Ti_3C_2 MXene. (B) FTIR spectrum of Ti_3C_2-PEG6-NH_2 with important NH_2-related vibrational stretched shown with arrows. (C) FTIR spectrum of Ti_3C_2-PEG6-$CH=CH_2$ with the carbonyl group (-C=O) identified in the red dotted box. (D) Expanded region of ^1H NMR spectrum of Ti_3C_2-PEG6-$CH=CH_2$ showing alkene ($-CH=CH_2$) region chemical shifts. (E) FTIR spectrum of Ti_3C_2-PEG6-N_3 with azide ($-N_3$) related stretch identified in the red dotted box.

ω-PEG6-modified Ti_3C_2 MXenes show good solubility in non-polar organic solvents, and no major changes in the optical spectra are detected. Specifically, no significant UV-vis absorption peak shifts are observed, suggesting the lack of oxidation (Figure 4.13A). This result is in agreement with our previous data. Further spectroscopy analyses were conducted to ensure the terminal functional groups remained intact under our reaction conditions. FTIR analysis was conducted to confirm that the amine group in Ti_3C_2-PEG6-NH_2 is unaffected during the surface modification. As illustrated in Figure 4.13B, the appearance of a N-H related deformation stretch at 1672 cm^{-1}, broad N-H stretch at 3297 cm^{-1} (red box) and new C-H stretch at 2831 cm^{-1} are observed. Ti_3C_2-PEG6-CH=CH$_2$ were characterized by ^{1}H and FTIR spectroscopic techniques. The FTIR spectrum reveals a new carbonyl stretch at 1667 cm^{-1}, which is assigned to the acetyl carbonyl (Figure 4.13C). As shown in Figure 4.13D, ^{1}H NMR spectrum shows chemical shifts at 6.30, 5.91 and 5.81 ppm that are assigned to terminal double bond protons. Finally, Ti_3C_2-PEG6-N_3 were analyzed by FTIR that shows the presence of an N=N=N stretch 2089 cm^{-1} (Figure 4.13E).[236] Overall, the collective results presented in Figure 5 verify that our optimized covalent surface modification approach allows incorporation of further chemically reactive functionality on the surface of Ti_3C_2 MXenes through the use of heterofunctional PEG6 ligands. Overall, our demonstrated chemistry should be applicable to other non-titanium MXene types including molybdenum carbides[139] and double transition metal based MXenes (*e.g.*, magnetic[387] and high entropy MXenes[388]) containing hydroxyl T_x surface terminations.

4.4 Conclusion

In summary, we have developed an esterification chemistry to covalently attach PEG6-COOH to $Ti_3C_2T_x$ MXene flakes without any negative oxidation events as confirmed by the Raman analysis. Temperature dependent analyses (*i.e.,* hot-stage in-situ XRD and TGA) along with FTIR spectroscopy characterizations provide conclusive evidence of covalent attachment of PEG6 ligands. This method has allowed a high loading of PEG6 ligands (~14% by mass) onto the surface of Ti_3C_2 MXene flakes that resulted in a significant improvement in their dispersibility in a wide range of both polar and non-polar organic solvents with a high concentration (2.88 mg/mL in $CHCl_3$). PEG6 ligands, through constructive ligand-ligand hydrophobic and vdWs interactions, also improve the uniform stacking of thin films both by drop casting and vacuum filtering methods without the need for annealing to remove solvent molecules. We have achieved these benefits without significantly compromising the electrical conductivity of the Ti_3C_2 MXene, maintaining conductivities over 16,000 S cm^{-1}. Additionally, FTIR and ^{1}H NMR analyses clearly support ω-functionalized PEG6 ligand (ω: -NH$_2$, -N$_3$, -CH=CH$_2$) attachment onto the surface of MXenes resulting in the successful addition of chemical functionalities (incorporation of valency), to Ti_3C_2 MXene materials. Taken together, these surface modifications and the possibility of tuning surface functionalities of MXenes provide knowledge and mechanisms to create widely dispersible, biocompatible, and reactive 2D MXene flakes with high precision over their surface chemistry for enhanced use in future applications.

4.5 Experimental Section

4.5.1 Materials.

Chloroform ($CHCl_3$, >99%), dichloromethane (DCM, 99.5%), toluene (99.9%), methanol (MeOH, 99.9%) were purchased from Fisher. Acetonitrile (ACN, 99.8%), N,N-dimethylformamide (DMF, 99.8%), 4-(dimethylamino) pyridine (DMAP, ≥98.0%), methoxy polyethylene glycol 350 (>99%), succinic anhydride (>99%), and triethylamine (TEA, >99%) were purchased from Sigma-Aldrich. 1,4 dioxane (99.8%) was purchased from Alfa-Aesar. Isopropanol (99%) was purchased from Pharmco, and dicylcohexylcarboiimide (DCC, 99%) was purchased from Acros Ogranics. NH_2-PEG6-COOH, CH_2=CH-PEG6-COOH, and N_3-PEG6-COOH were purchased from Biochempeg. CH_3-PEG6-COOH was synthesized in the laboratory according to published procedure (see Supporting Information).[389] All solvents were used without further purification.

4.5.2 $Ti_3C_2T_x$ MXene Synthesis.

$Ti_3C_2T_x$ MXene flakes used in this study were prepared from its MAX phase precursor Ti_3AlC_2 through selective etching followed by delamination processes as described in the literature.[373] Briefly, the Ti_3AlC_2 MAX phase precursor was prepared from a powder mixture of TiC, Ti, and Al in the mass ratio of 2:1:1 followed by reactive sintering at 1415 °C for 2 h under Ar flow.[136] The $Ti_3C_2T_x$ MXene was prepared from the Ti_3AlC_2 MAX phase precursor *via* selective etching of 4.0 g of Ti_3AlC_2 in 12 mL HF (50 wt%, Millipore Sigma), 72 mL HCl (12 M, Millipore Sigma), and 36 mL of deionized water for 24 h at 35 °C. After etching, the multilayer $Ti_3C_2T_x$ powder was repeatedly washed with water until the pH of the solution was greater than 6.0. After acid neutralization, the multilayer powder was then delaminated with 4.0 g of anhydrous LiCl (Acros Organics) in 200 mL deionized water at 65 °C stirred at 600 RPM for 1 h under Ar flow. After delamination, the solution was repeatedly washed with deionized water before final centrifugation at 2380 RCF for 30 min to yield an aqueous solution comprised of single-flakes of $Ti_3C_2T_x$ MXenes.

4.5.3 Ti_3C_2-PEG6 Synthesis.

$Ti_3C_2T_x$ in H_2O was transferred to DMF *via* solvent exchange transferring 1.25 mg Ti_3C_2 into a 1.5 mL centrifuge tube and adding 0.5 mL IPA before shaking and centrifuging at 13400 rpm for 15 min. The supernatant was decanted and 1.0 mL DMF was added. The pellet was redispersed *via* bath sonication and centrifuged again. This DMF addition step was repeated twice more. The pellet was redispersed in 1.0 mL DMF, and then UV-vis spectra were collected in the absorption mode for quality assurance purposes. The pristine Ti_3C_2 MXene in DMF was added to a 100 mL round bottom flask along with ~1.5 mmol PEG6-COOH and 0.15 mmol DMAP. Small amounts of DMF were used to wash all the centrifuge tubes so the total amount of DMF did not exceed 8.0 mL. The reaction mixture was stirred in an ice bath for 5 min and then and 0.15 mmol DCC dissolved in 15 mL $CHCl_3$ was added to the reaction *via* drop funnel over 5 min under N_2. The round bottom flask was placed under N_2 and allowed to run overnight with vigorous stirring. The product was placed in a 50 mL centrifuge tube and centrifuged for 10 min at 10,000 rpm. The supernatant was decanted and 5 mL of $CHCl_3$ was added to redisperse the product *via* bath sonication. This washing step was repeated additional 3 times. The product was stored as $CHCl_3$ dispersion under ambient conditions.

4.5.4 Characterization. .

Conductivity of $Ti_3C_2T_x$ and $Ti_3C_2T_x$-PEG films was determined using a four-point probe method. Approximately 0.5 mL $CHCl_3$ (1.0 mg/mL concentration) solution was drop-casted on an anodic alumina membrane substrate and followed by vacuum-assisted filtration to prepare a thin film. After filtration, these thin films were dried on the membrane in a vacuum oven at 100 °C overnight to remove any residual solvents. After drying, these films were tested with a Keithley 2400 SourceMeter paired with 4 electrodes which were spaced in an equidistant 1 cm x 1 cm square to determine the resistance values. To calculate conductivity from resistance values, the film thickness was determined from the cross-sectional SEM analysis. TGA data of pure PEG6-COOH, Ti_3C_2 MXene and Ti_3C_2-PEG6 were collected *via* drop-casting of each respective solution into an alumina crucible followed by drying at 100 °C in a vacuum oven for 1 h. This drop-casting and drying process was repeated until the total solid mass was roughly 10 - 20 mg in the alumina crucible. The crucibles were stored in a vacuum environment until analysis. TGA experiments were conducted using a TA Q600 simultaneous thermal analyzer, which was tared using a blank alumina crucible with an alumina lid before running. The TGA experiment was conducted by covering the alumina crucible containing the sample with an alumina lid and ramping up to 800 °C at a ramp rate of 3.5 °C/min under a 50 mL/min Ar (99.998% purity) flow. UV-vis absorption spectra were collected using a Varian-Cary 50 Scan UV-visible spectrophotometer over a range of 300-1000 nm of the dispersion using a 1 cm x 1 cm quartz cuvette using the respective solvent as background. ^{1}H NMR spectra were recorded on a Bruker Avance III 500 instrument at 500 MHz frequency with 750 scans using $CDCl_3$ as solvent. Fourier transform infrared (FTIR) spectra were collected using a Thermo Scientific Nicolet iS10 spectrometer and analyzed using Omnic 8.2 software package with air atmosphere as the background. Samples were drop cast from $CHCl_3$ onto a 4 mm KBr plate and dried in 60 °C oven before collecting 100 scans with a 64-scan background in ambient atmosphere. Raman spectroscopy was conducted on samples drop cast on silicon substrates using a XploRA Plus Raman Microscope from Horiba Scientific. A 785 nm laser at 25% power, 1800 line/mm grating and 100x objective were used to collect spectra with an acquisition time of 1 second and 3 to 5 accumulations. Contact angle images were obtained on a ramé-hart 150 w Fiber Optic Illuminator using DropImage Standard software. Samples were prepared by dropping 2 μL of nanopure water on a drop cast sample film that had been dried overnight in a 100 °C vacuum oven. X-ray diffraction (XRD) analyses were conducted on a Bruker D8 Discover X-ray diffractometer (Cu Kα, $\lambda = 1.54$ Å) using a 2D VÅNTEC-500 detector. Full spectra were obtained of drop cast films from 5-75° 2θ with 5° 2θ steps and 60 s/step acquisition times. Hot stage XRD analysis was conducted using Parr DHS 1100 domed hot stage where samples were vacuum filtered on alumina membrane (~20 nm pore size) before being secured onto hot stage and placed under flowing Ar atmosphere (~50 MPa). Full scans were run before and after annealing without graphite dome as described above with an acquisition time of 20 s/step. Annealing was done in 3 steps from 40 °C to 100 °C to 200 °C to 300 °C before cooling back to 40 °C. Spectra were obtained from 5-10° 2θ in 5° 2θ steps with a scan rate of 60 s/step immediately after temperature was reached and after sustaining the temperature for 30 min. The temperature was immediately ramped at a rate of 60 °C/min after the 30 min scan. Zeta potential measurements were conducted in water on a Nano XS90 Zetasizer from Malvern Panalytical Inc. using 12 zeta runs at ambient temperatures. TEM images were obtained using a Tecnai G2 12 Bio Twin instrument equipped with AMT CCD Camera operating at 120 kV. Samples were prepared in either water (Ti_3C_2) or chloroform (Ti_3C_2-PEG6) and 10 μL of the dispersion was drop-casted onto formvar or carbon-coated copper TEM grids (Electron Microscopy Sciences). Samples were allowed to sit for 10 seconds before any excess solvent was wicked away with filter paper. SEM cross section images were obtained using a JEOL 7800f field-emission SEM microscope with an acceleration voltage of 15 keV.

CHAPTER 5. CONCLUDING REMARKS

The work described herein highlights how the surface chemistries of a variety of 2D nanomaterials impacted their morphologies, optoelectronic responses, and physicochemical properties. Through the development of colloidal surface ligation techniques, we were able to expand the processibility and applicability of halide perovskites, transition metal oxides, and MXenes. These represent three very important disparate classes of materials that cover a vast range of important technologies that impact catalysis, energy harvesting and storage, sensing, and nanocomposites. Specifically, we were able to: 1) synthesize 2D lead free halide perovskite nanosheets in the quasi-Ruddlesden Popper phase; 2) investigate how surface trap state passivation in WO_{3-x} could be used to maximize N_e providing new methods to more accurately model LSPR responses in semiconductor NCs; and 3) alter the surface passivation of MXenes through covalent attachment of PEG6 ligands increasing their processibility in a wide range of non-polar solvents while also positively influencing the assembly of microstructure films.

Chapter 1 introduced the burgeoning field of 2D nanomaterials by describing their various compositions, electronic structures, and how surface chemistry impacts important morphological, optoelectronic, and physicochemical properties. Throughout this dissertation we focused on how the undercoordinated atoms at the surface of these materials are manipulated through surface ligand chemistry to alter these properties. Chapter 2 concentrated on using in-situ ligand engineering to control the morphology of bismuth-based halide perovskites. Through careful control of inorganic precursors and long chain aliphatic ligands we were able to insert amino head groups into the A site of the $Cs_3Bi_2X_9$ perovskite crystal structure to cause the formation of quasi-Ruddlesden Popper growth. Additionally, we demonstrated how ligand-ligand interactions could be utilized to alter the mesophase assembly which has important implications for overall applicability.

The knowledge of surface passivation of QDs in improving optoelectronic properties was applied to plasmonic 2D WO_{3-x} NPLs in Chapter 3. Through careful vibrational spectroscopic characterization of the bonding motif, coupled with electron paramagnetic resonance spectroscopy, we were able to determine that surface trap state passivation is necessary to maximize free carrier participation in the LSPR response. These analyses, along with redox titration of the NPLs, further highlighted the inaccuracies of applying the Drude model to semiconductor nanomaterials providing a means to increase the fundamental understanding of free carrier dynamics. In the future this will allow a much better material development of plasmonic TMOs catalytic, sensing, and SERS applications.

Lastly, Chapter 4 demonstrated the chemical transformation of the MXene surface through covalent attachment of PEG6 ligands. This modification greatly improved the dispersibility of MXenes into a wide range of non-polar solvents, thus drastically increasing their utility in future applications requiring more hydrophobic interfaces. Considering the recent discovery of MXenes (2011) and numerous potential applications for this material, expanding their surface chemistry "toolbox" is essential.

Overall, this dissertation provides information for the effective use of surface chemistry in a variety of 2D nanomaterial compositions. The work describes a variety of surface chemistry applications to overcome the unique challenges presented by each of the chosen materials which represent three critical fields of 2D nanomaterials. The knowledge gained will allow for the effective use of these 2D materials, and newly discovered compositions, in a wide variety of applications necessary for next generation technologies.

REFERENCES

1. Feynman, R. P., There's Plenty of Room at the Bottom. *Engineering and Science* **1960,** *23* (5), 22-36.
2. Brus, L. E., Electron–Electron and Electron-Hole Interactions in Small Semiconductor Crystallites: The Size Dependence of the Lowest Excited Electronic State. *The Journal of Chemical Physics* **1984,** *80* (9), 4403-4409.
3. Ekimov, A. I.; Efros, A. L.; Onushchenko, A. A., Quantum Size Effect in Semiconductor Microcrystals. *Solid State Communications* **1993,** *88* (11), 947-950.
4. Novoselov, K. S.; Geim, A. K.; Morozov, S. V.; Jiang, D.; Zhang, Y.; Dubonos, S. V.; Grigorieva, I. V.; Firsov, A. A., Electric Field Effect in Atomically Thin Carbon Films. *Science* **2004,** *306* (5696), 666-9.
5. Zhang, H., Ultrathin Two-Dimensional Nanomaterials. *ACS Nano* **2015,** *9* (10), 9451-69.
6. Liu, B.; Abbas, A.; Zhou, C., Two-Dimensional Semiconductors: From Materials Preparation to Electronic Applications. *Advanced Electronic Materials* **2017,** *3* (7), 1700045.
7. Hu, S.; Zhu, M., Ultrathin Two-Dimensional Semiconductors for Photocatalysis in Energy and Environment Applications. *ChemCatChem* **2019,** *11* (24), 6147-6165.
8. Zeng, M.; Xiao, Y.; Liu, J.; Yang, K.; Fu, L., Exploring Two-Dimensional Materials toward the Next-Generation Circuits: From Monomer Design to Assembly Control. *Chem Rev* **2018,** *118* (13), 6236-6296.
9. Chen, Y.; Fan, Z.; Zhang, Z.; Niu, W.; Li, C.; Yang, N.; Chen, B.; Zhang, H., Two-Dimensional Metal Nanomaterials: Synthesis, Properties, and Applications. *Chem Rev* **2018,** *118* (13), 6409-6455.
10. Tan, C.; Cao, X.; Wu, X. J.; He, Q.; Yang, J.; Zhang, X.; Chen, J.; Zhao, W.; Han, S.; Nam, G. H.; Sindoro, M.; Zhang, H., Recent Advances in Ultrathin Two-Dimensional Nanomaterials. *Chem Rev* **2017,** *117* (9), 6225-6331.
11. Bhimanapati, G. R.; Lin, Z.; Meunier, V.; Jung, Y.; Cha, J.; Das, S.; Xiao, D.; Son, Y.; Strano, M. S.; Cooper, V. R.; Liang, L.; Louie, S. G.; Ringe, E.; Zhou, W.; Kim, S. S.; Naik, R. R.; Sumpter, B. G.; Terrones, H.; Xia, F.; Wang, Y.; Zhu, J.; Akinwande, D.; Alem, N.; Schuller, J. A.; Schaak, R. E.; Terrones, M.; Robinson, J. A., Recent Advances in Two-Dimensional Materials Beyond Graphene. *ACS Nano* **2015,** *9* (12), 11509-11539.
12. Rao, C. N. R.; Sood, A. K.; Subrahmanyam, K. S.; Govindaraj, A., Graphene: The New Two-Dimensional Nanomaterial. *Angewandte Chemie International Edition* **2009,** *48* (42), 7752-7777.
13. Naguib, M.; Gogotsi, Y., Synthesis of Two-Dimensional Materials by Selective Extraction. *Accounts of Chemical Research* **2015,** *48* (1), 128-135.

14. Cai, Z.; Liu, B.; Zou, X.; Cheng, H. M., Chemical Vapor Deposition Growth and Applications of Two-Dimensional Materials and Their Heterostructures. *Chem Rev* **2018,** *118* (13), 6091-6133.

15. Nasilowski, M.; Mahler, B.; Lhuillier, E.; Ithurria, S.; Dubertret, B., Two-Dimensional Colloidal Nanocrystals. *Chemical Reviews* **2016,** *116* (18), 10934-10982.

16. Jin, H.; Guo, C.; Liu, X.; Liu, J.; Vasileff, A.; Jiao, Y.; Zheng, Y.; Qiao, S. Z., Emerging Two-Dimensional Nanomaterials for Electrocatalysis. *Chem Rev* **2018,** *118* (13), 6337-6408.

17. Allen, M. J.; Tung, V. C.; Kaner, R. B., Honeycomb Carbon: A Review of Graphene. *Chemical Reviews* **2010,** *110* (1), 132-145.

18. Novoselov, K. S.; Geim, A. K.; Morozov, S. V.; Jiang, D.; Katsnelson, M. I.; Grigorieva, I. V.; Dubonos, S. V.; Firsov, A. A., Two-Dimensional Gas of Massless Dirac Fermions in Graphene. *Nature* **2005,** *438* (7065), 197-200.

19. Guo, N.; Yam, K. M.; Zhang, C., Substrate Engineering of Graphene Reactivity: Towards High-Performance Graphene-Based Catalysts. *npj 2D Materials and Applications* **2018,** *2* (1), 1.

20. Choi, J. H.; Lee, J.; Byeon, M.; Hong, T. E.; Park, H.; Lee, C. Y., Graphene-Based Gas Sensors with High Sensitivity and Minimal Sensor-to-Sensor Variation. *ACS Applied Nano Materials* **2020,** *3* (3), 2257-2265.

21. Qiao, Y.; Li, X.; Jian, J.; Wu, Q.; Wei, Y.; Shuai, H.; Hirtz, T.; Zhi, Y.; Deng, G.; Wang, Y.; Gou, G.; Xu, J.; Cui, T.; Tian, H.; Yang, Y.; Ren, T.-L., Substrate-Free Multilayer Graphene Electronic Skin for Intelligent Diagnosis. *ACS Applied Materials & Interfaces* **2020,** *12* (44), 49945-49956.

22. Chen, B.; Wang, D.; Zhang, B.; Zhong, X.; Liu, Y.; Sheng, J.; Zhang, Q.; Zou, X.; Zhou, G.; Cheng, H.-M., Engineering the Active Sites of Graphene Catalyst: From Co2 Activation to Activate Li-Co2 Batteries. *ACS Nano* **2021,** *15* (6), 9841-9850.

23. Sarker, F.; Karim, N.; Afroj, S.; Koncherry, V.; Novoselov, K. S.; Potluri, P., High-Performance Graphene-Based Natural Fiber Composites. *ACS Applied Materials & Interfaces* **2018,** *10* (40), 34502-34512.

24. Molaei, M. J.; Younas, M.; Rezakazemi, M., A Comprehensive Review on Recent Advances in Two-Dimensional (2d) Hexagonal Boron Nitride. *ACS Applied Electronic Materials* **2021,** *3* (12), 5165-5187.

25. Dean, C. R.; Young, A. F.; Meric, I.; Lee, C.; Wang, L.; Sorgenfrei, S.; Watanabe, K.; Taniguchi, T.; Kim, P.; Shepard, K. L.; Hone, J., Boron Nitride Substrates for High-Quality Graphene Electronics. *Nature Nanotechnology* **2010,** *5* (10), 722-726.

26. Zhi, C.; Bando, Y.; Tang, C.; Kuwahara, H.; Golberg, D., Large-Scale Fabrication of Boron Nitride Nanosheets and Their Utilization in Polymeric Composites with Improved Thermal and Mechanical Properties. *Advanced Materials* **2009,** *21* (28), 2889-2893.

27. Li, L. H.; Xing, T.; Chen, Y.; Jones, R., Boron Nitride Nanosheets for Metal Protection. *Advanced Materials Interfaces* **2014,** *1* (8), 1300132.

28. Li, B.; Lai, C.; Zeng, G.; Huang, D.; Qin, L.; Zhang, M.; Cheng, M.; Liu, X.; Yi, H.; Zhou, C.; Huang, F.; Liu, S.; Fu, Y., Black Phosphorus, a Rising Star 2d Nanomaterial in the Post-Graphene Era: Synthesis, Properties, Modifications, and Photocatalysis Applications. *Small* **2019,** *15* (8), 1804565.

29. Ling, X.; Wang, H.; Huang, S.; Xia, F.; Dresselhaus, M. S., The Renaissance of Black Phosphorus. *Proceedings of the National Academy of Sciences* **2015,** *112* (15), 4523-4530.

30. Kocaarslan, A.; Eroglu, Z.; Yilmaz, G.; Metin, O.; Yagci, Y., Expanding the Scope of 2d Black Phosphorus Catalysis to the near-Infrared Light Initiated Free Radical Photopolymerization. *ACS Macro Letters* **2021,** *10* (6), 679-683.

31. Xia, Y.; Xiong, Y.; Lim, B.; Skrabalak, S. E., Shape-Controlled Synthesis of Metal Nanocrystals: Simple Chemistry Meets Complex Physics? *Angewandte Chemie International Edition* **2009,** *48* (1), 60-103.

32. Halas, N. J., Plasmonics: An Emerging Field Fostered by Nano Letters. *Nano Letters* **2010,** *10* (10), 3816-3822.

33. Willets, K. A.; Duyne, R. P. V., Localized Surface Plasmon Resonance Spectroscopy and Sensing. *Annual Review of Physical Chemistry* **2007,** *58* (1), 267-297.

34. Mayer, K. M.; Hafner, J. H., Localized Surface Plasmon Resonance Sensors. *Chemical Reviews* **2011,** *111* (6), 3828-3857.

35. Martirez, J. M. P.; Bao, J. L.; Carter, E. A., First-Principles Insights into Plasmon-Induced Catalysis. *Annual Review of Physical Chemistry* **2021,** *72* (1), 99-119.

36. Kale, M. J.; Avanesian, T.; Christopher, P., Direct Photocatalysis by Plasmonic Nanostructures. *ACS Catalysis* **2014,** *4* (1), 116-128.

37. Lv, R.; Robinson, J. A.; Schaak, R. E.; Sun, D.; Sun, Y.; Mallouk, T. E.; Terrones, M., Transition Metal Dichalcogenides and Beyond: Synthesis, Properties, and Applications of Single- and Few-Layer Nanosheets. *Acc Chem Res* **2015,** *48* (1), 56-64.

38. Zhao, J.; Wang, J.; Chen, Z.; Ju, J.; Han, X.; Deng, Y., Metal Chalcogenides: An Emerging Material for Electrocatalysis. *APL Materials* **2021,** *9* (5), 050902.

39. Heine, T., Transition Metal Chalcogenides: Ultrathin Inorganic Materials with Tunable Electronic Properties. *Accounts of Chemical Research* **2015,** *48* (1), 65-72.

40. Han, J. H.; Kwak, M.; Kim, Y.; Cheon, J., Recent Advances in the Solution-Based Preparation of Two-Dimensional Layered Transition Metal Chalcogenide Nanostructures. *Chem Rev* **2018,** *118* (13), 6151-6188.

41. Son, J. S.; Wen, X. D.; Joo, J.; Chae, J.; Baek, S. I.; Park, K.; Kim, J. H.; An, K.; Yu, J. H.; Kwon, S. G.; Choi, S. H.; Wang, Z.; Kim, Y. W.; Kuk, Y.; Hoffmann, R.; Hyeon, T., Large-Scale Soft Colloidal Template Synthesis of 1.4 Nm Thick Cdse Nanosheets. *Angew Chem Int Ed Engl* **2009,** *48* (37), 6861-4.

42. Wang, F.; Wang, Y.; Liu, Y.-H.; Morrison, P. J.; Loomis, R. A.; Buhro, W. E., Two-Dimensional Semiconductor Nanocrystals: Properties, Templated Formation, and Magic-Size Nanocluster Intermediates. *Accounts of Chemical Research* **2015,** *48* (1), 13-21.

43. Alam, S.; Asaduzzaman Chowdhury, M.; Shahid, A.; Alam, R.; Rahim, A., Synthesis of Emerging Two-Dimensional (2d) Materials – Advances, Challenges and Prospects. *FlatChem* **2021,** *30*, 100305.

44. Joseph, N.; Shafi, P. M.; Bose, A. C., Recent Advances in 2d-Mos2 and Its Composite Nanostructures for Supercapacitor Electrode Application. *Energy & Fuels* **2020,** *34* (6), 6558-6597.

45. Xie, H.; Li, Z.; Cheng, L.; Haidry, A. A.; Tao, J.; Xu, Y.; Xu, K.; Ou, J. Z., Recent Advances in the Fabrication of 2d Metal Oxides. *iScience* **2022,** *25* (1), 103598.

46. Timmerman, M. A.; Xia, R.; Le, P. T. P.; Wang, Y.; ten Elshof, J. E., Metal Oxide Nanosheets as 2d Building Blocks for the Design of Novel Materials. *Chemistry – A European Journal* **2020,** *26* (42), 9084-9098.

47. Ida, S.; Ishihara, T., Recent Progress in Two-Dimensional Oxide Photocatalysts for Water Splitting. *The Journal of Physical Chemistry Letters* **2014,** *5* (15), 2533-2542.

48. Radha, S. K.; Crowley, K.; Holler, B. A.; Gao, X. P. A.; Lambrecht, W. R. L.; Volkova, H.; Berger, M.-H.; Pentzer, E.; Pachuta, K. G.; Sehirlioglu, A., Ultrathin 2d-Oxides: A Perspective on Fabrication, Structure, Defect, Transport, Electron, and Phonon Properties. *Journal of Applied Physics* **2021,** *129* (22), 220903.

49. Bandi, S.; Srivastav, A. K., Review: Oxygen-Deficient Tungsten Oxides. *Journal of Materials Science* **2021,** *56* (11), 6615-6644.

50. Agrawal, A.; Johns, R. W.; Milliron, D. J., Control of Localized Surface Plasmon Resonances in Metal Oxide Nanocrystals. *Annual Review of Materials Research* **2017,** *47* (1), 1-31.

51. Hao, L.; Huang, H.; Zhang, Y.; Ma, T., Oxygen Vacant Semiconductor Photocatalysts. *Advanced Functional Materials* **2021,** *31* (25), 2100919.

52. Al-Hashem, M.; Akbar, S.; Morris, P., Role of Oxygen Vacancies in Nanostructured Metal-Oxide Gas Sensors: A Review. *Sensors and Actuators B: Chemical* **2019,** *301*, 126845.

53. Heo, S.; Dahlman, C. J.; Staller, C. M.; Jiang, T.; Dolocan, A.; Korgel, B. A.; Milliron, D. J., Enhanced Coloration Efficiency of Electrochromic Tungsten Oxide Nanorods by Site Selective Occupation of Sodium Ions. *Nano Letters* **2020,** *20* (3), 2072-2079.

54. Naguib, M.; Kurtoglu, M.; Presser, V.; Lu, J.; Niu, J.; Heon, M.; Hultman, L.; Gogotsi, Y.; Barsoum, M. W., Two-Dimensional Nanocrystals Produced by Exfoliation of Ti3 Alc2. *Adv Mater* **2011,** *23* (37), 4248-53.

55. Anasori, B.; Lukatskaya, M. R.; Gogotsi, Y., 2d Metal Carbides and Nitrides (Mxenes) for Energy Storage. *Nat Rev Mater* **2017,** *2* (2), 16098.

56. Okubo, M.; Sugahara, A.; Kajiyama, S.; Yamada, A., Mxene as a Charge Storage Host. *Accounts of Chemical Research* **2018,** *51* (3), 591-599.

57. Pogorielov, M.; Smyrnova, K.; Kyrylenko, S.; Gogotsi, O.; Zahorodna, V.; Pogrebnjak, A., Mxenes-a New Class of Two-Dimensional Materials: Structure, Properties and Potential Applications. *Nanomaterials* **2021,** *11* (12), 3412.

58. Chia, H. L.; Mayorga-Martinez, C. C.; Antonatos, N.; Sofer, Z.; Gonzalez-Julian, J. J.; Webster, R. D.; Pumera, M., Mxene Titanium Carbide-Based Biosensor: Strong Dependence of Exfoliation Method on Performance. *Analytical Chemistry* **2020,** *92* (3), 2452-2459.

59. Saparov, B.; Mitzi, D. B., Organic-Inorganic Perovskites: Structural Versatility for Functional Materials Design. *Chem Rev* **2016,** *116* (7), 4558-96.

60. Zhou, Y.; Chen, W., Hybrid Organic–Inorganic Halide Perovskites. *Journal of Applied Physics* **2020,** *128* (20), 200401.

61. Zhou, Y.; Zhou, H.; Deng, J.; Cha, W.; Cai, Z., Decisive Structural and Functional Characterization of Halide Perovskites with Synchrotron. *Matter* **2020,** *2* (2), 360-377.

62. Gong, J.; Flatken, M.; Abate, A.; Correa-Baena, J.-P.; Mora-Seró, I.; Saliba, M.; Zhou, Y., The Bloom of Perovskite Optoelectronics: Fundamental Science Matters. *ACS Energy Letters* **2019,** *4* (4), 861-865.

63. Silvera Batista, C. A.; Larson, R. G.; Kotov, N. A., Nonadditivity of Nanoparticle Interactions. *Science* **2015,** *350* (6257).

64. Boles, M. A.; Ling, D.; Hyeon, T.; Talapin, D. V., The Surface Science of Nanocrystals. *Nat. Mater.* **2016,** *15* (2), 141-153.

65. Schultz, T.; Frey, N. C.; Hantanasirisakul, K.; Park, S.; May, S. J.; Shenoy, V. B.; Gogotsi, Y.; Koch, N., Surface Termination Dependent Work Function and Electronic Properties of Ti3c2tx Mxene. *Chemistry of Materials* **2019,** *31* (17), 6590-6597.

66. Alivisatos, A. P., Semiconductor Clusters, Nanocrystals, and Quantum Dots. *Science* **1996,** *271* (5251), 933-937.

67. Kroupa, D. M.; Vörös, M.; Brawand, N. P.; McNichols, B. W.; Miller, E. M.; Gu, J.; Nozik, A. J.; Sellinger, A.; Galli, G.; Beard, M. C., Tuning Colloidal Quantum Dot Band Edge Positions through Solution-Phase Surface Chemistry Modification. *Nat. Commun.* **2017,** *8* (1), 15257.

68. Khabibullin, A. R.; Efros, A. L.; Erwin, S. C., The Role of Ligands in Electron Transport in Nanocrystal Solids. *Nanoscale* **2020,** *12* (45), 23028-23035.

69. Pujari, S. P.; Scheres, L.; Marcelis, A. T. M.; Zuilhof, H., Covalent Surface Modification of Oxide Surfaces. *Angewandte Chemie International Edition* **2014,** *53* (25), 6322-6356.

70. Fafarman, A. T.; Koh, W.-k.; Diroll, B. T.; Kim, D. K.; Ko, D.-K.; Oh, S. J.; Ye, X.; Doan-Nguyen, V.; Crump, M. R.; Reifsnyder, D. C.; Murray, C. B.; Kagan, C. R., Thiocyanate-Capped Nanocrystal Colloids: Vibrational Reporter of Surface Chemistry and Solution-Based Route to Enhanced Coupling in Nanocrystal Solids. *Journal of the American Chemical Society* **2011,** *133* (39), 15753-15761.

71. Brus, L., Electronic Wave Functions in Semiconductor Clusters: Experiment and Theory. *The Journal of Physical Chemistry* **1986,** *90* (12), 2555-2560.

72. Donegá, C. d. M., Synthesis and Properties of Colloidal Heteronanocrystals. *Chemical Society Reviews* **2011,** *40* (3), 1512-1546.

73. Alivisatos, A. P., Perspectives on the Physical Chemistry of Semiconductor Nanocrystals. *The Journal of Physical Chemistry* **1996,** *100* (31), 13226-13239.

74. Kagan, C. R.; Murray, C. B., Charge Transport in Strongly Coupled Quantum Dot Solids. *Nature Nanotechnology* **2015,** *10*, 1013.

75. Zhang, H., Introduction: 2d Materials Chemistry. *Chem Rev* **2018,** *118* (13), 6089-6090.

76. Dey, A.; Ye, J.; De, A.; Debroye, E.; Ha, S. K.; Bladt, E.; Kshirsagar, A. S.; Wang, Z.; Yin, J.; Wang, Y.; Quan, L. N.; Yan, F.; Gao, M.; Li, X.; Shamsi, J.; Debnath, T.; Cao, M.; Scheel, M. A.; Kumar, S.; Steele, J. A.; Gerhard, M.; Chouhan, L.; Xu, K.; Wu, X.-g.; Li, Y.; Zhang, Y.; Dutta, A.; Han, C.; Vincon, I.; Rogach, A. L.; Nag, A.; Samanta, A.; Korgel, B. A.; Shih, C.-J.; Gamelin, D. R.; Son, D. H.; Zeng, H.; Zhong, H.; Sun, H.; Demir, H. V.; Scheblykin, I. G.; Mora-Seró, I.; Stolarczyk, J. K.; Zhang, J. Z.; Feldmann, J.; Hofkens, J.; Luther, J. M.; Pérez-Prieto, J.; Li, L.; Manna, L.; Bodnarchuk, M. I.; Kovalenko, M. V.; Roeffaers, M. B. J.; Pradhan, N.; Mohammed, O. F.; Bakr, O. M.; Yang, P.; Müller-Buschbaum, P.; Kamat, P. V.; Bao, Q.; Zhang, Q.; Krahne, R.; Galian, R. E.; Stranks, S. D.; Bals, S.; Biju, V.; Tisdale, W. A.; Yan, Y.; Hoye, R. L. Z.; Polavarapu, L., State of the Art and Prospects for Halide Perovskite Nanocrystals. *ACS Nano* **2021,** *15* (7), 10775-10981.

77. Lee, M. M.; Teuscher, J.; Miyasaka, T.; Murakami, T. N.; Snaith, H. J., Efficient Hybrid Solar Cells Based on Meso-Superstructured Organometal Halide Perovskites. *Science* **2012,** *338* (6107), 643-647.

78. Protesescu, L.; Yakunin, S.; Bodnarchuk, M. I.; Krieg, F.; Caputo, R.; Hendon, C. H.; Yang, R. X.; Walsh, A.; Kovalenko, M. V., Nanocrystals of Cesium Lead Halide Perovskites (Cspbx(3), X = Cl, Br, and I): Novel Optoelectronic Materials Showing Bright Emission with Wide Color Gamut. *Nano Lett* **2015,** *15* (6), 3692-6.

79. Kovalenko, M. V.; Protesescu, L.; Bodnarchuk, M. I., Properties and Potential Optoelectronic Applications of Lead Halide Perovskite Nanocrystals. *Science* **2017,** *358* (6364), 745-750.

80. Jena, A. K.; Kulkarni, A.; Miyasaka, T., Halide Perovskite Photovoltaics: Background, Status, and Future Prospects. *Chemical Reviews* **2019,** *119* (5), 3036-3103.

81. Green, M. A.; Ho-Baillie, A.; Snaith, H. J., The Emergence of Perovskite Solar Cells. *Nature Photonics* **2014,** *8* (7), 506-514.

82. Zhang, F.; Zhong, H.; Chen, C.; Wu, X. G.; Hu, X.; Huang, H.; Han, J.; Zou, B.; Dong, Y., Brightly Luminescent and Color-Tunable Colloidal Ch3nh3pbx3 (X = Br, I, Cl) Quantum Dots: Potential Alternatives for Display Technology. *ACS Nano* **2015,** *9* (4), 4533-42.

83. Gao, Y.; Huang, C.; Hao, C.; Sun, S.; Zhang, L.; Zhang, C.; Duan, Z.; Wang, K.; Jin, Z.; Zhang, N.; Kildishev, A. V.; Qiu, C.-W.; Song, Q.; Xiao, S., Lead Halide Perovskite Nanostructures for Dynamic Color Display. *ACS Nano* **2018,** *12* (9), 8847-8854.

84. Kim, Y. H.; Cho, H.; Lee, T. W., Metal Halide Perovskite Light Emitters. *Proc Natl Acad Sci U S A* **2016,** *113* (42), 11694-11702.

85. Akkerman, Q. A.; Raino, G.; Kovalenko, M. V.; Manna, L., Genesis, Challenges and Opportunities for Colloidal Lead Halide Perovskite Nanocrystals. *Nat Mater* **2018,** *17* (5), 394-405.

86. Mao, L.; Stoumpos, C. C.; Kanatzidis, M. G., Two-Dimensional Hybrid Halide Perovskites: Principles and Promises. *J Am Chem Soc* **2019,** *141* (3), 1171-1190.

87. Dou, L.; Wong, A. B.; Yu, Y.; Lai, M.; Kornienko, N.; Eaton, S. W.; Fu, A.; Bischak, C. G.; Ma, J.; Ding, T.; Ginsberg, N. S.; Wang, L. W.; Alivisatos, A. P.; Yang, P., Atomically Thin Two-Dimensional Organic-Inorganic Hybrid Perovskites. *Science* **2015,** *349* (6255), 1518-21.

88. Teunis, M. B.; Johnson, M. A.; Muhoberac, B. B.; Seifert, S.; Sardar, R., Programmable Colloidal Approach to Hierarchical Structures of Methylammonium Lead Bromide Perovskite Nanocrystals with Bright Photoluminescent Properties. *Chemistry of Materials* **2017,** *29* (8), 3526-3537.

89. Shamsi, J.; Dang, Z.; Bianchini, P.; Canale, C.; Di Stasio, F.; Brescia, R.; Prato, M.; Manna, L., Colloidal Synthesis of Quantum Confined Single Crystal Cspbbr3 Nanosheets with Lateral Size Control up to the Micrometer Range. *Journal of the American Chemical Society* **2016,** *138* (23), 7240-7243.

90. Dahlman, C. J.; Venkatesan, N. R.; Corona, P. T.; Kennard, R. M.; Mao, L.; Smith, N. C.; Zhang, J.; Seshadri, R.; Helgeson, M. E.; Chabinyc, M. L., Structural Evolution of Layered Hybrid Lead Iodide Perovskites in Colloidal Dispersions. *ACS Nano* **2020,** *14* (9), 11294-11308.

91. Akkerman, Q. A.; Motti, S. G.; Srimath Kandada, A. R.; Mosconi, E.; D'Innocenzo, V.; Bertoni, G.; Marras, S.; Kamino, B. A.; Miranda, L.; De Angelis, F.; Petrozza, A.; Prato, M.; Manna, L., Solution Synthesis Approach to Colloidal Cesium Lead Halide Perovskite Nanoplatelets with Monolayer-Level Thickness Control. *J Am Chem Soc* **2016,** *138* (3), 1010-6.

92. Pan, A.; He, B.; Fan, X.; Liu, Z.; Urban, J. J.; Alivisatos, A. P.; He, L.; Liu, Y., Insight into the Ligand-Mediated Synthesis of Colloidal Cspbbr3 Perovskite Nanocrystals: The Role of Organic Acid, Base, and Cesium Precursors. *ACS Nano* **2016,** *10* (8), 7943-7954.

93. Sun, S.; Yuan, D.; Xu, Y.; Wang, A.; Deng, Z., Ligand-Mediated Synthesis of Shape-Controlled Cesium Lead Halide Perovskite Nanocrystals Via Reprecipitation Process at Room Temperature. *ACS Nano* **2016,** *10* (3), 3648-57.

94. Soe, C. M. M.; Nagabhushana, G. P.; Shivaramaiah, R.; Tsai, H.; Nie, W.; Blancon, J.-C.; Melkonyan, F.; Cao, D. H.; Traoré, B.; Pedesseau, L.; Kepenekian, M.; Katan, C.; Even, J.; Marks, T. J.; Navrotsky, A.; Mohite, A. D.; Stoumpos, C. C.; Kanatzidis, M. G., Structural and Thermodynamic Limits of Layer Thickness in 2d Halide Perovskites. *Proceedings of the National Academy of Sciences* **2019,** *116* (1), 58-66.

95. Spanopoulos, I.; Hadar, I.; Ke, W.; Tu, Q.; Chen, M.; Tsai, H.; He, Y.; Shekhawat, G.; Dravid, V. P.; Wasielewski, M. R.; Mohite, A. D.; Stoumpos, C. C.; Kanatzidis, M. G., Uniaxial Expansion of the 2d Ruddlesden–Popper Perovskite Family for Improved Environmental Stability. *Journal of the American Chemical Society* **2019,** *141* (13), 5518-5534.

96. Liu, Y.; Siron, M.; Lu, D.; Yang, J.; Dos Reis, R.; Cui, F.; Gao, M.; Lai, M.; Lin, J.; Kong, Q.; Lei, T.; Kang, J.; Jin, J.; Ciston, J.; Yang, P., Self-Assembly of Two-Dimensional Perovskite Nanosheet Building Blocks into Ordered Ruddlesden-Popper Perovskite Phase. *J Am Chem Soc* **2019,** *141* (33), 13028-13032.

97. Wang, A.; Muhammad, F.; Liu, Y.; Deng, Z., Lead-Free Mn-Doped Antimony Halide Perovskite Quantum Dots with Bright Deep-Red Emission. *Chemical Communications* **2021,** *57* (21), 2677-2680.

98. Sun, J.; Yang, J.; Lee, J. I.; Cho, J. H.; Kang, M. S., Lead-Free Perovskite Nanocrystals for Light-Emitting Devices. *J Phys Chem Lett* **2018,** *9* (7), 1573-1583.

99. Hao, F.; Stoumpos, C. C.; Cao, D. H.; Chang, R. P. H.; Kanatzidis, M. G., Lead-Free Solid-State Organic–Inorganic Halide Perovskite Solar Cells. *Nature Photonics* **2014,** *8* (6), 489-494.

100. Hoefler, S. F.; Trimmel, G.; Rath, T., Progress on Lead-Free Metal Halide Perovskites for Photovoltaic Applications: A Review. *Monatsh Chem* **2017,** *148* (5), 795-826.

101. Yang, B.; Chen, J.; Hong, F.; Mao, X.; Zheng, K.; Yang, S.; Li, Y.; Pullerits, T.; Deng, W.; Han, K., Lead-Free, Air-Stable All-Inorganic Cesium Bismuth Halide Perovskite Nanocrystals. *Angew Chem Int Ed Engl* **2017,** *56* (41), 12471-12475.

102. Leng, M.; Chen, Z.; Yang, Y.; Li, Z.; Zeng, K.; Li, K.; Niu, G.; He, Y.; Zhou, Q.; Tang, J., Lead-Free, Blue Emitting Bismuth Halide Perovskite Quantum Dots. *Angew Chem Int Ed Engl* **2016,** *55* (48), 15012-15016.

103. Pradhan, B.; Kumar, G. S.; Sain, S.; Dalui, A.; Ghorai, U. K.; Pradhan, S. K.; Acharya, S., Size Tunable Cesium Antimony Chloride Perovskite Nanowires and Nanorods. *Chemistry of Materials* **2018,** *30* (6), 2135-2142.

104. Goodenough, J. B., Perspective on Engineering Transition-Metal Oxides. *Chemistry of Materials* **2014,** *26* (1), 820-829.

105. Rao, C. N. R., Transition Metal Oxides. *Annual Review of Physical Chemistry* **1989,** *40* (1), 291-326.

106. Yang, H. G.; Sun, C. H.; Qiao, S. Z.; Zou, J.; Liu, G.; Smith, S. C.; Cheng, H. M.; Lu, G. Q., Anatase Tio2 Single Crystals with a Large Percentage of Reactive Facets. *Nature* **2008,** *453* (7195), 638-641.

107. King, P. D. C.; Veal, T. D.; Fuchs, F.; Wang, C. Y.; Payne, D. J.; Bourlange, A.; Zhang, H.; Bell, G. R.; Cimalla, V.; Ambacher, O.; Egdell, R. G.; Bechstedt, F.; McConville, C. F., Band Gap, Electronic Structure, and Surface Electron Accumulation of Cubic and Rhombohedralin2o3. *Physical Review B* **2009,** *79* (20).

108. Zhang, X.; Hejazi, M.; Thiagarajan, S. J.; Woerner, W. R.; Banerjee, D.; Emge, T. J.; Xu, W.; Teat, S. J.; Gong, Q.; Safari, A.; Yang, R.; Parise, J. B.; Li, J., From 1d Chain to 3d Network: A New Family of Inorganic–Organic Hybrid Semiconductors Mo3(L)X (M = Mo, W; L = Organic Linker) Built on Perovskite-Like Structure Modules. *Journal of the American Chemical Society* **2013,** *135* (46), 17401-17407.

109. Li, W.; Da, P.; Zhang, Y.; Wang, Y.; Lin, X.; Gong, X.; Zheng, G., Wo3 Nanoflakes for Enhanced Photoelectrochemical Conversion. *ACS Nano* **2014,** *8* (11), 11770-11777.

110. Song, F.; Bai, L.; Moysiadou, A.; Lee, S.; Hu, C.; Liardet, L.; Hu, X., Transition Metal Oxides as Electrocatalysts for the Oxygen Evolution Reaction in Alkaline Solutions: An Application-Inspired Renaissance. *J Am Chem Soc* **2018,** *140* (25), 7748-7759.

111. Novak, T. G.; Kim, J.; Tiwari, A. P.; Kim, J.; Lee, S.; Lee, J.; Jeon, S., 2d Moo3 Nanosheets Synthesized by Exfoliation and Oxidation of Mos2 for High Contrast and Fast Response Time Electrochromic Devices. *ACS Sustainable Chemistry & Engineering* **2020,** *8* (30), 11276-11282.

112. Alsaif, M. M. Y. A.; Field, M. R.; Murdoch, B. J.; Daeneke, T.; Latham, K.; Chrimes, A. F.; Zoolfakar, A. S.; Russo, S. P.; Ou, J. Z.; Kalantar-zadeh, K., Substoichiometric Two-Dimensional Molybdenum Oxide Flakes: A Plasmonic Gas Sensing Platform. *Nanoscale* **2014,** *6* (21), 12780-12791.

113. Manthiram, K.; Alivisatos, A. P., Tunable Localized Surface Plasmon Resonances in Tungsten Oxide Nanocrystals. *Journal of the American Chemical Society* **2012,** *134* (9), 3995-3998.

114. Comin, A.; Manna, L., New Materials for Tunable Plasmonic Colloidal Nanocrystals. *Chemical Society Reviews* **2014,** *43* (11), 3957-3975.

115. Prusty, G.; Lee, J. T.; Seifert, S.; Muhoberac, B. B.; Sardar, R., Ultrathin Plasmonic Tungsten Oxide Quantum Wells with Controllable Free Carrier Densities. *Journal of the American Chemical Society* **2020,** *142* (13), 5938-5942.

116. Migas, D. B.; Shaposhnikov, V. L.; Borisenko, V. E., Tungsten Oxides. Ii. The Metallic Nature of Magnéli Phases. *Journal of Applied Physics* **2010,** *108* (9), 093714.

117. Schirmer, O. F.; Salje, E., The W5+ Polaron in Crystalline Low Temperature Wo3 Esr and Optical Absorption. *Solid State Communications* **1980,** *33* (3), 333-336.

118. Salje, E.; Carley, A. F.; Roberts, M. W., The Effect of Reduction and Temperature on the Electronic Core Levels of Tungsten and Molybdenum in Wo3 and Wxmo1−Xo3—a Photoelectron Spectroscopic Study. *Journal of Solid State Chemistry* **1979,** *29* (2), 237-251.

119. Schirmer, O. F.; Salje, E., Conduction Bipolarons in Low-Temperature Crystalline Wo3-X. *Journal of Physics C: Solid State Physics* **1980,** *13* (36), L1067-L1072.

120. Viswanathan, K.; Brandt, K.; Salje, E., Crystal Structure and Charge Carrier Concentration of W18o49. *Journal of Solid State Chemistry* **1981,** *36* (1), 45-51.

121. Salje, E.; Güttler, B., Anderson Transition and Intermediate Polaron Formation in Wo3-X Transport Properties and Optical Absorption. *Philosophical Magazine B* **1984,** *50* (5), 607-620.

122. Faucheaux, J. A.; Jain, P. K., Plasmons in Photocharged Zno Nanocrystals Revealing the Nature of Charge Dynamics. *The Journal of Physical Chemistry Letters* **2013,** *4* (18), 3024-3030.

123. Seifollahi Bazarjani, M.; Hojamberdiev, M.; Morita, K.; Zhu, G.; Cherkashinin, G.; Fasel, C.; Herrmann, T.; Breitzke, H.; Gurlo, A.; Riedel, R., Visible Light Photocatalysis with C-Wo3–X/Wo3×H2o Nanoheterostructures in Situ Formed in Mesoporous Polycarbosilane-Siloxane Polymer. *Journal of the American Chemical Society* **2013,** *135* (11), 4467-4475.

124. Heo, S.; Kim, J.; Ong, G. K.; Milliron, D. J., Template-Free Mesoporous Electrochromic Films on Flexible Substrates from Tungsten Oxide Nanorods. *Nano Letters* **2017,** *17* (9), 5756-5761.

125. Cheng, H.; Klapproth, M.; Sagaltchik, A.; Li, S.; Thomas, A., Ordered Mesoporous Wo2.83: Selective Reduction Synthesis, Exceptional Localized Surface Plasmon Resonance and Enhanced Hydrogen Evolution Reaction Activity. *Journal of Materials Chemistry A* **2018,** *6* (5), 2249-2256.

126. Paik, T.; Cargnello, M.; Gordon, T. R.; Zhang, S.; Yun, H.; Lee, J. D.; Woo, H. Y.; Oh, S. J.; Kagan, C. R.; Fornasiero, P.; Murray, C. B., Photocatalytic Hydrogen Evolution from Substoichiometric Colloidal Wo3–X Nanowires. *ACS Energy Letters* **2018,** *3* (8), 1904-1910.

127. Tilley, R. J. D., The Crystal Chemistry of the Higher Tungsten Oxides. *International Journal of Refractory Metals and Hard Materials* **1995,** *13* (1), 93-109.

128. Lounis, S. D.; Runnerstrom, E. L.; Bergerud, A.; Nordlund, D.; Milliron, D. J., Influence of Dopant Distribution on the Plasmonic Properties of Indium Tin Oxide Nanocrystals. *J Am Chem Soc* **2014,** *136* (19), 7110-6.

129. Staller, C. M.; Robinson, Z. L.; Agrawal, A.; Gibbs, S. L.; Greenberg, B. L.; Lounis, S. D.; Kortshagen, U. R.; Milliron, D. J., Tuning Nanocrystal Surface Depletion by Controlling Dopant Distribution as a Route toward Enhanced Film Conductivity. *Nano Lett.* **2018,** *18* (5), 2870-2878.

130. Hong, W.; Wyatt, B. C.; Nemani, S. K.; Anasori, B., Double Transition-Metal Mxenes: Atomistic Design of Two-Dimensional Carbides and Nitrides. *MRS Bulletin* **2020,** *45* (10), 850-861.

131. Gogotsi, Y.; Anasori, B., The Rise of Mxenes. *ACS Nano* **2019,** *13* (8), 8491-8494.

132. Ghidiu, M.; Naguib, M.; Shi, C.; Mashtalir, O.; Pan, L. M.; Zhang, B.; Yang, J.; Gogotsi, Y.; Billinge, S. J. L.; Barsoum, M. W., Synthesis and Characterization of Two-Dimensional Nb4c3 (Mxene). *Chemical Communications* **2014,** *50* (67), 9517-9520.

133. Naguib, M.; Mashtalir, O.; Carle, J.; Presser, V.; Lu, J.; Hultman, L.; Gogotsi, Y.; Barsoum, M. W., Two-Dimensional Transition Metal Carbides. *ACS Nano* **2012,** *6* (2), 1322-1331.

134. Lipatov, A.; Lu, H.; Alhabeb, M.; Anasori, B.; Gruverman, A.; Gogotsi, Y.; Sinitskii, A., Elastic Properties of 2d Ti3c2tx Mxene Monolayers and Bilayers. *Science Advances* **2018,** *4* (6), eaat0491.

135. Wyatt, B. C.; Rosenkranz, A.; Anasori, B., 2d Mxenes: Tunable Mechanical and Tribological Properties. *Advanced Materials* **2021,** *33* (17), 2007973.

136. Mathis, T. S.; Maleski, K.; Goad, A.; Sarycheva, A.; Anayee, M.; Foucher, A. C.; Hantanasirisakul, K.; Shuck, C. E.; Stach, E. A.; Gogotsi, Y., Modified Max Phase Synthesis for Environmentally Stable and Highly Conductive Ti3c2 Mxene. *ACS Nano* **2021,** *15* (4), 6420-6429.

137. Naguib, M.; Halim, J.; Lu, J.; Cook, K. M.; Hultman, L.; Gogotsi, Y.; Barsoum, M. W., New Two-Dimensional Niobium and Vanadium Carbides as Promising Materials for Li-Ion Batteries. *Journal of the American Chemical Society* **2013,** *135* (43), 15966-15969.

138. Griffith, K. J.; Hope, M. A.; Reeves, P. J.; Anayee, M.; Gogotsi, Y.; Grey, C. P., Bulk and Surface Chemistry of the Niobium Max and Mxene Phases from Multinuclear Solid-State Nmr Spectroscopy. *Journal of the American Chemical Society* **2020,** *142* (44), 18924-18935.

139. Seh, Z. W.; Fredrickson, K. D.; Anasori, B.; Kibsgaard, J.; Strickler, A. L.; Lukatskaya, M. R.; Gogotsi, Y.; Jaramillo, T. F.; Vojvodic, A., Two-Dimensional Molybdenum Carbide (Mxene) as an Efficient Electrocatalyst for Hydrogen Evolution. *ACS Energy Letters* **2016,** *1* (3), 589-594.

140. Zha, X.-H.; Huang, Q.; He, J.; He, H.; Zhai, J.; Francisco, J. S.; Du, S., The Thermal and Electrical Properties of the Promising Semiconductor Mxene Hf2co2. *Scientific Reports* **2016,** *6* (1), 27971.

141. Zhang, Y.; Xia, W.; Wu, Y.; Zhang, P., Prediction of Mxene Based 2d Tunable Band Gap Semiconductors: Gw Quasiparticle Calculations. *Nanoscale* **2019,** *11* (9), 3993-4000.

142. El-Demellawi, J. K.; Lopatin, S.; Yin, J.; Mohammed, O. F.; Alshareef, H. N., Tunable Multipolar Surface Plasmons in 2d Ti3c2tx Mxene Flakes. *ACS Nano* **2018,** *12* (8), 8485-8493.

143. Hatter, C. B.; Shah, J.; Anasori, B.; Gogotsi, Y., Micromechanical Response of Two-Dimensional Transition Metal Carbonitride (Mxene) Reinforced Epoxy Composites. *Composites Part B: Engineering* **2020,** *182*, 107603.

144. Iqbal, A.; Shahzad, F.; Hantanasirisakul, K.; Kim, M.-K.; Kwon, J.; Hong, J.; Kim, H.; Kim, D.; Gogotsi, Y.; Koo, C. M., Anomalous Absorption of Electromagnetic Waves by 2d Transition Metal Carbonitride Ti₃Cnt<I>_X</I> (Mxene). *Science* **2020,** *369* (6502), 446-450.

145. Shayesteh Zeraati, A.; Mirkhani, S. A.; Sun, P.; Naguib, M.; Braun, P. V.; Sundararaj, U., Improved Synthesis of Ti3c2tx Mxenes Resulting in Exceptional Electrical Conductivity, High Synthesis Yield, and Enhanced Capacitance. *Nanoscale* **2021,** *13* (6), 3572-3580.

146. Xia, Y.; Mathis, T. S.; Zhao, M. Q.; Anasori, B.; Dang, A.; Zhou, Z.; Cho, H.; Gogotsi, Y.; Yang, S., Thickness-Independent Capacitance of Vertically Aligned Liquid-Crystalline Mxenes. *Nature* **2018,** *557* (7705), 409-412.

147. Zhang, C. J.; Pinilla, S.; McEvoy, N.; Cullen, C. P.; Anasori, B.; Long, E.; Park, S.-H.; Seral-Ascaso, A.; Shmeliov, A.; Krishnan, D.; Morant, C.; Liu, X.; Duesberg, G. S.; Gogotsi, Y.; Nicolosi, V., Oxidation Stability of Colloidal Two-Dimensional Titanium Carbides (Mxenes). *Chemistry of Materials* **2017,** *29* (11), 4848-4856.

148. Chae, Y.; Kim, S. J.; Cho, S.-Y.; Choi, J.; Maleski, K.; Lee, B.-J.; Jung, H.-T.; Gogotsi, Y.; Lee, Y.; Ahn, C. W., An Investigation into the Factors Governing the Oxidation of Two-Dimensional Ti3c2 Mxene. *Nanoscale* **2019,** *11* (17), 8387-8393.

149. Kang, R.; Zhang, Z.; Guo, L.; Cui, J.; Chen, Y.; Hou, X.; Wang, B.; Lin, C.-T.; Jiang, N.; Yu, J., Enhanced Thermal Conductivity of Epoxy Composites Filled with 2d Transition Metal Carbides (Mxenes) with Ultralow Loading. *Scientific Reports* **2019,** *9* (1), 9135.

150. Carey, M.; Hinton, Z.; Natu, V.; Pai, R.; Sokol, M.; Alvarez, N. J.; Kalra, V.; Barsoum, M. W., Dispersion and Stabilization of Alkylated 2d Mxene in Nonpolar Solvents and Their Pseudocapacitive Behavior. *Cell Reports Physical Science* **2020,** *1* (4), 100042.

151. Kim, D.; Ko, T. Y.; Kim, H.; Lee, G. H.; Cho, S.; Koo, C. M., Nonpolar Organic Dispersion of 2d Ti3c2tx Mxene Flakes Via Simultaneous Interfacial Chemical Grafting and Phase Transfer Method. *ACS Nano* **2019,** *13* (12), 13818-13828.

152. Zhang, Q.; Lai, H.; Fan, R.; Ji, P.; Fu, X.; Li, H., High Concentration of Ti3c2tx Mxene in Organic Solvent. *ACS Nano* **2021,** *15* (3), 5249-5262.

153. Maleski, K.; Mochalin, V. N.; Gogotsi, Y., Dispersions of Two-Dimensional Titanium Carbide Mxene in Organic Solvents. *Chemistry of Materials* **2017,** *29* (4), 1632-1640.

154. Daniel, M.-C.; Astruc, D., Gold Nanoparticles: Assembly, Supramolecular Chemistry, Quantum-Size-Related Properties, and Applications toward Biology, Catalysis, and Nanotechnology. *Chemical Reviews* **2004,** *104* (1), 293-346.

155. Shi, Y.; Lyu, Z.; Zhao, M.; Chen, R.; Nguyen, Q. N.; Xia, Y., Noble-Metal Nanocrystals with Controlled Shapes for Catalytic and Electrocatalytic Applications. *Chemical Reviews* **2021,** *121* (2), 649-735.

156. LaMer, V. K.; Dinegar, R. H., Theory, Production and Mechanism of Formation of Monodispersed Hydrosols. *Journal of the American Chemical Society* **1950,** *72* (11), 4847-4854.

157. Murray, C. B.; Norris, D. J.; Bawendi, M. G., Synthesis and Characterization of Nearly Monodisperse Cde (E = Sulfur, Selenium, Tellurium) Semiconductor Nanocrystallites. *Journal of the American Chemical Society* **1993,** *115* (19), 8706-8715.

158. Heuer-Jungemann, A.; Feliu, N.; Bakaimi, I.; Hamaly, M.; Alkilany, A.; Chakraborty, I.; Masood, A.; Casula, M. F.; Kostopoulou, A.; Oh, E.; Susumu, K.; Stewart, M. H.; Medintz, I. L.; Stratakis, E.; Parak, W. J.; Kanaras, A. G., The Role of Ligands in the Chemical Synthesis and Applications of Inorganic Nanoparticles. *Chemical Reviews* **2019,** *119* (8), 4819-4880.

159. Lim, S. J.; Ma, L.; Schleife, A.; Smith, A. M., Quantum Dot Surface Engineering: Toward Inert Fluorophores with Compact Size and Bright, Stable Emission. *Coordination Chemistry Reviews* **2016,** *320-321*, 216-237.

160. Pradhan, N.; Reifsnyder, D.; Xie, R.; Aldana, J.; Peng, X., Surface Ligand Dynamics in Growth of Nanocrystals. *Journal of the American Chemical Society* **2007,** *129* (30), 9500-9509.

161. Owen, J., The Coordination Chemistry of Nanocrystal Surfaces. *Science* **2015,** *347* (6222), 615-616.

162. O’Brien, M. N.; Jones, M. R.; Mirkin, C. A., The Nature and Implications of Uniformity in the Hierarchical Organization of Nanomaterials. *Proceedings of the National Academy of Sciences* **2016,** *113* (42), 11717-11725.

163. Zhu, C.; Chen, D.; Cao, W.; Lai, R.; Pu, C.; Li, J.; Kong, X.; Peng, X., Facet-Dependent on-Surface Reactions in the Growth of Cdse Nanoplatelets. *Angewandte Chemie International Edition* **2019,** *58* (49), 17764-17770.

164. Lovette, M. A.; Browning, A. R.; Griffin, D. W.; Sizemore, J. P.; Snyder, R. C.; Doherty, M. F., Crystal Shape Engineering. *Industrial & Engineering Chemistry Research* **2008,** *47* (24), 9812-9833.

165. Pun, A. B.; Mazzotti, S.; Mule, A. S.; Norris, D. J., Understanding Discrete Growth in Semiconductor Nanocrystals: Nanoplatelets and Magic-Sized Clusters. *Accounts of Chemical Research* **2021,** *54* (7), 1545-1554.

166. Yang, J.; Zeng, Z.; Kang, J.; Betzler, S.; Czarnik, C.; Zhang, X.; Ophus, C.; Yu, C.; Bustillo, K.; Pan, M.; Qiu, J.; Wang, L. W.; Zheng, H., Formation of Two-Dimensional Transition Metal Oxide Nanosheets with Nanoparticles as Intermediates. *Nat Mater* **2019,** *18* (9), 970-976.

167. Ithurria, S.; Tessier, M. D.; Mahler, B.; Lobo, R. P. S. M.; Dubertret, B.; Efros, A. L., Colloidal Nanoplatelets with Two-Dimensional Electronic Structure. *Nature Materials* **2011,** *10* (12), 936-941.

168. Bouet, C.; Mahler, B.; Nadal, B.; Abecassis, B.; Tessier, M. D.; Ithurria, S.; Xu, X.; Dubertret, B., Two-Dimensional Growth of Cdse Nanocrystals, from Nanoplatelets to Nanosheets. *Chemistry of Materials* **2013,** *25* (4), 639-645.

169. Chen, P. E.; Anderson, N. C.; Norman, Z. M.; Owen, J. S., Tight Binding of Carboxylate, Phosphonate, and Carbamate Anions to Stoichiometric Cdse Nanocrystals. *J. Am. Chem. Soc.* **2017,** *139* (8), 3227-3236.

170. Nevers, D. R.; Williamson, C. B.; Savitzky, B. H.; Hadar, I.; Banin, U.; Kourkoutis, L. F.; Hanrath, T.; Robinson, R. D., Mesophase Formation Stabilizes High-Purity Magic-Sized Clusters. *Journal of the American Chemical Society* **2018,** *140* (10), 3652-3662.

171. Liu, Y.; Zheng, X.; Fang, Y.; Zhou, Y.; Ni, Z.; Xiao, X.; Chen, S.; Huang, J., Ligand Assisted Growth of Perovskite Single Crystals with Low Defect Density. *Nature Communications* **2021,** *12* (1), 1686.

172. Yang, S.; Niu, W.; Wang, A. L.; Fan, Z.; Chen, B.; Tan, C.; Lu, Q.; Zhang, H., Ultrathin Two-Dimensional Organic-Inorganic Hybrid Perovskite Nanosheets with Bright, Tunable Photoluminescence and High Stability. *Angew Chem Int Ed Engl* **2017,** *56* (15), 4252-4255.

173. Zhang, L.; Sun, C.; He, T.; Jiang, Y.; Wei, J.; Huang, Y.; Yuan, M., High-Performance Quasi-2d Perovskite Light-Emitting Diodes: From Materials to Devices. *Light: Science & Applications* **2021,** *10* (1), 61.

174. Zheng, T.; Sang, W.; He, Z.; Wei, Q.; Chen, B.; Li, H.; Cao, C.; Huang, R.; Yan, X.; Pan, B.; Zhou, S.; Zeng, J., Conductive Tungsten Oxide Nanosheets for Highly Efficient Hydrogen Evolution. *Nano Letters* **2017,** *17* (12), 7968-7973.

175. Mehmood, F.; Pachter, R.; Murphy, N. R.; Johnson, W. E.; Ramana, C. V., Effect of Oxygen Vacancies on the Electronic and Optical Properties of Tungsten Oxide from First Principles Calculations. *Journal of Applied Physics* **2016,** *120* (23), 233105.

176. Lu, C.; Li, J.; Yan, J.; Li, B.; Huang, B.; Lou, Z., Surface Plasmon Resonance and Defects on Tungsten Oxides Synergistically Boost High-Selective Co2 Reduction for Ethylene. *Applied Materials Today* **2020,** *20*, 100744.

177. Hart, J. L.; Hantanasirisakul, K.; Lang, A. C.; Anasori, B.; Pinto, D.; Pivak, Y.; van Omme, J. T.; May, S. J.; Gogotsi, Y.; Taheri, M. L., Control of Mxenes' Electronic Properties through Termination and Intercalation. *Nature Communications* **2019,** *10* (1), 522.

178. Tablero Crespo, C., The Effect of the Halide Anion on the Optical Properties of Lead Halide Perovskites. *Solar Energy Materials and Solar Cells* **2019,** *195*, 269-273.

179. Leng, K.; Abdelwahab, I.; Verzhbitskiy, I.; Telychko, M.; Chu, L.; Fu, W.; Chi, X.; Guo, N.; Chen, Z.; Chen, Z.; Zhang, C.; Xu, Q.-H.; Lu, J.; Chhowalla, M.; Eda, G.; Loh, K. P., Molecularly Thin Two-Dimensional Hybrid Perovskites with Tunable Optoelectronic Properties Due to Reversible Surface Relaxation. *Nature Materials* **2018,** *17* (10), 908-914.

180. Huang, H.; Bodnarchuk, M. I.; Kershaw, S. V.; Kovalenko, M. V.; Rogach, A. L., Lead Halide Perovskite Nanocrystals in the Research Spotlight: Stability and Defect Tolerance. *ACS Energy Letters* **2017,** *2* (9), 2071-2083.

181. Joshi, G. K.; McClory, P. J.; Muhoberac, B. B.; Kumbhar, A.; Smith, K. A.; Sardar, R., Designing Efficient Localized Surface Plasmon Resonance-Based Sensing Platforms: Optimization of Sensor Response by Controlling the Edge Length of Gold Nanoprisms. *The Journal of Physical Chemistry C* **2012,** *116* (39), 20990-21000.

182. Hsu, S. W.; On, K.; Tao, A. R., Localized Surface Plasmon Resonances of Anisotropic Semiconductor Nanocrystals. *J. Am. Chem. Soc.* **2011,** *133* (47), 19072-5.

183. Faucheaux, J. A.; Stanton, A. L. D.; Jain, P. K., Plasmon Resonances of Semiconductor Nanocrystals: Physical Principles and New Opportunities. *The Journal of Physical Chemistry Letters* **2014,** *5* (6), 976-985.

184. Zandi, O.; Agrawal, A.; Shearer, A. B.; Reimnitz, L. C.; Dahlman, C. J.; Staller, C. M.; Milliron, D. J., Impacts of Surface Depletion on the Plasmonic Properties of Doped Semiconductor Nanocrystals. *Nature Materials* **2018,** *17* (8), 710-717.

185. Gibbs, S. L.; Staller, C. M.; Milliron, D. J., Surface Depletion Layers in Plasmonic Metal Oxide Nanocrystals. *Accounts of Chemical Research* **2019,** *52* (9), 2516-2524.

186. Nayak, L.; Mohanty, S.; Nayak, S. K.; Ramadoss, A., A Review on Inkjet Printing of Nanoparticle Inks for Flexible Electronics. *Journal of Materials Chemistry C* **2019,** *7* (29), 8771-8795.

187. Anto, B. T.; Sivaramakrishnan, S.; Chua, L.-L.; Ho, P. K. H., Hydrophilic Sparse Ionic Monolayer-Protected Metal Nanoparticles: Highly Concentrated Nano-Au and Nano-Ag "Inks" That Can Be Sintered to near-Bulk Conductivity at 150 °C. *Advanced Functional Materials* **2010,** *20* (2), 296-303.

188. Müller, K.; Bugnicourt, E.; Latorre, M.; Jorda, M.; Echegoyen Sanz, Y.; Lagaron, J. M.; Miesbauer, O.; Bianchin, A.; Hankin, S.; Bölz, U.; Pérez, G.; Jesdinszki, M.; Lindner, M.; Scheuerer, Z.; Castelló, S.; Schmid, M., Review on the Processing and Properties of Polymer Nanocomposites and Nanocoatings and Their Applications in the Packaging, Automotive and Solar Energy Fields. *Nanomaterials (Basel)* **2017,** *7* (4), 74.

189. Lee, H.-Y.; Shin, S. H. R.; Abezgauz, L. L.; Lewis, S. A.; Chirsan, A. M.; Danino, D. D.; Bishop, K. J. M., Integration of Gold Nanoparticles into Bilayer Structures Via Adaptive Surface Chemistry. *Journal of the American Chemical Society* **2013,** *135* (16), 5950-5953.

190. Bodnarchuk, M. I.; Boehme, S. C.; ten Brinck, S.; Bernasconi, C.; Shynkarenko, Y.; Krieg, F.; Widmer, R.; Aeschlimann, B.; Günther, D.; Kovalenko, M. V.; Infante, I., Rationalizing and Controlling the Surface Structure and Electronic Passivation of Cesium Lead Halide Nanocrystals. *ACS Energy Letters* **2019,** *4* (1), 63-74.

191. Xu, K. J.; Wang, R. T.; Xu, A. F.; Chen, J. Y.; Xu, G., Hysteresis and Instability Predicted in Moisture Degradation of Perovskite Solar Cells. *ACS Applied Materials & Interfaces* **2020,** *12* (43), 48882-48889.

192. Pan, J.; Shang, Y.; Yin, J.; De Bastiani, M.; Peng, W.; Dursun, I.; Sinatra, L.; El-Zohry, A. M.; Hedhili, M. N.; Emwas, A.-H.; Mohammed, O. F.; Ning, Z.; Bakr, O. M., Bidentate Ligand-Passivated Cspbi3 Perovskite Nanocrystals for Stable near-Unity Photoluminescence Quantum Yield and Efficient Red Light-Emitting Diodes. *Journal of the American Chemical Society* **2018,** *140* (2), 562-565.

193. Zuo, L.; Guo, H.; deQuilettes, D. W.; Jariwala, S.; Marco, N. D.; Dong, S.; DeBlock, R.; Ginger, D. S.; Dunn, B.; Wang, M.; Yang, Y., Polymer-Modified Halide Perovskite Films for Efficient and Stable Planar Heterojunction Solar Cells. *Science Advances* **2017,** *3* (8), e1700106.

194. Ma, C.; Park, N.-G., Paradoxical Approach with a Hydrophilic Passivation Layer for Moisture-Stable, 23% Efficient Perovskite Solar Cells. *ACS Energy Letters* **2020,** *5* (10), 3268-3275.

195. Pramanik, A.; Gates, K.; Patibandla, S.; Davis, D.; Begum, S.; Iftekhar, R.; Alamgir, S.; Paige, S.; Porter, M. M.; Ray, P. C., Water-Soluble and Bright Luminescent Cesium–Lead–Bromide Perovskite Quantum Dot–Polymer Composites for Tumor-Derived Exosome Imaging. *ACS Applied Bio Materials* **2019,** *2* (12), 5872-5879.

196. Wen, D.; Wang, X.; Liu, L.; Hu, C.; Sun, C.; Wu, Y.; Zhao, Y.; Zhang, J.; Liu, X.; Ying, G., Inkjet Printing Transparent and Conductive Mxene (Ti3c2tx) Films: A Strategy for Flexible Energy Storage Devices. *ACS Applied Materials & Interfaces* **2021,** *13* (15), 17766-17780.

197. Alhabeb, M.; Maleski, K.; Anasori, B.; Lelyukh, P.; Clark, L.; Sin, S.; Gogotsi, Y., Guidelines for Synthesis and Processing of Two-Dimensional Titanium Carbide (Ti3c2tx Mxene). *Chemistry of Materials* **2017,** *29* (18), 7633-7644.

198. Hu, T.; Hu, M.; Li, Z.; Zhang, H.; Zhang, C.; Wang, J.; Wang, X., Interlayer Coupling in Two-Dimensional Titanium Carbide Mxenes. *Physical Chemistry Chemical Physics* **2016,** *18* (30), 20256-20260.

199. Malaki, M.; Varma, R. S., Mechanotribological Aspects of Mxene-Reinforced Nanocomposites. *Advanced Materials* **2020,** *32* (38), 2003154.

200. Lim, S.; Park, H.; Yang, J.; Kwak, C.; Lee, J., Stable Colloidal Dispersion of Octylated Ti3c2-Mxenes in a Nonpolar Solvent. *Colloids and Surfaces A: Physicochemical and Engineering Aspects* **2019,** *579*.

201. Somorjai, G. A.; Li, Y., Impact of Surface Chemistry. *Proceedings of the National Academy of Sciences* **2011,** *108* (3), 917-924.

202. Bhosale, S. S.; Kharade, A. K.; Jokar, E.; Fathi, A.; Chang, S.-m.; Diau, E. W.-G., Mechanism of Photocatalytic Co2 Reduction by Bismuth-Based Perovskite Nanocrystals at the Gas–Solid Interface. *Journal of the American Chemical Society* **2019,** *141* (51), 20434-20442.

203. Alcantar, N. A.; Aydil, E. S.; Israelachvili, J. N., Polyethylene Glycol–Coated Biocompatible Surfaces. *Journal of Biomedical Materials Research* **2000,** *51* (3), 343-351.

204. Cong, S.; Yuan, Y.; Chen, Z.; Hou, J.; Yang, M.; Su, Y.; Zhang, Y.; Li, L.; Li, Q.; Geng, F.; Zhao, Z., Noble Metal-Comparable Sers Enhancement from Semiconducting Metal Oxides by Making Oxygen Vacancies. *Nature Communications* **2015,** *6* (1), 7800.

205. Sliozberg, Y.; Andzelm, J.; Hatter, C. B.; Anasori, B.; Gogotsi, Y.; Hall, A., Interface Binding and Mechanical Properties of Mxene-Epoxy Nanocomposites. *Composites Science and Technology* **2020,** *192*, 108124.

206. Sangwan, V. K.; Hersam, M. C., Electronic Transport in Two-Dimensional Materials. *Annu Rev Phys Chem* **2018,** *69*, 299-325.

207. Han, G. H.; Duong, D. L.; Keum, D. H.; Yun, S. J.; Lee, Y. H., Van Der Waals Metallic Transition Metal Dichalcogenides. *Chem Rev* **2018,** *118* (13), 6297-6336.

208. Johari, P.; Shenoy, V. B., Tunable Dielectric Properties of Transition Metal Dichalcogenides. *ACS Nano* **2011,** *5* (7), 5903-5908.

209. Das, S. R.; Wakabayashi, K.; Yamamoto, M.; Tsukagoshi, K.; Dutta, S., Layer-by-Layer Oxidation Induced Electronic Properties in Transition-Metal Dichalcogenides. *The Journal of Physical Chemistry C* **2018,** *122* (29), 17001-17007.

210. Parveen, S.; Paul, K. K.; Giri, P. K., Precise Tuning of the Thickness and Optical Properties of Highly Stable 2d Organometal Halide Perovskite Nanosheets through a Solvothermal Process and Their Applications as a White Led and a Fast Photodetector. *ACS Applied Materials & Interfaces* **2020,** *12* (5), 6283-6297.

211. Numata, Y.; Sanehira, Y.; Ishikawa, R.; Shirai, H.; Miyasaka, T., Thiocyanate Containing Two-Dimensional Cesium Lead Iodide Perovskite, Cs2pbi2(Scn)2: Characterization, Photovoltaic Application, and Degradation Mechanism. *ACS Applied Materials & Interfaces* **2018,** *10* (49), 42363-42371.

212. Aharon, S.; Etgar, L., Two Dimensional Organometal Halide Perovskite Nanorods with Tunable Optical Properties. *Nano Letters* **2016,** *16* (5), 3230-3235.

213. Li, J.; Luo, L.; Huang, H.; Ma, C.; Ye, Z.; Zeng, J.; He, H., 2d Behaviors of Excitons in Cesium Lead Halide Perovskite Nanoplatelets. *The Journal of Physical Chemistry Letters* **2017,** *8* (6), 1161-1168.

214. Stoumpos, C. C.; Cao, D. H.; Clark, D. J.; Young, J.; Rondinelli, J. M.; Jang, J. I.; Hupp, J. T.; Kanatzidis, M. G., Ruddlesden–Popper Hybrid Lead Iodide Perovskite 2d Homologous Semiconductors. *Chemistry of Materials* **2016,** *28* (8), 2852-2867.

215. Ruddlesden, S. N.; Popper, P., New Compounds of the K2nif4 Type. *Acta Crystallographica* **1957,** *10* (8), 538-539.

216. Li, J.; Yu, Q.; He, Y.; Stoumpos, C. C.; Niu, G.; Trimarchi, G. G.; Guo, H.; Dong, G.; Wang, D.; Wang, L.; Kanatzidis, M. G., Cs2pbi2cl2, All-Inorganic Two-Dimensional Ruddlesden–Popper Mixed Halide Perovskite with Optoelectronic Response. *Journal of the American Chemical Society* **2018,** *140* (35), 11085-11090.

217. Tsai, H.; Nie, W.; Blancon, J.-C.; Stoumpos, C. C.; Asadpour, R.; Harutyunyan, B.; Neukirch, A. J.; Verduzco, R.; Crochet, J. J.; Tretiak, S.; Pedesseau, L.; Even, J.; Alam, M. A.; Gupta, G.; Lou, J.; Ajayan, P. M.; Bedzyk, M. J.; Kanatzidis, M. G.; Mohite, A. D., High-Efficiency Two-Dimensional Ruddlesden–Popper Perovskite Solar Cells. *Nature* **2016,** *536* (7616), 312-316.

218. Xing, J.; Zhao, Y.; Askerka, M.; Quan, L. N.; Gong, X.; Zhao, W.; Zhao, J.; Tan, H.; Long, G.; Gao, L.; Yang, Z.; Voznyy, O.; Tang, J.; Lu, Z.-H.; Xiong, Q.; Sargent, E. H., Color-Stable Highly Luminescent Sky-Blue Perovskite Light-Emitting Diodes. *Nature Communications* **2018,** *9* (1), 3541.

219. Gao, P.; Bin Mohd Yusoff, A. R.; Nazeeruddin, M. K., Dimensionality Engineering of Hybrid Halide Perovskite Light Absorbers. *Nature Communications* **2018,** *9* (1), 5028.

220. Jung, H. J.; Stompus, C. C.; Kanatzidis, M. G.; Dravid, V. P., Self-Passivation of 2d Ruddlesden–Popper Perovskite by Polytypic Surface Pbi2 Encapsulation. *Nano Letters* **2019,** *19* (9), 6109-6117.

221. Zheng, K.; Pullerits, T., Two Dimensions Are Better for Perovskites. *The Journal of Physical Chemistry Letters* **2019,** *10* (19), 5881-5885.

222. Chen, Z.; Guo, Y.; Wertz, E.; Shi, J., Merits and Challenges of Ruddlesden–Popper Soft Halide Perovskites in Electro-Optics and Optoelectronics. *Advanced Materials* **2019,** *31* (1), 1803514.

223. Kinigstein, E. D.; Tsai, H.; Nie, W.; Blancon, J.-C.; Yager, K. G.; Appavoo, K.; Even, J.; Kanatzidis, M. G.; Mohite, A. D.; Sfeir, M. Y., Edge States Drive Exciton Dissociation in Ruddlesden–Popper Lead Halide Perovskite Thin Films. *ACS Materials Letters* **2020,** *2* (10), 1360-1367.

224. Liu, J.; Leng, J.; Wu, K.; Zhang, J.; Jin, S., Observation of Internal Photoinduced Electron and Hole Separation in Hybrid Two-Dimentional Perovskite Films. *Journal of the American Chemical Society* **2017,** *139* (4), 1432-1435.

225. Tian, X.; Zhang, Y.; Zheng, R.; Wei, D.; Liu, J., Two-Dimensional Organic–Inorganic Hybrid Ruddlesden–Popper Perovskite Materials: Preparation, Enhanced Stability, and Applications in Photodetection. *Sustainable Energy & Fuels* **2020,** *4* (5), 2087-2113.

226. Zhang, Y.; Yin, J.; Parida, M. R.; Ahmed, G. H.; Pan, J.; Bakr, O. M.; Bredas, J. L.; Mohammed, O. F., Direct-Indirect Nature of the Bandgap in Lead-Free Perovskite Nanocrystals. *J Phys Chem Lett* **2017,** *8* (14), 3173-3177.

227. Creutz, S. E.; Crites, E. N.; De Siena, M. C.; Gamelin, D. R., Colloidal Nanocrystals of Lead-Free Double-Perovskite (Elpasolite) Semiconductors: Synthesis and Anion Exchange to Access New Materials. *Nano Lett* **2018,** *18* (2), 1118-1123.

228. Wang, A.; Yan, X.; Zhang, M.; Sun, S.; Yang, M.; Shen, W.; Pan, X.; Wang, P.; Deng, Z., Controlled Synthesis of Lead-Free and Stable Perovskite Derivative Cs2sni6 Nanocrystals Via a Facile Hot-Injection Process. *Chemistry of Materials* **2016,** *28* (22), 8132-8140.

229. Zhang, J.; Yang, Y.; Deng, H.; Farooq, U.; Yang, X.; Khan, J.; Tang, J.; Song, H., High Quantum Yield Blue Emission from Lead-Free Inorganic Antimony Halide Perovskite Colloidal Quantum Dots. *ACS Nano* **2017,** *11* (9), 9294-9302.

230. Lhuillier, E.; Pedetti, S.; Ithurria, S.; Nadal, B.; Heuclin, H.; Dubertret, B., Two-Dimensional Colloidal Metal Chalcogenides Semiconductors: Synthesis, Spectroscopy, and Applications. *Acc Chem Res* **2015,** *48* (1), 22-30.

231. Yang, Y.; Lee, J. T.; Liyanage, T.; Sardar, R., Flexible Polymer-Assisted Mesoscale Self-Assembly of Colloidal Cspbbr3 Perovskite Nanocrystals into Higher Order Superstructures with Strong Inter-Nanocrystal Electronic Coupling. *Journal of the American Chemical Society* **2019,** *141* (4), 1526-1536.

232. Lawrence, K. N.; Johnson, M. A.; Dolai, S.; Kumbhar, A.; Sardar, R., Solvent-Like Ligand-Coated Ultrasmall Cadmium Selenide Nanocrystals: Strong Electronic Coupling in a Self-Organized Assembly. *Nanoscale* **2015,** *7* (27), 11667-77.

233. Canepa, P.; Gonella, G.; Pinto, G.; Grachev, V.; Canepa, M.; Cavalleri, O., Anchoring of Aminophosphonates on Titanium Oxide for Biomolecular Coupling. *The Journal of Physical Chemistry C* **2019,** *123* (27), 16843-16850.

234. Creutz, S. E.; Liu, H.; Kaiser, M. E.; Li, X.; Gamelin, D. R., Structural Diversity in Cesium Bismuth Halide Nanocrystals. *Chemistry of Materials* **2019,** *31* (13), 4685-4697.

235. Moral, R. F.; Bonato, L. G.; Germino, J. C.; Coelho Oliveira, W. X.; Kamat, R.; Xu, J.; Tassone, C. J.; Stranks, S. D.; Toney, M. F.; Nogueira, A. F., Synthesis of Polycrystalline Ruddlesden–Popper Organic Lead Halides and Their Growth Dynamics. *Chemistry of Materials* **2019,** *31* (22), 9472-9479.

236. Lawrence, K. N.; Dutta, P.; Nagaraju, M.; Teunis, M. B.; Muhoberac, B. B.; Sardar, R., Dual Role of Electron-Accepting Metal-Carboxylate Ligands: Reversible Expansion of Exciton Delocalization and Passivation of Nonradiative Trap-States in Molecule-Like Cdse Nanocrystals. *Journal of the American Chemical Society* **2016,** *138* (39), 12813-12825.

237. Zhou, Y.; Wang, F.; Buhro, W. E., Large Exciton Energy Shifts by Reversible Surface Exchange in 2d Ii–Vi Nanocrystals. *Journal of the American Chemical Society* **2015,** *137* (48), 15198-15208.

238. Tao, S.; Schmidt, I.; Brocks, G.; Jiang, J.; Tranca, I.; Meerholz, K.; Olthof, S., Absolute Energy Level Positions in Tin- and Lead-Based Halide Perovskites. *Nature Communications* **2019,** *10* (1), 2560.

239. Cao, D. H.; Stoumpos, C. C.; Farha, O. K.; Hupp, J. T.; Kanatzidis, M. G., 2d Homologous Perovskites as Light-Absorbing Materials for Solar Cell Applications. *Journal of the American Chemical Society* **2015,** *137* (24), 7843-7850.

240. Chen, Y.; Yu, S.; Sun, Y.; Liang, Z., Phase Engineering in Quasi-2d Ruddlesden–Popper Perovskites. *The Journal of Physical Chemistry Letters* **2018,** *9* (10), 2627-2631.

241. Rajavel, K.; Yu, X.; Zhu, P.; Hu, Y.; Sun, R.; Wong, C., Exfoliation and Defect Control of Two-Dimensional Few-Layer Mxene Ti3c2tx for Electromagnetic Interference Shielding Coatings. *ACS Applied Materials & Interfaces* **2020,** *12* (44), 49737-49747.

242. Kreibig, U.; Vollmer, M., *Optical Properties of Metal Clusters*. 1 ed.; Springer, Berlin, Heidelberg: Springer-Verlag Berlin Heidelberg, 1995.

243. Cooper, B. R.; Ehrenreich, H.; Philipp, H. R., Optical Properties of Noble Metals. Ii. *Physical Review* **1965,** *138* (2A), A494-A507.

244. Jiang, N.; Zhuo, X.; Wang, J., Active Plasmonics: Principles, Structures, and Applications. *Chemical Reviews* **2018,** *118* (6), 3054-3099.

245. Wang, H.; Brandl, D. W.; Le, F.; Nordlander, P.; Halas, N. J., Nanorice: A Hybrid Plasmonic Nanostructure. *Nano Letters* **2006,** *6* (4), 827-832.

246. Agrawal, A.; Cho, S. H.; Zandi, O.; Ghosh, S.; Johns, R. W.; Milliron, D. J., Localized Surface Plasmon Resonance in Semiconductor Nanocrystals. *Chemical Reviews* **2018,** *118* (6), 3121-3207.

247. Mayer, K. M.; Hafner, J. H., Localized Surface Plasmon Resonance Sensors. *Chem Rev* **2011,** *111* (6), 3828-57.

248. Masterson, A. N.; Muhoberac, B. B.; Gopinadhan, A.; Wilde, D. J.; Deiss, F. T.; John, C. C.; Sardar, R., Multiplexed and High-Throughput Label-Free Detection of Rna/Spike Protein/Igg/Igm Biomarkers of Sars-Cov-2 Infection Utilizing Nanoplasmonic Biosensors. *Analytical Chemistry* **2021,** *93* (25), 8754-8763.

249. Masterson, A. N.; Liyanage, T.; Kaimakliotis, H.; Gholami Derami, H.; Deiss, F.; Sardar, R., Bottom-up Fabrication of Plasmonic Nanoantenna-Based High-Throughput Multiplexing Biosensors for Ultrasensitive Detection of Micrornas Directly from Cancer Patients' Plasma. *Analytical Chemistry* **2020,** *92* (13), 9295-9304.

250. Valley, N.; Greeneltch, N.; Van Duyne, R. P.; Schatz, G. C., A Look at the Origin and Magnitude of the Chemical Contribution to the Enhancement Mechanism of Surface-Enhanced Raman Spectroscopy (Sers): Theory and Experiment. *The Journal of Physical Chemistry Letters* **2013,** *4* (16), 2599-2604.

251. Greeneltch, N. G.; Davis, A. S.; Valley, N. A.; Casadio, F.; Schatz, G. C.; Van Duyne, R. P.; Shah, N. C., Near-Infrared Surface-Enhanced Raman Spectroscopy (Nir-Sers) for the Identification of Eosin Y: Theoretical Calculations and Evaluation of Two Different Nanoplasmonic Substrates. *The Journal of Physical Chemistry A* **2012,** *116* (48), 11863-11869.

252. Gellé, A.; Jin, T.; de la Garza, L.; Price, G. D.; Besteiro, L. V.; Moores, A., Applications of Plasmon-Enhanced Nanocatalysis to Organic Transformations. *Chemical Reviews* **2020,** *120* (2), 986-1041.

253. Arnob, M. M. P.; Artur, C.; Misbah, I.; Mubeen, S.; Shih, W. C., 10×-Enhanced Heterogeneous Nanocatalysis on a Nanoporous Gold Disk Array with High-Density Hot Spots. *ACS Appl Mater Interfaces* **2019,** *11* (14), 13499-13506.

254. Linic, S.; Chavez, S.; Elias, R., Flow and Extraction of Energy and Charge Carriers in Hybrid Plasmonic Nanostructures. *Nature Materials* **2021,** *20* (7), 916-924.

255. Zhou, L.; Swearer, D. F.; Zhang, C.; Robatjazi, H.; Zhao, H.; Henderson, L.; Dong, L.; Christopher, P.; Carter, E. A.; Nordlander, P.; Halas, N. J., Quantifying Hot Carrier and Thermal Contributions in Plasmonic Photocatalysis. *Science* **2018,** *362* (6410), 69-72.

256. Kriegel, I.; Jiang, C.; Rodriguez-Fernandez, J.; Schaller, R. D.; Talapin, D. V.; da Como, E.; Feldmann, J., Tuning the Excitonic and Plasmonic Properties of Copper Chalcogenide Nanocrystals. *J. Am. Chem. Soc.* **2012,** *134* (3), 1583-90.

257. Palomaki, P. K.; Miller, E. M.; Neale, N. R., Control of Plasmonic and Interband Transitions in Colloidal Indium Nitride Nanocrystals. *J. Am. Chem. Soc.* **2013,** *135* (38), 14142-50.

258. Mattox, T. M.; Bergerud, A.; Agrawal, A.; Milliron, D. J., Influence of Shape on the Surface Plasmon Resonance of Tungsten Bronze Nanocrystals. *Chemistry of Materials* **2014,** *26* (5), 1779-1784.

259. Crockett, B. M.; Jansons, A. W.; Koskela, K. M.; Johnson, D. W.; Hutchison, J. E., Radial Dopant Placement for Tuning Plasmonic Properties in Metal Oxide Nanocrystals. *ACS Nano* **2017,** *11* (8), 7719-7728.

260. Agrawal, A.; Cho, S. H.; Zandi, O.; Ghosh, S.; Johns, R. W.; Milliron, D. J., Localized Surface Plasmon Resonance in Semiconductor Nanocrystals. *Chem. Rev.* **2018,** *118* (6), 3121-3207.

261. Kanehara, M.; Koike, H.; Yoshinaga, T.; Teranishi, T., Indium Tin Oxide Nanoparticles with Compositionally Tunable Surface Plasmon Resonance Frequencies in the near-Ir Region. *J. Am. Chem. Soc.* **2009,** *131* (49), 17736-7.

262. Gordon, T. R.; Paik, T.; Klein, D. R.; Naik, G. V.; Caglayan, H.; Boltasseva, A.; Murray, C. B., Shape-Dependent Plasmonic Response and Directed Self-Assembly in a New Semiconductor Building Block, Indium-Doped Cadmium Oxide (Ico). *Nano Lett.* **2013,** *13* (6), 2857-63.

263. Zhou, S.; Pi, X.; Ni, Z.; Ding, Y.; Jiang, Y.; Jin, C.; Delerue, C.; Yang, D.; Nozaki, T., Comparative Study on the Localized Surface Plasmon Resonance of Boron- and Phosphorus-Doped Silicon Nanocrystals. *ACS Nano* **2015,** *9* (1), 378-386.

264. Kramer, N. J.; Schramke, K. S.; Kortshagen, U. R., Plasmonic Properties of Silicon Nanocrystals Doped with Boron and Phosphorus. *Nano Lett.* **2015,** *15* (8), 5597-603.

265. Sachet, E.; Shelton, C. T.; Harris, J. S.; Gaddy, B. E.; Irving, D. L.; Curtarolo, S.; Donovan, B. F.; Hopkins, P. E.; Sharma, P. A.; Sharma, A. L.; Ihlefeld, J.; Franzen, S.; Maria, J.-P., Dysprosium-Doped Cadmium Oxide as a Gateway Material for Mid-Infrared Plasmonics. *Nat. Mater.* **2015,** *14* (4), 414-420.

266. Gullapalli, S. K.; Vemuri, R. S.; Ramana, C. V., Structural Transformation Induced Changes in the Optical Properties of Nanocrystalline Tungsten Oxide Thin Films. *Applied Physics Letters* **2010,** *96* (17), 171903.

267. Bange, K., Colouration of Tungsten Oxide Films: A Model for Optically Active Coatings. *Solar Energy Materials and Solar Cells* **1999,** *58*, 1-131.

268. Brown, P. R.; Kim, D.; Lunt, R. R.; Zhao, N.; Bawendi, M. G.; Grossman, J. C.; Bulović, V., Energy Level Modification in Lead Sulfide Quantum Dot Thin Films through Ligand Exchange. *ACS Nano* **2014,** *8* (6), 5863-5872.

269. Kilina, S. V.; Tamukong, P. K.; Kilin, D. S., Surface Chemistry of Semiconducting Quantum Dots: Theoretical Perspectives. *Acc. Chem. Res.* **2016,** *49* (10), 2127-2135.

270. Harris, R. D.; Bettis Homan, S.; Kodaimati, M.; He, C.; Nepomnyashchii, A. B.; Swenson, N. K.; Lian, S.; Calzada, R.; Weiss, E. A., Electronic Processes within Quantum Dot-Molecule Complexes. *Chem. Rev.* **2016,** *116* (21), 12865-12919.

271. Anderson, N. C.; Hendricks, M. P.; Choi, J. J.; Owen, J. S., Ligand Exchange and the Stoichiometry of Metal Chalcogenide Nanocrystals: Spectroscopic Observation of Facile Metal-Carboxylate Displacement and Binding. *J. Am. Chem. Soc.* **2013,** *135* (49), 18536-18548.

272. Morris-Cohen, A. J.; Donakowski, M. D.; Knowles, K. E.; Weiss, E. A., The Effect of a Common Purification Procedure on the Chemical Composition of the Surfaces of Cdse Quantum Dots Synthesized with Trioctylphosphine Oxide. *The Journal of Physical Chemistry C* **2010,** *114* (2), 897-906.

273. Paniagua, S. A.; Giordano, A. J.; Smith, O. N. L.; Barlow, S.; Li, H.; Armstrong, N. R.; Pemberton, J. E.; Brédas, J.-L.; Ginger, D.; Marder, S. R., Phosphonic Acids for Interfacial Engineering of Transparent Conductive Oxides. *Chemical Reviews* **2016,** *116* (12), 7117-7158.

274. Davidowski, S. K.; Lisowski, C. E.; Yarger, J. L., Characterizing Mixed Phosphonic Acid Ligand Capping on Cdse/Zns Quantum Dots Using Ligand Exchange and Nmr Spectroscopy. *Magnetic Resonance in Chemistry* **2016,** *54* (3), 234-238.

275. Williams, E. S.; Major, K. J.; Tobias, A.; Woodall, D.; Morales, V.; Lippincott, C.; Moyer, P. J.; Jones, M., Characterizing the Influence of Topo on Exciton Recombination Dynamics in Colloidal Cdse Quantum Dots. *The Journal of Physical Chemistry C* **2013,** *117* (8), 4227-4237.

276. Owen, J. S.; Chan, E. M.; Liu, H.; Alivisatos, A. P., Precursor Conversion Kinetics and the Nucleation of Cadmium Selenide Nanocrystals. *Journal of the American Chemical Society* **2010,** *132* (51), 18206-18213.

277. Gomes, R.; Hassinen, A.; Szczygiel, A.; Zhao, Q.; Vantomme, A.; Martins, J. C.; Hens, Z., Binding of Phosphonic Acids to Cdse Quantum Dots: A Solution Nmr Study. *The Journal of Physical Chemistry Letters* **2011,** *2* (3), 145-152.

278. Chen, P. E.; Anderson, N. C.; Norman, Z. M.; Owen, J. S., Tight Binding of Carboxylate, Phosphonate, and Carbamate Anions to Stoichiometric Cdse Nanocrystals. *Journal of the American Chemical Society* **2017,** *139* (8), 3227-3236.

279. Liu, W.; Bai, H.; Li, X.; Li, W.; Zhai, J.; Li, J.; Xi, G., Improved Surface-Enhanced Raman Spectroscopy Sensitivity on Metallic Tungsten Oxide by the Synergistic Effect of Surface Plasmon Resonance Coupling and Charge Transfer. *The Journal of Physical Chemistry Letters* **2018,** *9* (14), 4096-4100.

280. Dolai, S.; Nimmala, P. R.; Mandal, M.; Muhoberac, B. B.; Dria, K.; Dass, A.; Sardar, R., Isolation of Bright Blue Light-Emitting Cdse Nanocrystals with 6.5 Kda Core in Gram Scale: High Photoluminescence Efficiency Controlled by Surface Ligand Chemistry. *Chemistry of Materials* **2014,** *26* (2), 1278-1285.

281. Escalante, G.; López, R.; Demesa, F. N.; Villa-Sánchez, G.; Castrejón-Sánchez, V. H.; Cruz, I. V. d. l., Correlation between Raman Spectra and Color of Tungsten Trioxide (Wo3) Thermally Evaporated from a Tungsten Filament. *AIP Advances* **2021,** *11* (5), 055103.

282. Yan, J.; Wang, T.; Wu, G.; Dai, W.; Guan, N.; Li, L.; Gong, J., Tungsten Oxide Single Crystal Nanosheets for Enhanced Multichannel Solar Light Harvesting. *Advanced Materials* **2015,** *27* (9), 1580-1586.

283. Houweling, Z. S.; Geus, J. W.; de Jong, M.; Harks, P.-P. R. M. L.; van der Werf, K. H. M.; Schropp, R. E. I., Growth Process Conditions of Tungsten Oxide Thin Films Using Hot-Wire Chemical Vapor Deposition. *Materials Chemistry and Physics* **2011,** *131* (1), 375-386.

284. Chen, S.; Xiao, Y.; Xie, W.; Wang, Y.; Hu, Z.; Zhang, W.; Zhao, H., Facile Strategy for Synthesizing Non-Stoichiometric Monoclinic Structured Tungsten Trioxide (Wo(3-X)) with Plasma Resonance Absorption and Enhanced Photocatalytic Activity. *Nanomaterials (Basel)* **2018,** *8* (7), 553.

285. Wang, X. P.; Yang, B. Q.; Zhang, H. X.; Feng, P. X., Tungsten Oxide Nanorods Array and Nanobundle Prepared by Using Chemical Vapor Deposition Technique. *Nanoscale Res Lett* **2007,** *2* (8), 405-409.

286. Vargas-Consuelos, C. I.; Seo, K.; Camacho-López, M.; Graeve, O. A., Correlation between Particle Size and Raman Vibrations in Wo3 Powders. *The Journal of Physical Chemistry C* **2014,** *118* (18), 9531-9537.

287. Gouadec, G.; Colomban, P., Raman Spectroscopy of Nanomaterials: How Spectra Relate to Disorder, Particle Size and Mechanical Properties. *Progress in Crystal Growth and Characterization of Materials* **2007,** *53* (1), 1-56.

288. Sarycheva, A.; Gogotsi, Y., Raman Spectroscopy Analysis of the Structure and Surface Chemistry of Ti3c2tx Mxene. *Chemistry of Materials* **2020,** *32* (8), 3480-3488.

289. Jain, P. K.; El-Sayed, M. A., Surface Plasmon Resonance Sensitivity of Metal Nanostructures: Physical Basis and Universal Scaling in Metal Nanoshells. *The Journal of Physical Chemistry C* **2007,** *111* (47), 17451-17454.

290. Leng, X.; Pereiro, J.; Strle, J.; Dubuis, G.; Bollinger, A. T.; Gozar, A.; Wu, J.; Litombe, N.; Panagopoulos, C.; Pavuna, D.; Božović, I., Insulator to Metal Transition in Wo3 Induced by Electrolyte Gating. *npj Quantum Materials* **2017,** *2* (1), 35.

291. Mulvaney, P., Surface Plasmon Spectroscopy of Nanosized Metal Particles. *Langmuir* **1996,** *12* (3), 788-800.

292. Deák, P.; Aradi, B.; Frauenheim, T., Quantitative Theory of the Oxygen Vacancy and Carrier Self-Trapping in Bulk Tio${}_{2}$. *Physical Review B* **2012,** *86* (19), 195206.

293. Deák, P.; Kullgren, J.; Frauenheim, T., Polarons and Oxygen Vacancies at the Surface of Anatase Tio2. *physica status solidi (RRL) – Rapid Research Letters* **2014,** *8* (6), 583-586.

294. Gordon, T. R.; Cargnello, M.; Paik, T.; Mangolini, F.; Weber, R. T.; Fornasiero, P.; Murray, C. B., Nonaqueous Synthesis of Tio2 Nanocrystals Using Tif4 to Engineer Morphology, Oxygen Vacancy Concentration, and Photocatalytic Activity. *Journal of the American Chemical Society* **2012,** *134* (15), 6751-6761.

295. Lei, F.; Sun, Y.; Liu, K.; Gao, S.; Liang, L.; Pan, B.; Xie, Y., Oxygen Vacancies Confined in Ultrathin Indium Oxide Porous Sheets for Promoted Visible-Light Water Splitting. *Journal of the American Chemical Society* **2014,** *136* (19), 6826-6829.

296. Priebe, J. B.; Karnahl, M.; Junge, H.; Beller, M.; Hollmann, D.; Brückner, A., Water Reduction with Visible Light: Synergy between Optical Transitions and Electron Transfer in Au-Tio(2) Catalysts Visualized by in Situ Epr Spectroscopy. *Angew Chem Int Ed Engl* **2013,** *52* (43), 11420-4.

297. Naldoni, A.; Allieta, M.; Santangelo, S.; Marelli, M.; Fabbri, F.; Cappelli, S.; Bianchi, C. L.; Psaro, R.; Dal Santo, V., Effect of Nature and Location of Defects on Bandgap Narrowing in Black Tio2 Nanoparticles. *J Am Chem Soc* **2012,** *134* (18), 7600-3.

298. Zhang, N.; Li, X.; Ye, H.; Chen, S.; Ju, H.; Liu, D.; Lin, Y.; Ye, W.; Wang, C.; Xu, Q.; Zhu, J.; Song, L.; Jiang, J.; Xiong, Y., Oxide Defect Engineering Enables to Couple Solar Energy into Oxygen Activation. *Journal of the American Chemical Society* **2016,** *138* (28), 8928-8935.

299. Wang, Y.; Cai, J.; Wu, M.; Chen, J.; Zhao, W.; Tian, Y.; Ding, T.; Zhang, J.; Jiang, Z.; Li, X., Rational Construction of Oxygen Vacancies onto Tungsten Trioxide to Improve Visible Light Photocatalytic Water Oxidation Reaction. *Applied Catalysis B: Environmental* **2018,** *239*, 398-407.

300. Kramer, N. J.; Schramke, K. S.; Kortshagen, U. R., Plasmonic Properties of Silicon Nanocrystals Doped with Boron and Phosphorus. *Nano Letters* **2015,** *15* (8), 5597-5603.

301. Liu, W. K.; Whitaker, K. M.; Smith, A. L.; Kittilstved, K. R.; Robinson, B. H.; Gamelin, D. R., Room-Temperature Electron Spin Dynamics in Free-Standing Zno Quantum Dots. *Physical review letters* **2007,** *98* (18), 186804.

302. Brodard-Severac, F.; Guerrero, G.; Maquet, J.; Florian, P.; Gervais, C.; Mutin, P. H., High-Field 17o Mas Nmr Investigation of Phosphonic Acid Monolayers on Titania. *Chemistry of Materials* **2008,** *20* (16), 5191-5196.

303. Holland, G. P.; Sharma, R.; Agola, J. O.; Amin, S.; Solomon, V. C.; Singh, P.; Buttry, D. A.; Yarger, J. L., Nmr Characterization of Phosphonic Acid Capped Sno2 Nanoparticles. *Chemistry of Materials* **2007,** *19* (10), 2519-2526.

304. Farrell, Z. J.; Reger, N.; Anderson, I.; Gawalt, E.; Tabor, C., Route to Universally Tailorable Room-Temperature Liquid Metal Colloids Via Phosphonic Acid Functionalization. *The Journal of Physical Chemistry C* **2018,** *122* (46), 26393-26400.

305. Lambert, J. B.; Gronert, S.; Shurvell, H. F.; Lightner, D. A., *Organic Structural Spectroscopy*. 2nd edition ed.; Pearson Prentice Hall: United States, 2011.

306. Luschtinetz, R.; Seifert, G.; Jaehne, E.; Adler, H.-J. P., Infrared Spectra of Alkylphosphonic Acid Bound to Aluminium Surfaces. *Macromolecular Symposia* **2007,** *254* (1), 248-253.

307. Sardar, R.; Park, J.-W.; Shumaker-Parry, J. S., Polymer-Induced Synthesis of Stable Gold and Silver Nanoparticles and Subsequent Ligand Exchange in Water. *Langmuir* **2007,** *23* (23), 11883-11889.

308. Seip, C. T.; Granroth, G. E.; Meisel, M. W.; Talham, D. R., Langmuir−Blodgett Films of Known Layered Solids: Preparation and Structural Properties of Octadecylphosphonate Bilayers with Divalent Metals and Characterization of a Magnetic Langmuir−Blodgett Film. *Journal of the American Chemical Society* **1997,** *119* (30), 7084-7094.

309. Rudolph, W. W., Raman- and Infrared-Spectroscopic Investigations of Dilute Aqueous Phosphoric Acid Solutions. *Dalton Transactions* **2010,** *39* (40), 9642-9653.

310. Mack, T. G.; Jethi, L.; Andrews, M.; Kambhampati, P., Direct Observation of Vibronic Coupling between Excitonic States of Cdse Nanocrystals and Their Passivating Ligands. *The Journal of Physical Chemistry C* **2019,** *123* (8), 5084-5091.

311. Piergies, N.; Proniewicz, E.; Kim, Y.; Proniewicz, L. M., Interaction of N-Benzylamino(Boronphenyl)Methylphosphonic Acid Analogs with the Gold Colloidal Surface under Different Concentration and Ph Conditions. *Journal of Raman Spectroscopy* **2014,** *45* (7), 581-590.

312. Podstawka, E.; Olszewski, T. K.; Boduszek, B.; Proniewicz, L. M., Adsorbed States of Phosphonate Derivatives of N-Heterocyclic Aromatic Compounds, Imidazole, Thiazole, and Pyridine on Colloidal Silver: Comparison with a Silver Electrode. *The Journal of Physical Chemistry B* **2009,** *113* (35), 12013-12018.

313. Higo, M.; Kamata, S., Surface Reaction of Dialkyl Phosphite on Alumina and Magnesia Studied by Inelastic Electron Tunneling Spectroscopy. *The Journal of Physical Chemistry* **1990,** *94* (24), 8709-8714.

314. Conti, C. R.; McBride, J. R.; Strouse, G. F., Examining the Effect of Dopant Ionic Radius on Plasmonic M:Zno Nanocrystals (M = Al3+, Ga3+, In3+). *The Journal of Physical Chemistry C* **2021,** *125* (14), 7772-7779.

315. Liu, Z.; Beaulac, R., Nature of the Infrared Transition of Colloidal Indium Nitride Nanocrystals: Nonparabolicity Effects on the Plasmonic Behavior of Doped Semiconductor Nanomaterials. *Chemistry of Materials* **2017,** *29* (17), 7507-7514.

316. Schimpf, A. M.; Lounis, S. D.; Runnerstrom, E. L.; Milliron, D. J.; Gamelin, D. R., Redox Chemistries and Plasmon Energies of Photodoped In2o3 and Sn-Doped In2o3 (Ito) Nanocrystals. *J Am Chem Soc* **2015,** *137* (1), 518-24.

317. Chen, H.; Kou, X.; Yang, Z.; Ni, W.; Wang, J., Shape- and Size-Dependent Refractive Index Sensitivity of Gold Nanoparticles. *Langmuir* **2008,** *24* (10), 5233-5237.

318. Charles, D. E.; Aherne, D.; Gara, M.; Ledwith, D. M.; Gun'ko, Y. K.; Kelly, J. M.; Blau, W. J.; Brennan-Fournet, M. E., Versatile Solution Phase Triangular Silver Nanoplates for Highly Sensitive Plasmon Resonance Sensing. *ACS Nano* **2010,** *4* (1), 55-64.

319. M. J. T. Frisch, G. W. S., H. B.; Scuseria, G. E.; Robb, M. A.; Cheeseman, J. R.; Scalmani, G.; Barone, V.; Petersson, G. A.; Nakatsuji, H.; Li, X.; Caricato, M.; Marenich, A. V.; Bloino, J.; Janesko, B. G.; Gomperts, R.; Mennucci, B.; Hratchian, H. P.; Ortiz, J. V.; Izmaylov, A. F.; Sonnenberg, J. L.; Williams-Young, D.; Ding, F.; Lipparini, F.; Egidi, F.; Goings, J.; Peng, B.; Petrone, A.; Henderson, T.; Ranasinghe, D.; Zakrzewski, V. G.; Gao, J.; Rega, N.; Zheng, G.; Liang, W.; Hada, M.; Ehara, M.; Toyota, K.; Fukuda, R.; Hasegawa, J.; Ishida, M.; Nakajima, T.; Honda, Y.; Kitao, O.; Nakai, H.; Vreven, T.; Throssell, K.; Montgomery, J. A., Jr.; Peralta, J. E.; Ogliaro, F.; Bearpark, M. J.; Heyd, J. J.; Brothers, E. N.; Kudin, K. N.; Staroverov, V. N.; Keith, T. A.; Kobayashi, R.; Normand, J.; Raghavachari, K.; Rendell, A. P.; Burant, J. C.; Iyengar, S. S.; Tomasi, J.; Cossi, M.; Millam, J. M.; Klene, M.; Adamo, C.; Cammi, R.; Ochterski, J. W.; Martin, R. L.; Morokuma, K.; Farkas, O.; Foresman, J. B.; Fox, D. J., *Gaussian 16*, Revision C.01; Gaussian, Inc.: Wallingford, CT, 2016.

320. Senanayake, R. D.; Lingerfelt, D. B.; Kuda-Singappulige, G. U.; Li, X.; Aikens, C. M., Real-Time Tddft Investigation of Optical Absorption in Gold Nanowires. *The Journal of Physical Chemistry C* **2019,** *123* (23), 14734-14745.

321. R. K. Dennington, T. A. M., J., M. *Gaussview*, Version 6; Semichem Inc.: Shawnee Mission, KS, 2016.

322. Takeda, H.; Adachi, K., Near Infrared Absorption of Tungsten Oxide Nanoparticle Dispersions. *Journal of the American Ceramic Society* **2007,** *90* (12), 4059-4061.

323. Im, H.; Bantz, K. C.; Lee, S. H.; Johnson, T. W.; Haynes, C. L.; Oh, S.-H., Self-Assembled Plasmonic Nanoring Cavity Arrays for Sers and Lspr Biosensing. *Advanced Materials* **2013,** *25* (19), 2678-2685.

324. Prikulis, J.; Hanarp, P.; Olofsson, L.; Sutherland, D.; Käll, M., Optical Spectroscopy of Nanometric Holes in Thin Gold Films. *Nano Letters* **2004,** *4* (6), 1003-1007.

325. Peixoto, L. P. F.; Santos, J. F. L.; Andrade, G. F. S., Plasmonic Nanobiosensor Based on Au Nanorods with Improved Sensitivity: A Comparative Study for Two Different Configurations. *Analytica Chimica Acta* **2019,** *1084*, 71-77.

326. Larsson, E. M.; Alegret, J.; Käll, M.; Sutherland, D. S., Sensing Characteristics of Nir Localized Surface Plasmon Resonances in Gold Nanorings for Application as Ultrasensitive Biosensors. *Nano Letters* **2007,** *7* (5), 1256-1263.

327. Khalavka, Y.; Becker, J.; Sönnichsen, C., Synthesis of Rod-Shaped Gold Nanorattles with Improved Plasmon Sensitivity and Catalytic Activity. *Journal of the American Chemical Society* **2009,** *131* (5), 1871-1875.

328. Nehl, C. L.; Liao, H.; Hafner, J. H., Optical Properties of Star-Shaped Gold Nanoparticles. *Nano Letters* **2006,** *6* (4), 683-688.

329. Malinsky, M. D.; Kelly, K. L.; Schatz, G. C.; Van Duyne, R. P., Chain Length Dependence and Sensing Capabilities of the Localized Surface Plasmon Resonance of Silver Nanoparticles Chemically Modified with Alkanethiol Self-Assembled Monolayers. *Journal of the American Chemical Society* **2001,** *123* (7), 1471-1482.

330. Sherry, L. J.; Jin, R.; Mirkin, C. A.; Schatz, G. C.; Van Duyne, R. P., Localized Surface Plasmon Resonance Spectroscopy of Single Silver Triangular Nanoprisms. *Nano Letters* **2006,** *6* (9), 2060-2065.

331. Ghosh, S.; Lu, H.-C.; Cho, S. H.; Maruvada, T.; Price, M. C.; Milliron, D. J., Colloidal Reo3 Nanocrystals: Extra Re D-Electron Instigating a Plasmonic Response. *Journal of the American Chemical Society* **2019,** *141* (41), 16331-16343.

332. Lee, S. H.; Nishi, H.; Tatsuma, T., Tunable Plasmon Resonance of Molybdenum Oxide Nanoparticles Synthesized in Non-Aqueous Media. *Chemical Communications* **2017,** *53* (94), 12680-12683.

333. Bonaccorso, F.; Colombo, L.; Yu, G.; Stoller, M.; Tozzini, V.; Ferrari, A. C.; Ruoff, R. S.; Pellegrini, V., 2d Materials. Graphene, Related Two-Dimensional Crystals, and Hybrid Systems for Energy Conversion and Storage. *Science* **2015,** *347* (6217), 1246501.

334. Caldwell, J. D.; Aharonovich, I.; Cassabois, G.; Edgar, J. H.; Gil, B.; Basov, D. N., Photonics with Hexagonal Boron Nitride. *Nat Rev Mater* **2019,** *4* (8), 552-567.

335. Zhang, K.; Feng, Y.; Wang, F.; Yang, Z.; Wang, J., Two Dimensional Hexagonal Boron Nitride (2d-Hbn): Synthesis, Properties and Applications. *Journal of Materials Chemistry C* **2017,** *5* (46), 11992-12022.

336. Yang, T.; Song, T. T.; Callsen, M.; Zhou, J.; Chai, J. W.; Feng, Y. P.; Wang, S. J.; Yang, M., Atomically Thin 2d Transition Metal Oxides: Structural Reconstruction, Interaction with Substrates, and Potential Applications. *Advanced Materials Interfaces* **2019,** *6* (1), 1801160.

337. Lipatov, A.; Alhabeb, M.; Lu, H.; Zhao, S.; Loes, M. J.; Vorobeva, N. S.; Dall'Agnese, Y.; Gao, Y.; Gruverman, A.; Gogotsi, Y.; Sinitskii, A., Electrical and Elastic Properties of Individual Single-Layer Nb4c3tx Mxene Flakes. *Advanced Electronic Materials* **2020,** *6* (4), 1901382.

338. Chen, W. Y.; Lai, S.-N.; Yen, C.-C.; Jiang, X.; Peroulis, D.; Stanciu, L. A., Surface Functionalization of Ti3c2tx Mxene with Highly Reliable Superhydrophobic Protection for Volatile Organic Compounds Sensing. *ACS Nano* **2020,** *14* (9), 11490-11501.

339. Karahan, H. E.; Goh, K.; Zhang, C.; Yang, E.; Yıldırım, C.; Chuah, C. Y.; Ahunbay, M. G.; Lee, J.; Tantekin-Ersolmaz, Ş. B.; Chen, Y.; Bae, T.-H., Mxene Materials for Designing Advanced Separation Membranes. *Advanced Materials* **2020,** *32* (29), 1906697.

340. Ding, L.; Wei, Y.; Li, L.; Zhang, T.; Wang, H.; Xue, J.; Ding, L.-X.; Wang, S.; Caro, J.; Gogotsi, Y., Mxene Molecular Sieving Membranes for Highly Efficient Gas Separation. *Nature Communications* **2018,** *9* (1), 155.

341. Hui, X.; Ge, X.; Zhao, R.; Li, Z.; Yin, L., Interface Chemistry on Mxene-Based Materials for Enhanced Energy Storage and Conversion Performance. *Advanced Functional Materials* **2020,** *30* (50), 2005190.

342. Zhan, X.; Si, C.; Zhou, J.; Sun, Z., Mxene and Mxene-Based Composites: Synthesis, Properties and Environment-Related Applications. *Nanoscale Horizons* **2020,** *5* (2), 235-258.

343. Sokol, M.; Natu, V.; Kota, S.; Barsoum, M. W., On the Chemical Diversity of the Max Phases. *Trends in Chemistry* **2019,** *1* (2), 210-223.

344. Abdolhosseinzadeh, S.; Jiang, X.; Zhang, H.; Qiu, J.; Zhang, C., Perspectives on Solution Processing of Two-Dimensional Mxenes. *Materials Today* **2021**.

345. Heckler, J. E.; Neher, G. R.; Mehmood, F.; Lioi, D. B.; Pachter, R.; Vaia, R.; Kennedy, W. J.; Nepal, D., Surface Functionalization of Ti3c2tx Mxene Nanosheets with Catechols: Implication for Colloidal Processing. *Langmuir* **2021,** *37* (18), 5447-5456.

346. Kumar, S.; Lei, Y.; Alshareef, N. H.; Quevedo-Lopez, M. A.; Salama, K. N., Biofunctionalized Two-Dimensional Ti3c2 Mxenes for Ultrasensitive Detection of Cancer Biomarker. *Biosensors and Bioelectronics* **2018,** *121*, 243-249.

347. McDaniel, R. M.; Carey, M. S.; Wilson, O. R.; Barsoum, M. W.; Magenau, A. J. D., Well-Dispersed Nanocomposites Using Covalently Modified, Multilayer, 2d Titanium Carbide (Mxene) and in-Situ “Click” Polymerization. *Chemistry of Materials* **2021,** *33* (5), 1648-1656.

348. Bian, R.; Xiang, S.; Cai, D., Fast Treatment of Mxene Films with Isocyanate to Give Enhanced Stability. *ChemNanoMat* **2020,** *6* (1), 64-67.

349. Guo, Q.; Zhang, X.; Zhao, F.; Song, Q.; Su, G.; Tan, Y.; Tao, Q.; Zhou, T.; Yu, Y.; Zhou, Z.; Lu, C., Protein-Inspired Self-Healable Ti3c2 Mxenes/Rubber-Based Supramolecular Elastomer for Intelligent Sensing. *ACS Nano* **2020,** *14* (3), 2788-2797.

350. Mayorga-Burrezo, P.; Muñoz, J.; Zaoralová, D.; Otyepka, M.; Pumera, M., Multiresponsive 2d Ti3c2tx Mxene Via Implanting Molecular Properties. *ACS Nano* **2021**.

351. Brochier Salon, M.-C.; Abdelmouleh, M.; Boufi, S.; Belgacem, M. N.; Gandini, A., Silane Adsorption onto Cellulose Fibers: Hydrolysis and Condensation Reactions. *Journal of Colloid and Interface Science* **2005,** *289* (1), 249-261.

352. Paris, J. L.; Villaverde, G.; Cabañas, M. V.; Manzano, M.; Vallet-Regí, M., From Proof-of-Concept Material to Pegylated and Modularly Targeted Ultrasound-Responsive Mesoporous Silica Nanoparticles. *Journal of Materials Chemistry B* **2018,** *6* (18), 2785-2794.

353. Kanchana, U. S.; Mathew, T. V., Surface Functionalization of Zno Nanoparticles with Functionalized Bovine Serum Albumin as a Biocompatible Photochemical and Antimicrobial Agent. *Surfaces and Interfaces* **2021,** *24*, 101056.

354. Jing, H.; Yeo, H.; Lyu, B.; Ryou, J.; Choi, S.; Park, J.-H.; Lee, B. H.; Kim, Y.-H.; Lee, S., Modulation of the Electronic Properties of Mxene (Ti3c2tx) Via Surface-Covalent Functionalization with Diazonium. *ACS Nano* **2021,** *15* (1), 1388-1396.

355. Hotchen, C. E.; Maybury, I. J.; Nelson, G. W.; Foord, J. S.; Holdway, P.; Marken, F., Amplified Electron Transfer at Poly-Ethylene-Glycol (Peg) Grafted Electrodes. *Physical Chemistry Chemical Physics* **2015,** *17* (17), 11260-11268.

356. Liu, B.-T.; Guo, B.-W.; Balamurugan, R., Effect of Polyethylene Glycol Incorporation in Electron Transport Layer on Photovoltaic Properties of Perovskite Solar Cells. *Nanomaterials (Basel)* **2020,** *10* (9), 1753.

357. Jana, A.; Lawrence, K. N.; Teunis, M. B.; Mandal, M.; Kumbhar, A.; Sardar, R., Investigating the Control by Quantum Confinement and Surface Ligand Coating of Photocatalytic Efficiency in Chalcopyrite Copper Indium Diselenide Nanocrystals. *Chemistry of Materials* **2016,** *28* (4), 1107-1120.

358. Fedorková, A.; Oriňáková, R.; Oriňák, A.; Wiemhöfer, H.-D.; Kaniansky, D.; Winter, M., Surface Treatment of Lifepo4 Cathode Material with Ppy/Peg Conductive Layer. *Journal of Solid State Electrochemistry* **2010,** *14* (12), 2173-2178.

359. Lee, J. T.; Seifert, S.; Sardar, R., Colloidal Synthesis of Single-Layer Quasi-Ruddlesden–Popper Phase Bismuth-Based Two-Dimensional Perovskite Nanosheets with Controllable Optoelectronic Properties. *Chemistry of Materials* **2021**.

360. Zhang, C., Interfacial Assembly of Two-Dimensional Mxenes. *Journal of Energy Chemistry* **2021,** *60*, 417-434.

361. Zamhuri, A.; Lim, G. P.; Ma, N. L.; Tee, K. S.; Soon, C. F., Mxene in the Lens of Biomedical Engineering: Synthesis, Applications and Future Outlook. *BioMedical Engineering OnLine* **2021,** *20* (1), 33.

362. Pelaz, B.; del Pino, P.; Maffre, P.; Hartmann, R.; Gallego, M.; Rivera-Fernández, S.; de la Fuente, J. M.; Nienhaus, G. U.; Parak, W. J., Surface Functionalization of Nanoparticles with Polyethylene Glycol: Effects on Protein Adsorption and Cellular Uptake. *ACS Nano* **2015,** *9* (7), 6996-7008.

363. Zheng, M.; Davidson, F.; Huang, X., Ethylene Glycol Monolayer Protected Nanoparticles for Eliminating Nonspecific Binding with Biological Molecules. *Journal of the American Chemical Society* **2003,** *125* (26), 7790-7791.

364. Zheng, M.; Li, Z.; Huang, X., Ethylene Glycol Monolayer Protected Nanoparticles: Synthesis, Characterization, and Interactions with Biological Molecules. *Langmuir* **2004,** *20* (10), 4226-4235.

365. Neises, B.; Steglich, W., Simple Method for the Esterification of Carboxylic Acids. *Angewandte Chemie International Edition in English* **1978,** *17* (7), 522-524.

366. Hermawan, A.; Zhang, B.; Taufik, A.; Asakura, Y.; Hasegawa, T.; Zhu, J.; Shi, P.; Yin, S., Cuo Nanoparticles/Ti3c2tx Mxene Hybrid Nanocomposites for Detection of Toluene Gas. *ACS Applied Nano Materials* **2020,** *3* (5), 4755-4766.

367. Lim, K. R. G.; Handoko, A. D.; Nemani, S. K.; Wyatt, B.; Jiang, H.-Y.; Tang, J.; Anasori, B.; Seh, Z. W., Rational Design of Two-Dimensional Transition Metal Carbide/Nitride (Mxene) Hybrids and Nanocomposites for Catalytic Energy Storage and Conversion. *ACS Nano* **2020,** *14* (9), 10834-10864.

368. Kamysbayev, V.; Filatov, A. S.; Hu, H.; Rui, X.; Lagunas, F.; Wang, D.; Klie, R. F.; Talapin, D. V., Covalent Surface Modifications and Superconductivity of Two-Dimensional Metal Carbide Mxenes. *Science* **2020,** *369* (6506), 979-983.

369. Lioi, D. B.; Neher, G.; Heckler, J. E.; Back, T.; Mehmood, F.; Nepal, D.; Pachter, R.; Vaia, R.; Kennedy, W. J., Electron-Withdrawing Effect of Native Terminal Groups on the Lattice Structure of Ti3c2tx Mxenes Studied by Resonance Raman Scattering: Implications for Embedding Mxenes in Electronic Composites. *ACS Applied Nano Materials* **2019,** *2* (10), 6087-6091.

370. Hu, T.; Wang, J.; Zhang, H.; Li, Z.; Hu, M.; Wang, X., Vibrational Properties of Ti3c2 and Ti3c2t2 (T = O, F, Oh) Monosheets by First-Principles Calculations: A Comparative Study. *Physical Chemistry Chemical Physics* **2015,** *17* (15), 9997-10003.

371. Naguib, M.; Mashtalir, O.; Lukatskaya, M. R.; Dyatkin, B.; Zhang, C.; Presser, V.; Gogotsi, Y.; Barsoum, M. W., One-Step Synthesis of Nanocrystalline Transition Metal Oxides on Thin Sheets of Disordered Graphitic Carbon by Oxidation of Mxenes. *Chemical Communications* **2014,** *50* (56), 7420-7423.

372. Li, Y.; Zhou, X.; Wang, J.; Deng, Q.; Li, M.; Du, S.; Han, Y.-H.; Lee, J.; Huang, Q., Facile Preparation of in Situ Coated Ti3c2tx/Ni0.5zn0.5fe2o4 Composites and Their Electromagnetic Performance. *RSC Advances* **2017,** *7* (40), 24698-24708.

373. Wyatt, B. C.; Nemani, S. K.; Desai, K.; Kaur, H.; Zhang, B.; Anasori, B., High-Temperature Stability and Phase Transformations of Titanium Carbide (Ti(3)C(2)T(X)) Mxene. *Journal of physics. Condensed matter : an Institute of Physics journal* **2021,** *33* (22).

374. Seredych, M.; Shuck, C. E.; Pinto, D.; Alhabeb, M.; Precetti, E.; Deysher, G.; Anasori, B.; Kurra, N.; Gogotsi, Y., High-Temperature Behavior and Surface Chemistry of Carbide Mxenes Studied by Thermal Analysis. *Chemistry of Materials* **2019,** *31* (9), 3324-3332.

375. Ensing, B.; Tiwari, A.; Tros, M.; Hunger, J.; Domingos, S. R.; Pérez, C.; Smits, G.; Bonn, M.; Bonn, D.; Woutersen, S., On the Origin of the Extremely Different Solubilities of Polyethers in Water. *Nature Communications* **2019,** *10* (1), 2893.

376. Reichardt, C., Solvent Effects on the Absorption Spectra of Organic Compounds. In *Solvents and Solvent Effects in Organic Chemistry*, 3rd ed.; WILEY-VCH: Weinheim, 2003; pp 329-388.

377. Ren, C. E.; Hatzell, K. B.; Alhabeb, M.; Ling, Z.; Mahmoud, K. A.; Gogotsi, Y., Charge- and Size-Selective Ion Sieving through Ti3c2tx Mxene Membranes. *The Journal of Physical Chemistry Letters* **2015,** *6* (20), 4026-4031.

378. Zhao, S.; Zhang, H.-B.; Luo, J.-Q.; Wang, Q.-W.; Xu, B.; Hong, S.; Yu, Z.-Z., Highly Electrically Conductive Three-Dimensional Ti3c2tx Mxene/Reduced Graphene Oxide Hybrid Aerogels with Excellent Electromagnetic Interference Shielding Performances. *ACS Nano* **2018,** *12* (11), 11193-11202.

379. Jerie, K.; Baranowski, A.; Przybylski, J.; Gliński, J., Electrolytic Solutions in Ethylene Glycol: Ultrasonic and Positron Annihilation Studies. *Physics Letters A* **2004,** *323* (1), 148-153.

380. Maltesh, C.; Somasundaran, P., Effect of Binding of Cations to Polyethylene Glycol on Its Interactions with Sodium Dodecyl Sulfate. *Langmuir* **1992,** *8* (8), 1926-1930.

381. Poudel, L.; Podgornik, R.; Ching, W.-Y., The Hydration Effect and Selectivity of Alkali Metal Ions on Poly(Ethylene Glycol) Models in Cyclic and Linear Topology. *The Journal of Physical Chemistry A* **2017,** *121* (24), 4721-4731.

382. Chen, J.; Spear, S. K.; Huddleston, J. G.; Rogers, R. D., Polyethylene Glycol and Solutions of Polyethylene Glycol as Green Reaction Media. *Green Chemistry* **2005,** *7* (2), 64-82.

383. Li, G.; Jiang, K.; Zaman, S.; Xuan, J.; Wang, Z.; Geng, F., Ti3c2 Sheets with an Adjustable Surface and Feature Sizes to Regulate the Chemical Stability. *Inorganic Chemistry* **2019,** *58* (14), 9397-9403.

384. Connon, S. J.; Blechert, S., Recent Developments in Olefin Cross-Metathesis. *Angewandte Chemie International Edition* **2003,** *42* (17), 1900-1923.

385. Iha, R. K.; Wooley, K. L.; Nyström, A. M.; Burke, D. J.; Kade, M. J.; Hawker, C. J., Applications of Orthogonal “Click” Chemistries in the Synthesis of Functional Soft Materials. *Chemical Reviews* **2009,** *109* (11), 5620-5686.

386. Döhler, D.; Michael, P.; Binder, W. H., Cuaac-Based Click Chemistry in Self-Healing Polymers. *Accounts of Chemical Research* **2017,** *50* (10), 2610-2620.

387. Hantanasirisakul, K.; Anasori, B.; Nemsak, S.; Hart, J. L.; Wu, J.; Yang, Y.; Chopdekar, R. V.; Shafer, P.; May, A. F.; Moon, E. J.; Zhou, J.; Zhang, Q.; Taheri, M. L.; May, S. J.; Gogotsi, Y., Evidence of a Magnetic Transition in Atomically Thin Cr2tic2tx Mxene. *Nanoscale Horizons* **2020,** *5* (12), 1557-1565.

388. Nemani, S. K.; Zhang, B.; Wyatt, B. C.; Hood, Z. D.; Manna, S.; Khaledialidusti, R.; Hong, W.; Sternberg, M. G.; Sankaranarayanan, S. K. R. S.; Anasori, B., High-Entropy 2d Carbide Mxenes: Tivnbmoc3 and Tivcrmoc3. *ACS Nano* **2021**.

389. Harris, J. M., Laboratory Synthesis of Polyethylene Glycol Derivatives. *Journal of Macromolecular Science, Part C* **1985,** *25* (3), 325-373.

PUBLICATIONS

1. **Jacob T. Lee***, Debabrata Das*, Gregory A. Davis, Jr., Sumon Hati, Ramana V. Chintalapalle, Rajesh Sardar, The Optical Response of Thin Films Fabricated From Surface Modified Plasmonic Ultrathin WO_{3-x} Nanoplatelets. *Manuscript in Preparation*
2. **Jacob T. Lee**, Debabrata Das, Ramana V. Chintalapalle, Rajesh Sardar, Shape Control and Alloying of Plasmonic WO_{3-x} Through Ultrasmall Nanocluster Seeds. *Manuscript in Preparation*
3. **Jacob T. Lee**, Sumon Hati, Mackenzie M. Fahey, Jeffrey M. Zaleski, Rajesh Sardar; Surface Ligand Controlled Enhancement of Carrier Density in Plasmonic Tungsten Oxide Nanocrystals: Spectroscopic Observation of Trap-State Passivation *via* Multidentate Metal-Phosphonate Bonding. *Chemistry of Materials, Accepted*
4. **Jacob T. Lee*,** Brian C. Wyatt*, Gregory A. Davis Jr, Adrianna N. Masterson, Amber L. Pagan, Archit Shah, Babak Anasori, Rajesh Sardar; Chemically Active Polymeric Ligands Producing Highly Conductive and Ordered Microstructure Films. *ACS Nano.* **2021**, 15, 12, 19600-19612
5. **Jacob T. Lee,** Soenke Seifert, Rajesh Sardar; Colloidal Synthesis of Single-Layer Quasi-Ruddlesden-Popper PhaseBismuth-Based Two-Dimensional Perovskite Nanosheets with Controllable Optoelectronic Properites. *Chem. Mater.* **2021**, 33, 5914-5925.
6. Gyanaranjan Prusty*, **Jacob T. Lee***, Soenke Seifert, Barry B. Muhoberac, and Rajesh Sardar; Ultrathin Plasmonic Tungsten Oxide Quantum Wells with Controllable Free Carrier Densities. *J. Am. Chem. Soc.* **2020** *142* (13), 5938-5942
7. Yang Yang*, **Jacob T. Lee***, Thakshila Liyanage, and Rajesh Sardar. Flexible Polymer-Assisted Mesoscale Self-Assembly of Colloidal $CsPbBr_3$ Perovskite Nanocrystals into Higher Order Superstructures with Strong Inter-Nanocrystal Electronic Coupling. *J. Am. Chem. Soc.* **2019**, 141, 1526-1536